THERMAL STABILITY AND MECHANICAL PROPERTIES OF Fe-Cr NANOSTRUCTURES PREPARED BY MECHANICAL ALLOYING FOLLOWED BY SPARK PLASMA SINTERING

Ph.D. THESIS

by

V.M. SUNTHARAVEL MUTHAIAH

DEPARTMENT OF METALLURGICAL AND MATERIALS ENGINEERING
INDIAN INSTITUTE OF TECHNOLOGY ROORKEE
ROORKEE - 247667 (INDIA)
OCTOBER, 2018

THERMAL STABILITY AND MECHANICAL PROPERTIES OF Fe-Cr NANOSTRUCTURES PREPARED BY MECHANICAL ALLOYING FOLLOWED BY SPARK PLASMA SINTERING

A THESIS

Submitted in partial fulfilment of the requirements for the award of the degree

of

DOCTOR OF PHILOSOPHY

in

METALLURGICAL AND MATERIALS ENGINEERING

by

V.M. SUNTHARAVEL MUTHAIAH

DEPARTMENT OF METALLURGICAL AND MATERIALS ENGINEERING
INDIAN INSTITUTE OF TECHNOLOGY ROORKEE
ROORKEE - 247667 (INDIA)
OCTOBER, 2018

INDIAN INSTITUTE OF TECHNOLOGY ROORKEE
ROORKEE

CANDIDATE'S DECLARATION

I hereby certify that the work which is being presented in the thesis entitled "**THERMAL STABILITY AND MECHANICAL PROPERTIES OF Fe-Cr NANOSTRUCTURES PREPARED BY MECHANICAL ALLOYING FOLLOWED BY SPARK PLASMA SINTERING**" in partial fulfilment of the requirements for the award of the degree of Doctor of Philosophy and submitted in the **Department of Metallurgical and Materials Engineering**, Indian Institute of Technology Roorkee, Roorkee is an authentic record of my own work carried out during the period from January, 2014 to October, 2018 under the supervision of Dr. Suhrit Mula, Associate Professor, Department of Metallurgical and Materials Engineering, Indian Institute of Technology Roorkee, Roorkee.

The matter presented in this thesis has not been submitted by me for the award of any other degree of this or any other Institution.

(V.M. SUNTHARAVEL MUTHAIAH)

This is to certify that the above statement made by the candidate is correct to the best of my knowledge.

(Suhrit Mula)
Supervisor

The Ph.D. Viva-Voce Examination of **Mr. (V.M. SUNTHARAVEL MUTHAIAH)**, Research Scholar, has been held on .....

Chairman, SRC

Signature of External Examiner
Dr. B.S. Murty
Professor
Dept. of Metallurgical & Materials Engg.,
Indian Institute of Technology Madras
Chennai-600 036, India

This is to certify that the student has made all the corrections in the thesis.

Signature of Supervisor

Head of the Department

Dated

Acknowledgement

First of all, I would like to express my sincere gratitude, deepest respect and heartiest thanks to my supervisor, Dr. Suhrit Mula, Assistant Professor, Department of Metallurgical and Materials Engineering, Indian Institute of Technology, Roorkee for his valuable and intellectual guidance, unwavering support and encouragement throughout the tenure of my research work. This thesis could not have attained its present form both in content and presentation, without his active interest, timely help, painstaking efforts, direction and valuable guidance. The words prove to be insufficient to express my deep feelings and heartfelt thanks to my supervisor for their high benevolence guidance throughout my doctoral work.

I express my immense gratitude and indebtedness to Professor Anjan Sil, Head of Metallurgical and Materials Engineering Department, Dr. G.P. Chaudhari (Chairman SRC), Dr. B.V. Manoj Kumar (Internal member), Metallurgical and Materials Engineering Department and Dr. Kaushik Pal (External member), Department of Mechanical and Industrial Engineering, Indian Institute of Technology Roorkee for their continuous help, valuable suggestions and encouragements to pursue this work.

I am grateful to all my colleagues in the spark plasma sintering laboratory and also staff members of Metallography Laboratory and Materials Testing Laboratory, who have assisted me despite the difficulties they faced during the closure of the laboratory. I am also grateful to all the technical and administrative staff from the Department and Institute Instrumentation Centre, IIT Roorkee. I am thankful to the Professor Dr. R. Jayagathan, and Dr. Debrupa Lahiri, Assistant professor, provided me to access their laboratories.

Special thanks to my friends Mr. Nilesh Dorkar, Mr. Atul Sharma, Mr. Ashwin Godusu Mr. J.P. Moses., Dr. Ram Kishore and Dr. Sunil, who helped me at any time whenever I needed.

Finally, I would like to share this moment of happiness with my father, Mr. M.V. Muthurathinam, mother Mrs. V.M. Suheela, and my sisters Dr. V.M. Anithrajathi, V.M. Rajanadhini and V.M. Priyadharshini. I express my profound regards to my parents and sisters for their blessings and constant encouragement and inspiration to succeed in my endeavors. I would like to express my reverence and great admiration to my family and relatives V.M.

Rajavel Muthaiah, V.M. Illayaraja Muthaiaya, time being help and providing me constant encouragement.

Above all, I express my gratitude from the core of my heart to God for giving me courage, strength and patience to carry out my research work.

IIT Roorkee
Date: October 10, 2018 **(V.M. Suntharavel Muthaiah)**

Abstract

Iron (Fe)-based alloys, especially, Fe-Cr alloys have wide variety of applications in various industries such as nuclear, construction, automotive, oil, gas etc. due to their superior strength and formability, high corrosion resistance, minimum embrittlement and low maintenance cost. These alloys are also being used for high temperature applications primarily in energy conversion plants, refractory supports, hot acid containers, oven linings and heat exchangers. Demand to improve the efficiency as well as performance of the components in high temperature applications has increased enormously. Nowadays, it is well known that the nanocrystalline/ultrafine grained (nc/UFG) structure can provide significant strength and toughness to the materials, which have attracted considerable scientific interest in the recent past. However, the nc/UFG materials have high surface energy and high surface area/volume ratio. This makes them unstable and grain coarsening occurs as a result of sintering of these nc/UFG materials at medium to high temperature regime. Therefore, the nc/UFG Fe-Cr alloys must be stable to realize their unique mechanical properties. An appropriate type and quantity of insoluble oversize (compared to solvent atoms) solute atoms (e.g. Y, Nb, Zr, Hf etc.) dissolved in the matrix (e.g. Fe) could restrict grain growth successfully at elevated temperatures. First, the oversize insoluble solute atoms are brought into the solid solution of matrix by a non-equilibrium processing method, such as mechanical alloying (MA). The MA is preferred due to its effectiveness in preparing highly supersaturated solid solutions in non-equilibrium alloy system (e.g. Fe-Cr-Y/Zr/Nb) easily in large quantities. Then, the supersaturated solute atoms in the disordered solid solution are allowed to segregate along the matrix grain boundaries and/or precipitate out during annealing at suitable temperature/further processing. Thus, grain size stabilization at high temperature could be achieved by two approaches: first approach is the kinetic mechanism that involves precipitation of second-phase particles, which obstruct the mobility of grain boundary by Zener pinning. The second approach is the thermodynamic mechanism that involves segregation of oversize solute atoms along the matrix grain boundaries, which reduces grain boundary energy (γ) to zero (or close to zero). Hence, the stabilization of the nc/UFG Fe-Cr alloys (after addition of oversize solute atoms) could be attained through Zener pinning and/or thermodynamic approach depending on the phase evolution (i.e. solid solution/intermetallic compound etc.) during processing and/or

annealing. Hence, the MA followed by spark plasma sintering (SPS) could be an effective route to produce stabilize Fe-Cr nc/UFG alloys for high temperature applications.

First, four Fe-Cr alloys (Cr = 7, 11, 15 & 19 at.%) were developed by MA for 25 h and their thermal stability was investigated (all in at.%). It was found that the nc Fe-Cr alloys developed by MA dictated a poor thermal stability. Therefore, the Fe-7Cr (low Cr content) and Fe-15Cr (high Cr content) alloys were chosen to study their thermal stability further after addition of small quantity of insoluble solute atoms (i.e. 0.25, 0.5 & 1at.% of Y/Nb/Zr). Then, Fe-7Cr-X and Fe-15Cr-X (X=0.25, 0.5 & 1at.% of Y/Nb/Zr) alloys (after addition of suitable solute) were developed by MA under same conditions of milling (as done for Fe-Cr alloys). The feasibility of formation of the Fe-7Cr-X and Fe-15Cr-X disordered solid solutions was confirmed by XRD phase analysis & increase in the lattice parameter calculation, thermodynamic feasibility analysis (change in the Gibbs free energy estimation by Toop's model) and TEM-SAED analysis. The increase in the lattice parameter of the Fe-lattices (solvent) indicates the formation of ordered/disordered solid solution due to the dissolution of solute atoms (i.e. Cr and oversize solute atoms of Y/Nb/Zr) in Fe. Thermodynamic feasibility analysis as per Toop's model confirms that the energy barrier required to form the disordered solid solutions has been overcome by the total stored energy due to the grain boundary energy and lattice strain energy. Moreover, XRD phase analysis followed by TEM-SAED pattern analysis of the as-milled samples did not reveal any peak related to free Cr and Y/Nb/Zr or any intermetallic phase(s). This also confirmed the formation of the complete solid solutions of the Fe-7Cr-X and Fe-15Cr-X compositions by MA.

Then, the as-milled powder samples were annealed in batches from 600-1200°C under Ar+2%H_2 atmosphere. During annealing, the Fe-Cr-Y & Fe-Cr-Zr samples were found to decompose partially to form dilute quantity of $Fe_{17}Y_2$ & Fe_2Zr intermetallic phases, respectively, in the matrix of nanocrystalline solid solutions; whereas, the Fe-Cr-Nb alloys retained their complete solid solubility after the annealing (up to 1200°C). This is confirmed by XRD phase analysis followed by TEM-SAED pattern analysis. After the annealing at 1000°C, TEM grain size was found to retain within 100 nm for all the three alloys (i.e. 50, 53 and 55 nm for the Fe-15Cr-1Nb, Fe-15Cr-1Y and Fe-15Cr-1Zr alloys) with a corresponding hardness value of 8.3, 8.1 and 8.4 GPa, respectively. The estimated yield strength (YS) (as per Cahoon model) of the annealed Fe-15Cr-1Nb sample (at 1000°C) is found to be quite attractive (i.e. YS:1754 MPa) and correlated well with the hardness value (8.3 GPa) and its microstructural

features. Overall, it is found that the Fe-15Cr-1Nb, Fe-15Cr-1Y and Fe-15Cr-1Zr alloys showed excellent thermal stability in terms of the grain size stability (<100 nm) and retaining a quite high microhardness values (8-8.5 GPa). On the basis of the thermal stability, the suitable compositions, such as Fe-7Cr-X & Fe-15Cr-X (X: Y-1; Nb: 0.25, 1 and Zr: 1at.%) were chosen and consolidated by SPS at 800, 900 & 1000°C. Microstructural features of the SPSed samples characterized by optical and SEM were found to corroborate well with the sintered density obtained by Archimedes method. The relative sinter density of the SPSed (at 1000°C) Fe-15Cr-1Y, Fe-15Cr-1Nb & Fe-15Cr-1Zr alloys was estimated to be in the range of 97-98%. XRD phase analysis followed by TEM-SAED pattern analysis of the SPSed samples also confirmed the formation of $Fe_{17}Y_2$ & Fe_2Zr intermetallic phases in the Fe-Cr-Y and Fe-Cr-Zr alloys; whereas, the Fe-Cr-Nb alloys retained the complete solid solubility after the SPS. TEM grain size of the SPSed (at 1000°C) samples was found to stabilize within 100 nm (49, 72 and 61 nm, respectively, for Fe-15Cr-1Nb, Fe-15Cr-1Y and Fe-15Cr-1Zr alloys). The corresponding microhardness values were estimated to be 9.5, 9.6 and 9.45 GPa, respectively. The experimental compressive strength (UCS-2400 MPa, YS-1800 MPa for Fe-15Cr-1Nb; UCS-2600 MPa, YS-2000 MPa for Fe-15Cr-1Y and UCS-2200 MPa, YS-1600 MPa for Fe-15Cr-1Zr) of the SPSed (at 1000°C) samples depicted a very good correlation with the corresponding density, hardness and microstructural features. Analysis of various strengthening mechanisms of the SPSed Fe-15Cr-1Nb alloy was performed in the light of solid solution strengthening, grain size strengthening and dislocation strengthening and their quantitative contribution to the total YS was estimated. The estimated total YS (i.e. YS:1744 MPa) was found to correlate well with experimentally measured compressive YS (i.e. 1800 MPa) of the corresponding sample.

The best combination of hardness, wear resistance and corrosion behavior was achieved for the samples sintered at 1000°C. The high hardness, minimum coefficient of friction and extremely low wear volume & low corrosion rate obtained have been discussed in the light of solid solution strengthening, grain size strengthening, grain boundary segregation, densification and diffusion bonding and precipitation hardening by intermetallic phase ($Fe_{17}Y_2$ & Fe_2Zr) in the alloy matrix. The wear and corrosion resistance are found to be almost similar for the Fe-15Cr-1Y, Fe-15Cr-1Nb and Fe-15Cr-1Zr SPSed samples (e.g. wear volume and CR: 0.00196×10^{-2} mm^3 & 3.43 mpy for Fe-15Cr-1Y, 0.00169×10^{-2} mm^3 & 4.12 mpy for Fe-15Cr-1Nb and 0.00186×10^{-2} mm^3 & 4.02 mpy for Fe-15Cr-1Zr); but these are much superior as compared to

that of the other SPSed samples studied (0.0024×10^{-2} mm^3 & 3.46 mpy for Fe-7Cr-1Y, 0.0023×10^{-2} mm^3 & 6.03 mpy for Fe-7Cr-1Nb, 0.0025×10^{-2} mm^3 & 4.89 mpy for Fe-7Cr-1Zr). The SEM analysis of the worn surface and corroded features corroborated well with the wear resistance and corrosion behavior of the corresponding samples.

Overall, the Fe-15Cr-1Y/1Nb/1Zr alloys showed superior thermal stability and the SPSed samples of these alloys revealed highly attractive mechanical properties (hardness of 9-10 GPa), excellent wear resistance and outstanding compressive YS (1600-2000 MPa). Moreover, the corrosion resistance of these SPSed samples was found highly significant in aerated 3.5% NaCl solution. Therefore, the bulk-size samples of the Fe-Cr-Y/Nb/Zr alloys are expected to be highly suitable for applications in coal mining machinery parts (e.g. mining sliding shoes), cement industry (e.g. cement roller press), nuclear first wall reactor (750-950°C), automotive (e.g. exhaust system operating at 800-850°C), chemical processing unit (e.g. acid carrying pipes 320-450°C, petrochemical industries U-tube) etc., where high wear resistance and good corrosion resistance are essential.

Keywords: Fe-Cr-Y/Nb/Zr alloys; Mechanical alloying; Spark plasma sintering; Miedema's & Toop's models; Thermodynamic mechanisms; Grain boundary solute segregation; Kinetic mechanisms; Zener pinning; Nanoscale intermetallic; Electron microscopy.

Contents

List of figures

List of tables

List of symbols

$°C$	Degree Celsius
h	Hour
min	Minute
nm	Nanometer
μm	Micrometer
mm	Millimeter
GPa	Giga Pascal
MPa	Mega Pascal
kN	Kilo-Newton
N	Newton
λ	Wavelength
kV	Kilo Volt
mV	Milli Volt
mpy	Mile per year
kJ	Kilojoule
K_{HP}	Hall-Petch constant
d	Crystallite size
K	Kelvin
s^{-1}	Per second
Fe	Iron
Cr	Chromium
Y	Yttrium
Nb	Niobium
Zr	Zirconium
γ	Grain boundary energy
Q	Activation energy
P_z	Pinning pressure
μ_s	Chemical potential
ΔG	Gibbs free energy
ΔH	Enthalpy

ΔS	Entropy
G	Shear modulus
V	Molar volume
b	Burgers vector
ρ	Dislocation density
α	Dislocation strengthening constant
ξ	Elastic energy
σ_{ss}	Solid solution strengthening
σ_{gs}	Grain size strengthening
σ_{d}	Dislocation strengthening
R	Universal gas constant
v	Poisson ratio
C	Solute concentration
m^{-1}	Per meter
mm^{3}	Cubic millimeter
λ	Wave length
θ	Bragg angle
a	Lattice parameter
Hv	Vickers hardness
ε_{b}	Misfit strain of atomic size
σ_{UTS}	Ultimate tensile strength
σ_{Y}s	Yield strength

Abbreviations

AFM	Atomic force microscopy
ARB	Accumulative roll bonding
BCC	Body center cubic
BPR	Ball to powder weight ratio
BSE	Back scattered electron
COF	Coefficient of friction
CR	Corrosion rate
EBSD	Electron back scattered diffraction
EDS	Energy dispersive spectroscopy
ECAP	Equal channel angular pressing
FCC	Face center cubic structure
FG	Fine grain
Fig	Figure
FWHM	Full width half maximum
GAM	Grain average misorientation
GB	Grain boundary
HAGB	High angle grain boundary
HEBM	High energy ball mill
HIP	Hot isostatic pressing
HPT	High pressure torsion
HP	Hot pressing
LAGB	Low angle grain boundary
MA	Mechanical alloying
MAF	Multiaxial forging
MVS	Microwave sintering
nc	Nanocrystalline
OCP	Open circuit potential
OM	Optical microscopy
PCA	Process control agent
PLS	Pressure less sintering
SAED	Selected area electron diffraction
SE	Secondary electron
SEM	Scanning electron microscope
SPS	Spark plasma sintering
SPD	Severe plastic deformation
TEM	Transmission electron microscopy
UFG	Ultrafine grains
UCS	Ultimate compressive strength
YS	Yield strength

List of publications

Journals:

[1] **V.M. Suntharavel Muthaiah,** Hari Babu L, Carl C Koch, Suhrit Mula. "Feasibility of formation of nanocrystalline Fe-Cr-Y alloys: Mechanical properties and thermal stability", **Materials Characterization**, Volume 114, April 2016, Pages 43-53. (Impact Factor: **2.383**)

[2] Sooraj S, **V.M. Suntharavel Muthaiah,** P.C. Kang, Carl C Koch, Suhrit Mula, "Microstructural evolution and thermal stability of Fe-Zr metastable alloys developed by mechanical alloying followed by annealing", **Philosophical Magazine**, Volume 96, No. 25, June 2016, 2649-2670. (Impact Factor: **1.632**)

[3] **V.M. Suntharavel Muthaiah,** Suhrit Mula, "Influence of Cr and Y addition on microstructure, mechanical properties and corrosion resistance of SPSed Fe-based alloys". **Metallurgical and Materials Transaction A**, Volume 49, March 2018 No. 25, 990-1005. (Impact Factor: **1.874**).

[4] **V.M. Suntharavel Muthaiah,** Suhrit Mula, "Effect of Nb additions on the formation of Fe-7Cr and Fe-15Cr metastable alloys by mechanical alloying and their thermal stability", **Materials Research Express**, 5, May 2018, 056534. (Impact Factor: **1.069**).

[5] **V.M. Suntharavel Muthaiah,** Suhrit Mula, "Microstructural evolution and mechanical properties of spark plasma sintered nanocrystalline Fe-Cr-Nb alloys for nuclear applications". **Material Science Engineering A,** Volume 739, January 2019, 367-376. (Impact Factor: **3.414**).

[6] **V.M. Suntharavel Muthaiah,** Suhrit Mula, "Influence of Zr on Fe-Cr-Zr alloys prepared by mechanical alloying and spark plasma sintering: thermal stability and mechanical properties. (Communicated).

[7] **V.M. Suntharavel Muthaiah,** Suhrit Mula, "Wear behavior of spark plasma sintered nanocrystalline Fe-7Cr-1Y/Nb/Zr and Fe-15Cr-1Y/Nb/Zr alloys developed by mechanical alloying. (Communicated).

Conferences:

[1] **V.M. Suntharavel Muthaiah**, L. Hari Babu, Suhrit Mula, "Thermal Stabilization of nanocrystalline Fe-Cr alloys developed by mechanical alloying", International Conference on Advance Materials and Manufacturing Process for Strategic Sector in ICAMPS at Thiruvananthapuram, Kerala (12-15 May 2015).

[2] **V.M. Suntharavel Muthaiah,** Suhrit Mula, "Thermal stability and mechanical properties of spark plasma sintered Fe-Cr-Y alloys prepared by mechanical alloying", International Conference on Nano-materials for Structural, Functional and Energy Applications in ICAMMP - IV at IIT Kharagpur (5-7 November 2016).

[3] **V.M. Suntharavel Muthaiah,** Suhrit Mula, "Effect of Nb addition on structure and thermal stability of nanocrystalline Fe- Cr alloys developed by mechanical alloying". International Conference on Nano-materials for Structural, Functional and Energy Applications in ICAMMP - IV at IIT Kharagpur (5-7 November 2016).

[4] **V.M. Suntharavel Muthaiah,** Suhrit Mula. Spark plasma sintered Fe-Cr-Nb alloys for nuclear applications. NMD ATM 2017, BITS Pilani, KK Birla Goa Campus, 55th National Metallurgist day & 71st Annual technical meeting, 11-14 Nov, 2017.

[5] **V.M. Suntharavel Muthaiah,** Suhrit Mula. Formation of nanostructured Fe-Cr-Zr alloys and their thermal stability: microstructure and mechanical properties, NMD ATM 2018, Hotel, J W Marriott, Kolkata, 56^{th} National Metallurgist day & 72^{nd} Annual technical meeting, 14-16 Nov, 2018**.**

CHAPTER 1 Introduction

Iron (Fe), which exhibits BCC crystal structure at room temperature, may form FCC structure either by heating above 912°C or by alloying with different austenitizing elements. The properties of iron can be enhanced by adding various alloying elements, performing heat treatment operations to induce the desired properties for a desired application. Fe alloyed with various elements, which is termed as steel, has a wide range of applications such as various structural applications, automobile industry, making of magnets, other household appliances etc. Due to its high strength, low cost and ease of availability, the steel is very commonly used material in the world (Dubiel et al., 2015). Fe nanoparticles are used in magnetic recording media and transformer cores. Fe-Cr alloys have wide variety of applications in various industries such as nuclear, construction, automotive, oil and gas, chemical processing etc. due to their high corrosion resistance, minimum embrittlement and low maintenance cost (Baddoo 2008; Hishinuma et al., 1997; Matijasevic 2007; Oka et al., 2007). Fe-Cr alloys are being used for high temperature applications primarily in energy conversion plants, refractory supports, hot acid containers, oven linings and heat exchangers (Peckner et al., 1977). Demand to improve the efficiency and performance of the components in high temperature applications has increased enormously. It is now known that nanocrystalline (nc)/ultrafine grained (UFG) structure provides significant strength and toughness to the materials, which have attracted considerable scientific interest in the recent past (Li et al., 2009).

However, the nc/UFG materials have high surface energy and high surface area/volume ratio. This makes them unstable and grain coarsening occurs as a result of sintering of these nc/UFG materials at medium to high temperatures. Extensive grain growth occurs in pure nc metals due to reduction of excess grain boundary free energy that decreases grain boundary area and provides a very large driving force for grain growth (Alleg et al., 2013; Driver 2004; Koch 2007; Leyla et al., 2015; Mccrea et al., 2003; Murty et al., 2003). Even metals with high melting points, such as Fe are not exceptions to this phenomenon and demonstrate rapid grain growth at temperatures below their melting points (Darling et al., 2010). Appropriate insoluble oversize solute atoms when alloyed with metals are successful in restricting the grain growth at elevated temperatures (Darling et al., 2015; Detor et al., 2007; Koch et al., 2008; Millett et al., 2007; Weissmuller 1993). Hence in technological point of view, thermal stability becomes an

important phenomenon required to address as nc/UFG Fe-based alloys face a problem of grain coarsening when operated at medium to high temperatures, and this limits their functionality and industrial applications (Darling et al., 2010; Saber et al., 2012). Thus, it is most essential to develop nc/UFG alloys that are resistant to grain growth at high temperature to make their significant properties useful.

Grain size stabilization at high temperatures can be achieved by two approaches (Darling et al., 2010; Koch et al., 2012; Li et al., 2014). The first approach is kinetic mechanism that involves second-phase particle pinning (Zener pinning), solute drag, porosity, or chemical ordering to obstruct the mobility of grain boundary (Cahn 1962; Driver 2004; Hillert 1965; Libardi et al., 2007; Ringer et al., 1989). On the other hand, the second approach is thermodynamic mechanism that involves addition of solute atoms that segregates to the grain boundaries to reduce grain boundary energy γ to zero (Pellicer et al., 2011; Kirchheim 2002). Thus, stabilization of the nanostructured Fe-Cr materials could be achieved through mechanisms of Zener pinning and/or thermodynamic approach depending on the development of the phases (i.e. solid solution/intermetallic compound etc.) during processing and/or annealing or heat treatment. A number of studies (Darling et al., 2010; Li et al., 2014; Saber et al., 2012) have demonstrated the stabilization of Fe-based alloys by addition of solutes like Zr and Hf. The thermal stability specific to nc Fe-based alloys was predicted by Darling et al. (2011) through a regular solution model for grain boundary solute segregation. The model proposed that Y can provide satisfactory stabilization of Fe, but it causes an embrittling effect of Fe grain boundaries. Pure Ni exhibited kinetic stabilization at high temperature due to Y addition and retained a grain size of ~100 nm at 900°C (Darling et al., 2013). The effect of misfit solutes on the thermal stability of Cu-based alloys prepared by mechanical alloying was studied by various researchers like Cu-Nb (Mula et al., 2012), Cu-Y (Mula et al., 2015), Cu-Zr (Atwater et al., 2013; Azimi et al., 2011; Roy et al., 2013), Cu-Ta (Darling et al., 2013) and it was found that a higher extent of thermal stability was exhibited by the addition of Nb, Y and Zr in Cu.

Bulk metals and alloys with nc/UFG structure could be produced by various severe plastic deformation (SPD) techniques such as cryorolling, equal channel angular pressing (ECAP), accumulating roll bonding (ARB), multiaxial forging (MAF), high pressure torsion (HPT) (Valiev et al., 2000) etc. But, for immiscible alloy systems, such as Fe-Cr-Y, Fe-Cr-Nb and Fe-Cr-Zr, the SPD techniques cannot be useful to produce homogeneous nc/UFG solid solutions or

alloys. Therefore, other non-equilibrium processing routes must be followed to prepare such disordered solid solutions or alloys. Among the non-equilibrium processing routes, mechanical alloying (MA) is established to produce disordered solid solutions in large quantities easily even in non-equilibrium alloy systems (Suryanarayana, 2001). On the other hand, spark plasma sintering (SPS) is reported to be an efficient consolidation method to produce bulk near full density samples without much coarsening of the initial grains (Munir et al., 2006). Though, the SPS technique primarily was developed to produce bulk ceramic materials, it is reported (Koch et al., 2017) to produce bulk nanostructured metallic materials such as Al-Ni-Ti alloy (Mula et al., 2011), Ni (Song et al. 2012), Cu (Roy et al., 2014; Sasaki et al., 2009) and Fe-based alloys (Libardi et al., 2008; Toor et al., 2016) through SPS. Hence, combination of the MA and SPS could be an efficient route in producing bulk size nc/UFG samples (Munir et al., 2006; Suryanarayana, 2001). The major challenge in processing such nanostructured material is to obtain fully dense bulk size components retaining its nc/UFG features. Groza et al. (2007) reported to compact nc materials by many techniques including hot pressing (HP), hot isostatic pressing (HIP) and explosive compaction. The compaction of nc Fe-Cr alloys is very difficult due to their body-centered cubic (BCC) structure and associated with a high hardness value which requires a very high compaction pressure and high temperature for consolidation.

Gupta et al. (2008) reported that the annealing treatment of the ball-milled nc Fe-10wt.%Cr alloy was helpful for densification by conventional pressing using a pressure of 2.7 GPa. The high hardness value of ~10 GPa was reported for pure nc iron (grain size 10 nm) by Siegel (1995). It is reported that at least a pressure of ≥1/3rd of the hardness (i.e., 3.5 GPa pressure for 10 GPa hardness) of the material is essential for proper compaction (Siegel, 1995). Moreover, consolidation at high temperatures, the material loses its nc features leading to produce microcrystalline grains. Therefore, in order to optimize the compaction process, more advanced consolidation techniques are required for proper consolidation. Toor et al. (2016) reported that the SPS of ball-milled Fe-18Cr-2Si sample (at 1100°C with a heating rate of 50°C/min at a constant pressure of 60 MPa) showed the maximum densification of ~96.0%, which resulted in a hardness of 710 HV. This is corresponding to the minimum grain size of 20-40 nm. Sorour et al. (2011) investigated the SPS characteristics of the ball-milled Fe-Cr-B alloy. They reported a ~97% densification of the alloy when sintered at 1150°C with an applied pressure of 50 MPa and found a very high hardness of 9.7 GPa. Further, Brendon et al. (2015) examined the SPS

characteristics of the conventional grained Fe-30wt.% Ni mixture sintered at 1230°C with an applied pressure of 30 MPa. They reported an average grain size of 200 μm with 98.7% sintered density, and the corresponding microhardness value was 284 HV. They also found that the fracture morphology shifted from purely intergranular type to a transgranular fracture when the sintering temperature increased to 1230°C from 950°C. Sebayang et al. (2011) investigated the sintering behavior of the ball-milled Fe-20wt.% Cr samples consolidated by SPS and HP. The SPS was carried out at 800°C and 900°C with a heating rate of 400°C/min using a pressure of 120 MPa in graphite die-punch; whereas, the HP was done using a steel die-punch at a pressure of 25 MPa at 1000°C. The SPS was reported to be more effective in retaining the nc grain structure as compared to that by the HP (e.g.18 nm for spark plasma sintered (SPSed) as compared to 39 nm of the HPed sample) and found to have better mechanical properties (hardness of 8.31GPa for the SPSed sample in contrast to 4.94 GPa for HPed sample). The major advantage of the SPS over HP is the simultaneous compaction of the nc powder particles along with bonding to produce a highly dense bulk structure at a relatively low temperature with a less sintering time (typically a few minutes) (Munir et al., 2006). This helps to retain the nc/UFG features in the sintered samples. The important challenges during the SPS are to achieve full densification of the nc/UFG metallic powders without causing any significant grain growth in order to retain nc/UFG features.

Overall, it has been found that the nc/UFG bulk metallic samples could be produced in non-equilibrium alloy system successfully by making disordered solid solution followed by advanced consolidation of it. First oversize insoluble elements are brought into the solid solution by non-equilibrium processing methods, such as MA and then, the supersaturated solute atoms are allowed either to segregate into grain boundaries and/or precipitate out to pin the grain boundary movement. Therefore, the main objectives of the present study are to investigate the effect of oversize insoluble alloying elements (e.g. Y, Nb and Zr) on: (i) the formation of disordered Fe-Cr solid solutions by MA (feasibility for the formation of solid solution by thermodynamic analysis i.e. Gibbs free energy changes), (ii) on the thermal stability (grain size stability at elevated temperatures) and mechanisms of thermal stabilization and (iii) densification mechanisms by SPS and mechanical properties of the SPSed samples. The analysis of phase evolution and microstructural investigation were performed using x-ray diffraction (XRD), optical microscopy (OM), scanning electron microscopy (SEM),

transmission electron microscopy (TEM), atomic force microscopy (AFM) and electron back-scattered diffraction (EBSD). The mechanical properties, such as microhardness measurement and compressive strength analysis were carried out to evaluate the thermal stability and correlate with the microstructures. Wear and corrosion resistance of the SPSed samples were estimated for its practical applicability. Different strengthening mechanisms involved were discussed in detail to ascribe the high thermal stability and mechanical properties.

CHAPTER 2 State-of-the-art literature review

2.1 Introduction

This chapter describes about the literature review on the ultrafine grained/nanocrystalline materials thoroughly. The material having grain sizes in the range 100-1000 nm is defined as ultrafine grained (UFG) material and if the grain size is <100 nm, it is designated as nanocrystalline (nc) material. The nc/UFG materials are highly attractive for high strength structural applications because of their unique properties, such as high yield strength, excellent thermal stability etc. The stabilize nc/UFG iron (Fe) based alloys are highly suitable in various industrial applications such as nuclear first wall reactor, heat exchanger, marine parts, construction and chemical industries. The major benefit of producing nc/UFG metals and alloys principally is attributed to the Hall-Patch relationship, which implies to enhance the yield strength with decrease in the grain size. The thermal stability of the nc/UFG materials at high temperature is extremely important to exhibit superior mechanical properties for various structural applications such as nuclear, automobile and chemical industries.

2.2 Synthesis of nc/UFG materials

Several methods have been developed in worldwide to synthesize the nc/UFG materials for engineering applications. The typical processing methods can be divided into 2 major types (i) top-down and (ii) bottom-up techniques.

Top-down approach

The top-down approach involves starting with a bulk solid to finally obtain a nanostructured material. In this approach, a bulk starting material on application of strain/loading leads to formation of nc/UFG materials through grain refinement (Fig. 2.1). Typical examples are mechanical alloying through ball milling/cryomilling followed by consolidation of powder (Atwater et al., 2012; Suryanarayana et al., 2000; Dybiec 2007; Han et al., 2007; Koch, 1997; Mula et al., 2010) several severe plastic deformation (SPD) processes (Valiev et al., 2000), cryorolling (Kumar et al., 2015; Wang et al., 2002), high pressure torsion (Rogl et al. 2012) and multiaxial forging (Fuloria et al., 2015; Noda et al., 2005) It is well known that the composition and structure of nanocrystalline materials can be precisely controlled by processing them under non equilibrium conditions (Koch et al., 2008). Among the other

processing routes, mechanical alloying has been proved to be more effective in producing metastable as well as equilibrium phases at a moderate cost (Millett et al., 2007; Ray et al., 2006). Fe-based alloys have received considerable attention and nc/UFG microstructures in these alloys could be developed through these techniques. The SPD approach substantially requires large plastic strains for the development of homogeneous and equiaxed material with ultrafine and/or nanocrystalline structures.

Bottom-up approach

The bottom-up approach commences with ions, atoms, molecules or nanoscale clusters as building blocks, which are assembled to form bulk materials. Some typical examples are chemical vapour deposition, electro-deposition, inert gas condensation etc. (Gleiter, 2000) (Fig. 2.1). This gives rise to develop smaller size grains up to 100 nm. These are very much useful in electronic devices. This approach has some drawbacks of particle agglomeration, contamination and residual porosity. The nc/UFG materials obtained by both the approaches differ considerably in terms of dislocation density, grain boundaries, grain shape, grain size and the distribution of secondary elements/phases, which in turn impart their mechanical properties. The schematic representation of building up of the nc/UFG materials is shown in Fig. 2.1. Out of the 2 approaches, some of the top-down approach (Mechanical alloying) processing techniques are found to get greater attention in producing bulk size nc/UFG metallic materials.

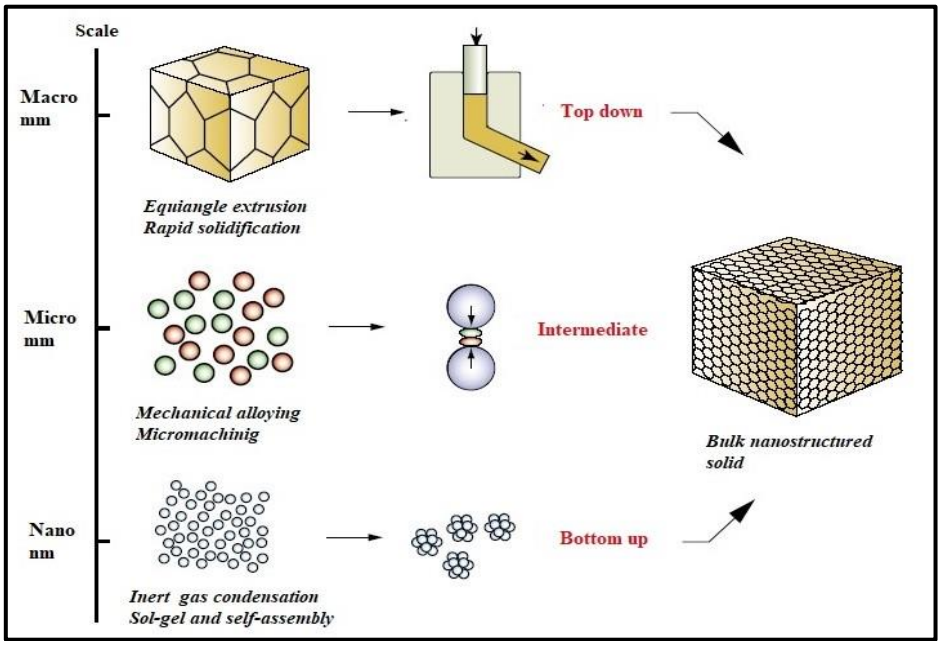

Fig. 2.1: Schematic representation of building up of ultrafine and nanocrystalline materials.

2.2.1 Mechanical alloying

Mechanical alloying (MA) is a very effective solid state powder processing method in which homogeneous materials can be developed from elemental powder particles. Mechanical alloying includes repeated fracturing, cold welding and re-welding of metal powders in a high energy ball mill (HEBM) (Detor et al., 2007; Koch et al., 2012). The MA is capable of forming different types of equilibrium and non-equilibrium alloys with extension of solid solubility. The non-equilibrium phase prepared by MA involves nanostructures, supersaturated solid solutions, metastable phases and amorphous alloys. The process of MA begins with blending of metal powder materials in appropriate quantity and loading the powder mixture into a grinding container (called vial) along with balls together it is called grinding media (Cahn, 1962; Koch, et al., 2013; Koch et al., 2012; Li et al., 2014; Libardi et al., 2007). The grinding media (vial and balls) can be made of hardened steel/stainless steel or tungsten carbide etc. Generally, vial and balls are made from the same materials to avoid cross contamination. This powder mixture is mechanically milled for a required period of time until the composition of powder particles becomes completely homogeneous. Different types of MA, such as, cryomilling, reactive ball milling, double mechanical alloying, rod milling and mechanically activated alloying.

2.2.2 The process of mechanical alloying

Mechanical alloying (MA) is well-established method used to produce nanoscale, metastable Fe-based alloys. The major variables consist of raw materials or basic materials, type of mills and process variables.

(a) Raw materials

The elemental powder materials used for mechanical alloying are commercially available and the size of powder particles is in the range of 1-200 μm. The size of milling balls must be larger than the particle size of the powder blend. The basic metal powders are into the category of pre-alloyed powders, refractory mixtures, master alloys and pure metals (Suryanarayana, 2001). The raw metal powders can be classified into three types, i.e. ductile-ductile in nature, ductile-brittle in nature and brittle-brittle in nature. The milling of the metal powders could be carried out under a liquid medium and it is known as wet milling. If there is no liquid medium is used, then it is called as dry milling. It is reported that wet milling has more benefits compared to dry milling. In dry grinding/milling, in the initial stage. cold welding occurs between the newly

formed surfaces which increases particle size; whereas, the surface energy is lowered due to adsorption of solvent molecules on the newly formed surfaces in wet grinding (Suryanarayana, 2001). Moreover, wet milling is reported to produce a solid solution without chemical reaction generally. The major drawback of wet grinding is the increased contamination of the milled powder product from the wet milling medium. Due to this reason, generally mechanical alloying is carried out in dry condition.

(b) Types of mills

There are various types of ball mills designed to carry out mechanical alloying/milling process. The types of mills include SPEX shaker mill, planetary ball mill and attritor mill etc. Type of specific mill is chosen subject to their demands, quantity of the product and type of product to be produced. Generally, the SPEX shaker mills are used for screening of alloy, though it is being used to produce extended solid solutions, intermetallic compounds or any other alloys. Planetary ball mill and attritor mill can produce a large quantity of milled powders as compared to that of the shaker mill. For laboratory application purpose, particularly designed mills are used.

(c) Process variables

Optimization of process variables is highly important to obtain the required microstructure/phases/alloys (Lin et al., 2012; Suryanarayana, 2001) various parameters that affect the final powder such as milling container, milling speed, milling time, powder to ball mass ratio, grinding medium, milling temperature, atmosphere of milling and process control agent (PCA). Mostly all the process variables are not totally independent. For example, the optimization of the milling time fully based on the type of milling machine, grinding medium, milling temperature and powder-to-ball mass ratio etc.

Milling container

Some specific types of milling container (vials) are used for mechanical milling/alloying such as stainless steel, bearing steel, hardened steel, tool steel, WC-lined steel, tempered steel, WC-Co and hardened chromium steel. Generally, the balls are made of the same materials as vial to avoid cross-contamination. The cross-contamination can be occurred between the powder materials and the milling container (vial). If the two materials (metal powder and the milling

container) are the same, then the propositions may be altered unless proper precautions are taken to compensate for the additional amount of the element incorporated into the powder.

Milling speed

Overall, milling efficiency increases with increasing in the milling speed. Moreover, the important thing is that if the milling speed exceeds a certain limit, the balls are pinned with the inner wall of the milling container and couldn't fall down to exert any impact force. Therefore, the maximum speed should be just below this critical value. The major drawback of higher milling speed increases the temperature of milling container as well as powder material during milling. This may be advantageous in some cases where diffusion is required to promote homogenization and/or alloying in the powders. However, in some cases, this increase in temperature may be a disadvantage because the increased temperature accelerates the transformation process and results in the decomposition of supersaturated solid solutions or other metastable phases formed during milling.

Milling time

Duration of milling is the most important key factor. Generally, the milling duration is chosen by repeated fracturing and re-welding between the powder particles and reaches a steady state condition between fracturing and re-welding. Then, on further grinding, fracturing dominates and could produce a supersaturated alloy with resultant particle size. The milling time fully depends on the other process variables such as type of mill, milling temperature, the intensity of milling and BPR. The major limitation in milling for a longer time is the rise of powder contamination and also can form undesirable phases. Therefore, the ball milling should be carried out for required time to produce desired microstructure. For the present study, the milling duration was kept for 25 h after standardization.

Grinding system and medium

The most common types of grinding balls are used in mechanical milling such as hardened steel, tool steel, hardened chromium steel, tempered steel, stainless steel, WC-lined steel, WC-Co and bearing steel. It is always desirable to have the grinding vessel and the grinding balls made of the same material to avoid cross contamination. The milling efficiency is also affected by the grinding balls size variation. It is found that during milling, using of mixed size balls

(both higher and smaller size), could reduce the amount of cold welding as well as the amount of powder coated onto the surface of the balls. For the current study stainless steel grinding balls were used.

Ball-to-powder weight ratio (BPR)

The powder-to-ball weight ratio is the most important process variable in the mechanical alloying/milling process. During milling, the BPR is normally maintained from a minimum 1:1 to the maximum value of 220:1. Generally, for the small capacity mill (e.g. SPEX), the BPR is kept at 10:1 and for the large capacity mill (e.g. planetary and attritor), the BPR is maintained at 50:1 or 100:1. For the current study, BPR is kept at 10:1.

Extent of filling the vial

Alloying between the powder particles occurs due to the large amount of impact forces. During milling, a large vacant space, at least 50% of the inner volume of the vial is required for the balls and the powder particles to move freely for proper impact. Therefore, the limit of extent of filling the vial should not exceed 50% of the inner volume of the vial with the powder material and the balls.

Milling atmosphere

Different milling atmospheres (N_2, H_2 & NH_3) are used as per desired specific purpose. Milling atmosphere holds a major role on the contamination to the powder. The argon (Ar), helium (He) gas atmospheres are generally used to prevent oxidation of the metal powders. Milling was carried out in the nitrogen gas atmospheres can produce nitrides. Hydrogen gas atmosphere can produce hydrides. The milling container contains any atmospheric air can produce oxides in the powder material, if elemental metal powders (very reactive in nature) are used. Most of the researchers use Ar or He atmosphere in dry milling condition; whereas, in wet milling, toluene could be useful to protect from air environment during milling.

Process control agents

Process control agent (PCA) is mainly added to decrease the effect of cold welding. The quantity of the PCA used and the type of powder milled could determine the final size, shape, and purity of the powder particles. A large quantity of the PCA normally reduces the particle size by 2-3 orders of magnitude. The amount of the PCA depends upon the factors: (i) cold

welding characteristics of the powder particles, (ii) chemical and thermal stability of the PCA and (iii) amount of the powder and grinding medium used. Some important PCAs include stearic acid, hexane, toluene, methanol and ethanol.

Temperature of milling

During milling the temperature is raised due to the elemental powder materials is plastically deformed. Hence, high atomic mobility (i.e. diffusion) is expected to play a pivotal role in solid state reaction/new phase formation, solid solubility extension and synthesis of nanocrystalline/amorphous phases. Therefore, the properties of the final product is decided on the final constituents of the material. Temperature of milling involves many factors such as system free energy, defects etc. which could promote the solid state reaction mechanism. It can directly change the element diffusivity and affects the recovery of defects in alloys. There have been conflicting reports on the formation of an amorphous phase as a function of the temperature of milling. Amorphization during MA involves the formation of micro-diffusion couples of the constituent powders followed by a solid-state amorphization reaction. Lower milling temperature is expected to form a nanocrystalline solid solution or amorphous phase. Hence, the milling was carried out at room temperature for present study to promote the formation of solid solution.

2.2.3 Mechanism of alloying

During milling of the powder blend, the collisions occur between ball to ball, ball to powder and ball to vial. When two balls collide, some amount of powder is trapped in between them. The impact force plastically deforms the entrapped powder particles leading to work hardening and fracture. In case of ductile materials, the powder got flattened and work hardened. Some new surfaces are created by fracture and are able to weld together in next collision. This causes increase in particle size as large as three times larger the starting particle. This can occur in ductile-ductile or ductile-brittle mixture particles (Suryanarayana, 2001). In the initial stage of milling, the process of cold-welding/re-welding and fracturing will continue, but cold-welding will be predominant over fracturing. The particles get work hardened after each impact. Due to the continued impacts of grinding balls, the grain structure of the particles is steadily refined. There will be a steady state between fracturing and re-welding after certain period of milling and the particle size continues to be the same (Suryanarayana, 2001). Steady-state equilibrium

is reached when a balance is achieved between the rate of cold welding and the rate of fracturing. At this stage, each particle will contain several layered structure and it can be called as composite particle. The composite particles will have a characteristic layered structure (Fig. 2.3) consisting of various combinations of the starting constituents. The distance between the layered structure is gradually reduced on further milling. At this stage, each particle contains substantially all of the starting ingredients in the same proportion of initial composition and the layered distance is reduced to extremely low level where diffusion of elemental atoms can take place across the layers. Thus, finally a homogeneous solid solution/alloy is produced by MA.

During MA, heavy plastic deformation is introduced into the particles due to the high energy milling. This deformation causes crystal defects such as dislocations, vacancies, stacking faults, and increased number of grain boundaries enhances the diffusivity of alloying (solute) elements into the solvent matrix. The grain boundary diffusion distance is reduced due to the particles size or microstructural refinement or decrease in the layered structure. During milling, there is always marginal increase in the temperature of the powder material, which helps for grain boundary diffusion to take place. Accordingly, proper alloying is taken place between the metallic elements (Suryanarayana, 2001; Pabi et al., 1996). Sometimes, bit temperature is raised (for diffusion to occur) for alloying to take place in the milled powder.

In planetary ball mill, the centrifugal force is produced by the vial rotating around its own axis and by the rotating support disk (shown in Fig.2.2). The centrifugal force acts on the vial consisting of material to be ground and the grinding balls. Now since the vial and the supporting disk rotate in opposite directions, the centrifugal forces alternately act in like and opposite directions. As a result, the grinding balls run down the inside wall of the vial- the friction effect followed by the material being ground and grinding balls lifting off and travelling freely through the inner chamber of the vial and colliding against the opposing.

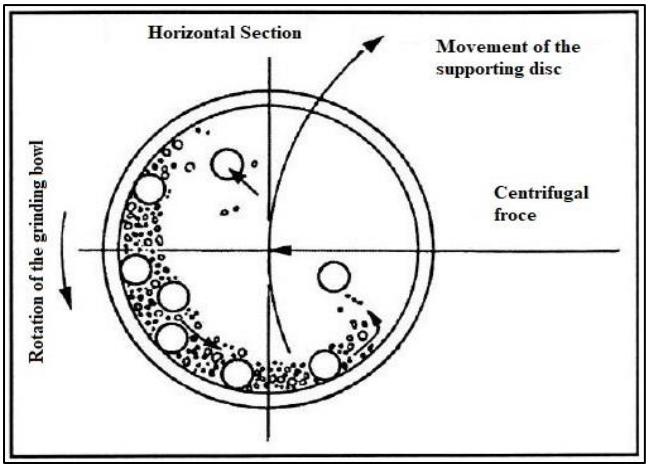

Fig. 2.2: Schematic diagram illustrative the motion of balls inside the mill (Suryanarayana, 2001).

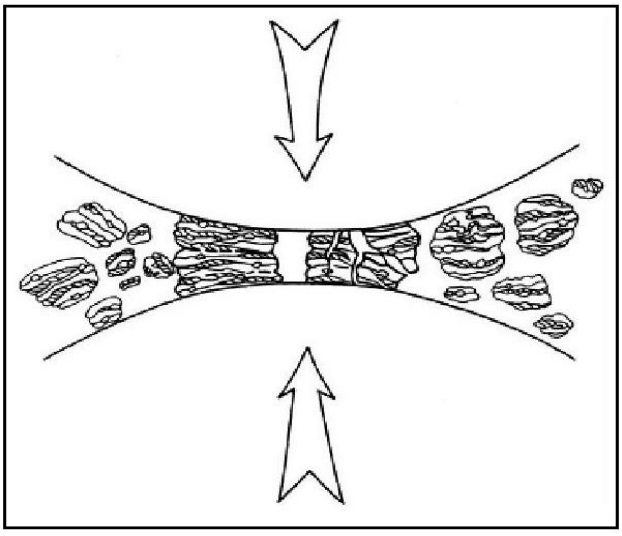
Fig. 2.3: Ball and powder collision during MA (Suryanarayana, 2001).

2.2.4 Major benefits in mechanical alloying (MA)

Mechanical alloying (MA) is a simple, economically feasible method with several technical benefits:

- MA includes solid state processing hence there are no defects of melting and casting.
- MA involves solid-state processing; therefore, all limitations that phase diagrams impose do not apply here.
- Possibility of solid solubility extension in many alloy systems reported (Koch, 1997; Xu et al., 1996).
- MA refines the matrix microstructure down to nanometer range.
- In mechanically alloyed samples amorphous structure could be developed (Suryanarayana, 2001).

2.3 Mechanical alloying to produce Fe-based nanostructured alloys

It is highly improbable to produce nanostructured Fe-based alloys by equilibrium methods as any equilibrium processing method does not produce nanocrystalline grains and also due to the fact of limited solid solubility of many solute elements in Fe matrix. In fact, any nanostructured alloys/materials cannot be developed by equilibrium methods. Therefore, nanostructured Fe-based alloys can be developed only by non-equilibrium methods like mechanical alloying, rapid solidification process etc. Mechanical alloying (MA) is the most promising technique among all non-equilibrium methods to produce nanostructured materials with better structural properties (Fecht, 1995). Moreover, the MA is reported to produce nanostructured alloys with the extension of solid solubility limit, i.e., the solute elements that cannot be dissolved or have limited solid solubility in solvent matrix by equilibrium methods, can produce solid solutions with more amount of solute dissolved in matrix by MA. Tehrani et al. (2011) studied on the effect of particle size of iron powder on α to γ phase transformation in the nanostructured high nitrogen content Fe-18Cr-10Mn-4Mo stainless steel. They used two different particle sizes and evaluated the grain size and internal lattice strain during milling for both iron particle sizes. They showed that the critical ferrite grain size for austenite nucleation is less than 10 nm. Additionally, the MA is very efficient in forming a solid solution from elemental powder blend exhibiting positive heat of mixing like Fe-Y, Cu-Nb. Fe-Al-Ni alloy synthesized by MA showed two different phases α_1-Fe (Al, Ni) and α_2-Fe (Al, Ni) with same crystal size but with different lattice parameters and microstrain. After 4 h of MA α_2-Fe (Al, Ni) disappears and chemically homogenized structure of α-Fe (Al, Ni) phase was produced (Archana et al., 2014; Archana et al., 2010; Hadef et al., 2011; Pabi et al., 1997). The MA of Fe-Cu binary system revealed large solid solution extension of Cu and it holds FCC crystal structures (Jiang et al., 1998). In the Fe-based powder blend, the grain size of the Fe-matrix decreases with increasing milling time; however, the decrease in particle size is not linear with milling time. Milling time of 144 h and more leads to serious cold-welding for the Fe-Cu alloys. The relative density of the sintered Fe-Cu alloys is influenced by the particle size of the powders before sintering (Hadef et al., 2011). The prior particle morphology of Fe-Cr powders was reported (Liu et al., 2010) to affect the relative sintered density of Fe-Cr alloys. The larger size particles resulted low sintered density; while, elongated particles showed higher hardness than that in the equiaxed grains after sintering. It was reported that the elongated particles contained precipitate

phase having larger residual strain (Liu et al., 2010).

2.4 Grain growth of Fe-based nanostructured materials prepared by MA

The primary objective of MA is to produce nanostructured/nanocrystalline homogeneous materials. It also aids extension of solid solution limit of certain alloy systems so that it gains superior mechanical properties. But, the nanosize features of the materials should be retained during its application or during further processing such as sintering, else, the materials would be transformed to conventional microcrystalline structure. Therefore, it is necessary to know about the grain growth behavior of solid solutions/alloys developed by MA so that some mechanisms would be devised to stabilize the nanostructured materials to realize its unique mechanical properties. The mechanism of grain growth in nanostructured alloys is in stark contrast with that of the polycrystalline alloys (Atkinson, 1988). This can easily be understood by considering the grain size of the polycrystalline material to be very small. The energy associated with a grain boundary is proportional to its corresponding surface area. Therefore, in order to accomplish a stable state, the system needs to diminish its grain boundary energy by increasing its grain size. The kinetics of normal grain growth could be defined as follow (Malow et al., 1997):

$$\frac{dD}{dt} = \frac{k}{D} \tag{2.1}$$

Here, D denotes the mean grain diameter after annealing time t and k denotes the rate constant that depends on temperature. Integrating the above equation gives grain size D at t=0 when ideal conditions are taken into consideration. Therefore, the above equation can be written as

$$D^2 - D_o^2 = kt \tag{2.2}$$

Generally, grain growth occurs in a parabolic manner for high purity metals. The grain growth under isothermal conditions could be best described by the equation given below (Hondros et al., 1983).

$$D^{1/n} - D_o^{1/n} = k't \quad \text{and} \quad D = (k't + D_0^{1/n})^n \tag{2.3}$$

Practically, the empirical constant n can be assumed to be ≤ 5. The grain growth can also be affected by the pinning forces inhibiting the grain boundary migration before the complete elimination of the curvature.

$$\frac{dD}{dt} = k\left(\frac{1/D}{1/D_m}\right) \tag{2.4}$$

Where, D_m stands for the maximum grain size resulting due to the pinning force. The final form of this analysis is given by the expression as follows.

$$\frac{D_0 - D}{D_m} + \ln\left(\frac{D_m - D_0}{D_m - D}\right) = kt \tag{2.5}$$

The unit of k is s^{-1}. The temperature dependent rate constant k or k' can be written in an Arrhenius type equation:

$$k = k_0 \exp\left\{\frac{-Q}{RT}\right\} \tag{2.6}$$

Where, Q and R denote the activation energy required for grain growth and molar gas constant, respectively.

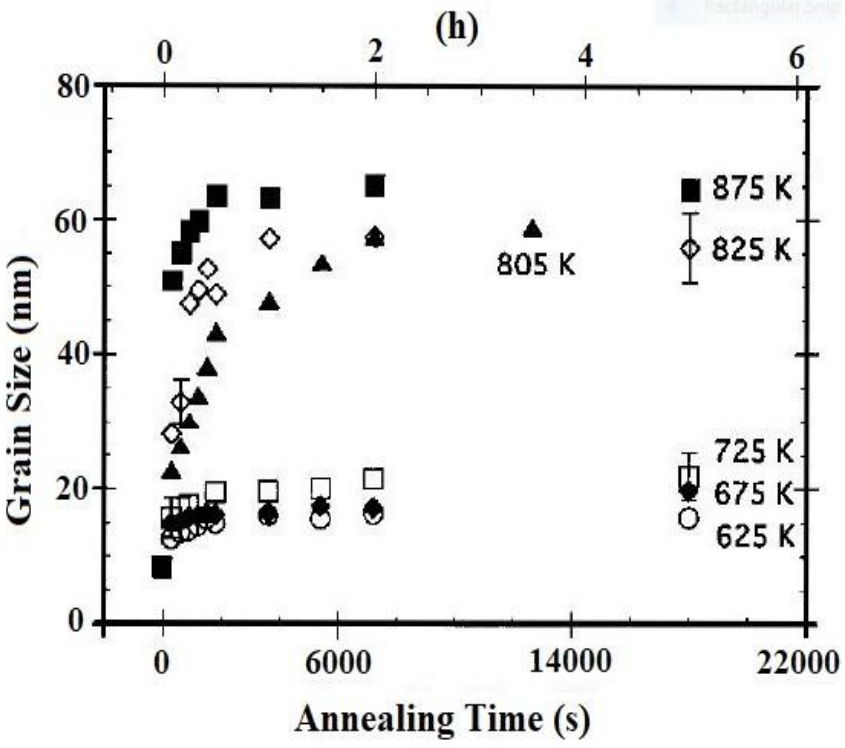

Fig. 2.4: Grain size as measured by XRD as a function of annealing time for nanocrystalline Fe annealed at various temperatures between 350°C and 600°C (Chen et al., 2009).

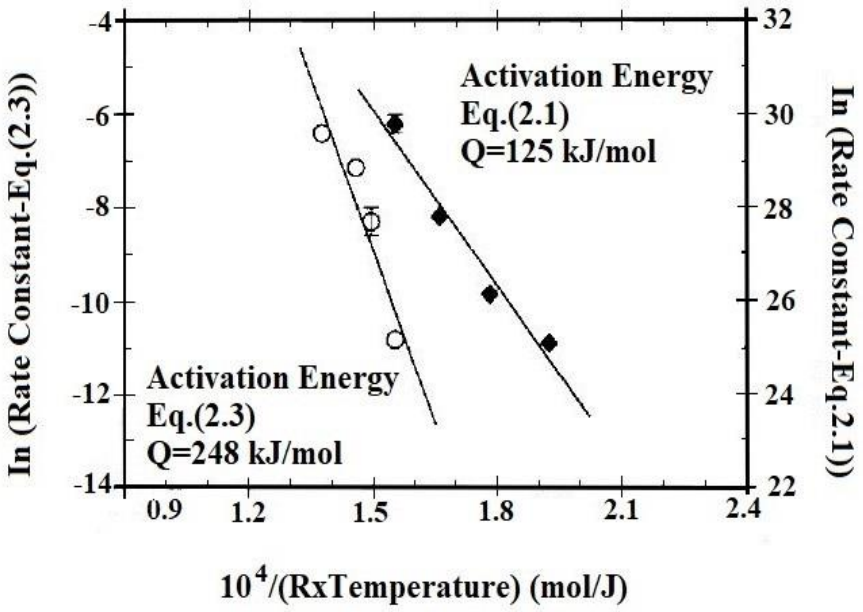

Fig. 2.5: Arrhenius plot of nanocrystalline Fe grain growth data analyzed according to equations (2.3) and (2.4). The slope of the linear fit in the plot is used to reduce the activation energy (Malow et al., 1997).

For an exponent n = 0.083 (Fig. 2.5), the estimated activation energy (Q) for grain growth of polycrystalline Fe without any pinning force is found to be less (i.e. 125 kJ/mol) as compared to the Q = 248 kJ/mol when pinning force was considered according to Burke approach (Malow & Koch, 1997). On the other hand, the value of Q of the polycrystalline Fe was 224 ± 25 kJ/mol estimated from DSC analysis (Malow & Koch, 1997).

2.5 Thermal stabilization mechanism

In the recent past decades to meet the great challenges and demand, considerable scientific interests have been made to improve the efficiency and performance of the components used in the high temperature applications (Li et al., 2009). Now, it is well-established that the components having nanoscale grain structures provide significantly high strength and toughness compared to their coarse grained counterpart. But, the stability of nanocrystalline/ultrafine grained (NC/UFG) materials face a severe problem of grain coarsening at moderate to high temperatures; and this limits their functionality and industrial applications (Saber et al., 2012; Darling et al., 2010). In technological point of view, therefore, the thermal stability is an important phenomenon to realize the unique properties of nanocrystalline materials. Thus, it is most essential to develop nanocrystalline alloys which are resistant to grain growth at high temperature. Extensive grain growth has been observed in pure

nanocrystalline metals due to the reduction of excess grain boundary free energy that decreases grain boundary area on grain coarsening and provides a very large driving force for grain growth (Alleg et al., 2013; Driver, 2004; Koch, 2007; McCrea, Palumbo eta l., 2003; Murty et al., 2003; Ray et al., 2010; Shanmugasundaram et al., 2006) At an annealing temperature of $0.5T_m$ (T_m is melting temperature in kelvin scale) or less, nanocrystalline metals of even high melting points such as Co, Ni, Fe etc. exhibit fast grain growth, which causes to produce again conventional micron size grains after sintering/consolidation (Darling et al., 2010). On the other side, nanocrystalline structures of low to medium melting temperature metals such as Sn, Al, Zn, Pb, Mg etc. show excessive grain coarsening even at room temperature. Addition of thermodynamically insoluble, larger size alloying elements such as Y, Nb, Hf, Zr etc. in nanocrystalline alloys is reported to restrict the grain growth successfully at elevated temperatures (Darling et al., 2015; Detor et al., 2007; Koch et al., 2008; Manna et al., 2008; Millett et al., 2007; Weissmüller, 1993). Two mechanisms, namely, kinetic and thermodynamic stabilizations are reported to exhibit good thermal stability of the NC/UFG materials (Darling et al., 2010; Koch et al., 2008; Koch et al., 2012; Li et al., 2014; Manna et al., 2012). Both the stabilization mechanisms are discussed in details in the subsequent sections.

2.5.1 Kinetic stabilization mechanisms

The kinetic stabilization mechanism contributes to the thermal stability by reducing the mobility of the grain boundary by second phase particles. There are several ways to attain this mobility reduction. Typically, this strategy involves effects such as chemical ordering, solute drag and Zener pinning (Koch et al., 2008).

Solute drag effect

The solute atoms affect mobility of the grain boundary when there is a significant concentration of solute present near the grain boundary (Youssef et al., 2004). When the grain growth driven by grain boundary energy takes place, the kinetics of growth depend on whether the grain boundary can break away or overcome the solute atmosphere. When the solute concentration is low, extensive grain growth can occur. Once the solute concentration is increased the solute atmosphere near the grain boundary becomes denser and the mobility is reduced. The two forces, solute drag force and grain boundary driving force, oppose each other in the kinetic effect. When driving force due to curvature of the grain in Eq.2.7 is low (e.g. in highly

coarsened microstructure), the solute has sufficient time to diffuse along the boundary and to move with the boundary as the grain grows. Once this driving force is increased (e.g. in nanocrystalline microstructure), the solute atoms must diffuse more quickly. In other words, at high grain boundary velocity, faster diffusing solute is needed to maintain drag force (Cahn, 1962). However, at higher temperatures, diffusion of solute is increased, and the significance of the pinning pressure depends on solvent-solute atoms interaction.

Diffusivity of solute, concentration of solute, and solvent-solute interaction are therefore the main factors. The grain size dependence of grain growth was studied by Michels et al. (1999) in nanocrystalline Pd-19Zr alloy. They reported that grain growth was inhibited when grain size and Zr concentration both increased. Two possible mechanisms were suggested for uptake of Zr: diffusion of Zr through the lattice, and the entrapment of Zr during the growth. Since the annealing temperature was about $0.47T_m$, lattice diffusion was not sufficient to explain this effect. Therefore, solute entrapment was the most probable mechanism. In the work by Krill et al. (1995), the effect of Zr on thermal stability of the Pd-19Zr alloy was attributed to the thermodynamic mechanism since Zr segregates to the grain boundary. Furthermore, in the results reported by VanLeeuwen et al. (2010), it was pointed out that energy reduction due to solute segregation is insufficient to stabilize the grain boundary, and at higher temperatures noticeable grain growth was taken place.

Second phase pinning (Zener) effect

The presence of the solute atoms can also affect the grain size stability through second phase formation. The second phase may be a precipitate or a dispersoids distributed throughout the alloy matrix. Zener pinning effect is less temperature sensitive than the solute drag effect (Driver, 2004). However, particle size and distribution of the second phase play a key role in the effect (Nes et al., 1985). Assuming spherical particles, the Zener pinning pressure is described by

$$P_z = (3F^*\gamma)/2r \qquad (2.7)$$

P_Z, F and r denotes, respectively, the pinning pressure on the grain boundary, volume fraction of second phase and radius of the spherical second phase particles; and γ is the interfacial energy. As given in Eq. 2.7, once the volume fraction of particles is increased or particle size is decreased, $P_{Z,}$ is raised and the stabilization through Zener pinning is enhanced. Therefore, a

large volume fraction of very small size particles is required to reduce the driving force for grain growth. Although this technique can produce relatively high temperature stabilization, coarsening or dissolution of second phase particles at higher temperatures will eliminate the stabilization of matrix grains (Porter et al., 1992). This effect could be controlled by solubility limit and diffusivity of solute at high temperatures.

2.5.2 Thermodynamic stabilization mechanism

This mechanism explains the reduction of driving force for grain boundary migration instead of pinning grain boundaries against grain growth. Solute addition is the main contribution in this regard. Solute atoms with strong tendency to segregate to grain boundary serve to reduce the driving force for grain growth (Liu et al., 2004). The reduction of interface energy by increasing solute content is theoretically described by the well-known Gibbs adsorption isotherm (Weissmuller, 1993).

$$d\gamma = -\Gamma_s d\mu_s \tag{2.8}$$

where, Γ_s is the segregated solute excess, which is the excess concentration of solute relative to the bulk equilibrium concentration of solute and μ_s is the solute chemical potential. According to the work of Hondros and Seah, the surface free energy, γ, can be reduced to a certain range due to solute additions in several binary alloys. This negative trend is intensified for solute atoms with large atomic size misfit (Cahn et al., 1996). This effect proposes that large atomic size misfit promotes grain boundary segregation and consequently reduces grain growth. This concept is developed in the work of Weissmuller (1993). The very first attempt to solve the Gibbs adsorption isotherm for nanostructured materials was done by Weissmuller (1993) gives

$$\gamma = \gamma_o + \Gamma_S[\Delta H_{seg} - T\Delta S_{seg}] \tag{2.9}$$

where, γ_0 is the non-segregated grain boundary Gibbs free energy, Γ_s, is the solute excess of the grain boundary, T is the absolute temperature. ΔH_{seg} and ΔS_{seg} are the enthalpy and entropy due to grain boundary segregation, respectively. The enthalpy of segregation, ΔH_{seg}, ideally involves the chemical contribution due to the chemical interaction of solute-solvent and the elastic strain contribution due to the atomic size misfit. This equation is employed to define thermodynamic stabilization as the condition where $\boldsymbol{\gamma}$ is reduced to be zero. However, if $\gamma = 0$ is assumed to be cohesive grain boundary energy, grain boundary cohesion is eliminated.

The definition of grain boundary energy in Eq. 2.9 is limited to a dilute solution containing a negligible volume fraction of interface. These boundary conditions are in contrast with nanocrystalline microstructures in which the volume fraction of grain boundary is significant. McLean (1957) suggested that the enthalpy of segregation (ΔH_{seg}) is the complete release of the elastic strain energy associated with the solute atomic size misfit. On the other hand, Defay et al. (1966) defined the segregation enthalpy in terms of chemical contributions. Furthermore, it was shown that neither the works of McLean (1957) nor the work of Defay et al. (1966) proposed a comprehensive model of the grain boundary segregation (Wynblatt et al., 1977) since each of these models consider only one of these two basic contributions.

$$\Delta H_{seg} = \Delta H_{chem} + \Delta H_{elas} \tag{2.10}$$

The chemical enthalpy contribution in this model, ΔH_{chem}, is described in terms of the surface energies of solute and solvent, atomic fractions of solute within the grain and at the grain boundary, and regular solution interaction parameter of A-B type of binary mixture. The elastic enthalpy of segregation, ΔH_{elas}, is expressed in terms of the released elastic strain energy (ΔE_{elas}) per solute atom A for an AB binary alloy as follows (Friedel, 2001).

$$\Delta H_{Seg} = -\Delta E_{elas} \frac{2K_A G_B (V_B - V_A)^2}{3K_A V_B + 4G_B V_A} \tag{2.11}$$

Where ΔE_{elas} is the total released elastic strain energy due to the atomic size misfit, K is the bulk modulus, G is the shear modulus and V is the molar volume of solute A and solvent B. There have been several analytical models explaining the thermodynamic stabilization through segregation. In the following section, details about Kirchheim and Liu and Kirchheim's models (Kirchheim, 2007) and the most recent approach given by Trelewicz et al. (2009) have been described.

2.6 Solute selection for stabilization of Fe-based alloys

It is apparent that the crystallite size/grain size of pure nanocrystalline Fe loses its stability at temperatures above 530°C due to abnormal grain growth (Darling et al., 2010). After annealing at 620°C, 50% of the microstructure was reported to consist of 150nm grains and the remaining grains were coarsened to the micron size. The grain structure abnormally grows at an annealing temperature of 750°C (Darling et al., 2010). As an attempt to control the grain growth of nanocrystalline pure Fe, the relative thermal stability of Fe-based nanocrystalline alloys by

solute segregation was predicted through a regular solution model in Darling et al. (2011). This thermodynamic model gives a practical approach in selecting stabilizing agents for Fe-based nanocrystalline alloys. Low elastic strain enthalpy and low atomic mismatch Ni was reported to be a poor thermal stabilizer for nanocrystalline Fe. Effect of Cr solute on thermal stability of nanocrystalline Fe is not significant due to its negligible size misfit with Fe atoms and has a very low elastic strain enthalpy. Owing to huge elastic strain enthalpy and atomic size misfit, Y and Zr additions are suggested to produce effective thermal stabilization (i.e. γ=0) of nanocrystalline Fe, whereas Ta could not. Ta solute additions cannot reduce grain boundary energy completely to zero but compared to Ni and Cr, it can bring significant thermal stability on nanocrystalline Fe microstructure. (Darling et al., 2010). reported that at 800°C, pure Fe attains 6 µm grain size while nanocrystalline Fe-1at.%Zr maintains a grain size of 45 nm. On the other hand, Fe-1at.%Ta shows a grain size of 82 nm.

From the overall works reported that a typical grain growth could be noticed with the addition of Cr and Ni solutes. The remarkable progress achieved from the additions of Y and Zr. Y was recommended to a good solute for grain size stabilization; however, Y was reported to cause embrittlement at Fe-matrix grain boundaries. Zr is proved to be an excellent candidate to attain thermodynamic stabilization of nanostructured Fe alloys (shown in Fig. 2.6). From the above studies, the following sequence could be proposed as per the increasing stabilizing effect by the various solute elements in Fe.

Fe-Y > Fe-Zr > Fe-Ta > Fe-Cr > Fe-Ni

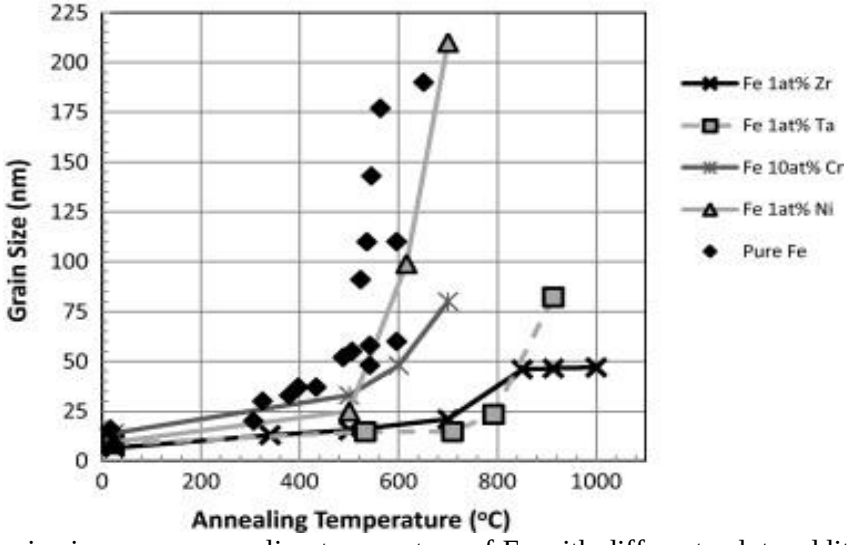

Fig. 2.6: XRD grain size versus annealing temperature of Fe with different solute additions (Darling et al., 2011).

2.7 Consolidation of nanocrystalline powders

Mechanical alloying is well established to produce powder particles with a nanoscale/ultrafine grained (UFG) microstructure. These nanoscale powder particles must be consolidated into the bulk form without much grain coarsening to realize its mechanical properties for the possible structural applications (Michael et al., 2008; Singh et al., 2013). Cold compaction of metal powders requires plastic yielding; therefore, high pressure order of several GPa is needed for strong nanocrystalline metals such as Fe or its alloys. Hot compaction assists densification by allowing plastic deformation of metals at high temperatures and pressures. The problem is that a combination of pressure and temperature is required for a good particle bonding in order to reach the theoretical density. This should be done without significant coarsening of the nanoscale/UFG microstructure. Unfortunately, conventional consolidation methods as well as hot pressing could not guarantee to produce bulk size NC/UFG material. Thus, the attainment of thermal stability can exploit the consolidation conditions (i.e. temperature and pressure) to obtain highly dense bulk materials for advanced structural applications.

2.7.1 Spark plasma sintering

Spark plasma sintering (SPS) is an advanced consolidation method to produce NC/UFG bulk size sample without much grain coarsening. The main features of the SPS technique that the DC pulsed current directly passed over the graphite die and punches and also simultaneously compacting the metallic or ceramic powder particles. Resistance heating of the non-conducting powder material is found to be very effective in consolidation by SPS technique. The other conventional sintering methods, which require high temperature holding for a long period are unable to accomplish the high density after consolidation. So, better processing route needs to be chosen. The various important sintering techniques are hot isostatic pressing (HIP), hot pressing (HP), microwave sintering (MVS), pressure-less sintering (PLS) and spark plasma sintering (SPS). The most advanced technique till date for sintering of metallic (or) ceramic powders is reported to be the SPS. This method is adored for its unique advantages like low sintering temperature, low holding time and in-situ cleaning of oxide surface by cleaner powder materials to achieved high consolidated density.

A schematic diagram representing the major section of spark plasma sintering machine is shown in Fig. 2.7. Generally, the die and punch are made up of graphite or tungsten carbide

material. Initially, the powder material is loaded in the graphite die-punch and then required load is applied. The graphite die-punch can withstand the maximum external pressure of 100MPa. The applied pressure is generally maintained at a constant value, though it may be changed step by step. A real-time measurement of sintering temperature is made by using a K-type (or) R-type thermocouple, which is placed prior over a horizontal die-hole (~12 mm aside from the filled powder material). Generally, the sintering can be performed under standard vacuum, ultra-high vacuum and inert gas atmosphere (argon) based on the characteristic of powder material. The heat is generated in the system by ON-OFF DC pulse voltage and a current from a pulse generator. The high applied stress/pressure activates diffusion-oriented processes and the electric field present in the system enhances the diffusion rate. The plasma generated within the material eliminates/decreases the oxide layer/adsorbed gas, if any. Thus, the process allows direct contacts between the powder particles. Therefore, bonding between the particles and subsequently neck formation becomes easier. Hence, finally almost all the pores are eliminated to develop near full density sample. The spark plasma sintering (SPS) can develop highly dense bulk samples without much affecting the grain structures of various metals and ceramics due to its rapid heating rate, minimum holding time and a comparatively lower sintering temperature. Ashby (2008) stated that at sintering conditions, the product microstructure fully depends on the die/punches geometry, powder material and also the heating volume, irrespective of the electrical features of the specimen. For the conductive material, it depends on heating volume involves, the powder, punches and certain level to the die, but for the non-conductive material it only involves the die-punch. For the conductive material, as the heating volume increases rapidly, the grain size of the sintered sample decreases. It is inversely for the non-conductive material and leads to grain growth.

In spark plasma sintering, consolidation of powders takes place basically because of two factors: (i) an initially activated pulsed current and (ii) DC current by which both of heating and densification can be attained simultaneously (Ertorer et al., 2011; Groza et al., 2000). The major advantages of the SPS are as follows: low sintering temperatures, very fast heating rates (up to 600^{o}C/min), rapid cooling rates because of their low thermal inertia and forced cooling, short holding time, high pressure applied during sintering, high throughput due to high current (>1000A) and low voltage (<10 V), clean grain boundaries because of plasma activation and flexible sintering environment. These advantages differentiate it from conventional sintering.

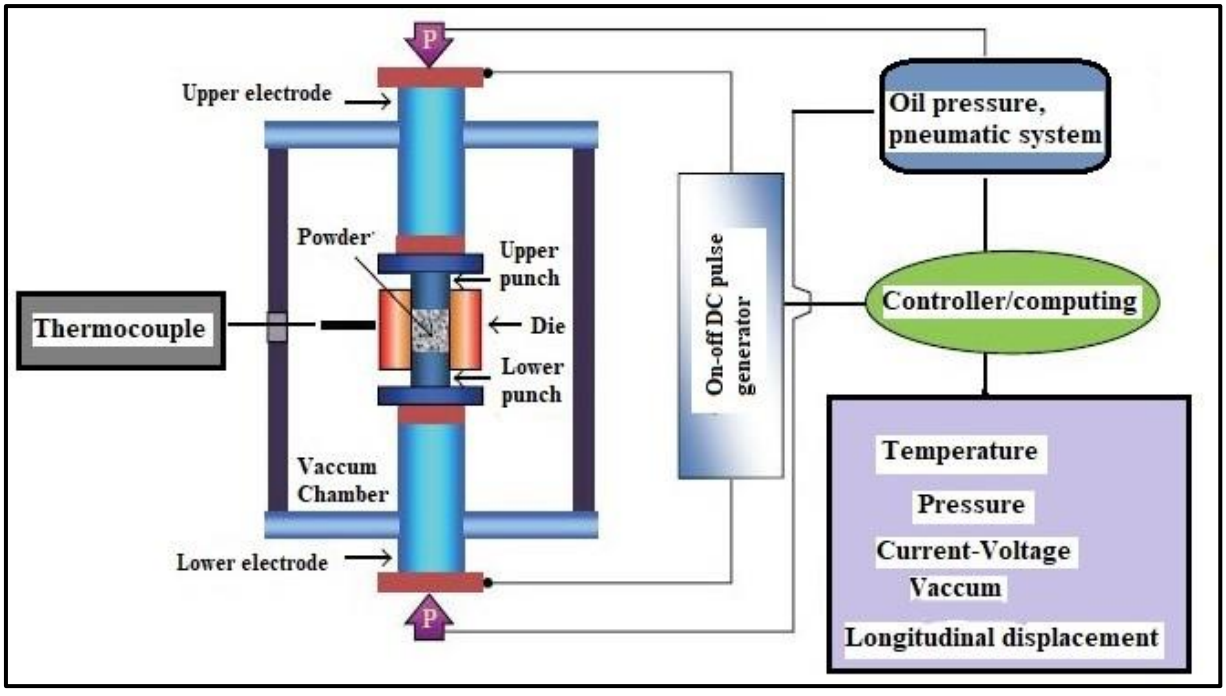

Fig. 2.7 Schematic diagram of spark plasma sintering machine (Hulbert et al., 2009).

This method is used to process different kinds of powder materials, such as metal and alloys (Mamedov., 2002; Nygren et al., 2004), porous materials (Fabregue et al., 2012; Ouyang et al., 2017), composites (Robles-Hernandez et al. 2010), functional grade material (Eriksson et al., 2013), nanostructured materials (Sebayang et al., 2011), textured materials (Ning et al., 2007), nanostructured and amorphous coatings (Mulukutla et al., 2010), non-equilibrium composites (Mulukutla et al., 2010) and amorphous materials (Xiao et al., 2012). Moreover, the above-described characteristics have major advantages such as achieving higher sintered density with small grain size without any addition of additives. This is the only technique, which can produce several engineering materials such as armour materials, ferroelectrics, biomaterials, magnetics, piezoelectrics, transparent ceramics, pyroelectrics, superconductors etc. (Munir et al., 2006).

Due to the enhanced sintering ability of this technique over other sintering methods, many attempts have been made to understand the exact consolidation mechanism of SPS. Joule heating and a mechanism suggesting plasma formation between particles have been proposed to explain the sintering behaviour. Although Joule heating remains widely (Hulbert et al., 2009; Khor et al., 2003; Omori, 2000; Wang et al., 2000) investigated phenomenon during the spark plasma sintering process, any plasma or spark produced in ultra-fast in situ voltage

measurements, in situ atomic emission spectroscopy and visual observation, it concluded that there is no plasma or spark produced. But, mechanisms of the SPS still remain imprecise. The DC current (ON-OFF), which is used for simultaneous development of spark discharge and rapid heating (Joule effect) between the powder particles in the initial stage of the SPS, is generally reported to be responsible to achieve high sintered density in the SPS (Munir et al., 2006). Further, the applied pulse current removes the thin oxide layers of the metallic materials, surface impurities and adsorbents induced by plasma generation and thus enhancement in the bonding between the powder particles is achieved (Goodwin et al., 1997). These special effects result in low heat input and create bonding between the powders particles with a limited chemical interaction amongst different elements and control grain sizes (Brendon et al., 2015). In spark plasma sintering, external pressure is applied not only to create electrical contacts between die, punch and powders particles, but also progressively promotes densification by reorganization of the powder particles and neck formation through diffusion bonding due to localized deformation at the contact points (shown in Fig.2.8) (Omori, 2000). Nanostructured powders material densification may occur by some specific mechanisms such as plastic deformation, grain boundary sliding (Siegel, 1995), grain growth and grain rotation (Zhu et al., 1996) and even by grain boundary melting due to large Hertzian stress (Zhu et al., 1996). Overall, all the factors together play their pivotal role to achieve such high level of densification.

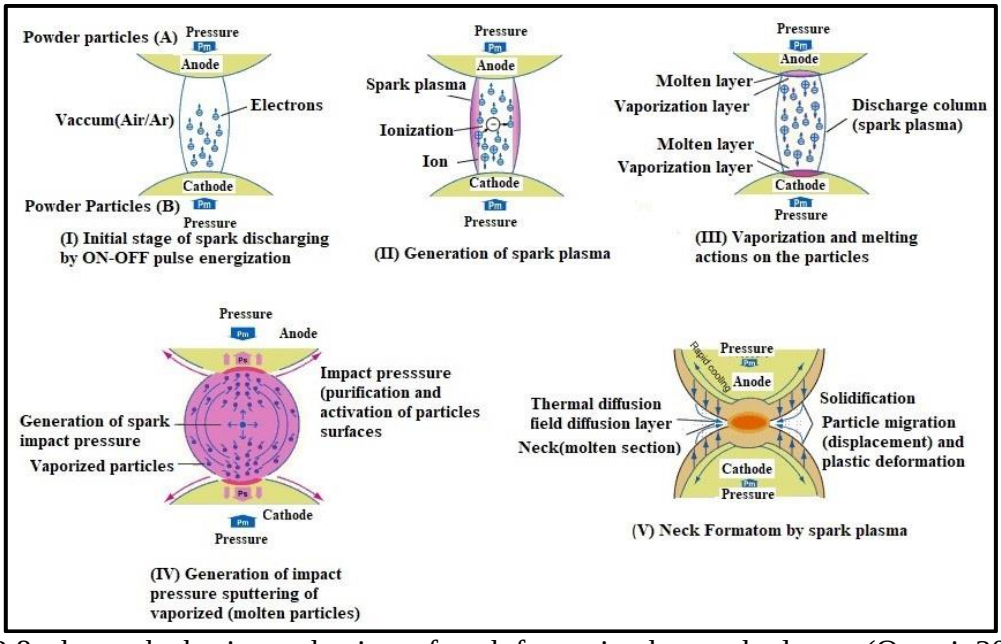

Fig.2.8: shows the basic mechanism of neck formation by spark plasma (Omori, 2000).

2.8 International status

Mechanical alloying

There are several reports available for the structure, properties and thermodynamic stabilization of Fe-based nanocrystalline alloys. From the various studies, some important works are discussed here under columns of international and national status. A group of researchers under the supervision of Dr. Carl C. Koch at North Carolina State University, USA has done several works on Fe-based nanocrystalline alloys to stabilize its grain size at high temperatures. Inherent instability of nanocrystalline materials with respect to grain growth can be mitigated by adding atomic species that segregates to the grain boundaries (Dake et al., 2012). Fe-based alloys investigated by this method show effective stabilizing of the nanocrystalline Fe-based up to 900ºC. Above this temperature, grain size stability is suddenly lost and rapid grain growth occurs between 900-1000ºC. It is stated that one of the reasons behind the instability of grain size is the α→γ phase transformation of Fe.

One important motivation for investigating Zr additions to Fe-Cr alloys, in addition to the possible applications for thermally stable nanocrystalline ferritic alloys, is the fact that the α → γ transformation can be eliminated altogether when the Cr content is sufficiently large. Significant differences in the temperature dependence of the Zr-addition the thermal stabilization effect of alloys with 10-18at.% Cr would be important for the relevance of α → γ transformation effect. Gupta et al. (2008) successfully prepared a nanocrystalline Fe–10%Cr alloy by ball-milling route. In the absence of suitable hot compaction facility, the alloy powder could be successfully compacted close to the desired density by employing a step of prior annealing of the powder before consolidation. Grain growth behavior of Fe-10at.%Cr nanocrystalline alloy was investigated at 500, 600 and 700°C. At 500°C, no appreciable grain growth was observed after the initial grain growth. However, sudden and rapid grain growth was observed after 90 min at 600°C and 30 min at 700°C. Therefore, to improve the stability of nanocrystalline Fe, change in grain boundary energy through solute segregation in grain boundaries was performed by Darling et al. (2015). Also, they (Darling et al., 2015) prepared stability maps to predict the thermal stability for various individual binary system such as Fe-Ni, Fe-Cu, Fe-Al, Fe-Mg, Fe-Ti etc. They validated the approach by numerical calculations of Fe-Zr alloy demonstrating grain size stabilization up to 900ºC. They concluded that in alloy

systems with suitable elastic and mixing enthalpy of segregation, thermodynamic stabilization of grain size is possible up to high homologous temperatures.

In continuation of the above described work, relative thermal stability specific to Fe-based nanocrystalline alloys was predicted by using a regular solution model for grain boundary solute segregation (Darling et al., 2011). This practical approach assists in selecting stabilizing agents for nanocrystalline Fe based alloys. It was stated that stabilization of nanocrystalline Fe-based alloys is more prominent by Y, Zr and Ta and to some extent by Cr and Ni. Another model with thermodynamic approach was presented to evaluate the thermal stability of binary alloys such as Fe-Zr, Cu-Zr, Cu-Nb, Cu-Y, Cu-W, Cu-Cr, Ni-Y and Ni-W which are applicable to strongly segregating size-misfit solutes (Brammer et al., 2010; Mukhopadhyay et al., 2008; Saber et al., 2013). This model incorporates elastic strain energy due to size misfit in addition to chemical effects. In this research, Saber et al. (2013) proposed that without investigating experimentally, numerical results can be obtained for binary alloys for which thermal stabilization is expected. As per their observation, although the model cannot exactly predict the temperature and solute range for thermodynamic stabilization, it can provide a significant trend. Darling et al. (2010) reported that 4at.% Zr addition to pure Fe could stabilize a nanocrystalline grain size up to 900°C. Model calculations suggested that thermodynamic stabilization would be effective for the Fe-4at.% Zr alloy system in this temperature range. Intermetallic formation was observed at higher temperatures in conjunction with the grain growth. An issue that is raised for the interpretation of the Fe-Zr results is the possible effect of the $\alpha \rightarrow \gamma$ allotropic phase transformation at 913°C in pure Fe. Thermal stabilization of nanocrystalline Fe was employed with the addition of dilute amount of Zr. As a result, nanocrystalline ball milled sample of Fe-4 at.% Zr retained grain size of 52 nm at 1373ºC whereas pure Fe reaches a grain size of 6µm at approximately 700ºC (Darling et al., 2010). This phenomenal thermal stability is attributed to Zr segregation to grain boundaries and thermal stabilization mechanism. Alloys having lesser Zr contents reported less stability but significantly better comparing to pure Fe. Cr acts as a stabilizer to nanocrystalline Fe but not as effective as Zr due to its atomic size very close to Fe. So, grain boundary segregation by elastic strain energy cannot be expected.

Zr is proved as to be a good stabilizer and it was described that 1-4at.% Zr additions influence the thermal stability of mechanically alloyed Fe-Cr alloys (Darling et al., 2010; Saber et al., 2012). They noticed that grain size retained in nanoscale regime up to 900ºC, which is possibly due to Zener pinning mechanism. Zener (kinetic) pinning by nanoscale intermetallic particles, (the main source of grain size stabilization here), could also contribute to strengthening to retain hardness of 7 GPa. They deduced that phase transformation could be eliminated when Cr content is sufficiently large. Fe-Cr samples alloyed with 4at.% Hf maintained nanoscale grain size up to 1000ºC (Li et al., 2014). Compared to Fe-Cr-Zr alloy, second phase formation in Fe-Cr-Hf alloy can be enhanced leading to Zener pinning effect. As per the literature, by adding a ternary solute element, Hf, lattice parameter of Fe-Cr is increased. It was also elaborated that up to 400ºC hardness was retained at 8 GPa and there was no effective increase in grain size. From 400-800ºC, gradually increasing the Hf content led to excellent grain size stabilization but hardness dropped to 5.2 GPa. Yttrium is proved to be an excellent alloying element as stabilizing agent (Darling et al., 2013). Mechanical alloyed (8h at cryogenic temperature) of Ni with 1, 5 and 10 at.% Y showed thermal stability after isochronal annealing up to 1100ºC. Increase in Y content exhibited high temperature stabilization of nanocrystalline Ni within 100 nm up to 900ºC. Results of this experiment revealed that Zener pinning is the effective mechanism in retaining a nanostructure up to 900ºC.

Spark plasma sintering and mechanical properties

The major challenge in the processing of nanocrystalline (NC) powder materials is to obtain fully dense bulk material without losing their nanofeatures. Groza (2007) reported to compact NC materials by many techniques including hot compaction, hot isostatic compaction and explosive compaction. The compaction of NC Fe-Cr alloys is very difficult due to their body-centered cubic (BCC) structure and high hardness values, which require high temperature and pressure for compaction. Gupta et al. (2008) reported that annealing of the ball-milled nc Fe-10Cr alloys could be helpful to compact by conventional pressing using a pressure of 2.7 GPa. The high hardness value (10 GPa) of pure NC iron (grain size 10 nm) was reported in (Siegel, 1995). Hence, an applied pressure of 1/3rd of its hardness i.e., ~3.5 GPa and high temperature are essential for better compact density. The NC materials at elevated temperature lead to grain growth and hence the material loses its nanofeatures through conventional sintering method.

Because, it requires a combination of high temperature and pressure for effective consolidation. Toor et al. (2016) reported that the SPS of ball-milled samples of Fe-18Cr-2Si alloy (sintered at 1100°C with a heating rate of 50°C/min at a constant pressure of 60 MPa) showed the maximum densification of ~96.0% with a corresponding hardness of 710 HV and there was minimum grain coarsening (20-40 nm). Sorour et al. (2011) investigated SPS characteristics of ball milled Fe-Cr-B alloy sintered at 1150°C with a heating rate of 225°C/min using a constant pressure of 50 MPa. They reported a ~97% densification of the alloy by SPS and found a very high hardness of 9.7 GPa. Further, Brendon et al. (2015) did the SPS of conventional grained Fe-30% Ni mixture at 1230°C at a heating rate of 40-50°C/min using a pressure of 30 MPa. They achieved a very high sintered density of 98.7% corresponding to a grain size of 200μm and microhardness value was only 284HV. They also found that the fracture type changed from purely intergranular to a transgranular fracture when the sintering temperature increased to 1230°C from 950°C. Sebayang et al. (2011) investigated the sintering behavior of ball milled Fe-20wt.% Cr samples consolidated by SPS and hot pressing (HP). The SPS was carried out at 800 and 900°C with a heating rate of 400°C/min using a pressure of 120 MPa, whereas the HP was done in the steel die at a pressure of 25 MPa at 1000°C. The Fe-Cr samples prepared by SPS were found more effective than those prepared by HP in retaining nanocrystalline structure (e.g. 18 nm for SPSed compared to 39 nm for HPed sample) and reported to have better mechanical properties (hardness of 8.31 GPa for SPSed sample in contrast to 4.94 GPa only for HPed sample.

2.8.1 National status

The influence of Nb addition on the thermal stability of nc Cu was studied by Mula et al. (2012). It was reported that the complete dissolution of solute Nb atoms in Cu matrix was achieved after 8h of MA at room temperature using a SPEX8000M mill. Moreover, the dissolution of Nb was confirmed by XRD pattern analysis and change in Gibb's free energy. Nb was found to be a good stabilizing agent and maintained a grain size of ~25 nm even after annealing at 600ºC. Microhardness was found to be 4.5 GPa after annealing at 600ºC. This was ascribed to the segregation of Nb atoms in the grain boundaries of matrix.

The influence of Y additions on the thermal stabilization of nc Cu was studied by Mula et al. (2015). It was reported that the complete dissolution of solute Y atoms in Cu matrix occurred

after 8h of milling at room temperature using a SPEX8000M mill. Moreover, it was confirmed by XRD pattern analysis and Gibb's free energy change calculation using Miedema's semi-empirical model. After annealing at 800ºC, the Cu-Y alloys were found to form some intermetallic phases, which increased the thermal stability by Zener pinning mechanism. The addition of Y was found to be a good stabilizing agent for Cu matrix and maintained a grain size of ~35 nm even after annealing at 800ºC. The high microhardness was ascribed to the formation of intermetallic phases and retaining of nanocrystalline grains. Finally, it was reported that Zener pinning and thermodynamic mechanisms of Y segregation both were effective to yield the high thermal stability of NC Cu-Y alloys.

At Indian Institute of Technology Kharagpur, the structure as well as thermal stability of nanocrystalline materials was investigated Murty et al. (2003). It was traced that due to the presence of high density interfaces of nano-sized grains, grain growth was extremely large even at room temperature. The experiments implied that lattice strain has direct effect on stability because strain release always occurs prior or simultaneously with grain growth and also suggested that grain growth cannot be solely controlled by Zener pinning.

2.9 Strengthening mechanisms for the Fe-based alloys

Stabilized nanocrystalline/ultrafine grained (UFG/NC) Fe-Cr alloys can be used as potential structural materials due to their high yield strength as compared to their coarse grained counterparts. The various strengthening mechanisms are involved to produce stabilized Fe-Cr based alloys with high yield strength. The solid-solution strengthening, grain size refinement, precipitation hardening and dislocation strengthening play the major roles to strengthen the Fe-Cr based alloys (Rohatgi et al., 2001; Sarma et al., 2008; Yedla et al., 2010). The different strengthening mechanisms, which are relevant to the present work, are discussed briefly in the subsequent sections.

2.9.1 Solid solution strengthening

Solid solution strengthening is well-established and successful method for improving the strength of metallic materials. Atoms of alloying elements added in the parent metal occupy either interstitial (interstitial solid solution) or substitutional (substitutional solid solution) sites in the lattice of matrix (parent metal) and increases the strength of parent material due to distortion in lattices as shown in Figs. 2.9a & b. The stress fields generated around the solute

atoms interact with the stress fields of a moving dislocation and thus restricting the motion of dislocations thereby increasing the stress required for plastic deformation. Fe-based alloys are mostly alloyed with substitutional alloying elements such as Cr, Ni etc. As per the Hume-Rothery rules (Dieter, 1961), the substitutional solid solution strengthening depends on: concentration and size of solute atoms, valency and shear modulus of solute atoms. Moreover, the atomic size difference between parent and solute metals should be less than 15%. The crystal structure of the metals and the valency of the atoms must be the same for good substitutional solid solubility.

The strengthening increment by a solute ($\Delta\sigma_{ss}$) due to concentration (C) of a solute atom is defined as

$$\Delta\sigma_{ss} = HC_{\alpha} \tag{2.12}$$

Where, α & H are constants. A higher concentration of solute atoms will obstruct more dislocations as compared to low solute concentration, thereby increasing the strength (Dieter, 1961).

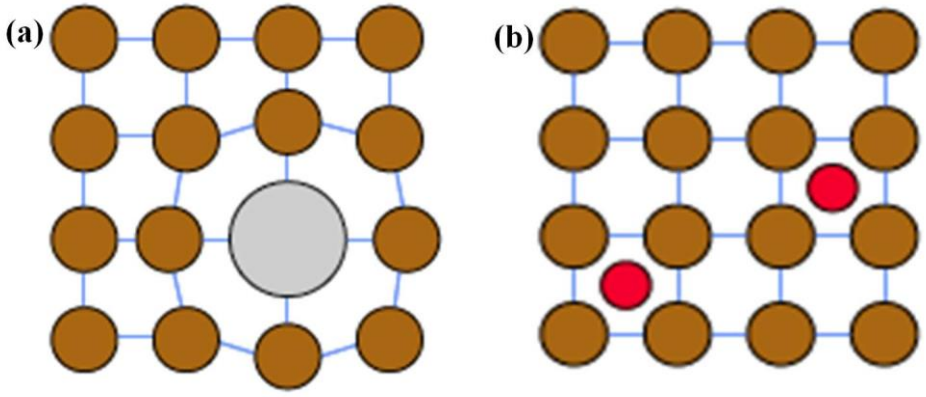

Fig. 2.9: (a) Substitutional atom (b) Interstitial atom (Callister et al., 2007).

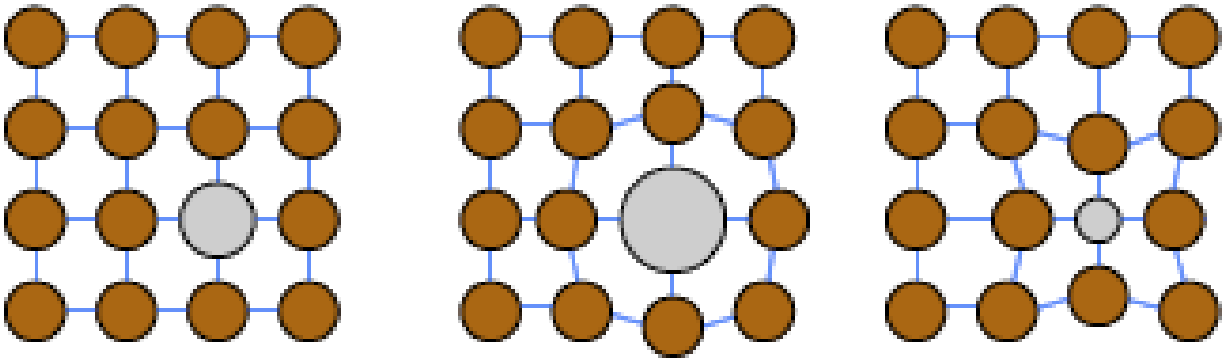

Fig. 2.10: Effect of solute size (Callister et al., 2007).

The degree of strength fully depends on the alloying element and relative difference between the size of solute/alloying element and solvent atoms. Fig. 2.10 shows a large atomic size difference generating more distortion in the crystalline lattice. This extra distortion further impedes the progress of dislocations resulting in higher strength. For example, the atomic radii of Fe (1.26Å) and Cr (1.28 Å) are very close to each other and Cr gives very low atomic distortion in Fe-lattices. Atomic sizes of Niobium (1.47 Å), Yttrium (1.81 Å) and Zirconium (1.56 Å) (Clementi et al., 1967) are much larger than Fe atoms and give the maximum strength. These elements give a larger return on the strength because of more distortion in the parent Fe lattices.

2.9.2 Grain boundary strengthening

In polycrystalline materials, orientation of grains changes abruptly on moving from one grain to another across the grain boundary. During deformation, it becomes difficult for the dislocations to move from one grain to another grain due to the random orientation of grains and dislocation moves on a particular slip plane. Due to this reasons, the dislocation during deformation initially piles up near the grain boundary. This pile-up of dislocations will be more rapid in smaller size grains. Thus, it restricts the motion of dislocations easily in smaller size grains. Therefore, the material with smaller size grains strain hardens which increases the strength. If the grain boundary is low angle grain boundary, the hindering of dislocations is less; while the high angle grain boundaries can impede the motion of dislocation effectively. Thus, the strength of the material increases. Fig. 2.11a shows dislocation moving along a slip plane approaching grain boundary. Fig. 2.11b shows low and high-angle grain boundaries with respect to atom positions adjacent to the grain boundaries.

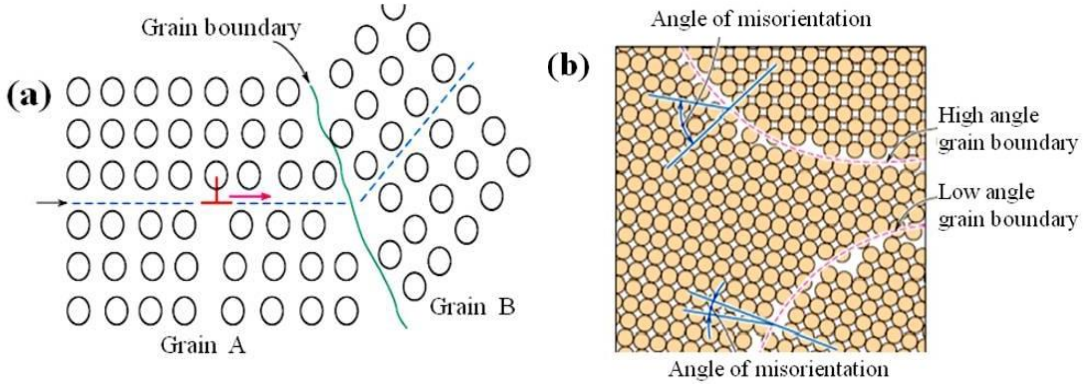

Fig. 2.11: (a) Dislocation motion approaching a grain boundary (b) Low and high-angle grain boundaries with respect to adjacent atom positions (Callister et al., 2007).

As the grain size is reduced, the mean distance travelled by dislocation decreases, and impede the dislocations at grain boundary. This results in the increase of the YS of a material. This is explained through well-known Hall-Petch relation (Hall, 1951; Hansen, 2004; Petch, 1953) in various studies.

$$\sigma_{\mathrm{y}} = \sigma_o + kd^{-1/2} \tag{2.13}$$

Where, σ_{y}, σ_{o}, d and k denotes, respectively, the yield strength, friction stress, grain size and k is the locking parameter that estimates the hardening contribution made by grain boundary. The YS of the material is inversely proportional to its grain size (i.e. the decreases grain size with increase in the strength). The above relation is not valid for extremely fine grained polycrystalline materials (grain sizes <10 nm) and then it is called as reverse Hall-Petch relation (Gleiter, 2000, Chokshi et al., 1989). Chokshi et al. (1989) was the first research group to report on the decrease in hardness with decrease in the grain size in the nanometric range <1μm. They mainly discussed about the inverse Hall-Petch relation for nanocrystalline copper and palladium at ambient temperature.

2.9.3 Dislocation strengthening

Shear stress, which is essential to make dislocation slip, constantly increases with increasing shear strain value during plastic deformation of a metal. The increase in the value of shear stress, which is needed to cause slip due to previous plastic deformation, is called strain hardening. It can be taken place as the dislocations interact with each other and create barriers which hinder their motion through crystal lattice (Zhao et al., 2008). Hardening due to dislocation interaction is a complicated problem as it involves large number of dislocations. It is difficult to specify group behavior in a simple mathematical way. According to Taylor equation, there is a correlation between dislocations density and YS as

$$\sigma_{\mathrm{y}} = \sigma_{\mathrm{f}} + \alpha M G b \rho^{1/2} \tag{2.14}$$

Where b, ρ and G denotes, respectively, the Burgers vector, dislocation density and bulk shear modulus. From equation (2.14), it can be seen that the YS is directly proportional to the dislocations density. Therefore, with the increase in dislocations density during plastic deformation, the YS of the material increases significantly.

2.9.4 Precipitation strengthening

Plastic deformation of materials takes place when large numbers of dislocations able to move freely. To enhance the mechanical properties of materials (i.e. yield strength), it is essential to restrict the mobility of these dislocations. Presence of precipitates offers resistance to dislocation motion either by Orowan mechanism (bypassing of precipitates by dislocations) or by Friedel mechanism (shearing of precipitates by dislocations) as shown, respectively, in Figs. 2.12a and b (Arzt, 1998; Dieter, 1961; Shin et al. 2003). The hardness and strength of metal alloy can be improved by the production of uniformly dispersed particles of secondary phase in original phase matrix. The phase transformation can be attained by thermal or mechanical treatments. This process is called precipitation hardening. The very small dispersed particles of new phase are known as precipitates. In most of the binary systems, alloying above a value of concentration will cause the formation of a second phase as per equilibrium phase diagram. The dislocation movement in the matrix is efficiently restricted by the uniformly dispersed coherent precipitates. They have to bend around and bypass the particles. The strengthening in metal is inversely proportional to the dispersed particle spacing. But, at elevated temperatures the microstructure tends to become unstable as the particles undergo coarsening to become incoherent to the matrix. The strength correspondingly decreases with increase in the inter-particles' spacing.

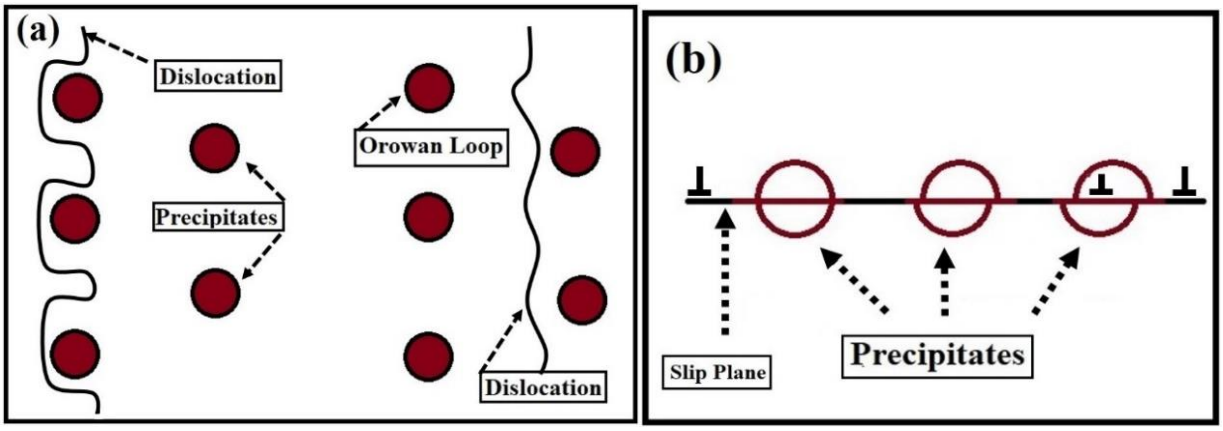

Fig. 2.12: (a) Bowing and bypassing between precipitates and dislocation through Orowan mechanism, (b) shearing of precipitates by dislocations through Friedel mechanism (Dieter, 1961; Shin et al., 2003).

2.10 Research gap and formulation of problem for the present study

A detailed literature survey has been carried out on the development of Fe-based alloys developed by mechanical alloying followed by consolidation using different methods such as

spark plasma sintering (SPS). The important findings from the literature and on the basis of that, the following research gaps have been enlisted to formulate the problem for the present study.

2.10.1 Important findings from the literature review

- Few studies were carried out on high temperature stabilization and annealing effect on microstructural changes of nanostructured Fe-based alloys with or without adding a suitable insoluble solute element.
- Most of the studies investigated only the thermal stability of Fe-based binary alloys (e.g. Fe-Y, Fe-Zr etc.) in terms of hardness measurement and grain size evaluation after annealing.
- The Fe-based nc/UFG alloys showed poor mechanical properties at high temperatures. Extensive grain growth in nc Fe-based alloys at high temperatures is found to be the reason for the loss of mechanical properties.
- Hindering the grain growth of Fe-based alloys at elevated temperatures improves their mechanical properties.
- Zr, Y, Ta, W, Nb & Sb were reported to be good stabilizers for Cu- and Ni-based alloys. In few studies, Zr and Hf were described to act as good stabilizers for nanocrystalline Fe-based alloys.

2.10.2 Research gaps

Most of the studies were found to focus on the thermal stability of Fe-based binary alloys on the basis of grain size evaluation and hardness measurements after annealing at different temperatures. Few studies were conducted the sintering characteristics by hot pressing, hot isostatic pressing, explosive compaction and SPS.

But,

- Detailed investigation has not been made on the thermal stability of ternary Fe-Cr-X (X=Zr, Y, Nb, Hf) alloys prepared by mechanical alloying in single study.
- Analysis of the stabilization mechanisms (solute drag, Zener pinning, grain-boundary segregation) was not made in detail for Fe-Cr-X (X=Zr, Y, Nb, Hf) alloys and also not validated with the mechanical properties and microstructure.

- Thermodynamic feasibility has not been studied for the formation of ternary Fe-Cr-X (X=Zr, Nb, Y, Hf) nanocrystalline disordered solid solutions developed by MA through estimating of Gibbs free energy change using Miedema's and Toop's models and not verified by the experimental results (i.e. stored energy in the material).
- Spark plasma sintering characteristics of the disordered solid solutions and its effect on the microstructure and mechanical properties (such as hardness, wear and compressive strength) have not been investigated at all. Corrosion resistance of the sintered Fe-Cr-X (X=Zr, Y, Nb, Hf) alloys was also not studied.
- Analysis of each strengthening mechanism involved in the Fe-Cr-X alloys (e.g. solid solution strengthening, grain boundary strengthening, precipitate hardening and dislocation strengthening) contributing to the total yield strength has not been reported so far.

2.10.3 Objectives of the present investigation

Based on the literature review carried out and research gaps observed, the following major objectives are identified for the present study.

- Thermodynamic feasibility of the formation of ternary Fe-Cr-X (X=Zr/Nb/Y) disordered solid solutions prepared by mechanical alloying. It would be made through estimating the theoretical Gibbs free energy change required using Miedema's and Toop's models and validate the same with the experimentally obtained total stored free energy in the as-milled samples.
- Detailed investigation on the thermal stability (up to 1200°C) of the mechanically alloyed disordered solid solutions through measurement of microhardness and microstructural features by XRD, TEM-SAED and EBSD analysis. Analysis of the stabilization mechanisms, i.e. Zener pinning, solute drag, grain-boundary segregation and validate the same with the mechanical properties and microstructure of the corresponding alloy.
- Study the spark plasma sintering characteristics of the stabilize disordered solid solutions and its effect on the microstructure and mechanical properties, such as microhardness, wear and compressive strength. Moreover, corrosion resistance also will be investigated for the same.

- Analysis of the relevant strengthening mechanisms (such as solid solution strengthening, grain boundary hardening, precipitation strengthening and dislocation strengthening) and their contributions to the total yield strength (YS). Validation of the calculated YS will be made with the experimental YS.
- Overall comparison of the microstructural evolution & thermal stability and mechanical properties of the Fe-Cr-X (X=Y/Nb/Zr) alloys, before and after the spark plasma sintering. Correlation of the microstructure and mechanical properties will be made.

In order to achieve the above mentioned objectives, the overall thesis is organized in five chapters: Introduction (Chapter 1), literature review (Chapter 2), Materials, experimental and characterization details (Chapter 3), Results and discussion (Chapter 4) and Conclusions (Chapter 5). A flow-chart depicting the interlinking of the chapters and their contribution towards achieving the overall goal is shown in Fig. 2.13.

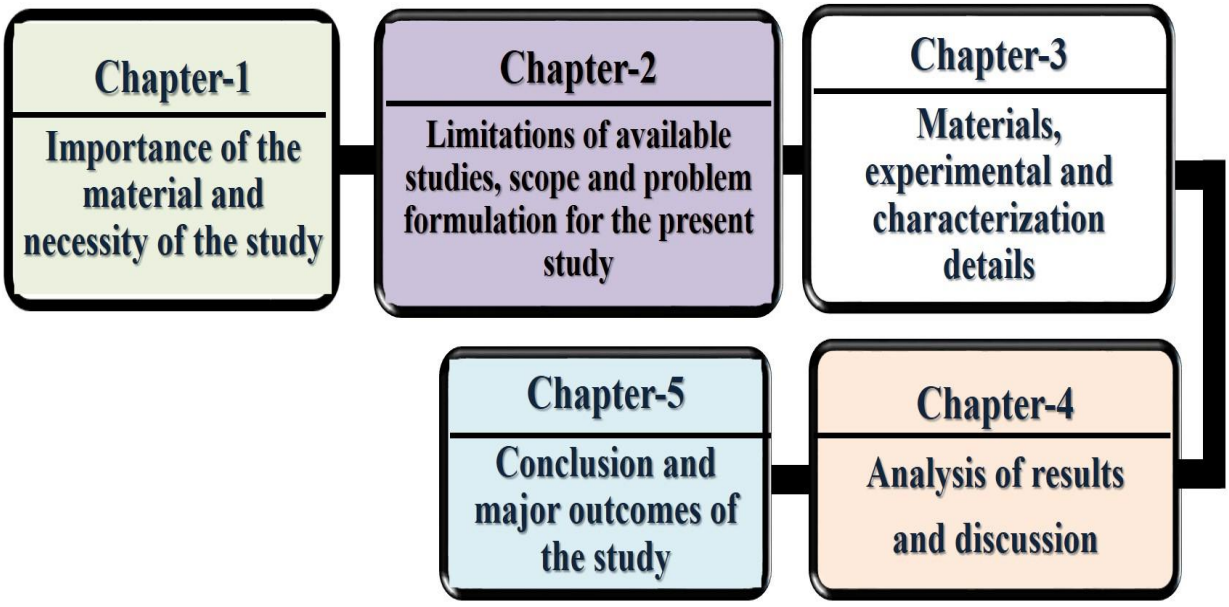

Fig. 2.13: Contribution of each chapter to overall objectives.

2.10.4 Plan of the present study

Detailed plan of the present study is summarized in the following flow chart (Fig. 2.14) for the convenience.

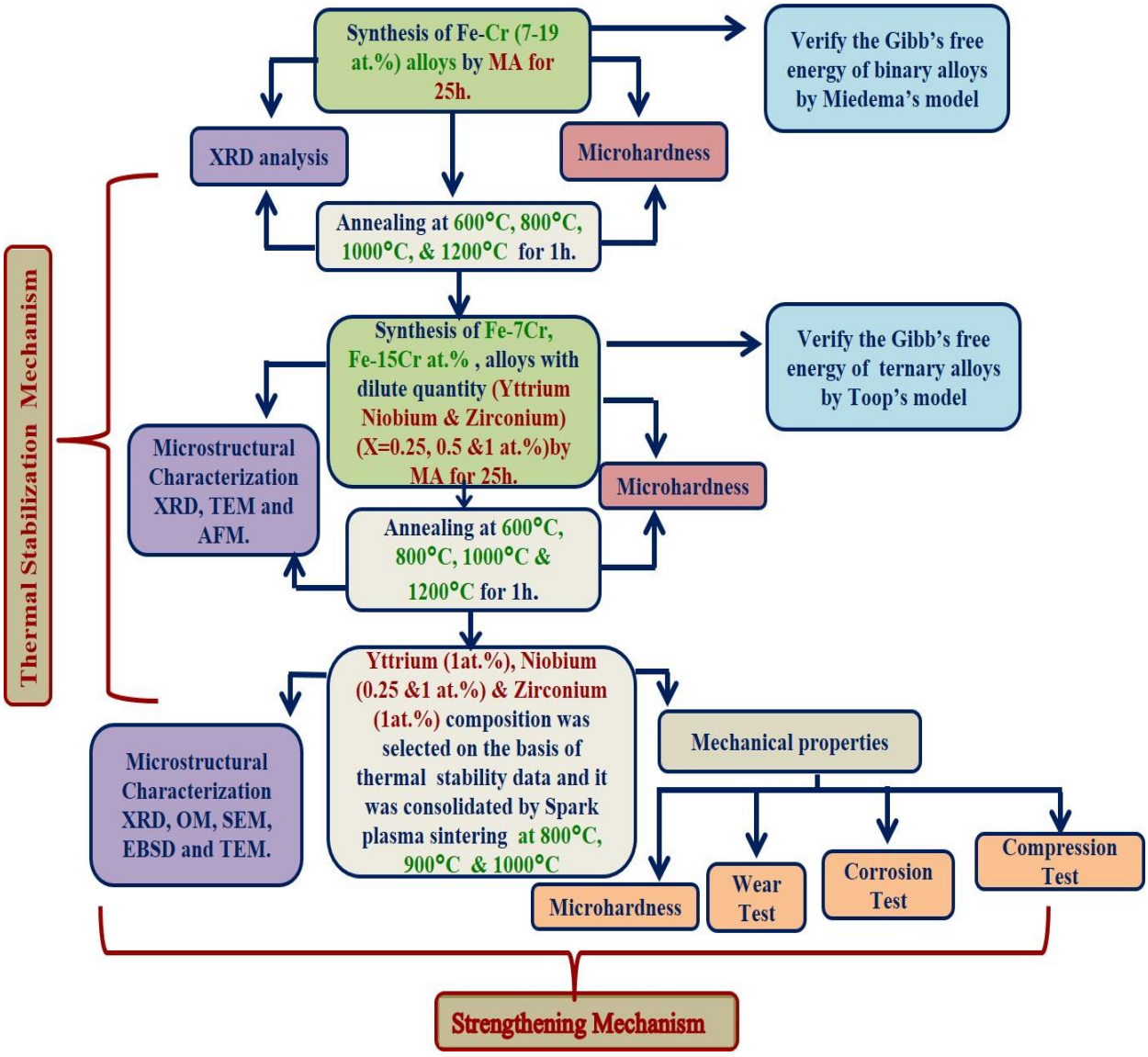

Fig. 2.14: Flow diagram of detailed plan of the present study.

CHAPTER 3 Materials, experimental and characterization details

This chapter deals with the detailed study of the materials' synthesis and processing, experimental procedures and characterization techniques used in the present investigation. Initially, mechanical alloying was carried out to synthesize Fe-Cr alloys with 7, 11, 15 & 19% Cr (all in at.%). Further, the Fe-7Cr and Fe-15Cr alloys have been chosen to study their thermal stability after addition of small quantity of insoluble solute atom (i.e. 0.25, 0.5 & 1.at% of Y, Nb & Zr). These two alloy systems were reproduced after addition of X% of solute atoms by mechanical alloying for 25 h. Then the as-milled Fe-7Cr-X and Fe-15Cr-X alloy powders were annealed in batches from 600-1200℃ under Ar+2%H atmosphere. On the basis of the thermal stability, the best alloy compositions were chosen and consolidated by spark plasma sintering at 800, 900 & 1000℃. After that the as-milled, annealed and spark plasma sintered (SPSed) samples were subjected to a series of characterizations using different techniques, e.g., microstructural characterization by X-ray diffraction (XRD), optical microscopy (OM), scanning electron microscopy (SEM), electron backscatter diffraction (EBSD), atomic force microscopy (AFM), and transmission electron microscopy (TEM). Mechanical properties were investigated by using Vickers microhardness test, wear test and compression test. Corrosion behavior of the SPSed samples was studied using potentiodynamic polarization test in the present study. The details of materials, experimental methods and characterization techniques have been described in the subsequent sections.

3.1 Starting Materials

Laboratory grade elemental powders of Fe, Cr, Y, Nb and Zr (Alpha Aesar make, with purity >99%) with particle sizes of 20-100 μm were used to design the Fe-based alloys studied. Table 3.1 shows details of the alloy compositions.

Table 3.1: Composition of the alloys

Alloy Compositions all are in (at.%)								
Solute atoms	Fe-7Cr			Fe-11Cr	Fe-15Cr			Fe-18Cr
Yttrium (Y)	0.25	0.5	1	-	0.25	0.5	1	-
Niobium (Nb)	0.25	0.5	1	-	0.25	0.5	1	-
Zirconium (Zr)	0.25	0.5	1	-	0.25	0.5	1	-

3.2 Experimental techniques

3.2.1 Mechanical alloying

Mechanical alloying (MA) technique was employed to synthesize Fe-7% Cr and Fe-15% Cr alloys (all in at.%) in addition with 0.25, 0.5 and 1 at.% X (X=Y, Nb & Zr) to investigate effect of solute atoms on ternary Fe-Cr-X alloy formation and their thermal stability. Elemental powders of Fe, Cr, Y, Nb and Zr (Alpha Aesar make, with purity >99%) with particle sizes of 20-100 µm were used to blend the alloy compositions in high purity argon atmosphere (purity <10 ppm O_2). The MA was carried out for 25 h at room temperature in 440 grade hardened steel grinding media using a SPEX 8000M shaker mill (as shown in the Fig. 3.1a). The grinding system (hardened steel vial 8007) consisted of 17 numbers 8 mm diameter and 16 numbers 6 mm diameter stainless steel balls (Fig. 3.1b). Prior to milling, the elemental powder material was sealed in vial in a high purity argon atmosphere in the glove box (Fig. 3.1c). The ball to powder weight ratio was maintained at 10:1 throughout the milling duration (i.e. 25 h).

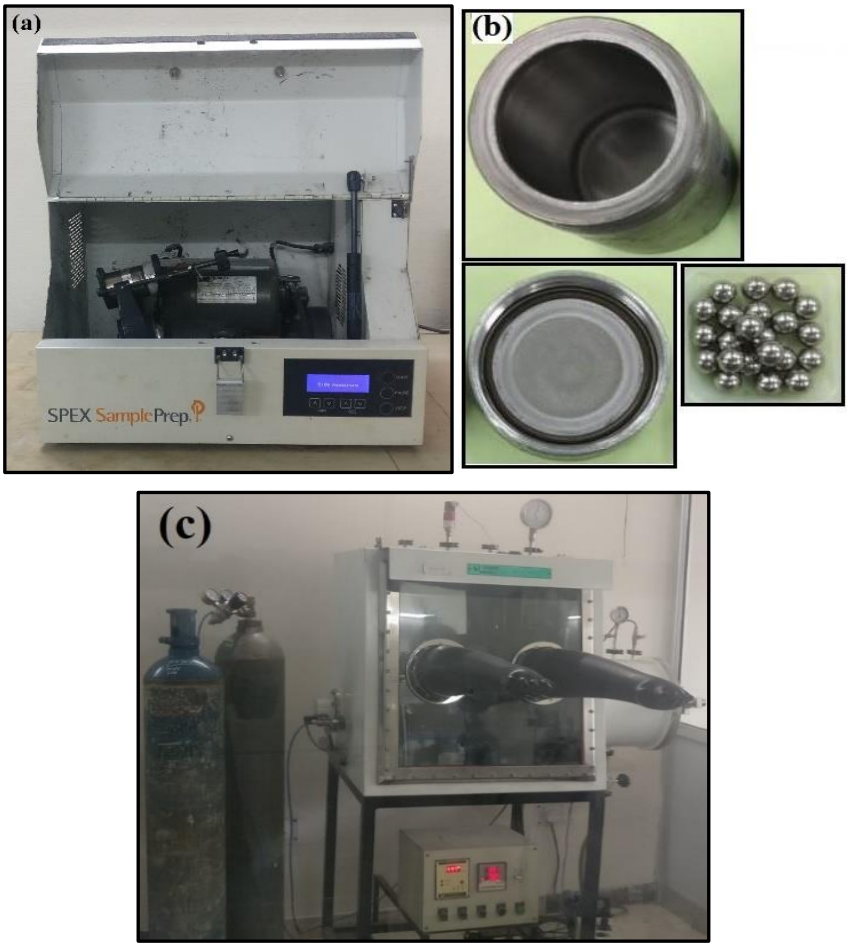

Fig. 3.1: Photograph (a) SPEX 8000M shaker mill, (b) Grinding media (vial) and balls used for mechanical alloying (MA), (c) Glove box for sealing the elemental powers.

3.2.2 Annealing equipment and conditions

Fig. 3.2a shows a photograph of the tubular furnace used in the present study to anneal the samples up to 1200°C. The Fe-7Cr-X and Fe-15Cr-X alloys (all in at.%) with varying quantity of insoluble solute atoms 0.25, 0.5 and 1 at.% X (X=Y, Nb & Zr). Tungsten carbide die-punch was used to compact the as-milled samples at a pressure of 1.8 GPa using a hydraulic press (Fig. 3.2b) with the dimension of 10 mm diameter and 2 mm thickness. The compacted disk samples were placed in ceramic boats into a quartz tube along with a specially designed thermocouple placed at the same position. The tube was vacuum down to <50 milli-torr (6.66 pascal) and refilled with 2% H_2 (bal. Ar) atmosphere. The same process was repeated three times and then the tube was allowed to pressurize to ~2psi (13789.51 pascal). The batch annealing was carried out for the compact disk samples under an ultrahigh purity Ar+2% H_2 atmosphere for 1 h at 600, 800, 1000 and 1200°C. If more than one sample was to be run simultaneously in the same boat, the samples were placed accordingly. After reaching the desired temperature, the holding period for annealing (i.e. 1 h) was recorded. Then, the furnace was rolled off quickly. Depending on annealing temperature, the rate at which the furnace (heating system) was rolled off was varied to reduce under thermal shock on the tube (i.e. cooled more slowly for higher temperatures). The tube as well as the sample (inside the tube) was kept within the furnace in switch off condition till it cooled down to 300°C. The cooling rate was recorded through the thermocouple controller. Typical cooling rate was ~2-3°C/s at a higher temperature range. At lower temperature range (below 300°C), the tubular furnace was taken out of the furnace and allowed to cooled down to room temperature in normal air cooling. After annealing, the samples were prepared for characterization.

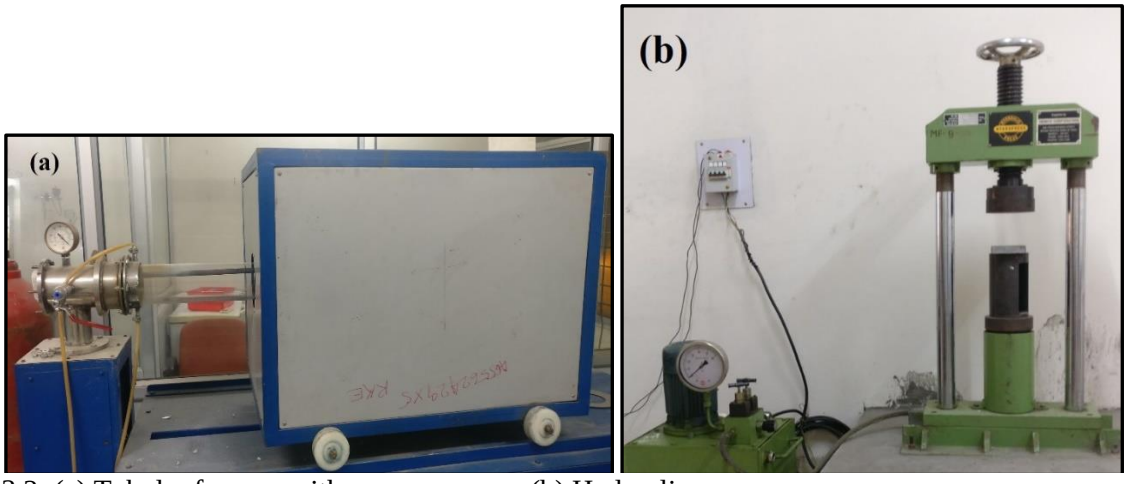

Fig. 3.2: (a) Tubular furnace with vacuum pump, (b) Hydraulic press.

3.2.3 Consolidation by spark plasma sintering (SPS)

Spark plasma sintering (SPS) machine Dr. Sinter 625 (Fig. 3.3a) was used to consolidate the nanocrystalline Fe-Cr-X (X=Y, Nb, Zr) alloys. The best alloy compositions were chosen from the annealed samples on the basis of their thermal stability (i.e. grain size and microhardness values). Further, consolidation by SPS was carried out for Fe-7Cr-1Y, Fe-15Cr-1Y, Fe-7Cr-0.25Nb, Fe-7Cr-1Nb, Fe-15Cr-0.25Nb, Fe-15Cr-1Nb, Fe-7Cr-1Zr and Fe-15Cr-1Zr alloys. The calculated amount of as-milled powder sample was spilled into the graphite die-punch so that the sintered sample dimensions could be 10 mm diameter with ~5 mm thickness (Fig. 3.3b). The SPS was carried out at 800, 900 and 1000°C under high purity argon atmosphere using Dr. Sinter 625 machine. The heating rate was maintained at 100°C/min and holding time was kept for 5 min at each sintering temperature. The pressure was maintained at 60 MPa (i.e. 4.7 kN) throughout the sintering process. The sintering temperature was monitored through real-time measurement by a K-type thermocouple which is fixed permanently in the SPS machine.

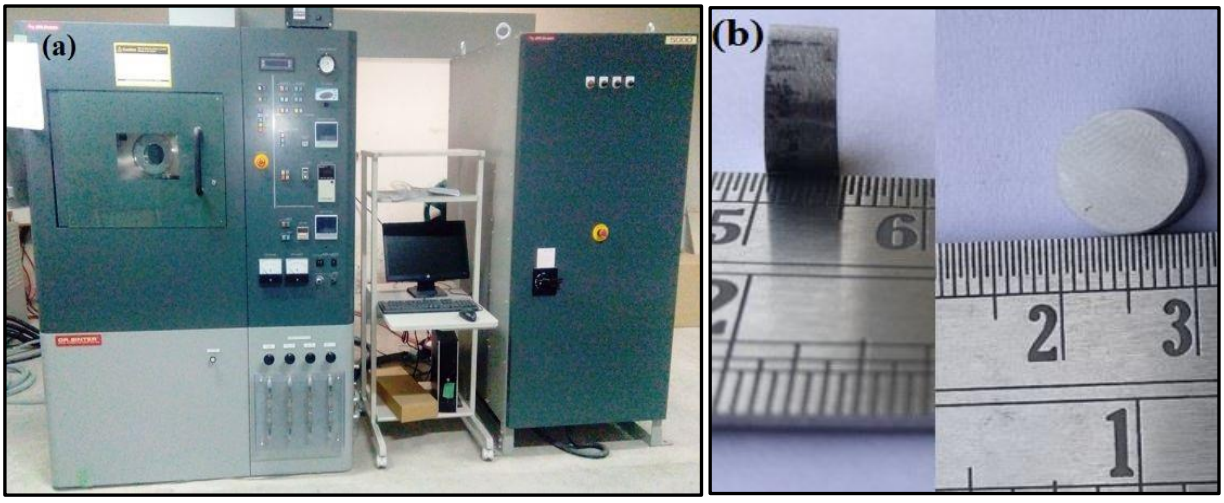

Fig. 3.3: (a) Photograph of the (Dr. Sinter 625) spark plasma sintering (b) Spark plasma sintered samples.

3.3 Microstructural characterization

3.3.1 X-ray diffraction (XRD)

The X-ray diffraction (XRD) phase analysis was carried out by Cu Kα radiation (λ=1.542Å) in a Bruker AXS D8 X-ray diffractometer (Fig. 3.4). X'pert high score plus software was used to remove the background subtraction and peak stripping of $K\alpha_2$. The XRD phase analysis was carried out at different stages, i.e. for the as-milled, annealed and SPSed samples for the Fe-Cr-X (X=0.25, 0.5 & 1.at %) alloys with addition of insoluble solute atom (Yttrium, Niobium & Zirconium). The XRD patterns were recorded from the 2θ position of 30° to 90° with a scan

rate of 1˚/min and the XRD machine was operated at an accelerating voltage of 40 kV. The peak broadening, peak shift and peak intensity of the XRD patterns analysis were made at different stages of as-milled, annealed and SPSed samples. The XRD analysis was studied to determine dislocation density, crystallite size, lattice microstrain and lattice parameter, which are useful tool to quantify and also investigate the strengthening mechanisms. The average crystallite size and lattice microstrain were estimated from the XRD line profile analysis of three major peaks after eliminating the instrumental peak broadening (B_i) and broadening due to strain (B_s). The instrumental broadening (B_i) was obtained by running the standard polycrystalline silicon sample. Then, B_i was subtracted from observed peak width (B_o) using the geometric mean of Gaussian and Lorentzian profiles ($B_r^2 = (B - B_i)\sqrt{B^2} - B_i^2$). This gives B_r, i.e. broadening due to crystallite size (B_c) + broadening due to strain (B_s). The broadening due to strain is eliminated using the plot between $B_r Cos\theta$ *vs*. $Sin\theta$ using the Williamson-Hall method. The precise lattice parameter was calculated from three major XRD peaks by the extrapolation of a_{Fe} against ($\cos^2\theta/\sin\theta$) plot to $\cos\theta = 0$.

Fig. 3.4: Photograph of the XRD unit θ/2θ (Bruker AXS D8) advance diffractometer.

3.3.2 Optical microscopy (OM)

The spark plasma sintered samples with the dimensions of 10 mm diameter and 5 mm thickness were cold-mounted to ease of polishing process. Polishing was carried out with different grades (320-2000 grit size) silicon carbide (SiC) abrasive emery papers. During polishing, the sample was turned by 90˚ for each successive paper for effective polishing. After finishing the polishing with the 2000 grit size SiC paper, the sample achieved a uniform surface. This finer

size abrasive paper causes less surface deformation. The SPSed samples were thoroughly cleaned with a jet of air after each paper grinding to remove the loose particles attached to the sample surface. Then, the SPSed sample was moved to cloth-polishing system. Cloth polishing was accommodated in two steps, rough and fine cloth polishing. A variable speed wheel was used for polishing. The rough polishing was done with alumina (Al_2O_3) with 0.02 µm size. A teaspoon of Al_2O_3 abrasive powder was applied near the center of cloth-wheel, moistened with distilled water, then converted into paste. Finally, the alumina (Al_2O_3) solution in distilled water was used for final polishing. After final polishing, the SPSed samples were cleaned initially with running water and then by ethyl alcohol. Finally, the dried sample was etched with a reagent solution of methanol (95 ml) + nitric acid (5ml) (called as Nital) for 10 s and washed with distilled water and dried up. Microstructure was examined with LEICA DMI 5000 M optical microscope (Fig. 3.5).

Fig. 3.5: LEICA DMI 5000 M optical microscope.

3.3.3 Scanning electron microscope (SEM) and electron backscatter diffraction (EBSD)

A ZEISS 51-ADD0048 scanning electron microscope (Fig. 3.6) was used to study the surface morphology after etching SPSed samples. Micrographs were captured at a proper accelerating voltage for the best possible resolution using secondary electron and back-scattered electron imaging modes. The backscattered imaging mode is more prominent than that of secondary imaging mode. The EBSD 51-1385-026 model was attached with the SEM equipment. EBSD is a microstructural characterization technique, which uses backscattered Kikuchi pattern to examine the misorientation of grains and texture or preferred orientation of grains in a polycrystalline material. It furnishes the information about the orientations of the subgrains and grains in a polycrystalline material that cannot easily be obtained from the SEM/TEM analysis. Therefore, in the present study, the samples of Fe-15Cr-1Y alloy sintered at 1000°C were

characterized using the EBSD technique. The photograph of the SEM equipped with EBSD can be seen from Fig. 3.7.

The EBSD measurement was done by placing a flat/electropolished crystalline sample in the SEM chamber tilted at an angle ~70° from horizontal axis towards the diffraction camera. The EBSD detector consists of a phosphor screen, a CCD camera and a compact lens. The phosphor screen is placed inside the specimen chamber of the SEM, which is at an angle of about 90° to the pole piece and is attached to a compact lens for focusing the image on the CCD camera. This arrangement of the instrument allows some of the electrons entering the sample to backscatter and escape. These electrons might leave the sample surface, at the Bragg condition and diffract to produce Kikuchi bands inside the SEM. The schematic of EBSD setup is shown in Fig. 3.7. The obtained Kikuchi lines are collected by CCD camera and analyzed using specialized computer software using an optimized Hough transform. To get a good diffraction patterns/Kikuchi bands, the sample was well prepared to achieve extremely high mirror finished surface. The sintered sample was initially mechanically polished using SiC abrasive papers of different grit sizes, usually varying from 320-2000. To avoid embedding of abrasive particles water was used to flush away abrasives particles. These samples were then cloth polished using a colloidal solution of alumina (Al_2O_3) of 0.02 µm size. Then, the sample was electropolished in an electrolyte of 20% perchloric acid in methanol at −40°C and the electropolishing system was operated at 21 V for 50 s. The EBSD scan was performed on the polished sample with a step size of 0.05 µm and subsequently analyzed by TSL-OIM software.

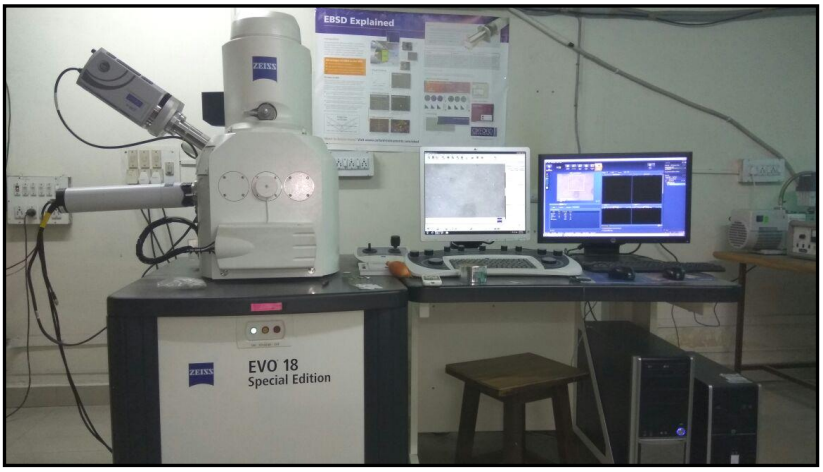

Fig. 3.6: The photograph of ZEISS 51-ADD0048.

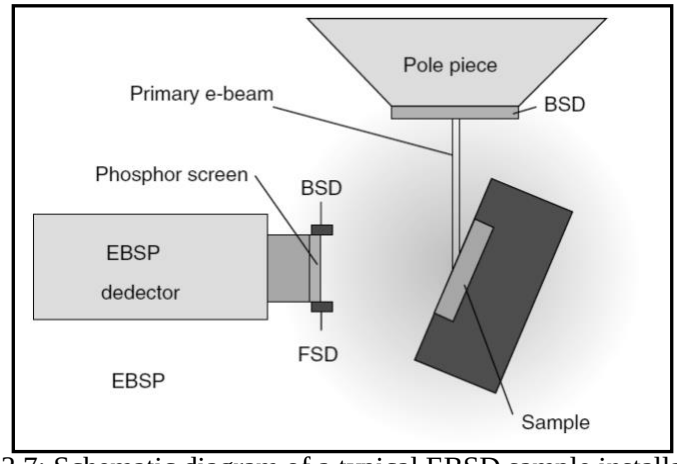

Fig. 3.7: Schematic diagram of a typical EBSD sample installation.

3.3.4 Transmission electron microscopy (TEM)

The microstructural features, which are not accessible using optical microscopy and SEM, could easily be revealed and analyzed by using transmission electron microscopy (TEM). It can magnify the specimens in the region of 10^{-6} m to 10^{-9} m to detect the submicron and nanometer level constituents by imaging and diffraction techniques. TEM is used to determine the grain size along with other different types of phases and their distribution through bright field and/or dark field imaging and selected area electron diffraction patterns. In present work, the TEM analysis was carried out by using a FEI Technai 20 TEM (Fig. 3.8c) operated at 200 kV. The selected samples from the as-milled and annealed powder specimens were prepared by drop cast technique on a 3 mm-diameter carbon-coated Cu-grid with 200 mesh size. Whereas, the SPSed specimens were prepared by using twin-jet electro-polishing for the TEM investigation. A small amount of powder (as-milled and annealed) sample was sonicated for 15 min, and then approx. 2 min were allowed to settle down the larger size particles in the bottom of the container. After that with the help of micro-pipette, one drop of liquid (preferably from the top surface of the liquid) was drop cast on to the Cu-grid. The sintered samples were initially mechanically polished with different grades of SiC abrasive papers (325-2000 grit size) to thin down to <100 μm for the TEM study. Then, the specimens of 3 mm diameter disc were punched out using Gatan model 656 from the thin foil to perform electro-polishing (Fig. 3.8a). The sintered samples were electropolished by a FEI twin-jet electro-polishing equipment (Fig. 3.8b) operated at 30 V using a solution of 95% methanol + 5% perchloric acid at room temperature.

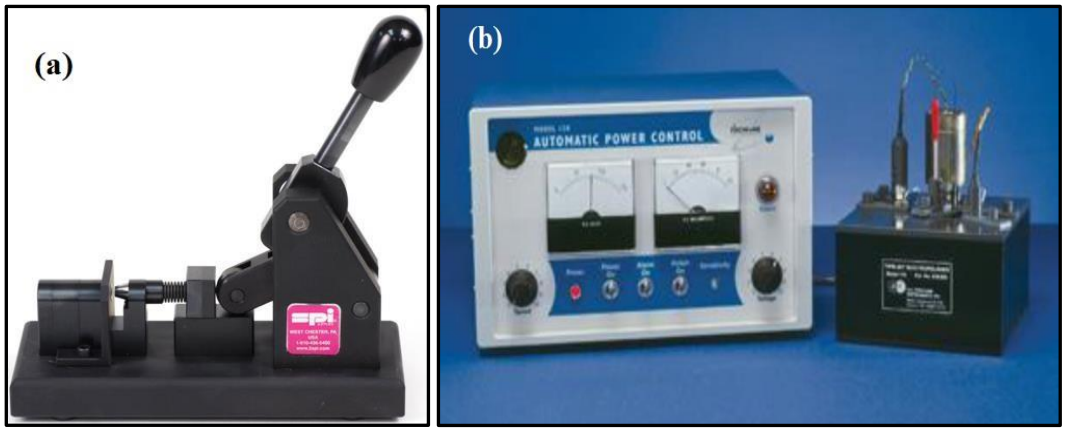

Figs. 3.8: (a) Gatan model 656 punches to produce the 3-mm disk, (b) Fischione automatic Twin-Jet electropolishing system.

Fig. 3.8c: Photograph of the TEM unit (FEI Tecnai-20 G2S-TEM).

3.3.5 Atomic force microscopy (AFM)

Atomic force microscopy (AFM) analysis was performed on the as-milled and annealed compacted disk samples using a silicon nitrate probe in VECCO di Innova NTEGRA classic, atomic force microscope (Model: TS-150). Photograph of the AFM microscope is shown in Fig. 3.9. In the present investigation, this instrument is used mainly to estimate average crystallite size of the specimens.

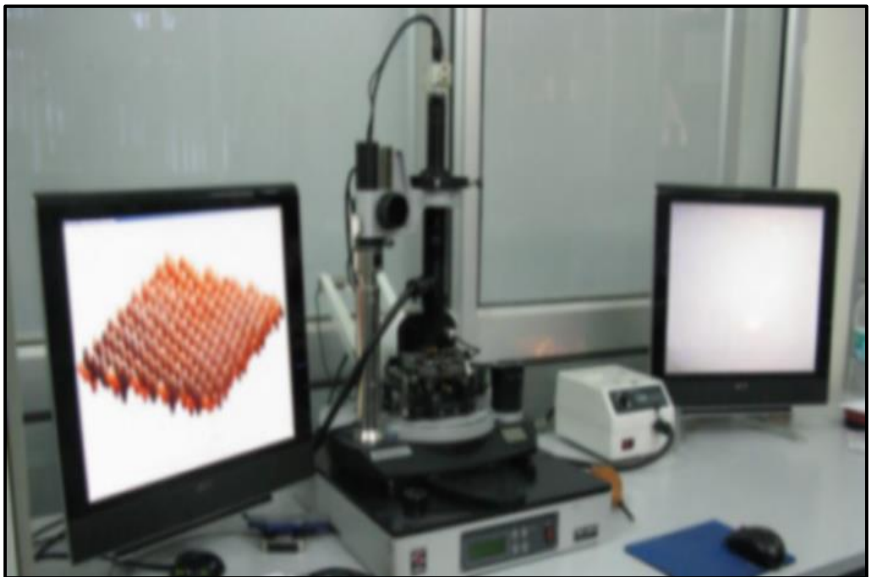

Fig. 3.9: Photograph of the NTEGRA classic atomic force microscope.

3.4 Mechanical testing

3.4.1 Vickers microhardness measurement

Hardness is defined as the property of a material, which measures the resistance offered by it to plastic deformation. The Vickers microhardness machine consists of a diamond indenter with a right pyramid shape having a square base and an angle of 136° between its opposite faces. The microhardness test was performed to evaluate hardness values (HV) of the disc samples of the as-milled, annealed and SPSed samples. Fig. 3.10 shows a photograph of Vickers microhardness testing machine (FEI-VM50) used in the present study. The specimens were polished mechanically with different grades of SiC abrasive papers (325-2000 grit size). Further, the specimens were polished with fine cloth by using a colloidal solution of Al_2O_3 (size 0.02 μm) powders and washed with distilled water. Vickers microhardness measurements were performed on the polished surface using a constant 50 g load. The load was applied at a speed of 15 μm per second with a dwell time of 15 s for each indentation. The appropriate load of 50 g was chosen to avoid influences of the indentation plastic zone with particle boundaries. A particle diameter-to-indent depth of at least 10:1 was maintained for the hardness test of the as-milled and annealed samples. The average of 10 such measurements was taken to report statistical variation for each hardness value.

Fig. 3.10: Future tech microhardness tester FM-800 and fully-automatic hardness testing system ARS 9000.

3.4.2 Relative density measurement

Relative density of the SPSed samples was estimated by using Mettler Toledo weighing machine with density kit setup (Fig. 3.11) which uses Archimedes' principle to calculate the density of the material. The sintered sample was first weighed in air and then weighed within distilled water. By the reduction in weight, the density of the sample is found out using Archimedes' principle. Each sample was tested 5 times after properly removing the moisture content in the sintered sample to ascertain the accuracy of the density. The relative density was found by dividing the density obtained during measurement to the theoretical density of the composition.

Fig. 3.11: Mettler Toledo weighing machine with density kit setup.

3.4.3 Wear test

The dry sliding wear test of the sintered samples was performed on a ball-on-disc type tribometer (TR-201E-M2, DUCOM, Bangalore, India) shown in Fig. 3.12. The dimensions of the cylindrical sintered samples were 10 mm in diameter and 5 mm in thickness. Acetone was used to clean the surface of the sintered samples before wear test. A single crystal spherical alumina ball (Al_2O_3) ~2000 HV with a diameter of 10 mm was used as a counter-body. The sample, which was fixed with circular stainless steel plate, was rotated against the stationery Al_2O_3 ball fixed with the machine. The applied loads were maintained at 5, 10 & 20 N for each sample and the rotational speed was kept constant at 500 rpm for each test. The wear experiments were carried out at an ambient condition (at room temperature) in air for a duration of 25 min. The coefficient of friction was calculated from the ratio of the frictional force to the normal load (i.e. 5, 10 & 20 N). The coefficient of friction was measured at real time by using an electronic sensor which naturally records the frictional force generates between the counter body and the specimen.

Fig. 3.12: The photograph of ball on disc DUCOM T-81.

3.4.4 Surface profilometer

The surface profile of the worn specimens was analysed using a profilometer (Model: SJ 400, Mitutoyo, Japan) through the measurements of width and depth of the wear scars (Fig. 3.13). For each type of sample, minimum 3 wear tracks and 10 such measurements per track were examined to obtain the average value of the width and wear depth of the wear scar. Subsequently, the worn surfaces were examined using SEM to correlate wear behavior with the wear results.

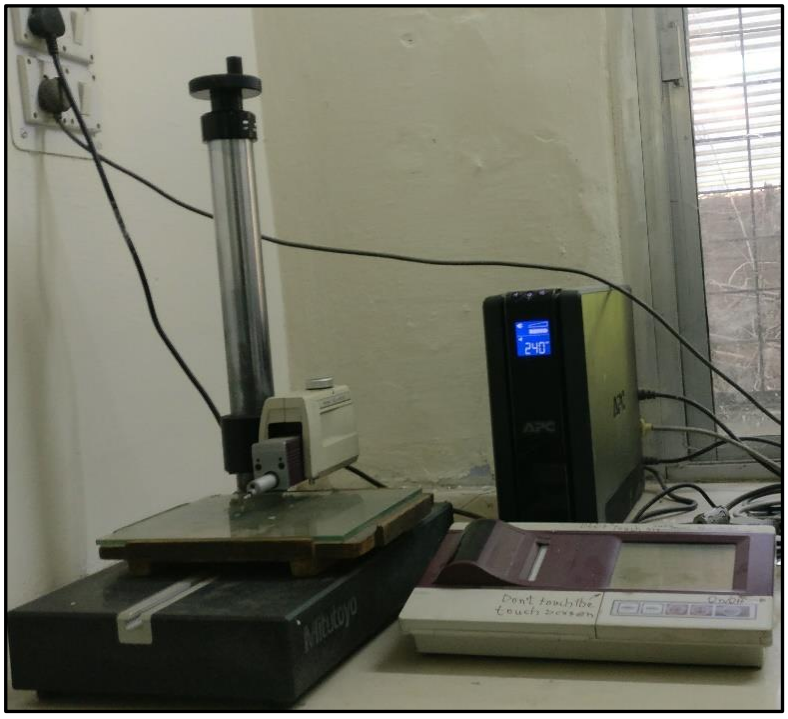

Fig. 3.13: Surface profilometer.

3.4.5 Compression Test

Compression test was carried out at room temperature using a universal testing (Hounsfield Model ZD-20) machine (Fig. 3.14a). The uniaxial compression test was conducted using a strain rate of 1×10^{-3} s^{-1}. Further, the compression test samples were prepared precisely from the SPSed samples using a wire-cut electro-discharge machine (EDM). The sample dimensions were maintained as 2mm×2mm×4mm according to ASTM E9-89a (2000) standard (shown in the Fig. 3.14b).

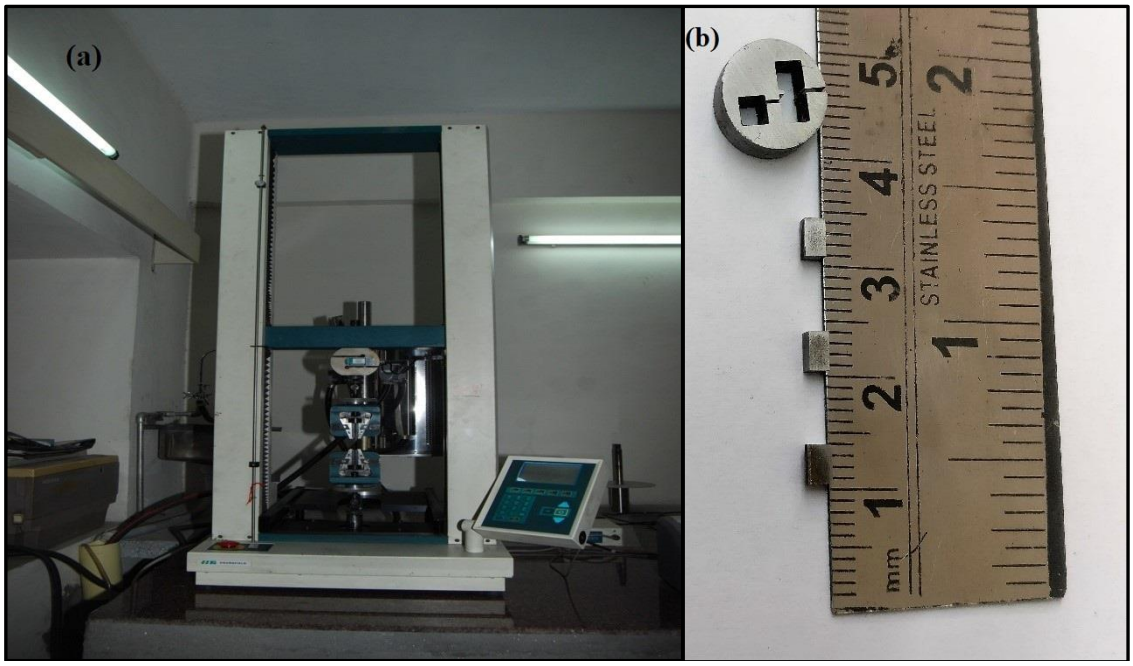

Fig. 3.14: (a) The photograph of the S-Series, H25K-S compression testing machine, (b) Compression test samples.

3.4.6 Corrosion behavior

The corrosion study (potentiodynamic polarization test) of the sintered samples was performed on the Grammy potentiodynamic polarization setup shown in the Fig. 3.15. The tests were carried out in an aerated 3.5wt.% aqueous NaCl solution at room temperature. Before the tests, the samples were polished by different grades (325-2000) of SiC abrasive emery papers followed by cloth polishing with alumina powder (0.02μm). A graphite rod and a saturated calomel electrode (SCE) were used as the auxiliary electrode and reference electrode, respectively. Moreover, the sintered specimen functioned as the working electrode. The electrodes were kept in a flat cell such that an area of $1cm^2$ of the sintered specimen was exposed to the test solution. A ratio between solution volume to specimen surface area was maintained at 300 ml/cm^2. Prior to the polarization test, the specimens were stabilized by keeping in the solution for a duration of 110 min. During this period, the variation in the open circuit potential was recorded as a function of time. The polarization test was carried out at a scan rate of 100 mV/min from −250 mV to +500 mV in the cathodic and anodic directions, respectively. Tafel extrapolation method was used to calculate the corrosion current density (i_{corr}) and corrosion potential (E_{corr}) from the polarization curves. After the polarization test, nature of the corrosion attack of the sintered samples was determined through FE-SEM image analysis.

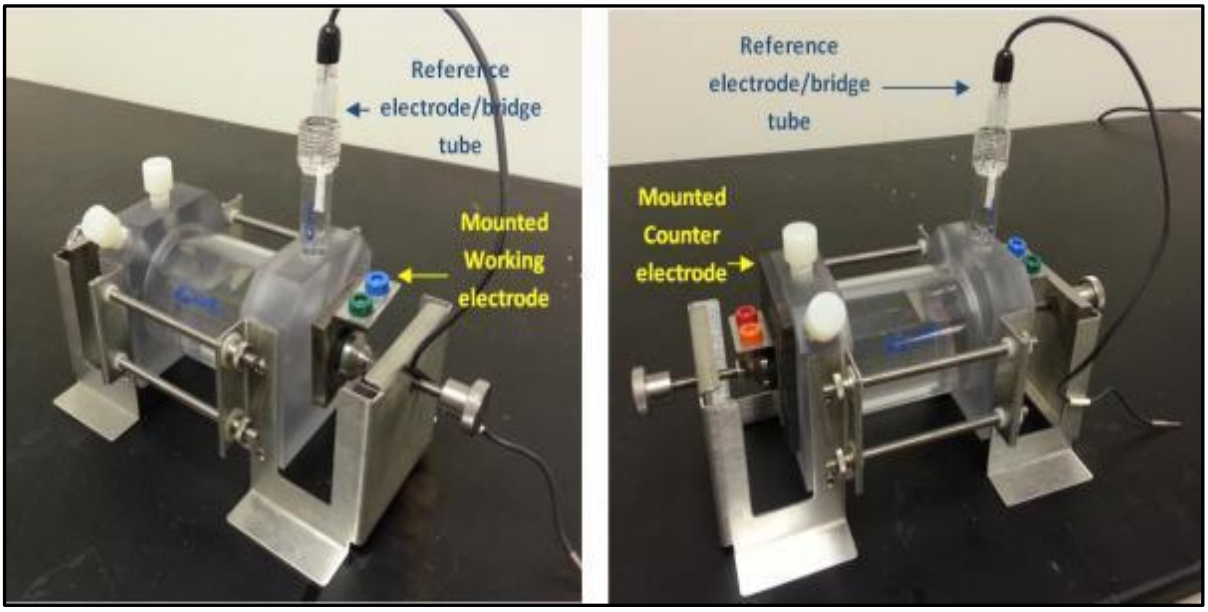

Fig. 3.15: Grammy potentiodynamic polarization setup.

CHAPTER 4 Results and discussion

The detailed results, their analysis and in-depth discussion have been described in this chapter. The major findings of the study and their analysis with explanation have been summarized in the subsequent sections. Initially, four Fe-Cr alloys (Cr=7, 11, 15 & 19 at.%) have been developed by MA and their thermal stability has been investigated. After that, Fe-7Cr and Fe-15Cr alloys have been reproduced after addition of small amount (0.25-1 at.%) of oversize solute atoms of Y, Nb and Zr to develop Fe-7Cr-X and Fe-15Cr-X alloys (X= Y/Nb/Zr). Effect of solute addition on the thermal stability has been studied for the Fe-7Cr-X and Fe-15Cr-X alloys. Finally, spark plasma sintering (SPS) of some selected stabilize grade alloys has been carried out and their mechanical properties have been investigated and correlated with the microstructural features.

4.1 Development of Fe-Cr alloys by Mechanical alloying (MA)

In this section, effect of Cr content in Fe-Cr alloys has been discussed. First, Fe-7%, Fe-11%, Fe-15% & Fe-19% Cr (all in at.%) alloys have been synthesized by MA for 25 h with an aim to verify the effect of Cr content on their thermal stability and mechanical properties.

4.1.1 Phase evolution of Fe-Cr alloys and its analysis

Fig. 4.1a shows XRD patterns of the 25 h milled samples of Fe-Cr alloys. It can be noticed that the Cr peaks are not detectable from the XRD patterns for any compositions. Therefore, as per the XRD analysis, it indicates a complete dissolution of Cr in Fe after 25 h of milling. Moreover, it can be noticed that the Fe peak intensity gradually decreased and broadened with the increase in the Cr concentration. It can also be noticed that the peaks are shifted to the lower 2θ position (one is shown in the inset of Fig. 4.1a for (110) peak) as a function of Cr content. The shifting of a peak to the lower 2θ position is an indication of increase in the lattice parameter of Fe, which is due to the dissolution of Cr atoms in Fe-based solid solution. Therefore, the lattice parameter of Fe-based alloys (a_{Fe}) was calculated from the 3 prominent peaks to confirm the dissolution of Cr in Fe. The a_{Fe} values were calculated by extrapolation of plot of a_{Fe} *vs.* ($\cos^2\theta/\sin\theta$) to $\cos\theta = 0$ (Cullity, 1978; Jiang et al., 1999) and the variation of a_{Fe} is shown in Fig. 4.1b. It can be noticed that the a_{Fe} increases from 2.8674 to 2.8781Å because of dissolution of 7% Cr in the Fe-based solid solution. The maximum increase in the a_{Fe}

(2.8860 Å) was detected for the 19% Cr alloy. It is already mentioned that any Cr peak is not detected from the relevant XRD patterns (although XRD has limited detectability). Hence, the increase in the lattice parameter of Fe is due to the dissolution of Cr only. Therefore, on the basis of the XRD analysis, it can be concluded that the added Cr was completely dissolved in Fe lattice to form Fe-based solid solution after 25 h of MA.

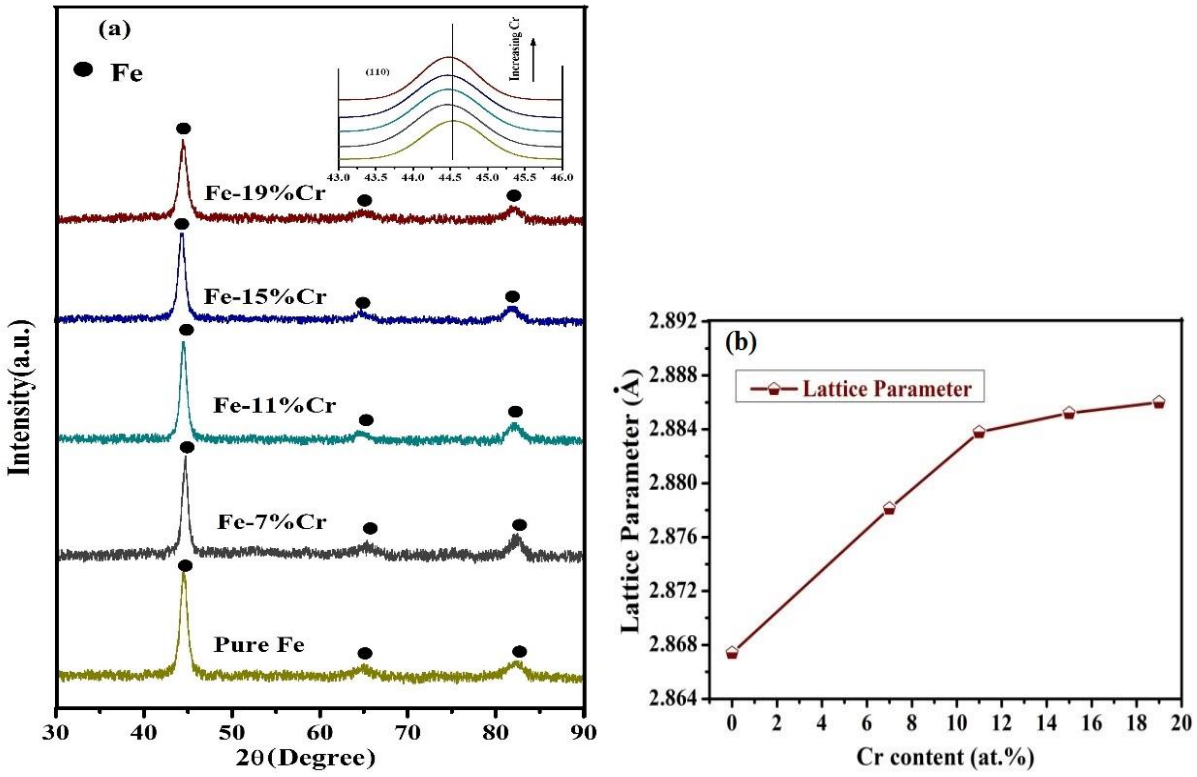

Fig. 4.1: (a) XRD patterns of 25 h milled Fe-Cr alloys (Cr = 0, 7, 11, 15, 19 at.%), (b) Variation of lattice parameter of 25 h milled samples as a function of Cr concentration.

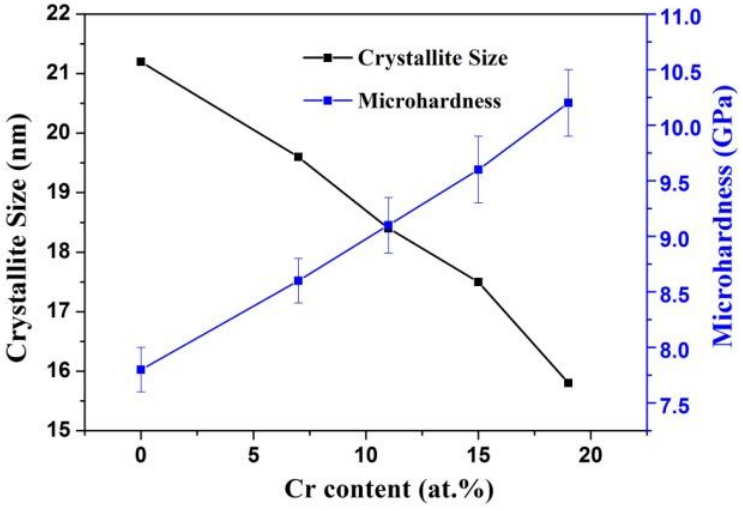

Fig. 4.2: Crystallite size and corresponding microhardness of the as-milled Fe-Cr alloys.

XRD analysis has been made to determine the changes in the crystallite size of the as-milled samples using Williamson-Hall method to exclude the broadening due to lattice strain (Cullity, 1978; Suryanarayana et al., 1998). Fig. 4.2 shows the variation of crystallite size and corresponding microhardness values of the as-milled Fe-Cr alloys as a function of Cr content. The crystallite size is found to decrease with increase in the Cr content and attained a value as low as ~16 nm for 19% Cr alloy. The corresponding microhardness value is estimated to be quite high (~10 GPa). The crystallite size of the other compositions is found to be bit larger as the Cr content decreased; whereas, the corresponding microhardness values decreased with decreasing Cr content.

4.1.2 Thermal stability and mechanical properties

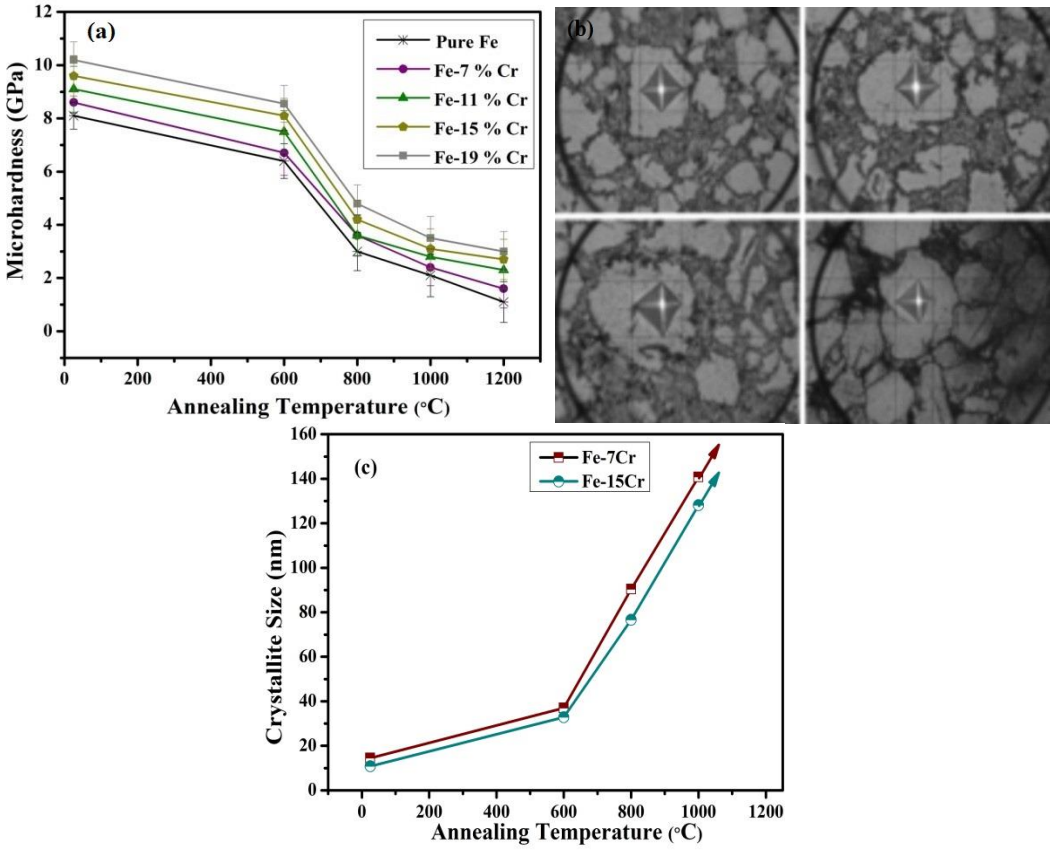

Fig. 4.3: (a) Vickers microhardness of different Fe-Cr alloy compositions as a function of annealing temperatures, (b) Indentation made within the particle during microhardness measurements, (c) Variation of crystallite size of Fe-Cr alloys as a function of annealing temperature.

The as-milled samples were annealed in batches at various temperatures up to 1200°C for 1 h under high purity Ar+2%H_2 atmosphere using a tubular furnace. Microhardness measurement was carried out on the annealed samples. The thermal stability of the Fe-Cr nanostructures is found to be disappointing as could be seen from Fig. 4.3a. The Vickers microhardness

measurements were carried out on individual particles within the compacts as shown in Fig. 4.3b. Each indentation was made on the central region of bigger size particles to avoid the influences of the indentation plastic zone with particle boundaries. It can be noted (from Fig. 4.3a) that for all the compositions, the microhardness values decreased slowly up to 600°C, and thereafter it diminished sharply with increase in the annealing temperature up to 1200°C. The sharp decrease in the hardness is mainly due to the coarsening of nanocrystalline grains within the particles. The variation of crystallite size (i.e. XRD grain size) is shown in Fig. 4.3c, which clearly indicates that the grain size sharply increased with increasing the annealing temperature. This indicates a poor thermal stability of the nanocrystalline Fe-Cr alloys. Based on the crystallite size and microhardness data (obtained from Figs. 4.2 & 4.3a), the Fe-7Cr and Fe-15Cr alloys have been selected to reproduce these alloys again after addition of Y to investigate the effect of Y on the Fe-Cr-Y alloy formation and their thermal stability.

4.1.3 Summary

(a) XRD patterns of the as-milled Fe-Cr alloys showed that the peaks related to Cr are not detectable from the XRD profiles of any compositions. Moreover, any peak related to any intermetallic phase(s) is also not detectable from the XRD patterns of any compositions. Lattice parameter (a_{Fe}) of the Fe-Cr alloys increases from 2.8674 to 2.8781Å because of dissolution of 7% Cr in the Fe-based solid solution. The maximum increase in the a_{Fe} (2.8860Å) was detected for the 19% Cr alloy, which indicates the dissolution of Cr added in Fe.

(b) The crystallite size decreased with increase in the Cr content and attained a value as low as ~16 nm for 19% Cr alloy. The corresponding microhardness value is found to be quite high (~10 GPa) for the corresponding as-milled sample. The microhardness values decreased slowly up to 600°C during annealing, and thereafter it diminished sharply with increase in the annealing temperature up to 1200°C. The sharp decrease in the hardness is mainly due to coarsening of the nanocrystalline grains (shown in Fig. 4.3c). This indicates a poor thermal stability of the nanocrystalline Fe-Cr alloys developed by MA.

4.2 Development of Fe-Cr-Y alloys

On the basis of crystallite size and microhardness data of the as-milled and annealed (600-1200°C) samples of Fe-Cr alloys (Cr=7, 11, 15 & 19 at.%), Fe-7Cr and Fe-15Cr alloys were selected for further investigation. These two alloys were reproduced in addition with Y to investigate the effect of Y on the formation of Fe-Cr-Y solid solutions and their thermal stability. Fe-7Cr and Fe-15Cr alloys after adding Y (Y=0.25, 0.5 and 1 at. %) were reproduced by MA under same conditions of milling. After that, the formation of ternary Fe-Cr-Y solid solutions has been analyzed for phase evolution, microstructure and their thermal stability. On the basis of the thermal stability of the alloys, some selected alloys were consolidated by SPS. The SPSed samples were further analyzed for the microstructure, mechanical properties and corrosion behavior.

4.2.1 Formation of Fe-Cr-Y alloys by MA and its thermal stability

The selected Fe-7Cr-Y and Fe-15Cr-Y (Y=0.25, 0.5, 1at.%) alloys were developed by MA for 25 h under the same milling conditions as followed in the Fe-Cr system. Then, phase evolution, their microstructural features and thermal stability have been investigated and discussed in details in the subsequent sections.

4.2.1.1 Effect of Y on phase evolution of Fe-Cr-Y alloys and its microstructural analysis

The XRD data of the as-milled samples of Fe-7Cr-Y and Fe-15Cr-Y alloys were recorded and corresponding XRD profiles are shown in Figs. 4.4a and b, respectively. It can be noted that the peaks related to Cr as well as Y are not detectable from the XRD profiles of the as-milled samples. Earlier it was discussed that none of the Cr peaks was detected from the XRD patterns of the Fe-Cr alloys. Moreover, any peak related to any intermetallic phase(s) is also not detectable from the XRD patterns of any compositions. Within the limit of the XRD detectability and analysis, it can be considered that the added Cr and Y were completely dissolved in Fe-based alloys after 25 h of MA. It can also be noticed that the width of the Fe peaks is broadened and the corresponding intensity decreased with increase in the Y content. This is because of 2 reasons: decrease in the crystallite size (Cullity, 1978) and increase in the lattice strain due to dissolution of oversize Y atoms (Suryanarayana et al., 1998) in the Fe-based solid solution.

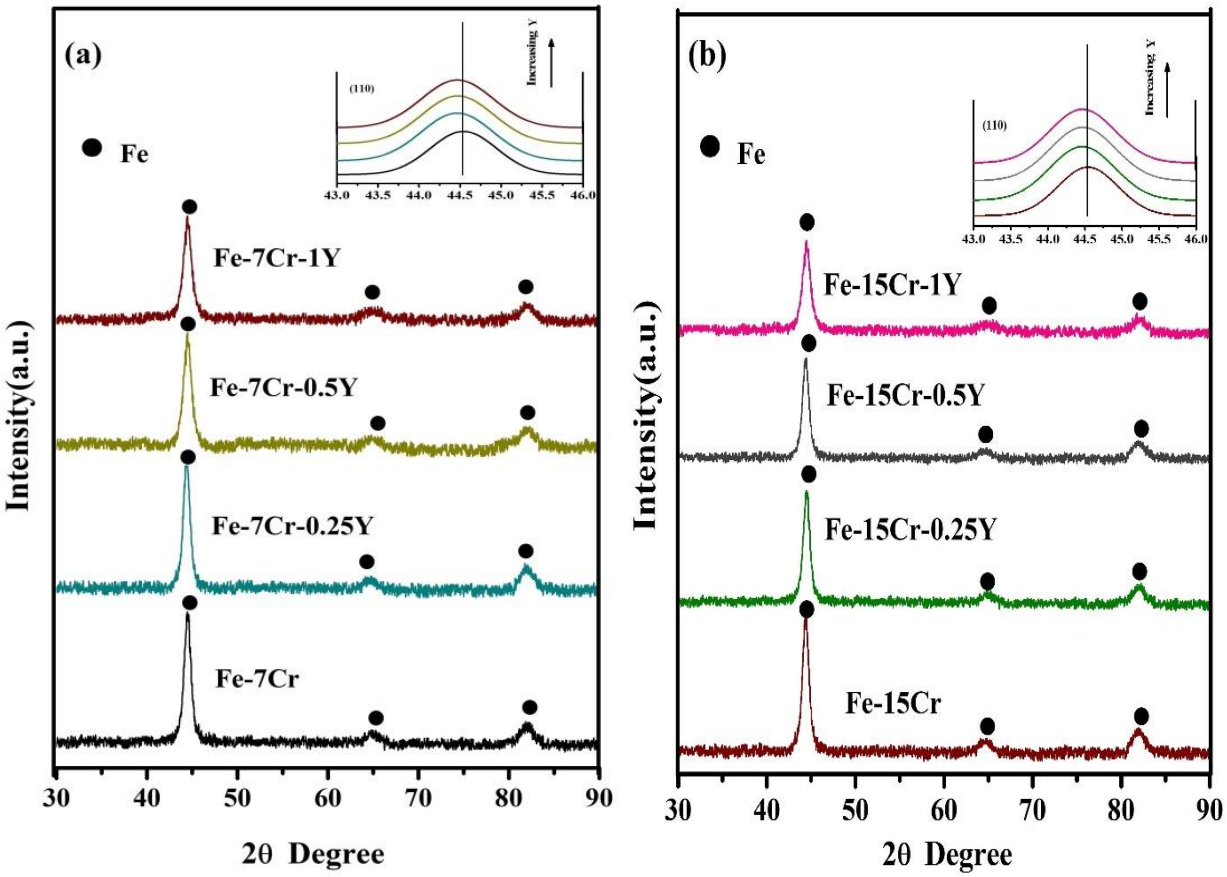

Fig. 4.4: XRD patterns of 25 h milled samples; (a) Fe-7Cr-Y and (b) Fe-15-Y (Y=0.25, 0.5 and 1 at.%). Peak shift, peak broadening and decrease in the intensity is illustrated for (110) plane in the inset.

The dissolution of Y atoms in Fe-Cr alloys during MA increases number of defects especially dislocation density, point defects etc. Consequently, the crystallite size also reduced to a minimum saturated level which is reflected in the broadening of the peaks. A shift of peak position of the Fe-based alloys towards left (lower 2θ position) can also be ascertained as Y content increased (in the inset of Figs. 4.4a and b). The peak shift towards lower 2θ position indicates the increase in the lattice parameter of the solid solution (Cullity, 1978) (also discussed earlier for Fe-Cr alloys). It is known that the alloying elements which dissolved in the solid solution can only take part in the changes of the lattice parameter of the alloy (Mula et al., 2009). Therefore, the change in the lattice parameter is an important tool for the confirmation of formation of any solid solution (Mula et al., 2009; Suryanarayana et al., 1998).

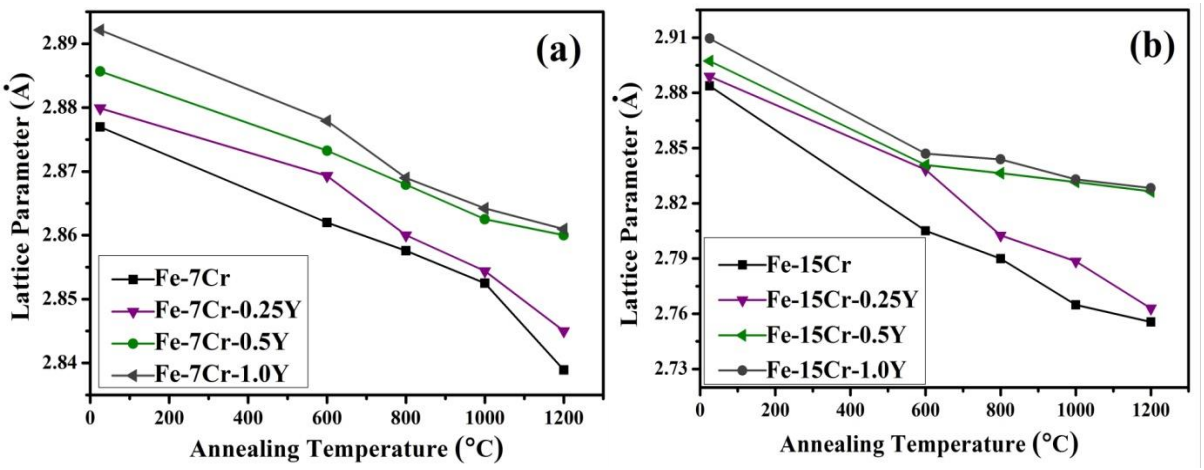

Fig. 4.5: Variation of lattice parameter of 25 h milled samples of (a) Fe-7Cr (b) Fe-15Cr alloys as a function of Y concentration and annealing temperatures.

The variation of a_{Fe} of Fe-7Cr-Y and Fe-15Cr-Y nanostructures is evaluated and the corresponding a_{Fe} is compared with that of the annealed samples of same alloy (shown in Figs.4.5a and b, respectively). It is to be noted that, in case of the as-milled samples, there is a gradual increase in the a_{Fe} as a function of Y. It was noticed that, when 7at.% Cr was added, the a_{Fe} increased to 2.876Å from 2.868Å (for pure Fe). This value further increased to 2.892Å due to the dissolution of 1at.% Y in the same composition (Fig. 4.5a). The variation of the a_{Fe} is found to follow the similar trend for Fe-15Cr-Y alloys too (shown in Fig. 4.5b). However, the changes of a_{Fe} is found to be more in the latter case, i.e. a_{Fe}=2.910Å for the as-milled sample of Fe-15Cr-1Y. It is already mentioned earlier that the XRD is a weak technique because of its limited detectability. Hence, the calculation of the change in the lattice parameter on the basis of the XRD analysis cannot confirm the complete solid solubility of a solute in a solvent. Therefore, the calculation of Gibbs free energy change using Miedema's model (for binary alloys) and Toop's model (for ternary system) has been carried out to predict the dissolution limit of Cr and Y in the as-milled Fe-based alloys (discussed later in the section 4.2.1.2). As the annealing temperature increased, the a_{Fe} gradually decreased and the trend is similar for all the compositions as shown in Figs. 4.5a and b. Beyond the annealing temperature of 800°C, the reduction in the lattice parameter found to be prominent. This can be attributed to the 2 reasons: (i) the excess solute atoms, preferably Y (as Cr has spontaneous solid solubility in Fe) might have precipitated out of the solid solution to segregate along the grain boundary areas and/or (ii) the formation of intermetallic compound(s) at high temperatures. It should be remembered that the alloying elements which take part in the formation of intermetallic phase(s) or

segregate along grain boundary, cannot play any role in the increase in the lattice parameter of the solid solution (Mula et al., 2009).

TEM analysis of the as-milled sample

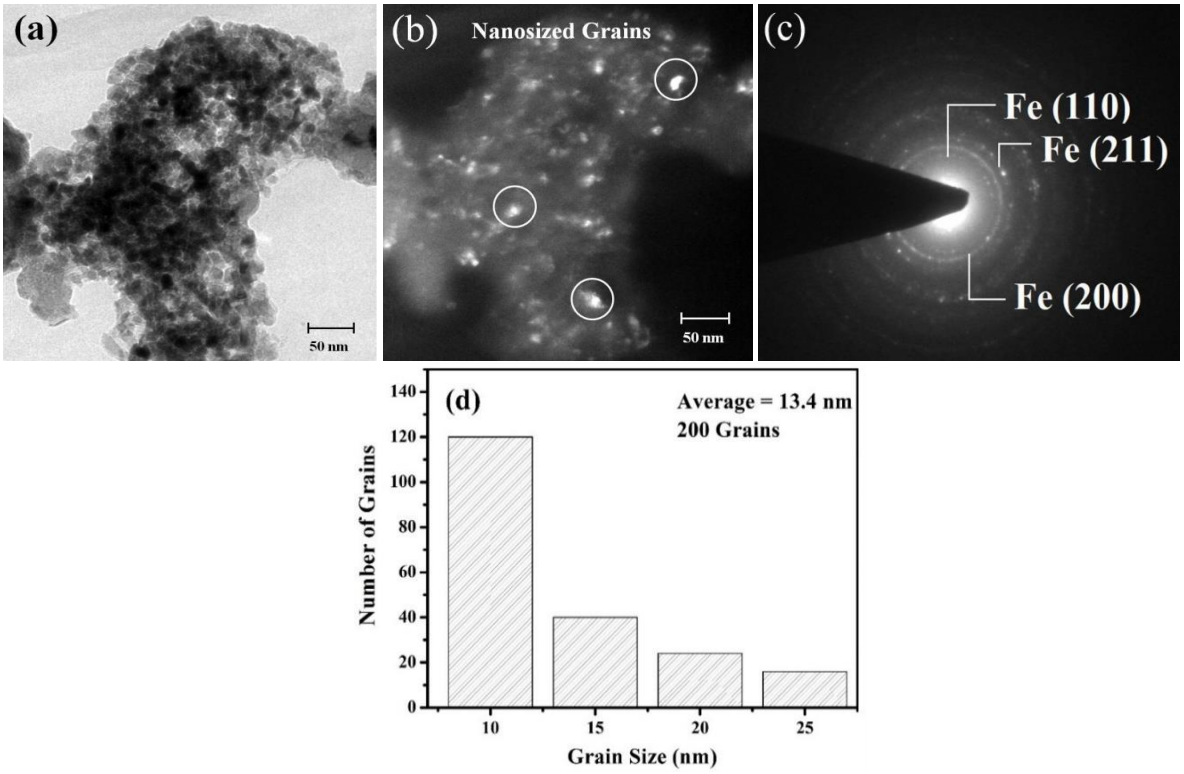

Fig.4.6**:** (a) Bright field TEM image, (b) Dark field TEM image, (c) SAED pattern of the as-milled Fe-15Cr-1Y (d) statistical distribution of grain size estimated from 200 grains.

TEM analysis was carried out for the as-milled powder sample of Fe-15Cr-1Y to evaluate the grain size and crystallinity. Fig.4.6a & b represents a bright and dark field TEM micrograph along with a corresponding SAED pattern (shown in the Fig. 4.6c). The bright field TEM imaging was unsuccessful to reveal the grain size due to the agglomeration of powder particles. It is known that the dark field imaging mode is more powerful due to higher contrast obtained than that of the bright field imaging technique (Williams et al., 1996). Therefore, the dark field TEM imaging was carried out and analyzed to estimate the morphology and grain size of the as-milled samples (as shown in Fig. 4.6b). The nanosize grains (bright spots indicated by circles) can clearly be observed from Fig. 4.6b. The average grain size was estimated from the statistical distribution of 200 grains from such dark field TEM images as one is shown in Fig. 4.6b. The average grain size is found to be 13.4 nm (Fig.4.6d) based on statistical measurements. This is corroborated well with the XRD grain size (~8 nm). The XRD grain size

analysis has been discussed later in the thermal stability section. The XRD grain size is found to be bit smaller than that of the TEM analysis as the broadening contribution from the small domains and other defects cannot be eliminated from the total XRD line broadening. The continuous smooth rings in the SAED pattern (shown in Fig. 4.6c) clearly indicate that the grain size is very fine and is in the lower range of the nanometer scale (<100 nm). Also, all the rings correspond to Fe-based alloy only, which confirms that Cr and Y dissolved completely in the solid solution after 25 h of MA.

4.2.1.2 Thermodynamic analysis

Formation of ternary Fe-Cr-Y disordered solid solutions by MA requires to store extra internal energy (Gibbs free energy) in terms various defects such as grain boundary, dislocations etc. Hence, the metastable solid solutions have been analyzed to verify free energy change required for the same as per the Toop's model. The calculation of free energy change as per Toop's model requires the analysis of Miedema's semi-empirical model for the binary solid solutions first. The details of the Miedema's semi-empirical model, Toop's model and analytical calculation of Gibbs free energy change have been discussed below sequentially.

The change in the Gibbs free energy required to form ordered/disordered binary solid solution from pure elements A and B as per the Miedema's semi-empirical model can be obtained from the Eq.4.1 given below:

$$\Delta G^m = \Delta H^m - T\Delta S^m \tag{4.1}$$

where, ΔH^m and ΔS^m are the change in enthalpy and entropy due to mixing for the formation of ordered/disordered solid solution. T is the absolute temperature at which the solid solution is formed. According to the Miedema's semi-empirical model, the change in entropy of mixing, ΔS^m, can be computed from Eq.4.2.

$$\Delta S^m = R\sum_{i=1}^{n} X_i \ln X_i \tag{4.2}$$

where, R (= 8.314 J/mol K) is the universal gas constant, X_i denotes the mole fraction of element 'i' and n is the total number of elements present in the alloy. The change in enthalpy of mixing, ΔH^m, can be obtained by the sum of three enthalpies given by Eq.4.3:

$$\Delta H^m = \Delta H_{elastic} + \Delta H_{chemical} + \Delta H_{structural} \tag{4.3}$$

Where, $\Delta H_{elastic}$, the elastic contribution is due to the atomic size mismatch in the solid solution, $\Delta H_{chemical}$, the chemical contribution to the enthalpy change occurs due to the breaking of atomic bonds and $\Delta H_{structural}$, the enthalpy contribution is due to structural changes for the formation of the solid solution. $\Delta H_{structural}$ is a very small positive value which is neglected in the estimation of enthalpy of mixing.

The elastic part of enthalpy of mixing, $\Delta H_{elastic}$ can be computed from Eq.4.4 (Miedema et al.,1980b) as given below:

$$\Delta H_{elastic} = X_A X_B (X_A \Delta E_{AinB} + X_B \Delta E_{BinA}) \tag{4.4}$$

where, ΔE_{AinB} is the change in elastic energy caused by the element *A* dissolved in element *B* and ΔE_{BinA} is the change in elastic energy caused by the element *B* dissolved in element *A*. ΔE_{AinB} and ΔE_{BinA} can be calculated from the Eq.4.5 (Miedema et al., 1980b), where *K* and *G* are the bulk and shear modulus, respectively.

$$\Delta E_{AinB} = \frac{2K_A G_B (\Delta V)^2}{3K_A V_B + 4G_B V_A} \quad \text{and} \quad \Delta E_{BinA} = \frac{2K_B G_A (\Delta V)^2}{3K_B V_A + 4G_A V_B} \tag{4.5}$$

$\Delta H_{chemical}$ for binary system can be determined by using Eq.4.6 (Miedema et al., 1980b) as described below:

$$\Delta H_{chemical} = \frac{2 p f(C^S)(X_A V_A^{2/3} + X_B V_B^{2/3})}{(n_{ws}^A)^{-1/3} + (n_{ws}^B)^{-1/3}} \left[-(\Delta\phi)^2 + \frac{Q}{P}(n_{ws}^{1/3})^2 - \frac{S}{P} \right] \tag{4.6}$$

where, *V* is the molar volume; n_{ws} is the electron density and ϕ is the work function of the constituent elements. *P* and *Q* are empirical constants related to constituent elements. $f(C^s)$ is the concentration function for solid solutions which can be found from the Eq.4.7 and Eq.4.8.

$$f(C^S) = C_A^S C_B^S \tag{4.7}$$

$$C_A^S = \frac{x_A V_A^{2/3}}{x_A V_A^{2/3} + x_B V_B^{2/3}} \quad \text{and} \quad C_B^S = \frac{x_B V_B^{2/3}}{x_A V_A^{2/3} + x_B V_B^{2/3}} \tag{4.8}$$

The ΔS^m for ternary Fe-Cr-Y alloys was calculated using Eq.4.2. Finally, the change in the Gibbs free energy as per the Toop's model, ΔG_{Toop}, was calculated using Eq.4.9 (as shown below) and is shown in Fig. 4.7c. The ΔG_{Toop} required to form the solid solutions of Fe-7Cr-0.25Y, Fe-7Cr-0.5Y, Fe-7Cr-1Y, Fe-15Cr-0.25Y, Fe-15Cr-0.5Y and Fe-15Cr-1Y compositions

are found to be positive, and the calculated values (using Eqs. 4.10-4.13) are shown in Table 4.2 for the convenience.

$$\Delta H^{m} = \left(\frac{X_{Cr}}{X_{Fe}+X_{Cr}}\right)\Delta H^{m}_{Fe-Cr}(X_{Fe},1-X_{Fe}) + \left(\frac{X_{Y}}{X_{Fe}+X_{Y}}\right)\Delta H^{m}_{Fe-Y}(X_{Fe},1-X_{Fe}) + (X_{Cr}+X_{Y})^{2}\Delta H^{m}_{Cr-Y}\left(\frac{X_{Cr}}{X_{Cr}+X_{Y}},\frac{X_{Y}}{X_{Cr}+X_{Y}}\right) \quad (4.9)$$

The enthalpy of mixing, ΔH^{m} for the Fe-Cr-Y ternary alloys was calculated using asymmetrical model (also called Toop's model) predicted by Toop (Toop 1965). This is basically based on the extension of Miedema's model to consider the effect of third element. The Toop's model avoids the large deviation of calculated values from the experiment when constituent elements have different physical properties (Toop 1965). In this model, initially $\Delta H_{elastic}$ and $\Delta H_{chemical}$ of 3 binary systems, i.e. Fe-Cr, Fe-Y and Cr-Y were calculated individually, and then finally ΔH^{m} for ternary alloys (Fe-Cr-Y) was computed through interpolation methods, applying the Toop's model (Toop 1965) given in Eq.4.9.

The parameters required for the thermodynamic analysis according to Miedema's semi-empirical (Miedema et al., 1980a; Niessen et al., 1988; Ray et al., 2010) for Fe-Cr, Fe-Y and Cr-Y systems are presented in Table 4.1.

Table 4.1: Parameters required for the thermodynamic analysis as per Miedema's model for Fe-Cr, Fe-Y and Cr-Y binary systems (Miedema et al. 1980a; Niessen et al., 1988).

Parameters	**Fe**	**Cr**	**Y**
$n_{ws}^{1/3}$ **(cm^{-1})**	1.77	1.73	1.21
V_m **(cm^3 mol^{-1})**	7.09	7.12	19.72
Φ **(V)**	4.5	4.65	3.2
K **(* 10^{10} Nm^{-2})**	17	16.02	4.1
G **(* 10^{10} Nm^{-2})**	8.2	11.53	2.6
T **(K)**	1811	2130	1795

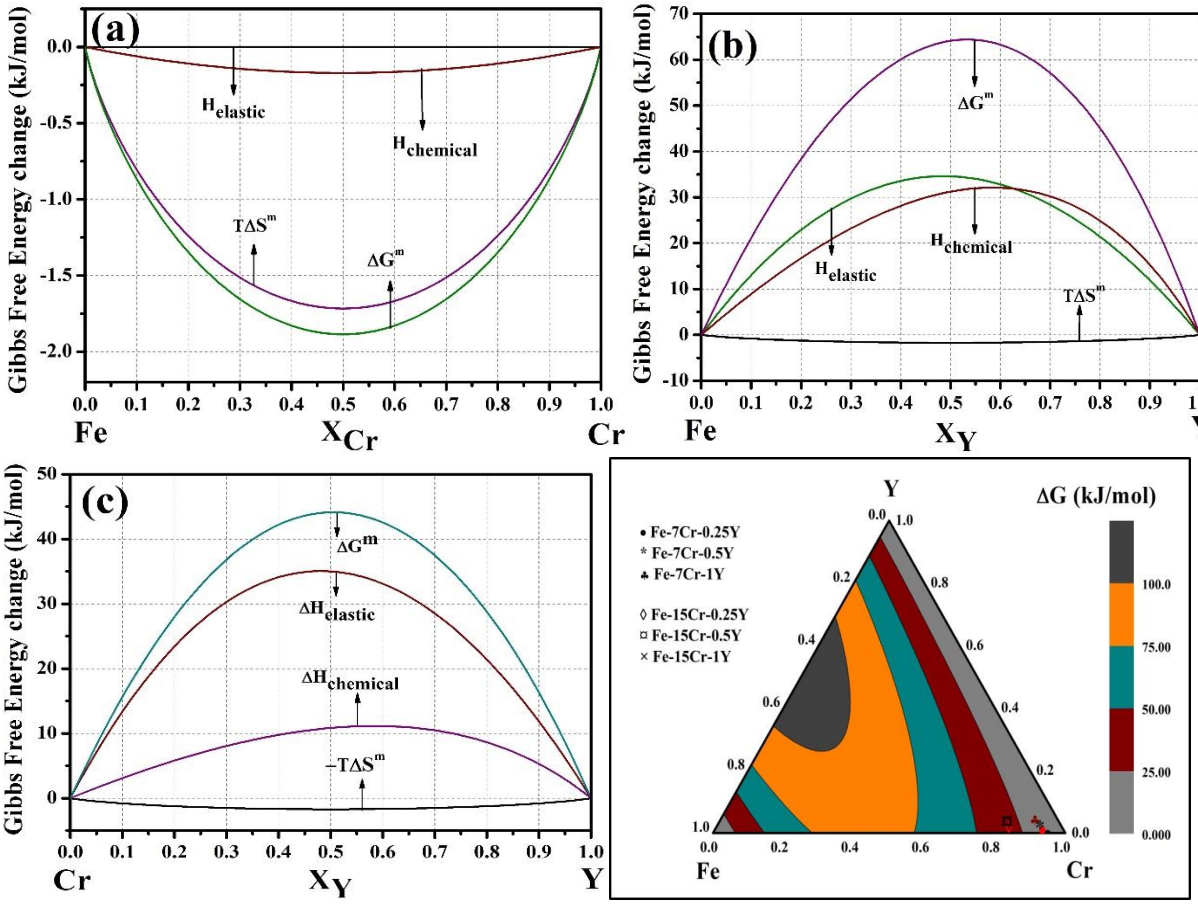

Fig. 4.7: Enthalpy, entropy and Gibbs free energy change for the formation of stable/metastable solid solution in (a) Fe-Cr (b) Fe-Y (c) Cr-Y, and (d) Fe-Cr-Y ternary system.

The enthalpy, entropy and Gibbs free energy changes for the formation order/disordered solid solutions of Fe-Cr, Fe-Y and Cr-Y at room temperature was calculated using above described Miedema's model, and the relevant plots are shown in Figs. 4.7a-c. Total Gibbs free energy changed is negative for Fe-Cr binary system. This signifies that the formation of Fe-Cr solid solution is spontaneous and does not necessarily require a non-equilibrium technique. The atomic size difference between Fe and Cr is very small (their position in the periodic table is also close to each other), and as per the Hume-Rothey's rule, they can easily form substitutional solid solution (Callister at al., 2007). The Gibbs free energy change for Fe-Y and Cr-Y binary systems is found to be positive for whole compositional range. Therefore, there is no driving force to form respective solid solutions spontaneously from the elemental Fe, Cr and Y powders. Therefore, the formation of solid solutions in Fe-Y and Cr-Y systems cannot be achieved by any equilibrium method. The formation of Fe-Cr-Y solid solution and solid solubility extension of Y in Fe and Cr are possible only by non-equilibrium techniques such as MA (Suryanarayana 2001).

The $\Delta H_{chemical}$ and $\Delta H_{elastic}$ both are positive for Fe-Y alloy and very close to each other. This is because of small difference in the work function of constituent elements and large atomic size mismatched between the two elements, respectively. In case of Cr-Y alloy, the elastic enthalpy contribution is dominant due to the large atomic size difference between Cr (0.128 nm) and Y atoms (0.180 nm). The positive values of $\Delta H_{chemical}$ of Fe-Y and Cr-Y binary alloys indicate that there is a very less chance for Y to react chemically with Fe or Cr to form intermetallic phases.

Calculation of Gibbs free energy change

The energy barrier to be overcome to form disordered solid solution can be achieved by 2 major factors: (i) the excess energy stored in the as-milled samples in the form of surface energy (due to the crystallite size refinement) and (ii) microstrain energy (due increase in the dislocation density). Increase in the Gibbs free energy, ΔG_b, due to reduction in the crystallite size can be computed from Eq.4.10 (Dieter 1961).

$$\Delta G_b = \gamma\left(\frac{A}{V}\right)V_m \tag{4.10}$$

where, γ = 636 mJ/m^2 is the grain boundary free energy of pure Fe, A/V is the surface area to volume ratio of the average grain size and V_m is the molar volume. The grain size of the mechanically alloyed sample is assumed to be spherical for the estimation of the Gibbs free energy change of the solid solution. The Gibbs free energy changed due to the reduction in the crystallite size (ΔG_b) of the Fe-7Cr and Fe-15 Cr alloys as a function of Y is shown in Figs. 4.8a and b, respectively.

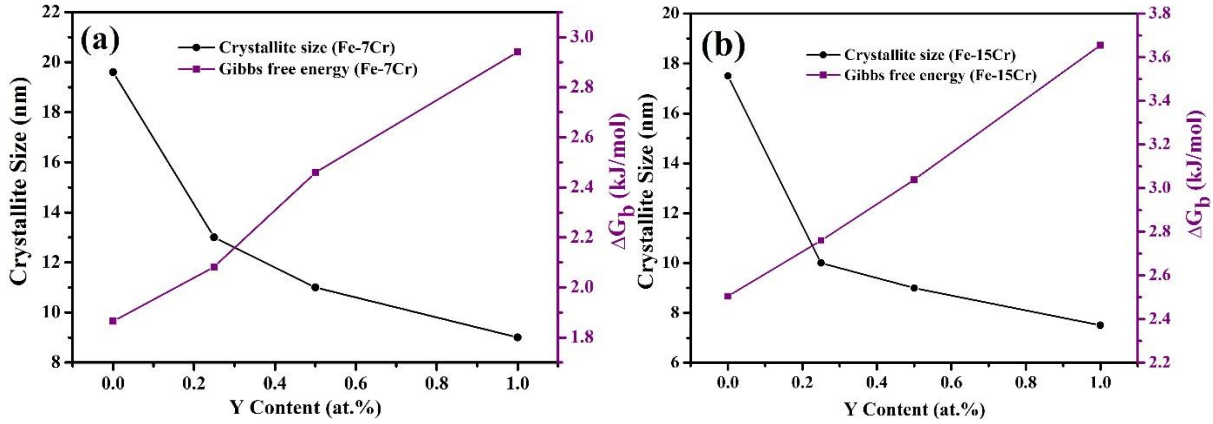

Fig. 4.8: Change in Gibbs free energy due to decrease in crystallite size of (a) Fe-7Cr (b) Fe-15Cr alloy system as a function of Y.

Figs. 4.8a and b show the variation of the crystallite size and corresponding Gibbs free energy changed as a function of Y content, respectively, for the Fe-7Cr and Fe-15Cr alloys. The crystallite size was calculated from 3 major peaks after eliminating the broadening effect due to lattice microstrain by using the plot between $B_r Cos\theta$ *vs*. $Sin\theta$ (Cullity 1978). The crystallite size is found to decrease with increase in the Y content. It is found to be 19.6 nm for Fe-7Cr alloy, and the crystallite size gradually decreased in addition of Y for the same alloy milled under same conditions. The lowest value of the crystallite size estimated to be 9 nm when 1% Y is added. Similarly, the crystallite size of Fe-15Cr alloy decreased to 7.5 nm from a value of 17.5 nm after addition of 1% Y (Fig. 4.8b). This tendency illustrates that the reduction of the crystallite size is influenced by the dissolution of more amount of Y in Fe-Cr solid solution. The dissolution of larger size Y atoms in Fe-based alloy introduced more number of defects and dislocations strain, which contributed further refinement of the crystallite size. The decrease in the crystallite size leads to the increase in the surface free energy, ΔG_b, which was calculated by using the Eq.4.10 described earlier. This can be noted that the ΔG_b increased from 1.865 kJ/mol (for the as-milled Fe-7 Cr alloy) to 2.940 kJ/mol for the milled sample of Fe-7Cr-1Y. Similarly, ΔG_b increased to 3.656 kJ/mol due to addition of 1% Y from a value of 2.505 kJ/mol which corresponds to Fe-15Cr.

The change in the microstrain free energy, ΔG_s, due to the dislocations density could be estimated from Eq.4.11 (Dieter 1961) is shown in Figs.4.9a and b, respectively.

$$\Delta G_s = \xi \rho V_m \tag{4.11}$$

where, ρ is dislocation density, V_m is the molar volume of Fe and ξ is the elastic strain energy per unit length of dislocations. ξ can be computed using Eq.4.12 (Dieter 1961).

$$\xi = \left(\frac{\Delta G b^2}{4\pi} \right) \ln \left(\frac{R_e}{b} \right) \tag{4.12}$$

where, G is the shear modulus, b is the Burgers vector and R_e is the outer cut-off radius. R_e can be taken as the crystallite size of the solid solution in nanocrystalline materials (Dieter 1961). Dislocation density ρ, can be calculated from Eq.4.13.

$$\rho = \frac{2\sqrt{3}}{D \times b}\left(\varepsilon^2\right)^{1/2} \tag{4.13}$$

where D is the crystallite size and ε is the lattice microstrain which can be obtained from the XRD analysis.

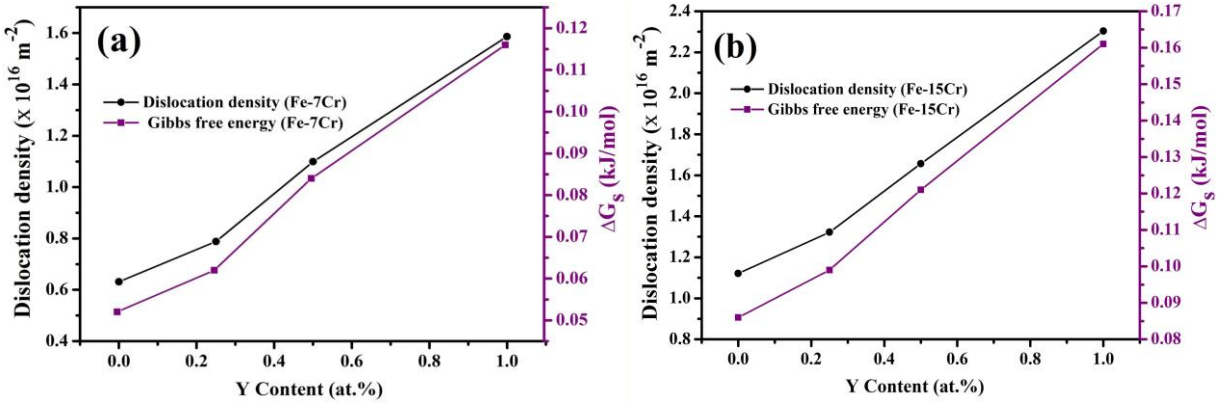

Fig. 4.9: Variation of Gibbs free energy change due to increase in dislocation density (a) Fe-7Cr (b) Fe-15Cr alloy system as a function of Y.

Figs. 4.9a and b, respectively, show the increase in the Gibbs free energy changed due to the increase in the dislocation density for Fe-7Cr and Fe-15Cr alloys. It was found that ΔG_s was 0.06 kJ/mol corresponding to a dislocation density, ρ = 0.787 × 10^{16} m^{-2} for Fe-7Cr-0.25Y alloy; whereas, ΔG_s for Fe-15Cr alloy with same Y content (i.e. 0.25%) was found to be 0.09 kJ/mol. ΔG_s gradually increased with Y content and attained a value of ~0.116 and ~0.161 kJ/mol, respectively, for Fe-7Cr and Fe-15Cr alloy both with 1% Y. Therefore, it can be noticed that increase in the ΔG_s is very less when compared to that due to the reduction in crystallite size, ΔG_b.

Table 4.2: Total Gibbs free energy change (ΔG_b+ΔG_s) due to the reduction in crystallite size and due to the increase in the dislocation density is compared with that estimated from the Toop's model.

Alloy (all in at.%)	**ΔG_b (kJ/mol)**	**ΔG_s (kJ/mol)**	**$\Delta G_T = \Delta G_b + \Delta G_s$ (kJ/mol)**	**ΔG_{Toop} (kJ/mol)**
Fe-7Cr-0.25Y	2.081	0.062	2.143	1.208
Fe-7Cr-0.5Y	2.459	0.084	2.543	1.783
Fe-7Cr-1Y	2.940	0.116	3.056	2.926
Fe-15Cr-0.25Y	2.760	0.099	2.859	1.679
Fe-15Cr-0.5Y	3.039	0.121	3.160	2.316
Fe-15Cr-1Y	3.656	0.161	3.817	3.581

Total Gibbs free energy changed, i.e. $\Delta G_T = \Delta G_b + \Delta G_s$, estimated to be 3.817 kJ/mol for the as-milled sample of Fe-15Cr-1Y. For the same composition, the theoretical value of the Gibbs free energy changed required, ΔG_{Toop}, as per the Toop's model (modified Miedema's model for ternary alloys as discussed earlier in section) is 3.581 kJ/mol. It can be observed from Table 4.2 that ΔG_T is higher than ΔG_{Toop} for all the Fe-Cr-Y compositions investigated in the present study. Therefore, it can be concluded that the total stored energy, ΔG_T, in the as-milled alloy is large enough than the required energy (ΔG_{Toop}) to produce disordered solid solution as per the Toop's model. The assumption made for the above calculation is: the enthalpy changed due to structural contribution, $\Delta H_{strcutural}$, from Y is avoided for practical simplicity (as it shows a very small positive value). Also the lattice microstrain, crystallite size and dislocation density calculated from the XRD data can have human errors.

4.2.1.3 Thermal stability and mechanical properties

The as-milled samples of Fe-Cr-Y alloys were annealed in batches at 600, 800, 1000 and 1200°C under controlled Ar+2% H_2 atmosphere for 1 h, and then XRD study was carried out to detect the microstructural changes, if any. The XRD data were analyzed to estimate the changes in the crystallite size and phase transformation, if any. The heat treated samples were also examined to verify the change of the microhardness values compared to that of the as-milled sample. Thus, the changes in the crystallite and corresponding microhardness value of the annealed samples can enlighten their stability at higher temperatures.

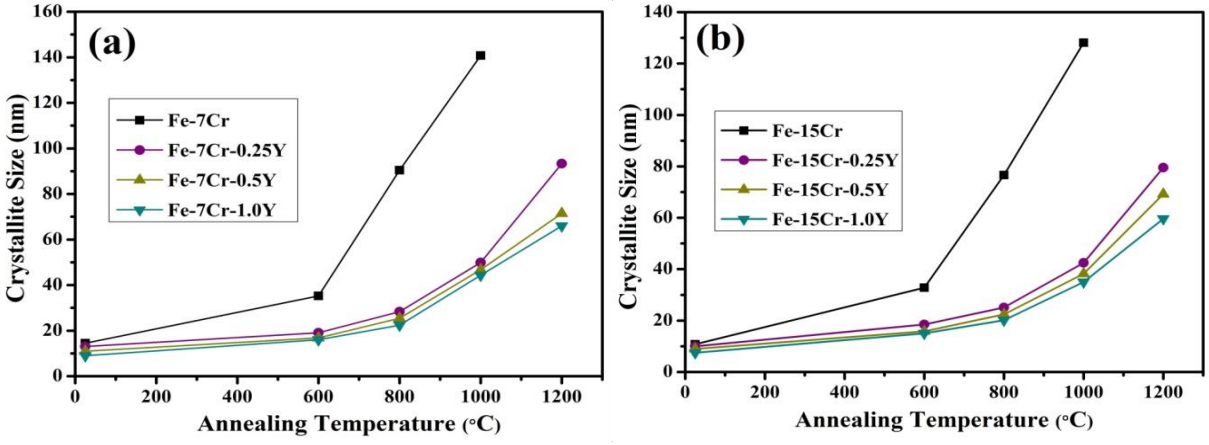

Fig. 4.10: Variation of Crystallite size vs. annealing temperatures for (a) Fe-7Cr (b) Fe-15Cr alloy system as a function of Y.

Figs. 4.10a and b, respectively, show the variation of crystallite size of the annealed samples of Fe-7Cr-Y and Fe-15Cr-Y alloys. It can be observed from the figures that the influence of annealing temperature on the crystallite size almost has similar effect for both the Fe-Cr-Y alloys. The same alloys without Y showed an abnormal grain coarsening (grain size >100 nm) at an annealing temperature above 600°C. But, a superior thermal stability is obtained due to addition of small quantity of Y (up to 1%). The crystallite size is found to be as low as 9 and 7.5 nm, respectively, for the as-milled samples of Fe-7Cr-1Y and Fe-15Cr-1Y alloys (as discussed earlier). It can be noticed that the crystallite size increased considerably for the alloys having less or without Y when annealing temperature was raised above 600°C. While the alloys with 1% Y, i.e., Fe-15Cr-1Y and Fe-7Cr-1Y annealed at 1000°C, exhibited an excellent thermal stability, and retained a crystallite size of ~35 and 44 nm, respectively. The retention of the nanocrystalline grains around 50 nm even after annealing at 1000°C indicates that Y has a significant stabilizing effect on Fe-Cr alloys at high temperatures.

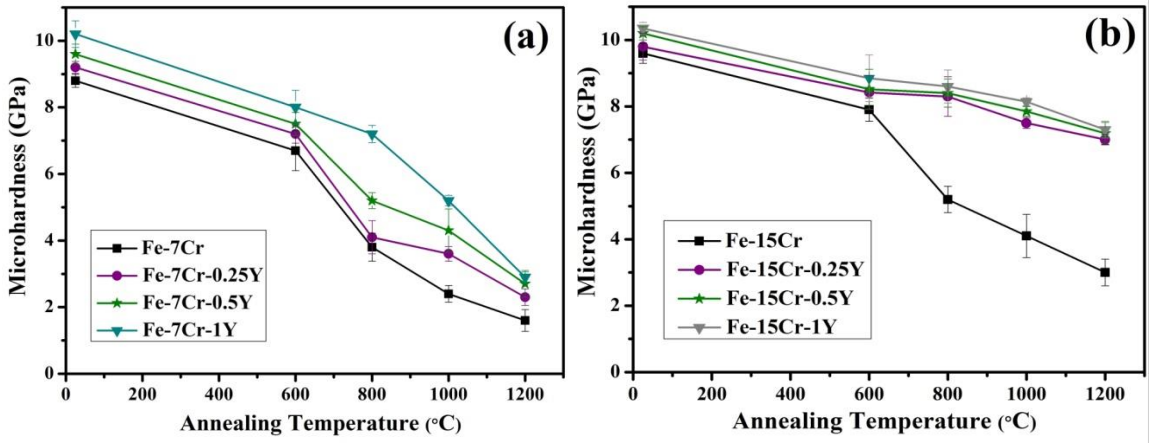

Fig. 4.11: Vickers microhardness vs. annealing temperatures for (a) Fe-7Cr (b) Fe-15Cr alloy system as a function of Y.

Figs. 4.11a and b, respectively, show the variation of microhardness values of Fe-7Cr-Y and Fe-15Cr-Y alloys annealed at various temperatures up to 1200°C. The same has been compared with the hardness of the same alloys without Y. The microhardness values are found to decrease sharply as a function of annealing temperature for Fe-7Cr-Y (Fig. 4.11a); while, Fe-15Cr-Y alloy showed a better stability of the hardness (Fig. 4.11b). It is also to be noted from Fig. 4.11a that the reduction in the hardness with temperature is more for the less Y alloys. On the other hand, only a minor decrease in the hardness values is observed with increase in the annealing temperature. Moreover, a significant deviation is not perceived in the hardness values for all the Fe-15Cr-Y alloys (Fig. 4.11b) at the particular annealing temperature. For example,

in case of samples annealed at 800°C: the hardness values vary only from 8.3 (for 0.25% Y) to 8.6 GPa (for 1% Y). The hardness value of the annealed sample (at 800°C) of Fe-7Cr-1Y is found to be ~7.2 GPa corresponding to a grain size of 22 nm; whereas, a hardness of ~8.6 GPa was measured for the annealed specimen (at 800°C) of Fe-15Cr-1Y alloy having a similar level of grain size (20 nm). It can be noticed that an extra hardness of 1.4 GPa is obtained for the Fe-15Cr-1Y alloy though both were annealed at the same conditions at 800°C and retained almost same grain size. Therefore, it can be ascertained that the solid solution strengthening due to more amount of Cr plays a vital role in maintaining such a high value of hardness. It should also be noted that all the Fe-15Cr-Y alloys showed much better thermal stability even after annealing at 1200°C compared to that of the Fe-15Cr alloy (without Y). For example, after annealing at 1000°C, the hardness of Fe-15Cr-0.25Y alloy is found to be as high as 7.5 GPa (grain size 42 nm) compared to only 4 GPa (grain size >100 nm) for the same alloy without Y. Therefore, it can be ascertained that the addition of 0.25% Y in Fe-15Cr alloy is highly significant to achieve an outstanding thermal stability; while even 1% Y in Fe-7Cr alloy does not reveal enough stability at 1000°C (5.2 GPa). From this observation, it can be confirmed that a suitable combination of Cr and Y can play the pivotal role in the stabilization of Fe nanocrystalline grains and maintain a high level of the hardness even after annealing at 1000°C. Darling et al. (2013) investigated the effect of Y (up to 10at.%) on the thermal stability of Ni, and effective thermal stability was reported to have up to 800°C where the crystallite size was 35 nm. The kinetic pinning mechanism was stated to be responsible for retaining the nanocrystalline Ni at such high temperature. Hf addition up to 4 at.% was reported to maintain nanoscale grain size (<40 nm) in Fe-14Cr alloy at 1000°C and the corresponding measured hardness value was 5.2 GPa (Li et al., 2014). The thermodynamic contribution due to solute segregation to the grain boundaries was reported to be the possible strengthening mechanism of the thermal stabilization. Zr addition up to 4at.% was reported to effectively stabilize Fe-10Cr and Fe-18Cr alloys and maintained a high hardness of 7 GPa after annealing at 900°C (Saber et al., 2012). The stabilization effect was identified to be as a result of Zener pinning at grain boundaries by Fe-Zr intermetallic precipitates or segregation of Zr atoms to the grain boundary region (Saber et al., 2012). In the present study, the addition of only 1 at.% Y to Fe-7Cr and Fe-15Cr alloys showed an excellent thermal stability up to 1000°C and maintained nanocrystalline grain size of 44 and 35 nm, respectively. The corresponding hardness values were measured to be 5.2 and 8.1 GPa, respectively. The thermodynamic mechanism of solute segregation along

the grain boundaries as well as kinetic mechanism of Zener pinning by second phase particles (such as Y and $Fe_{17}Y_2$) are found to be responsible to achieve such high thermal stability.

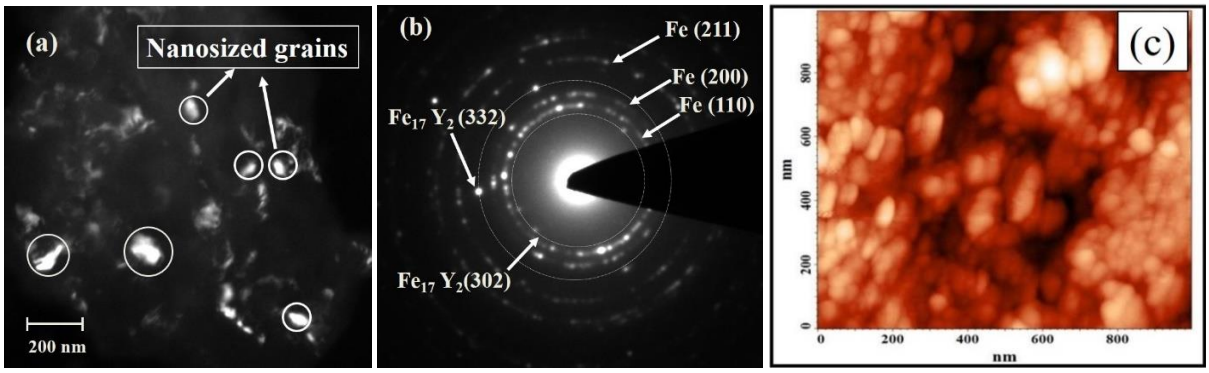

Fig. 4.12: (a) Dark field TEM image (b) SAED pattern 15Cr-1Y alloy annealed at 1000°C for 1 h and (c) AFM micrograph of Fe-15Cr-1Y alloy annealed at 1000°C for 1 h.

The calculated crystallite size from the XRD data may not be reliable especially when the values exceed 50 nm. There is certain limitation of the XRD study (Cullity 1978) and it also includes human error during analyzing the diffraction patterns. Hence, the grain size was validated through TEM and AFM analysis (Sarathi et al., 2007). It can be remembered that after annealing at 1000°C, the sample of Fe-15Cr-1Y alloy showed a grain size ~35 nm as per the XRD data (Fig. 4.10b) with a corresponding microhardness value of 8.1 GPa (Fig. 4.11b). Thus, it can be concluded that the effective thermal stability was achieved for the Fe-15Cr-1Y alloy up to 1000°C, and therefore, the TEM and AFM analysis were performed for the same annealed sample to confirm the XRD grain size. Figs. 4.12a, and c, respectively, show the TEM and AFM micrographs of Fe-15Cr-1Y alloy annealed at 1000°C. The SAED pattern in Fig. 4.12b clearly indicates that the grain sizes are still within nanometer range (<100 nm) even after annealing at 1000°C, and the average grain size is found to be ~53 nm. The formation of $Fe_{17}Y_2$ intermetallic phase has been verified from the extra rings of the SAED pattern as indicated in the Fig. 4.12b. It can be remembered that the peaks corresponding to $Fe_{17}Y_2$ phase were also detected from the XRD pattern. The mean grain size obtained from the analysis of the AFM micrograph (Fig. 4.12c) is found to be ~48 nm which corroborates well with the TEM grain size (53 nm).

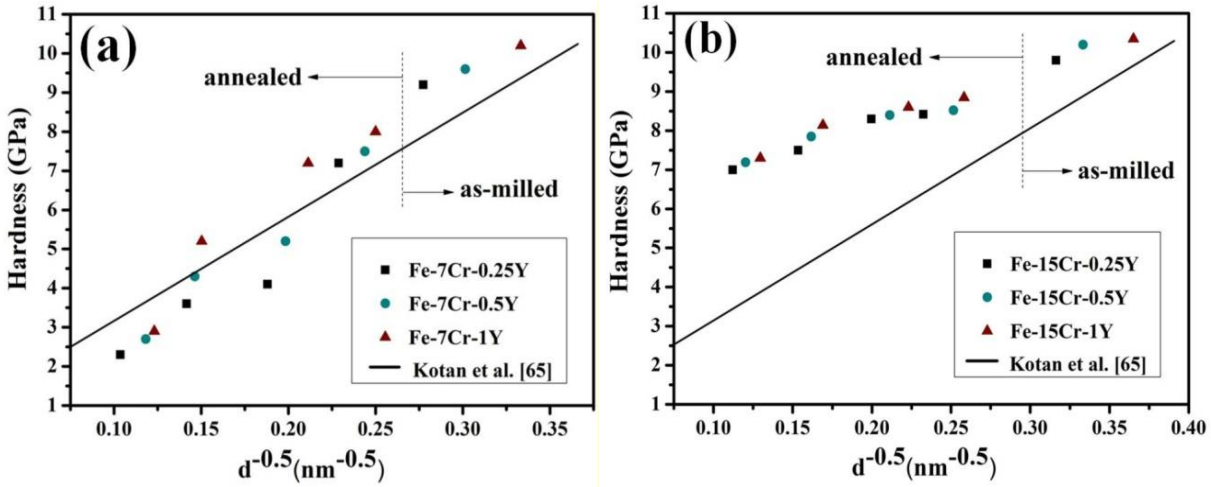

Fig. 4.13: Hall-Petch plot for the hardness values of as-milled and annealed samples of (a) Fe-7Cr-Y (b) Fe-15Cr-Y alloys.

Hall-Petch plots (as shown in Fig. 4.13) are constructed for the Fe-Cr-Y alloys investigated in the present study and this is compared with the classical Hall-Petch relationship reported for the pure Fe by (Kotan et al., 2012) and (Shen et al., 2007) in their studies. The strengthening effect due to Cr and Y can be ascertained from the deviation of the classical H-P relation of the pure Fe. It is observed that the deviation is more for the high solute content alloys. It can be noticed from Fig. 4.13b that the Fe-15Cr-Y alloys show extra hardening effect compared to that of the Fe-7Cr-Y alloys. The extra hardening is mainly due to 2 reasons; (i) the solid solution strengthening by Cr and (ii) extra grain size refinement in presence of more amount of solute (as indicated in the Fig. 4.13b). The formation of complete solid solution was already confirmed from the XRD phase analysis, Gibbs free energy changed calculation using Toop's model and SAD pattern (TEM) analysis. The extra hardening effect can also be realized for some of the annealed samples. The strengthening effect of the Fe-7Cr-Y alloys is found to retain a bit only for Fe-7Cr-1Y composition up to 1000°C (Fig. 4.13a). The other Fe-7Cr-Y alloys showed a sharp decrease in the hardness values due to the coarsening of grains just above 600°C. On the other hand, the extra hardening of all the Fe-15Cr-Y alloys is found to preserve up to 1200°C. Although there is bit decrease in the hardness with annealing temperature, the retained strengthening effect is much higher as compared to that of the Fe-7Cr-Y alloys. This observation again confirmed that not only the Y, but also the Cr played an important role in the high thermal stability of the Fe-based alloys. The reduction in the hardness up to the annealing temperature of 600°C may be attributed to the grain boundary relaxation and annihilation of stored dislocations. In the intermediate range of the annealing temperatures

(600-1000°C), the solid solution strengthening due to Y is reduced because of the formation of $Fe_{17}Y_2$ phase. Conversely, the ultrafine $Fe_{17}Y_2$ phase played an important role in maintaining the high strength by precipitation strengthening. Therefore, the solid solution strengthening by Cr and Y as well as the precipitation hardening played the crucial role in achieving such high strength in the Fe-15Cr-1Y alloy. The overall decrease in the strength at higher temperatures (≥1000°C) is due to the coarsening of the matrix grains as well as precipitate particles.

4.2.1.4 Summary

The Fe-Cr-Y metastable solid solutions were successfully prepared by MA from the elemental powder blends of pure Fe, Cr and Y. Feasibility of the formation of such alloys was verified by analytical models using experimental data of the present study. The stored Gibbs free energy changed (estimated by the Toop's model) and SAED (TEM) pattern analysis also confirmed the formation of such alloys.

(a) The nanocrystalline alloy powders of Fe-15Cr-Y showed an excellent thermal stability compared to that of the Fe-7Cr-Y. The average crystallite size is found to be very low (~8 nm) for the as-milled sample of Fe-15Cr-1Y. After annealing even at 1000°C, the grain size (by TEM analysis) is found reasonably less and stabilized at ~53 nm corresponding to a quite high hardness value (8.1 GPa). The high thermal stability is ascribed to the mechanisms of solute segregation (Y), solid solution strengthening (by Cr) and precipitation hardening (by $Fe_{17}Y_2$).

(b) It is also to be noted that the effective thermal stability of the alloy is realized provided a sufficient amount of Cr (15 at.%) is present along with a small quantity of Y (0.25-1 at.%). This signifies that the solid solution strengthening by Cr played a significant role in achieving such high thermal stability when a small amount of Y is added.

Therefore, it can be concluded that the thermodynamic mechanism (segregation of Y atoms) along with kinetic mechanism (Zener pinning by second phase particles) is found very effective to produce the stabilized Fe-15Cr nanostructures for high temperature/nuclear applications.

4.2.2 Consolidation of Fe-7Cr-1Y and Fe-15Cr-1Y alloys by SPS

This section deals with the investigation of microstructural stability, mechanical properties and corrosion behavior of the spark plasma sintered (SPSed) Fe-7Cr-1Y and Fe-15Cr-1Y alloys. Because of the superior thermal stability of the Fe-7Cr-1Y and Fe-15Cr-1Y (as compared to

other Fe-Cr-Y alloys) spark plasma sintering was carried out for these two alloys only at 800, 900 and 1000°C to investigate their bulk mechanical properties.

4.2.2.1 Microstructural analysis of SPSed samples

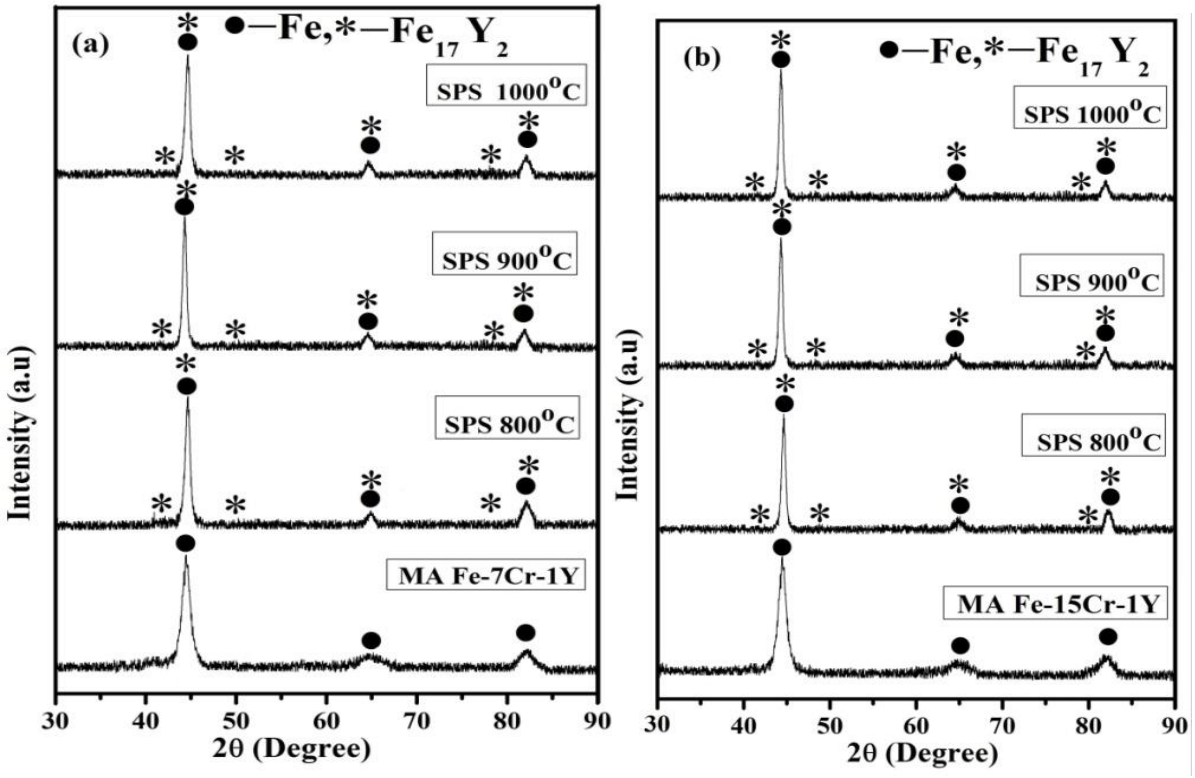

Fig. 4.14: XRD patterns of the as-milled and SPSed samples of (a) Fe-7Cr-1Y and (b) Fe-15Cr-1Y alloys sintered at various temperatures.

Figs. 4.14a and b, respectively, show the XRD analysis of the Fe-7Cr-1Y and Fe-15Cr-1Y alloys both in as-milled and SPSed conditions. It can be observed that the Cr and Y peaks are not visible from the XRD patterns of the as-milled samples of both the alloys. Therefore, as per the XRD patterns, it can be observed that the complete solid solution is formed after MA for 25 h. Formation of complete solid solutions of Fe-Cr-Y alloys and their thermal stability have been discussed in details in our previous work published in (Muthaiah et al., 2016). Chemical analysis was carried out for the as-milled sample of the Fe-15Cr-1Y alloy to confirm whether any oxygen pick-up was there in the as-milled sample. The chemical composition of the milled powder revealed Fe-84.1%, Cr-14.55%, Y-0.95% and O-0.4% (all in at.%), which shows a bit amount of oxygen picked up by the material from the milling media and/or during material handling. The trace amount oxygen picked up was possibly due to the Y atoms because of its high affinity to oxygen, which is also suggested by other researchers (Saber et al., 2014; Xu et

al., 2015). But, the oxide formation of Y was not possible to detect by the XRD phase analysis because of its limitation of the detectability (at least 2 wt.% should be present) (Cullity 1978; Suryanarayana et al.,1998). Formation of yttrium oxide could play a pivotal role to improve the thermal stability of the milled alloy through Zener pinning (Saber et al., 2014; Xu et al., 2015). Increase in the thermal stability of Fe-based alloys due to formation of small amount of oxides was also reported by other researchers (Roy et al., 2009; Saber et al., 2014; Xu et al., 2015). Formation of HfO_2 nanoparticles (av. size ~4 nm) during annealing (at 900ºC for 1h) of Fe-14at.%Cr-4at.%Hf alloy reported to increase its thermal stability. The thermal stability also increased due to the formation of other second-phase particles such as HfC, $M_{23}C_6$ and Fe-Cr-Hf intermetallic. The nanosize particles dispersed throughout the ferritic matrix could provide effective kinetic pinning to stabilize nanocrystalline grain structure (Xu et al., 2015). Xu et al. (2014) reported the formation of ZrO_2 nanoparticles during subsequent annealing of the Fe-14at.%Cr-1.5at.%Zr alloy, instead of forming the oxide during mechanical alloying (Xu et al., 2014). The formation of ZrO_2 nanoparticles during annealing suggested that the milled nanocrystalline powder adsorbed oxygen (~0.2 wt.%) because of the high affinity of Zr to oxygen (ΔG_f =-1037 kJ/mol). They also reported that uniformly dispersed nanosize ZrO_2 particles (av. size ~3.7 nm) rendered the Fe-based alloy powders to achieve high thermal stability (retained nanocrystalline structure even after annealing at 900°C for 1 h) (Xu et al., 2014).

For both the compositions, the XRD phase analysis of the SPSed samples clearly shows the formation of $Fe_{17}Y_2$ intermetallic phase, which is correlated with the phase evolution of the annealed samples of the same composition (Muthaiah et al., 2016). It can also be observed (especially from the lower angle peaks) that as compared to the as-milled samples, the peak intensity gradually increased and peak width (Fe 110 reflection) at FWHM decreased as a function of increase in the sintering temperature. Further, the decrease in the peak width and increase in the peak intensity could be ascribed to the increase in the crystallite size and release of the accumulated lattice strain, which decreased net dislocation density. Saenko et al. (2017) reported experimental and calculated enthalpies for the formation of $Fe_{17}Y_2$ (-1.78 to -8.7 kJ $(mol\ at)^{-1}$) phase at a temperature range from 0 to 298 K (Saenko et al., 2017). They mentioned that $Fe_{17}Y_2$ and $Fe_{23}Y_6$ compounds were unstable at 0 K based on the results of Ab-initio calculations as per the work reported in Mihalkovic et al. (2004). Additionally, no experimental data is available about any phase transformation in the Fe-Y binary system at low temperatures

(Saenko et al., 2017). Based on the experimental results of heat capacity measurement by Mandal et al. (2004), the standard entropy of $Fe_{17}Y_2$ compound at 298.15 K is found to be 34.5 $JK^{-1}mol^{-1}$. Rybalka (2015) analyzed the kinetic model for the H_2 induced direct phase transformation of $Fe_{17}Y_2$. The author reported that effective activation energy (Q) for the same (i.e. formation of $Fe_{17}Y_2$) varying from 162-242 kJ/mol as the temperature varies from 330 to 750°C. The author also correlated that there was a good agreement with the Q for diffusion of Fe atoms in Rare-Earth metals (250 kJ/mol) and self-diffusion of Fe in α-Fe (250.6 kJ/mol) (Rybalka 2015).

In an ODS alloy (Fe-Cr containing Ti & Y_2O_3), it was reported that the formation of Y-Ti-O (e.g. $Y_2Ti_2O_7$) oxides at room temperature requires an enthalpy of -3874 kJ mol^{-1} as reported by (Pasebani et al., 2014). The formation of Cr-Y-Ti-O nanoclusters was explained through the mechanism of concentration and diffusion rates of the initial oxide species formed during the milling process. Further, initial stages of sintering as well as the thermodynamic nucleation barrier and their enthalpy of formation also played pivotal roles in the formation of nanocluster oxides. Schneibel et al. (2008) investigated the internal oxidation of $Fe_{17}Y_2$ and $Fe_{11}TiY$ intermetallic phases to produce ODS alloys containing 30% of oxide particles (Y_2O_3, $YFeO_3$, $Y_2Ti_2O_7$, and Fe_2TiO_4) distributed in a Fe-based solid solution matrix. The ODS alloy showed a good thermal stability up to 600°C with oxides particles of ~20 nm size; thereafter, substantial coarsening of the oxides was reported. The coarsening of the oxides particles was ascertained to the high volume fraction of dispersoids, which caused faster coarsening due to short diffusion distance and short particle-particle distance. The presence of impurities segregated at the dispersoids-matrix interfaces also could play important role in faster coarsening (Schneibel et al., 2008).

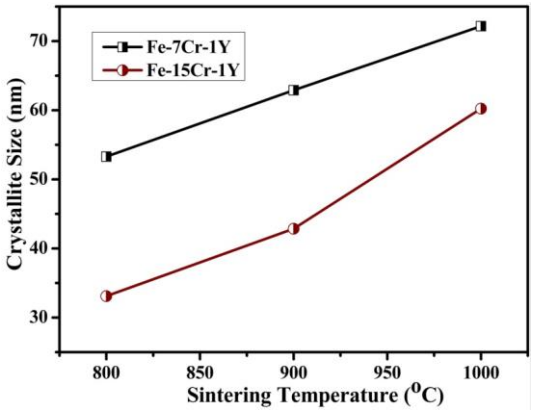

Fig. 4.15: Variation of crystallite size as a function of sintering temperatures for the Fe-7Cr-1Y and Fe-15Cr-1Y alloys.

Variation of crystallite size *vs.* sintering temperature is shown in Fig. 4.15. The three major XRD peaks were used to determine the average crystallite size by using Williamson-Hall analysis (Cullity 1978; Suryanarayana et al., 1998). The effect of peak broadening caused by the lattice strain was removed by using the plot of $B_r Cos\theta$ *vs.* $Sin\theta$. The peak broadening was evaluated by measuring the width of the peak at intensity equal to half of the maximum intensity (FWHM). The average crystallite size is determined to be ~53 nm and 33 nm, respectively, for the of the Fe-7Cr-1Y and Fe-15Cr-1Y samples, which were sintered at 800°C. Further, the crystallite size increased to 72 nm and 60 nm, respectively, when the sintering temperature was raised to 1000°C. Moreover, coarsening of the crystallite size is found to be sluggish in case of the Fe-15Cr-1Y samples as compared to the Fe-7Cr-1Y samples. It could be noticed that when a large amount of Cr is dissolved in presence of Y, the solid solution strengthening is more effective to stabilize it. Overall for both the compositions, the average crystallite size is found to remain well within 100 nm even after sintering at 1000°C. The major role of Cr in the nanocrystalline Fe was only to enhance the strengthening to the matrix and not for the grain size stabilization (Darling et al., 2011; Li et al., 2014; Saber et al., 2012). The average crystallite size of the as-milled Fe-7Cr-1Y and Fe-15Cr-1Y alloys was found to be 9 and 7.5 nm, respectively, and the same samples showed 16 and 15 nm crystallite size after annealing at 600ºC. Without any Y, the Fe-15Cr showed a crystallite size of 128 nm when annealed at 1000°C (Suryanarayana et al., 1998). It can be noticed that Cr could play a pivotal role in grain size stabilization in presence of 1at.% Y up to a certain temperature (i.e. 600ºC). Thereafter above 600ºC, it clearly showed a tendency to grain coarsening but retaining the grain size within 100 nm even after annealing at 1000°C. The growth rate of the crystallite size at higher temperatures is found to be bit higher for the high Cr content alloy (i.e. Fe-15Cr-1Y). This may be due to the weak stabilizing effect of Cr in Fe based alloys as also suggested by various researchers (Darling et al., 2011; Li et al., 2014; Saber et al., 2012). Darling et al. (2011) investigated that the solute atom of Cr and Ni are poor candidates for the thermodynamic stabilization of nanocrystalline Fe; whereas, the nanocrystalline Fe was strongly stabilized by Zr (Darling et al., 2011). Saber et al. (2012) reported that the crystallite size of Fe-10at.% Cr and Fe-18 at.% Cr was estimated to be 80 and 70 nm, respectively, after annealing at 600ºC. Thereafter, the grain growth took place. For example, the grain size was found to be 7μm for the Fe-10at.% Cr alloy after annealing at 900ºC. They also reported that

the addition of 4at.% Zr to the Fe-10% Cr and Fe-18% Cr stabilizing the grains at <100 nm after annealing at 1000ºC (Saber et al., 2012). Li et al. (2014) also reported that addition of 4at.% Hf to the Fe-14Cr alloy stabilized the grain size at less than 100 nm after annealing at 1000ºC; whereas, the Fe-14Cr alloy without Hf addition showed the grain size ~140 nm when the sample was annealed at 600°C (Li et al., 2014). Therefore, overall, it can be concluded that Cr could enhance the thermal stability in presence of oversize solute atoms such as Zr, Y etc. This is also observed in the present study.

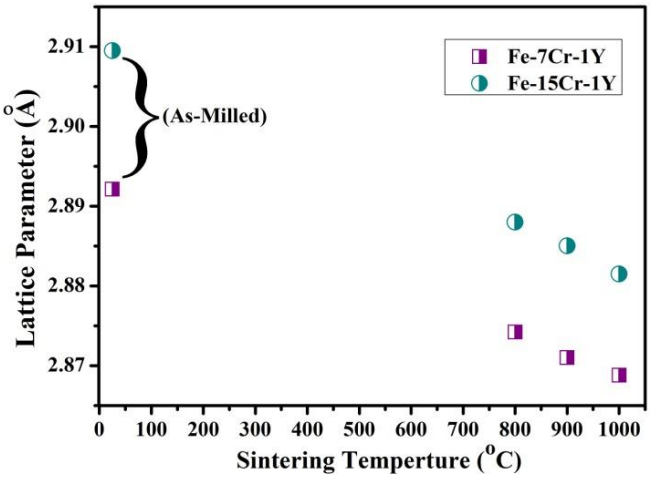

Fig. 4.16: Variation of the lattice parameter of the Fe-7Cr-1Y and Fe-15Cr-1Y alloys SPSed at various temperatures as compared to that of the as-milled samples.

The variation of the lattice parameter is displayed in Fig. 4.16. The lattice parameter (a_{Fe}) of the Fe-15Cr-1Y as-milled sample is found to be 2.909Å as compared to 2.892 Å for the Fe-7Cr-1Y in the same condition as reported in our previous study (Muthaiah et al., 2016). The a_{Fe} of the alloys sintered at 800ºC is determined to be 2.874Å and 2.888Å, respectively. The a_{Fe} of the sintered samples is found to decrease with increase in the sintering temperature and the trend is similar for both alloys. The a_{Fe} was found to be 2.868Å and 2.881Å, respectively, after sintering at 1000°C. The reduction in the lattice parameter is found to be prominent with an increase in the sintering temperature. This could be attributed to the 2 reasons: (i) the excess solute atoms, especially oversize Y atoms (Cr has little role as it has spontaneous solid solubility in Fe) could have precipitated out of the solid solution to segregate along the grain boundary areas and/or (ii) the formation of intermetallic compound(s) such as $Fe_{17}Y_2$ at high temperature. In the present study, formation of the $Fe_{17}Y_2$ phase already been detected and definitely, the a_{Fe} decreased due to the formation of $Fe_{17}Y_2$ phase as Y atoms had to come out of the solid solution to form the intermetallic phase. It is to be noted that the amount of the alloying content (i.e. Y) precipitated out of the solid solution to form $Fe_{17}Y_2$ intermetallic phase

and/or segregated along the grain boundaries played an important role in the decrease of the a_{Fe} of the Fe-based solid solution (Kumar et al., 2017; Mula et al., 2009).

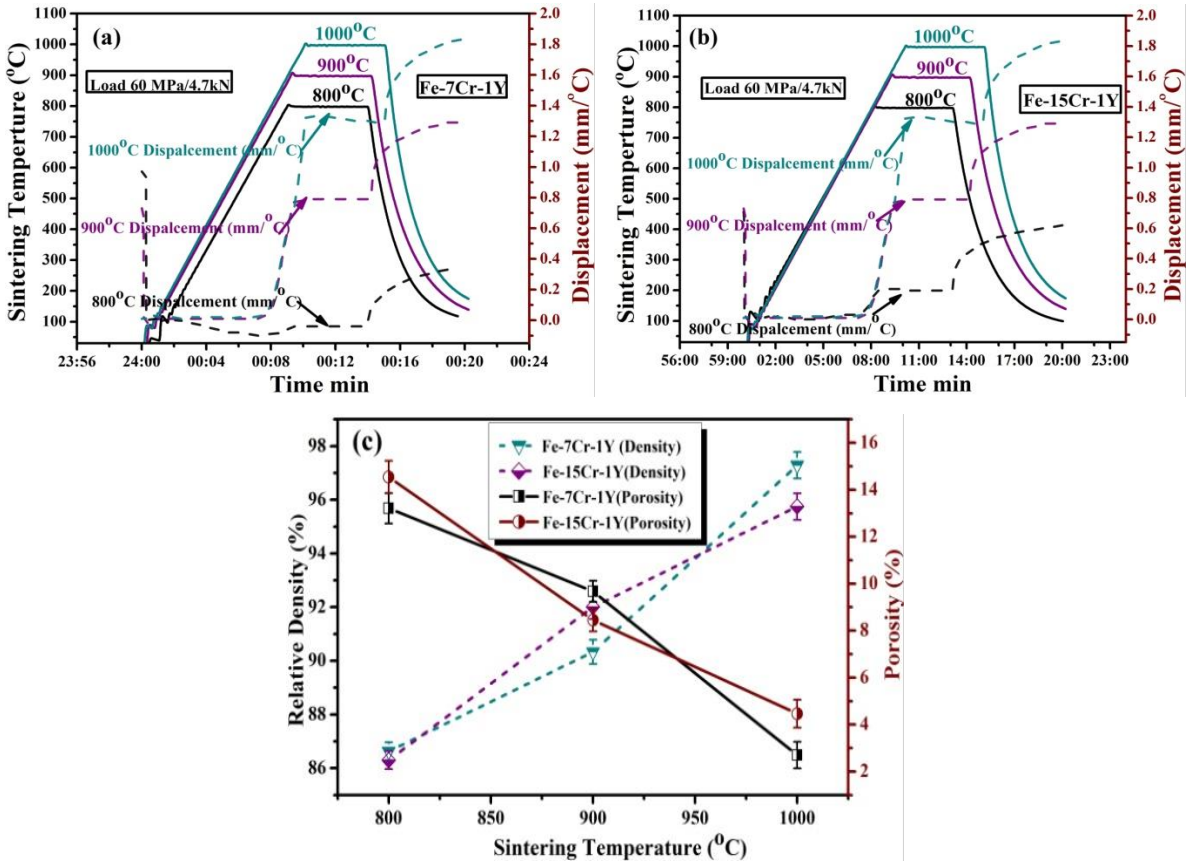

Fig. 4.17: Temperature profiles during SPS of (a) Fe-7Cr-1Y and (b) Fe-15Cr-1Y alloys at different temperatures. (c) Relative density and porosity as a function of sintering temperatures.

Figs. 4.17a and b, respectively, show typical temperature and displacement (mm/°C, dotted lines) profiles as a function of dwell time over the densification during SPS of the nanostructured Fe-7Cr-1Y and Fe-15Cr-1Y alloys. The sintering was carried out at 800, 900 and 1000°C by applying a constant pressure of 60 MPa for a holding period of 5 min; while a heating rate of 100°C/min was used to raise the sintering temperature. Fig. 4.17c indicates that the relative density achieved during the SPS at different sintering temperatures could easily be measured indirectly from the corresponding displacement profile (mm/°C). The densification of the alloy powders during SPS was monitored through the analysis of the displacement curves simulated from the software (wave logger) installed with the SPS machine (Brendon et al., 2015; Yang et al., 2017) The displacement of the specimen could be affected either by the pressure, time and/or the temperature. Archimedes principle was used to determine the relative density of the sintered samples. The relative density was measured to be ~86 and 87%,

respectively, for the Fe-7Cr-1Y and Fe-15Cr-1Y samples when the SPS was performed at 800°C (Fig. 4.17c). It can be noticed that the sintered density increases with increasing sintering temperature and the maximum sintered density achieved is 96 and 97%, respectively, for the Fe-7Cr-1Y and Fe-15Cr-1Y samples, when sintered at 1000°C. Figs. 4.17c also indicates the level of porosity present in the respective sintered samples. The larger sintered density could be ascribed to the prevalent grain-boundary and bulk diffusion at the higher sintering temperature, due to which the porosity level decreased to enhance proper bonding between the particles.

The spark plasma sintering (SPS) can develop highly dense bulk samples without much affecting the grain structures of various metals and ceramics due to its rapid heating rate, minimum holding time and a comparatively lower sintering temperature (Mamedov 2002). But, mechanisms of the SPS still remain imprecise. The DC current (ON-OFF), which is used for simultaneous development of spark discharge and rapid heating (Joule effect) between the powder particles in the initial stage of the SPS, is generally reported to be responsible to achieve high sintered density in the SPS (Munir 2006). Further, the pulse current developed removes the thin oxide layers of the metallic materials, surface impurities and adsorbents induced by plasma generation and thus enhancement in the bonding between the powder particles is achieved (Goodwin et al., 1997). These special effects result in low heat input and create bonding between the powders particles with a limited chemical interaction amongst different elements and control grain sizes (Brendon et al., 2015). In SPS, external pressure is applied not only to create electrical contacts between die, punch and powders particles, but also progressively promotes densification by reorganization of the powder particles and neck formation through diffusion bonding due to localized deformation at the contact points (Fougere et al., 1995). Nanostructured powders material densification may occur by some specific mechanisms such as plastic deformation, grain boundary sliding (Averback et al., 1996), grain growth and grain rotation (Zhu et al., 1996) and even by grain boundary melting due to large Hertzian stress (Zhang et al., 2005). Overall, all the factors together play their pivotal role to achieve such high level of densification by SPS.

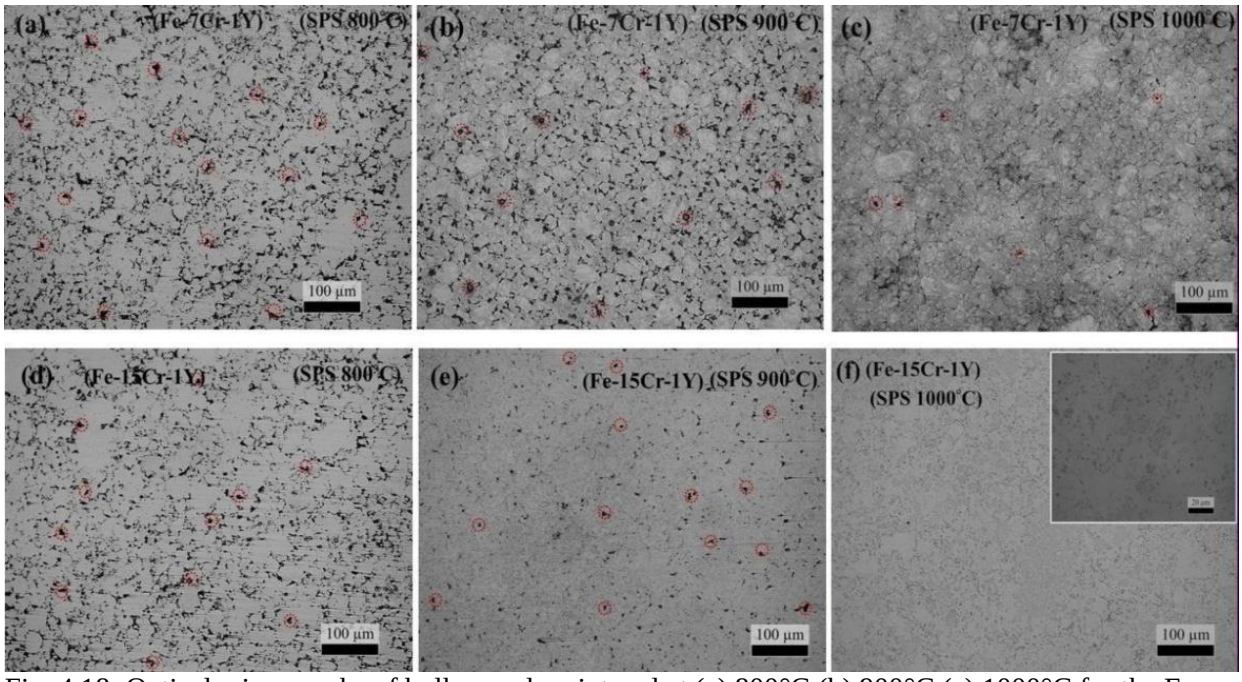

Fig. 4.18: Optical micrographs of bulk samples sintered at (a) 800°C (b) 900°C (c) 1000°C for the Fe-7Cr-1Ycomposition; and (d) 800°C (e) 900°C (f) 1000°C for the Fe-15Cr-1Y composition.

The optical micrographs of the sintered specimens are shown in Figs. 4.18a-f. From the micrographs of the sintered samples, it can be observed that the amount of porosities decreases with increasing the sintering temperature. It can be observed from Figs. 4.18a and d, that the samples, which were sintered at 800ºC, have a lot of porosities and the corresponding sintered density was found to be low for both the samples, i.e., 86% (Fe-7Cr-1Y) and 87% (Fe-15Cr-1Y) only. The microstructures exhibited a few large and a lot of small porosities as a result of improper bonding and densification. Also, numerous free-standing particles, which do not exhibit any neck-formation with the adjacent particles, could be observed from the micrographs of the samples sintered at 800 and 900°C. This may be ascribed to the insufficient grain-boundary diffusion at low sintering temperature with less dwell time (5 min). A significant enhancement in the relative sintered density was achieved when the samples were sintered at 1000ºC. The maximum sintered density of both the alloy samples is found to be 96 and 97%, respectively, when the SPS was done at 1000ºC. The corresponding porosity level also decreased to a very low level as could be observed from Figs. 4.18c and f. It can be noticed from Figs. 4.18f that the grain size is not resolved clearly in any case. Therefore, higher magnification microscopy, such as TEM and EBSD are required to reveal the nanosize/ultrafine grains (discussed later in this section). The porosity level is found to be almost eliminated for the Fe-15Cr-1Y sample SPSed at 1000°C, which can be ascertained from

the highly magnified image as shown in the inset of Fig. 4.18f and a near full density structure were developed.

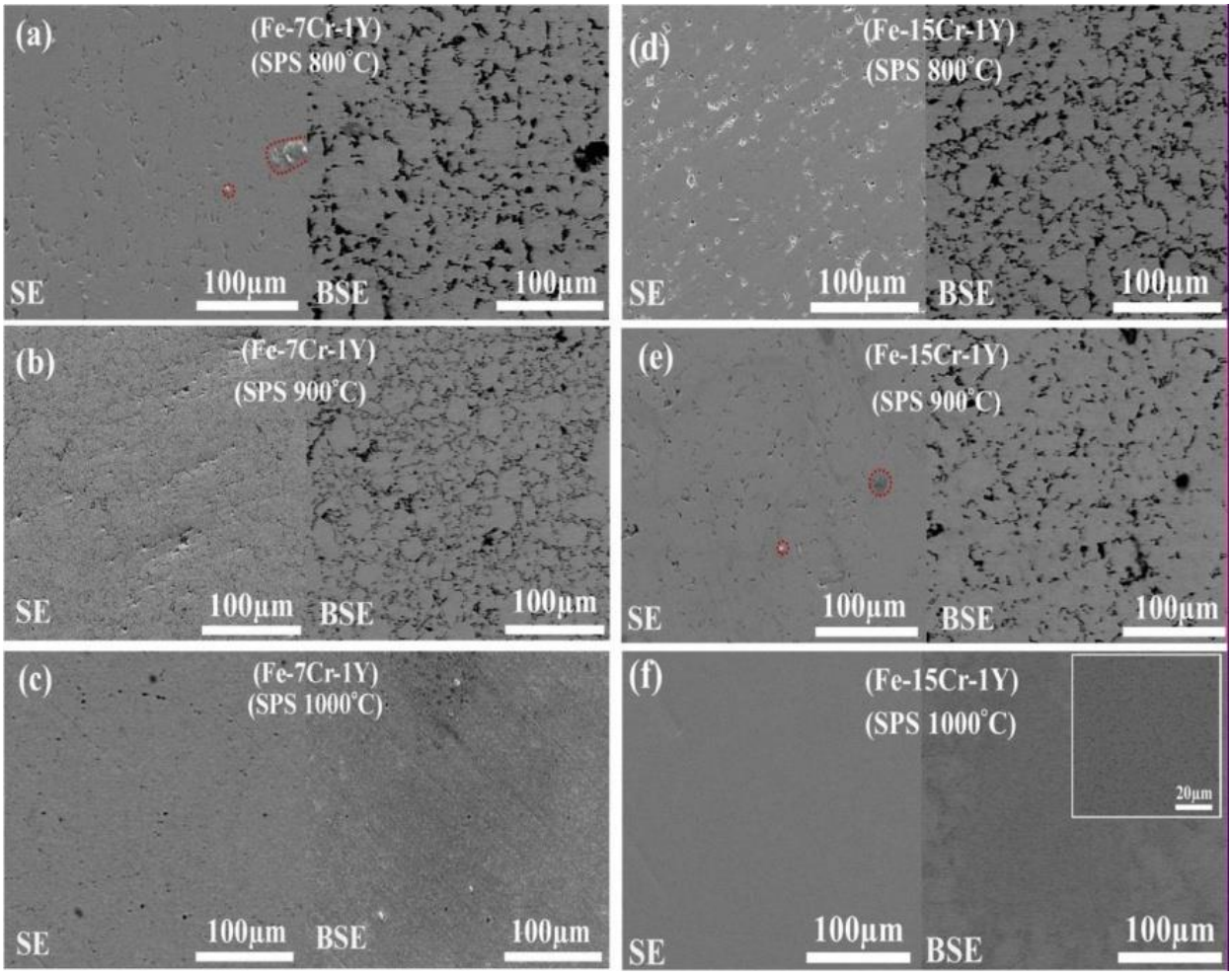

Fig. 4.19: FE-SEM (Secondary and Backscattered electron) micrographs of the Fe-Cr-Y alloy samples sintered at various temperatures.

Secondary electron (SE) and backscattered electron (BSE) images were recorded to reveal the level of porosity and densification clearly. Figs. 4.19a-f show the SE as well as BSE images of each sample of the Fe-7Cr-1Y and Fe-15Cr-1Y alloys sintered at 800, 900 and 1000°C. It can be noticed that the BSE mode is more prominent as compared to the SE mode to corroborate the sintered density. The BSE micrographs clearly revealed the presence of number of small pores in the low temperature SPSed samples (800 & 900°C). When the sintering temperature increased to 1000ºC, almost no porosity could be observed and achieved almost a near-full density samples for both the alloys. In some images, presence of alumina (Al_2O_3) particles could be seen (encircled with red color), which are plausibly embedded during cloth polishing of the samples. Therefore, it can be concluded that the optical and SEM images of the SPSed

samples revealed the surface morphology comprising of larger and small size porosities. Further, it is corroborated well with the relative sintered density obtained by the Archimedes' principle.

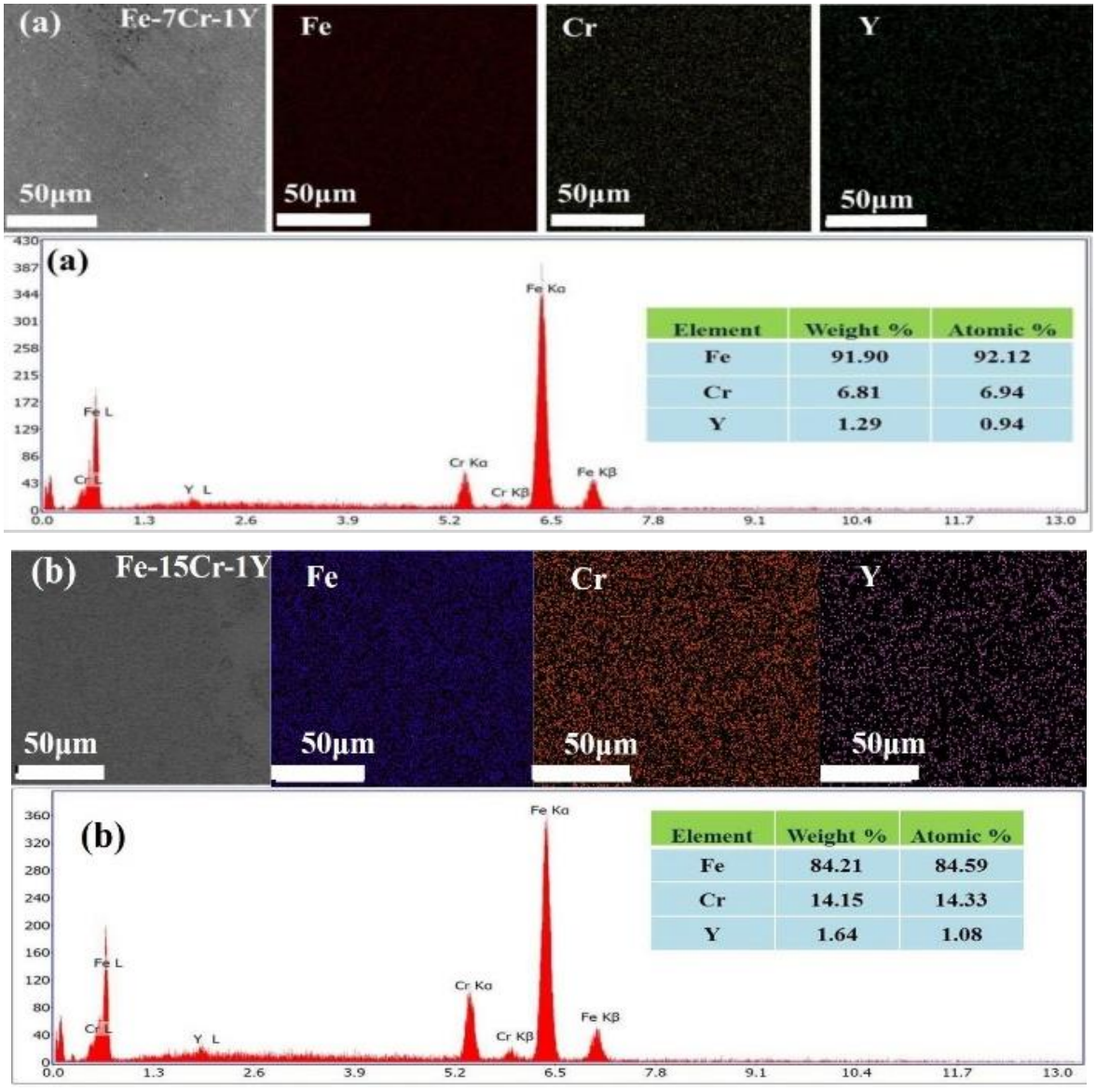

Fig. 4.20: Backscattered electron images of (a) Fe-7Cr-1Y and (c) Fe-15Cr-1Y alloys SPS sintered at 1000ºC corresponding to elemental area maps. (b) EDS data for the Fe-7Cr-1Y (d) EDS data for the Fe-15Cr-1Y.

Figs. 4.20a and b, respectively, show BSE images along with elemental mapping and EDS results of Fe-7Cr-1Y and Fe-15Cr-1Y samples SPSed at 1000°C. Homogenous distribution of chromium (Cr) and yttrium (Y) in the Fe matrix could clearly be seen from the elemental distribution on the bulk samples. The quantitative EDS analysis confirmed that the elemental

distribution in the alloys was highly homogeneous and revealed almost same composition similar to the blend compositions of the alloys.

TEM analysis of the sintered sample

Bright field TEM images along with corresponding SAED patterns of the Fe-15-Cr-1Y alloy sintered at 1000°C presented in Figs. 4.21a-c. Figs. 4.21a and b clearly show that the grain sizes are varying from nanometer to ultrafine range (i.e. a bimodal grain structure). The bright field TEM images clearly show that the grain sizes are retained well within the ultrafine range (along with some nanocrystalline grains) even after the SPS at 1000°C. The SAED pattern was recorded from the region as shown in Fig. 4.21a.

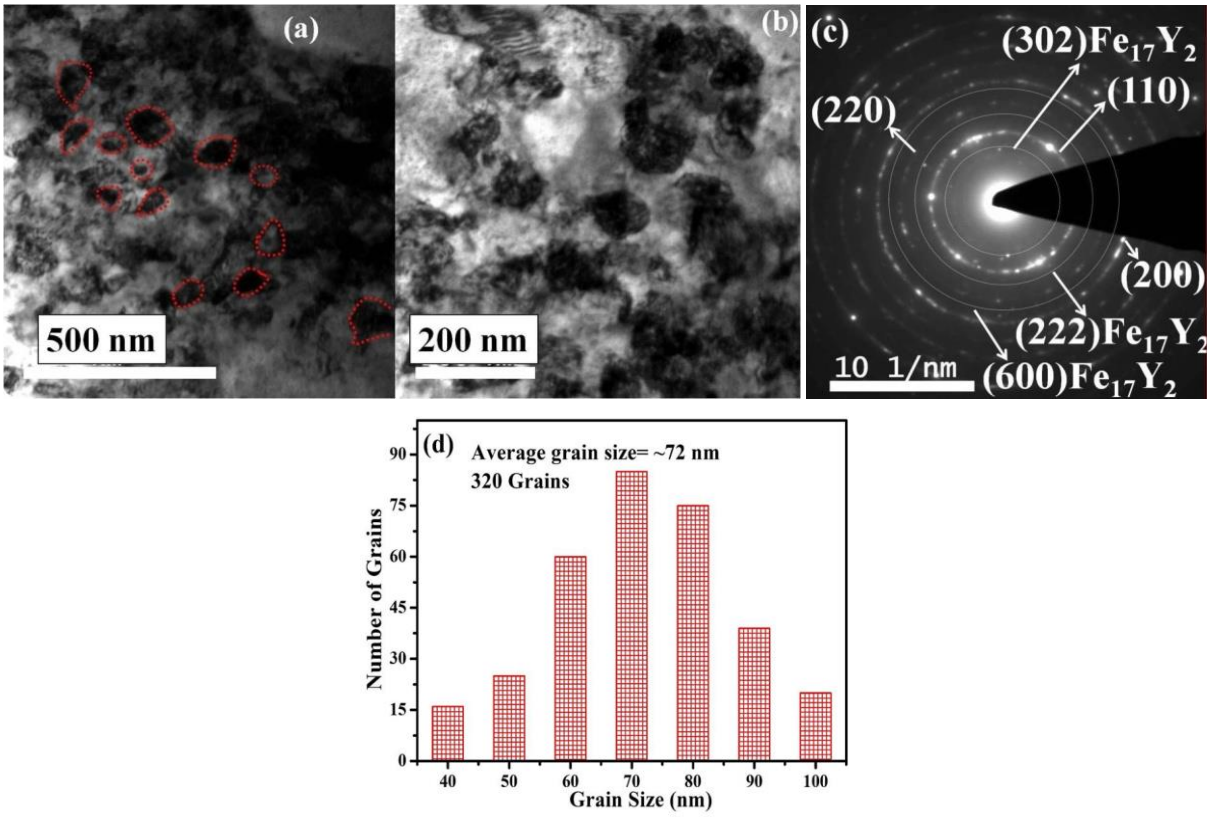

Fig. 4.21: Bright field TEM images of (a) and (b) Fe-15Cr-1Y sample SPS sintered at 1000°C sample with lower and higher magnification. (c) Selected area diffraction pattern (SAED) Fe-15Cr-1Y sample sintered at 1000ºC. (d) Statistical grain size distribution of 320 grains obtained from the TEM images as shown in Figs. 4.21a & b.

As shown in Fig. 4.21c, the corresponding SAED pattern shows continuous rings along with some brighter spots indicating the presence of nanocrystalline features along with some larger size grains in the microstructure. As indicated in Fig. 4.21c, the rings are identified as the major reflections from the Fe (110), (220), (200) planes along with the reflections from the hcp

intermetallic phase, $Fe_{17}Y_2$ (222), $Fe_{17}Y_2$ (600) and $Fe_{17}Y_2$ (302). Presence of the hcp intermetallic $Fe_{17}Y_2$ phase was also detected from the XRD phase analysis of the sintered sample (Fig. 4.14b). Neither, the SAED nor the XRD pattern exhibited the presence of any free Cr and Y elements. This indicates the dissolution of the added Cr and Y in the disordered Fe-based solid solutions formed during MA; and Y partially transformed to $Fe_{17}Y_2$ intermetallic phase during the SPS process. Formation of the $Fe_{17}Y_2$ intermetallic phase played an important role to stabilize the matrix grains in nanometer level at high temperature and also enhanced the hardness of the sintered Fe-Cr-Y alloys as discussed later section (Fig. 4.23a). The Y atoms also played a distinguishing role in strengthening of the Cu-Y alloys as reported in (Mula et al., 2015).

EBSD analysis

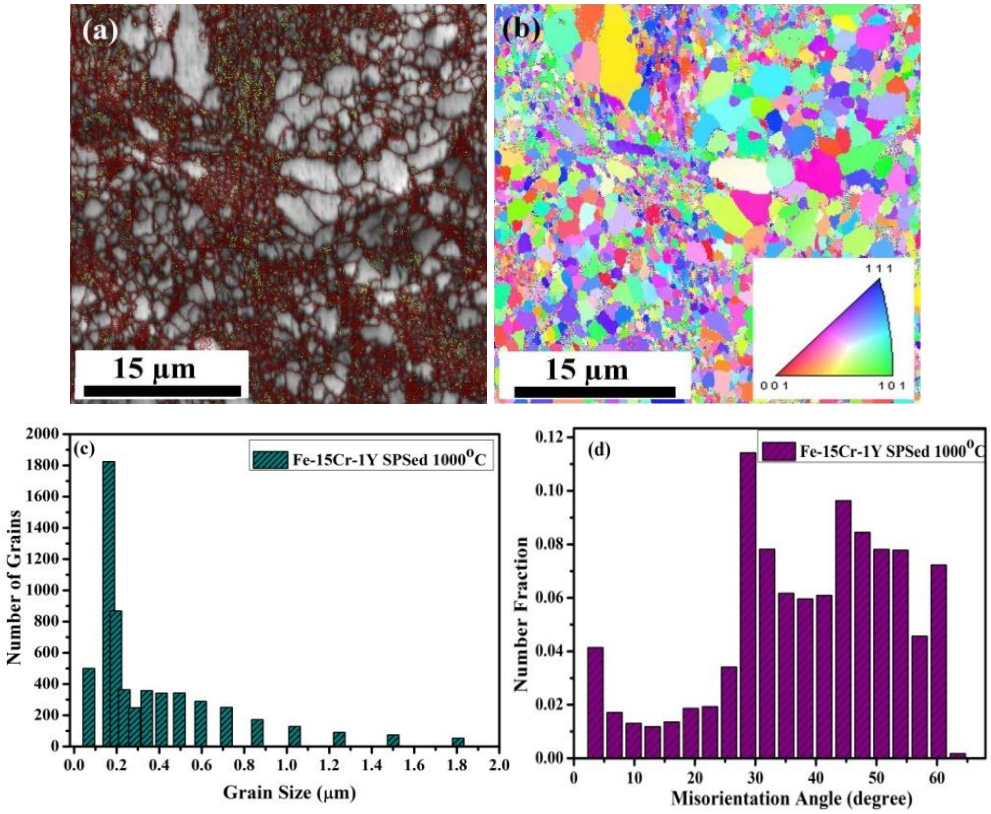

Fig. 4.22 EBSD images of the Fe-15Cr-1Y sample sintered at 1000°C (a) Grain boundary map (red lines-HABs and yellow lines-LABs), (b) Inverse pole figure, (c) Average grain size distribution and (d) Grain boundary misorientation profile.

Figs. 4.22a and b, respectively, show the EBSD grain boundary map (HABs and LABs) and inverse pole figure of the SPSed Fe-15Cr-1Y sample sintered at 1000°C. According to the analyzed data shown in the Figs. 4.22a & d, the major fraction of the grains is of high angle

grain boundaries (HABs). It can be noticed that almost no black region is revealed from the EBSD image (Fig. 4.22b) indicating a high sintered density of the Fe-15Cr-1Y SPSed sample (~97%). Fig. 4.22b shows the inverse pole figure with grain boundary map of the sintered sample, which depicts a bimodal grain structures: more than 50% grains (in numbers) are within a range of 200 nm and remaining grains are in the range 200 nm - 2 µm. The different grain colors indicate the orientation of each grain as shown in the inset unit triangle (Fig. 4.22b). The average grain size distribution was calculated from Fig. 4.22b and is shown in Fig. 4.22c. Fig. 4.22d shows misorientation angle of the sintered sample, which depicts that a small fraction of the grains is of low angle grain boundaries (LABs-up to 15°) and the majority is in the range of high angle grain boundaries (HABs) with misorientation angles 15° to 60°. It is to be noted that the EBSD grain size distribution is corroborating well with that obtained by TEM study; both revealing a dual size grain structure (i.e. up to less than 200 nm and 200 nm - 2 µm). Overall, the EBSD analysis shows better grain size distribution as compared to that obtained by TEM. This is due to the fact that the TEM analysis is done on extremely small sample region as compared to the sample size used for the EBSD.

4.2.2.2 Mechanical properties of SPSed samples

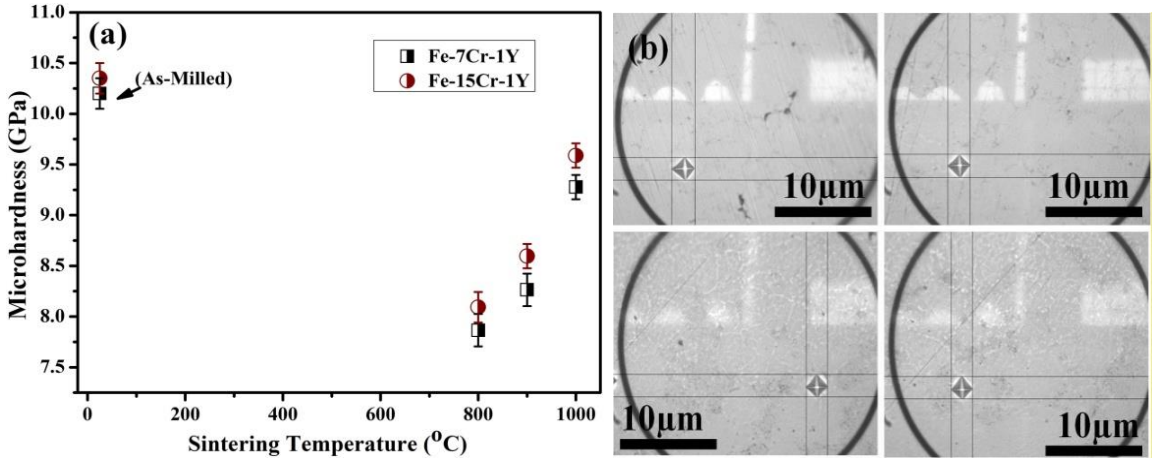

Fig. 4.23: (a) Variation of microhardness values as a function of sintering temperatures. (b) Showing indentation marks made within the surface during microhardness measurements.

Fig. 4.23a shows the variation of microhardness values of the Fe-7Cr-1Y and Fe-15Cr-1Y alloys as a function of the sintering temperature. An important observation is that the microhardness value increased gradually with increase in the sintering temperature; and the maximum microhardness value for both the alloys (9.27 GPa and 9.58 GPa, respectively) was obtained after sintering at 1000°C. Further, the highest hardness of the sintered samples is

found to be less as compared to that of the as-milled samples. It is to be noted that the microhardness value for the as-milled Fe-7Cr-1Y and Fe-15Cr-1Y alloys was determined to be 10.2 and 10.4 GPa, respectively. The average crystallite size of the as-milled Fe-7Cr-1Y and Fe-15Cr-1Y samples was estimated to be ~9 and 7.5 nm, respectively (Muthaiah et al., 2016). It could be observed from Fig. 4.15 that the average crystallite size of the Fe-7Cr-1Y and Fe-15Cr-1Y alloys sintered at 1000ºC was found to be 72 and 60 nm. Overall, the crystallite size and microhardness values gradually increased with an increase in the sintering temperature. In general, this is contradictory: an increase in the crystallite size would decrease the hardness value. Hence, the increase in the hardness value due to the densification overcompensates the decrease in the hardness because of the grain coarsening. Hence, the enhancement in the hardness value at higher sintering temperature can be accomplished mainly by two factors, viz. (i) an increase in the sintered density at elevated sintering temperature and (ii) formation of the harder intermetallic phase, i.e. $Fe_{17}Y_2$ uniformly distributed within the matrix (Figs. 4.14a & b). It can be noted that the maximum hardness of the sintered samples is less than that of the as-milled samples. This can be ascribed mainly to the coarsening of grains and presence of bit porosity (96 & 97% densification) of the sintered samples. The hardness measurement of the sintered samples was done randomly on the polished surface, which may include the influence of small pores; whereas, the indentation on the as-milled samples was made within the larger size particles. Fig. 4.23b shows the indentation marks made on the surface of the sintered samples during microhardness measurements. The particle diameter-to-indenter depth ratio was kept at 10:1 to avoid the effect of indentation plastic zone during the hardness tests. Further, the distance between the indentations was fixed at 1:3 for the hardness measurements. Each reported value of the hardness is an average of 10 such measurements. Zhang et al. (2005) also reported that the average microhardness value increased due to increase in the sintered density of the Fe-0.8%C steel sintered at higher temperature although the crystallite size increased with sintering temperature. Hussein et al. (2015) reported that the hardness value of the Nb-Zr alloys increased significantly due to the enhanced sintered density at higher sintering temperatures.

Compression test

Fig. 4.24 shows typical stress-strain curves accumulated during compression tests of the Fe-7Cr-1Y and Fe-15Cr-1Y samples sintered at 1000°C. The compression tests were repeated for three times to confirm the repeatability of the data.

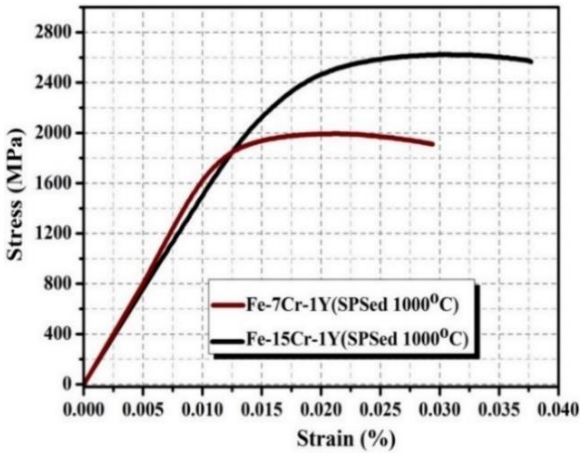

Fig. 4.24: Variation of compressive stress-strain curves of Fe-7Cr-1Y and Fe-15Cr-1Y samples SPSed at 1000°C.

The ultimate compressive strength (UCS) of the SPSed Fe-7Cr-1Y and Fe-15Cr-1Y samples (sintered at 1000°C) was 2000 and 2600MPa, respectively. The corresponding yield strength is estimated to be 1600 and 1800MPa, respectively. The compressive strength value of the Fe-15Cr-1Y sample is significantly higher than that of the Fe-7Cr-1Y sample sintered at same conditions due to the fact of more amount Cr dissolved in the matrix. Moreover, as discussed earlier that the relative density was the maximum for the Fe-15Cr-1Y sample sintered at same conditions (Fig. 4.24). From the stress-strain curves, it could be observed that the failure has occurred after the significant amount of plastic deformation, i.e. after certain amount of yielding (Bisht et al., 2012). The extremely high yield strength of Fe-15Cr-1Y sample can be attributed to three major strengthening mechanisms, namely, solid solution strengthening (high amount of Cr), grain size refinement (Hall-Petch effect) and dislocation strengthening.

Wear Properties

Recently, an attention has been made to replace the traditional ZG35CrMnSi steel by stabilized Fe-based alloys such as Fe-Cr-B alloys (Hongbin et al., 2017) to improve the service life of the coal mining machine parts. The major part of the shearer is the sliding shoes, where the wear resistance is extremely important. A very high hardness value of the same alloy is reported in our earlier study (Muthaiah et al., 2016). In the present work also, the SPSed samples of the Fe-Cr-Y alloys show very high levels of hardness (8-9.5 GPa) for the sample sintered at 1000°C. Therefore, this stabilized Fe-Cr-Y alloy could be a possible candidate to replace the traditional materials such as ZG35CrMnSi steel for high wear resistance applications (e.g. sliding shoes).

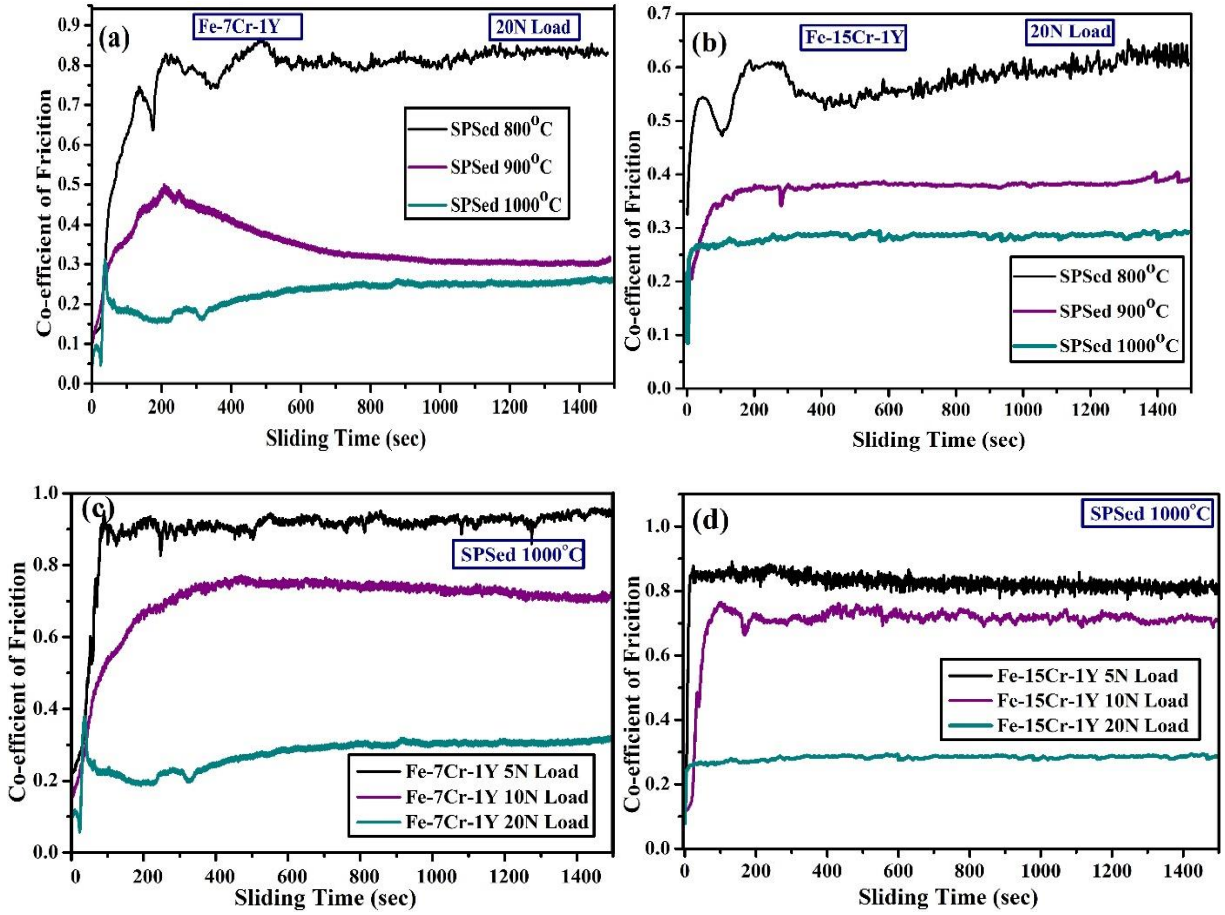

Fig. 4.25: Variation of coefficient of friction as a function of sliding time for the samples sintered at different temperatures (a) Fe-7Cr-1Y (b) Fe-15Cr-1Y. Effect load on the wear behavior is shown in figure (c) Fe-7Cr-1Y (d) Fe-15Cr-1Y as a function of sliding time.

The dry sliding wear behavior of the SPSed Fe-7Cr-1Y and Fe-15Cr-1Y samples has been investigated and the variation of coefficient of friction (COF) of the specimens as a function of time is displayed in Fig.4.25a & b. As could be seen from the plots, the COF gradually decreases as the sintering temperature increased for both the alloys (Fig.4.25a & b). As the sintering temperature increased from 800 to 1000°C, the COF of the Fe-7Cr-1Y samples decreased from 0.8 to 0.3 (Fig. 4.25a). The same for the Fe-15Cr-1Y SPSed samples decreased to 0.28 from 0.6 (Fig. 4.25b) as the sintering temperature increased to 1000°C from 800°C. Moreover, the COF of the Fe-15Cr-1Y samples is found to be less than that of the Fe-7Cr-1Y samples sintered at any particular temperature. As discussed earlier (in the Fig. 4.17 and Fig. 4.18), the sintered density increased with increasing sintering temperatures. The enhancement of the wear resistance, therefore, could be ascribed to the proper bonding of the powder particles and near full density achieved during sintering at higher temperature, i.e. at 1000ºC. The wear resistance was reported to improve due to the addition of 4% nanosize SiC particles

in Cu-Cr alloys developed by MA followed by microwave sintering (Mula et al., 2011). Further, they also reported that at higher sintering temperature (900°C), the wear resistance increased due to the proper bonding of the powder particles. It can be noticed that the sample sintered at 800ºC showed more ups & downs in the COF values as compared to that of the 900 and 1000ºC sintered samples. This is due to the presence of more amount of porosities and particles pull out from the surface of the low-density sample. Thus, the pull out materials (called wear debris) frequently come in contact between the ball and material surfaces, which is reflected as ups and down in the COF *vs*. time plot. This, in turn, increases the formation of more amount of wear debris particles in the low temperature sintered sample. Shashanka et al. (2017) investigated the wear behavior of ferritic stainless steel sintered at different temperatures (1000-1400°C). Wear depth is reported to decrease with increase in the sintering temperature as higher hardness is resulted due to proper densification at higher sintering temperature. Zhang et al. (2015) reported similar type of results in the dry sliding wear behavior of Fe-14Mo-15Cr-2Y-15C-6B (all in at.%) thin film metallic glass. This is an important phenomenon during the initial stage of wear, as the formation of the thin oxide layer occurs due to the oxygen-affinitive metals viz. iron, chromium etc. present in the alloy. Further, when this oxide layer attains certain thickness, it breaks into metal oxide debris. The oxide debris is entrapped between the contact surface of the ball and sample; which, in turn, increases the frictional force further during sliding and induces extra wear. The wear resistance of the sintered sample is found to correlate well with the Vickers hardness values of the corresponding sample (Fig. 4.23a), i.e. the sample, which showed higher hardness, is less susceptible to wear. This is effective only when proper bonding between the particles is achieved and produces almost a fully dense structure. Many other researchers also reported that the highly dense Fe-based alloys having high Cr and Y showed excellent tribological performance and wear resistance (Archard 1953; Cui et al., 2007; Sahani et al., 2011). The Cr and Y elements played a vital role to improve the wear resistance and decreased the coefficient of friction (Archard 1953; Cui et al., 2007).

Effect of load variation on the COF of the SPSed Fe-7Cr-1Y and Fe-15Cr-1Y samples (sintered at1000°C) as a function of sliding time is shown in Figs. 4.25c & d, respectively. It can be noted that the COF values of the sintered samples decrease with increasing the load from 5 to 20 N. The COF values of the Fe-7Cr-1Y sintered samples (at 1000°C) is measured to be 0.9, 0.7 & 0.3, respectively, for the 5, 10 & 20N loading condition (Fig. 4.25c). Similar trend of the

COF (0.8, 0.69 & 0.28) could be observed for the Fe-15Cr-1Y alloy samples sintered at 1000°C tested under same conditions (i.e. 5, 10 & 20N load) (Fig. 4.25d).

It could be seen that the COF value of any particular sample is higher at lower loading condition (say 5N) as compared to that of the higher load (say 20N). Chowdhury et al. (2013a, b) also reported that the COF of SS304 decreases with an increase in the applied load (10-20N). It is understood that at higher normal load, time to reach steady friction is less. This is because of the surface roughness and other oxide layer, moisture etc. attain a steady level at a shorter period of time at higher normal load. The wear debris particles increase with increase in the applied load and hence wear rate. The amount of wear debris attained at higher load (say at 20N) is greater than that at lower loading condition (say at 10N). As a result, at 20N load more wear debris is trapped between the two contacting surfaces and breaks up the maximum contacting interface to a sufficiently small size and reduces the wear depth further (Shashanka et al., 2017). Li et al. (2010) study the wear behavior of AZ31 magnesium alloy with and without irradiation (by high-intensity pulsed ion beam). They used a 3mm diameter AISI 52100 steel ball as a counter body to carry out the sliding wear tests with a variation of load from 0.1 to 0.5N. At an applied load, they also reported a decrease in the COF as well as fluctuation of the same (i.e. COF) in the irradiated samples. This is due to the fact that the formation of a hardened surface layer possibly delayed the fatigue crack initiation during repetitive tribological actions. Therefore, it reduced the production of wear debris, which could increase the fluctuations of friction coefficient. It is also demonstrated that fluctuation and average value of COF decreased with increasing the sliding load. The fluctuation is reduced at higher load mainly due to the increased contacting area; whereas, lower COF at higher load can be ascertained to the better lubrication created by the wear debris and its oxidation. At the lower normal loads, plowing action is resulted due to the less contact of asperities, which increases the COF (Chowdhury et al., 2013a, b). Better conformity is obtained between the contacting surfaces due to increase in the normal load, thereby reduces the plowing action. And it results in the reduced COF. Oxidation may take place on the metal surface as the surface temperature increases. It is known that oxide layer can provide lubricating action which decreases the friction between the contact surfaces. Surface roughness is increased, which reduces the total contact area between the surfaces, thereby reduces the COF. Larger amount of wear debris is also supposed to decrease the COF due to increase in the load (Chowdhury et al., 2013b).

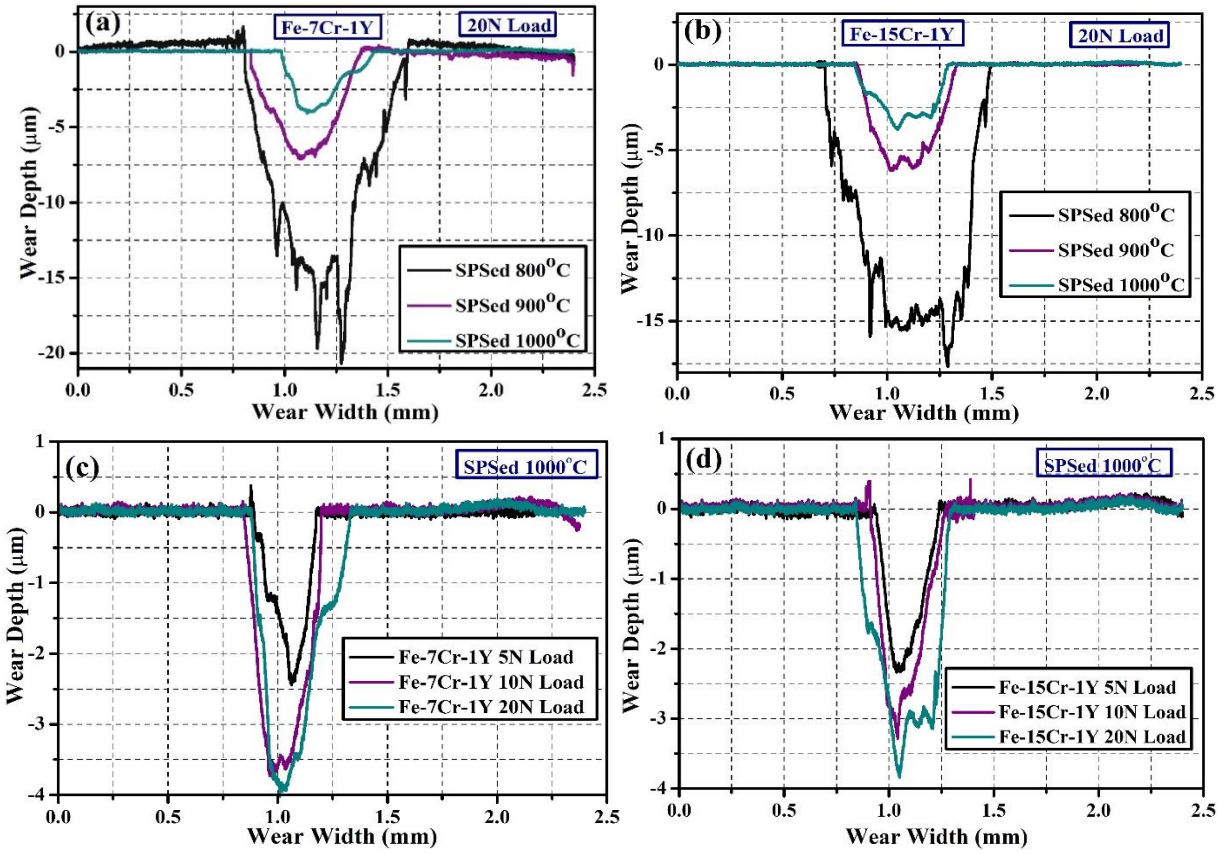

Fig. 4.26: Representative cross-sectional surface profiles of the worn tracks of (a) Fe-7Cr-1Yand (b) Fe-15Cr-1Y alloy samples sintered at different temperatures. Effect load on the wear track is shown in figure (c) Fe-7Cr-1Y (d) Fe-15Cr-1Y.

Figs. 4.26a and b, respectively, show the cross-sectional surface profiles of the worn tracks of the sintered Fe-7Cr-1Y and Fe-15Cr-1Y samples tested under 20N load. Both, the depth and width of the sliding wear tracks were measured at different locations by using surface profilometer. Figs. 4.26a and b clearly indicate that the wear depth and wear width values are larger for the samples, which were sintered at lower temperature (e.g. Fe-7Cr-1Y:17.5 μm & 0.79 mm and Fe-15Cr-1Y:15 μm & 0.94 mm for the sample sintered at 800°C). The worn depth and width of the same samples tested under the same load (i.e. 20N) decreased to only 4.0 μm & 0.47 mm and 3.7 μm & 0.43 mm, respectively, as the sintering temperature increased to 1000ºC. At the beginning, the wear width and depth increased very rapidly due to the initial loading effect and presence of porosities. This effect is more prevalent for the low-density samples as large amount of loosely bound particles are pulled out from the surface. Therefore, more wear debris would be accumulated on the surface of the low-density samples.

Figs. 4.26c and d show the effect of load on the wear profiles of the Fe-7Cr-1Y and Fe-15Cr-1Y samples sintered at 1000°C. It can be observed that wear width and depth increase with

increase in the load for both the alloys. For example, the wear width and depth of the Fe-15Cr-1Y samples are found to gradually increase (i.e. 2.4 µm & 0.29 mm, 3.35 µm & 0.37 mm and 3.7 µm & 0.43 mm) as the load increases from 5N to 20N. Moreover, the wear width and depth for the Fe-15Cr-1Y samples (e.g. 3.7 µm & 0.43 mm) is found to be less than that of the Fe-7Cr-1Y (4.0 µm & 0.47 mm). The possible wear mechanisms of the sintered samples at various loads already discussed in the previous section. Overall, it is concluded that the COF is correlated well with wear width and depth of the corresponding sample.

On the basis of the surface profiles, the wear volume was calculated using Archard's formula (Archard 1953) as follows:

Wear volume (mm^3) = 2π×track radius× track width ×wear depth.

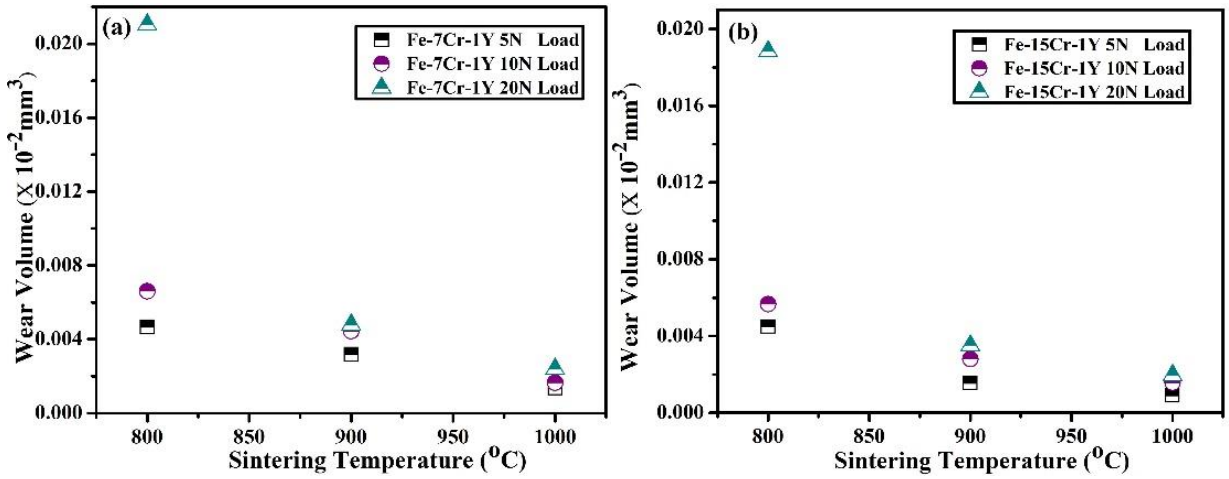

Fig. 4.27: Variation of wear volume of the sintered samples as a function of sintering temperature tested at different loads (a) Fe-7Cr-1Y and (b) Fe-15Cr-1Y.

Figs. 4.27a & b, respectively, demonstrate the wear volume of the sintered samples as a function of sintering temperature. It can be noted that the wear volume decreased with increase in the sintering temperatures for both the alloys. For the samples sintered at 800ºC with 20N load, the wear volume is estimated to be 0.02104 and 0.01883×10^{-2} mm^3, respectively, for the low and high Cr content alloys. The wear volume decreased to only 0.00196 and 0.0024×10^{-2} mm^3, respectively, when the sintering was carried out at 1000ºC. As mentioned earlier that the wear resistance increased due to the increase in the relative sintered density and formation proper bonding between the alloy particles. Also, the Cr and Y played a vital role to improve the wear resistance due to their solid solution strengthening and precipitation hardening effect (Cui et al. 2007; Wang et al., 2003).

Moreover, effect of variation of applied load on the wear volume could be estimated and correlated with the wear profile of the corresponding sample. It can be noted that at any particular sintering temperature (say at 800°C), the wear volume of both the alloys gradually increases with increasing the applied load. For example, the wear volume of the Fe-7Cr-1Y alloy sintered at 800°C is estimated to be 0.0046×10^{-2}, 0.0066×10^{-2} and 0.02104×10^{-2} mm^3, respectively, for the 5, 10 and 20N applied load (Fig. 4.27a). The wear volume is found to decrease to very low level when the sintering temperature was raised to 1000ºC. For example, the wear volume of the Fe-15Cr-1Y samples tested at 5-20N is estimated to be 0.0009×10^{-2}, 0.00157×10^{-2} and 0.00196×10^{-2} mm^3, respectively. Moreover, it can be observed from the Figs. 4.27a & b that at any particular sintering temperature, the wear volume of the Fe-15Cr-1Y sample (sample sintered at 1000°C: 0.00196×10^{-2} mm^3) is relatively less than that of the Fe-7Cr-1Y sample (sample sintered at 1000°C: 0.0024×10^{-2} mm^3) sintered at same condition.

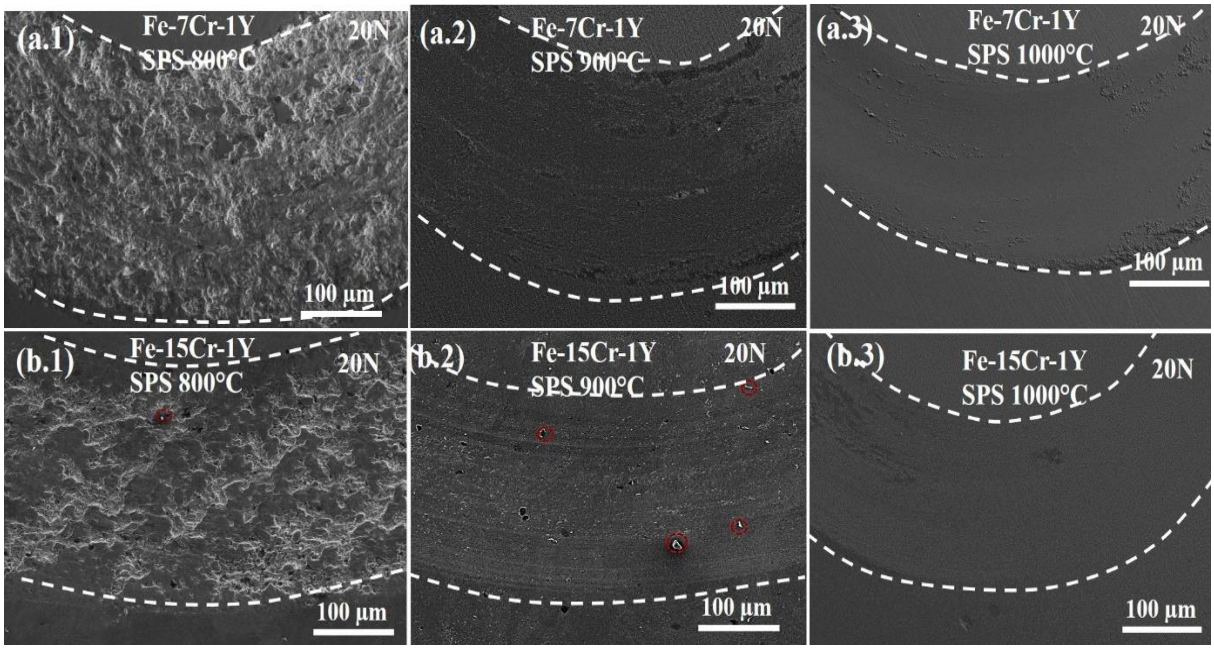

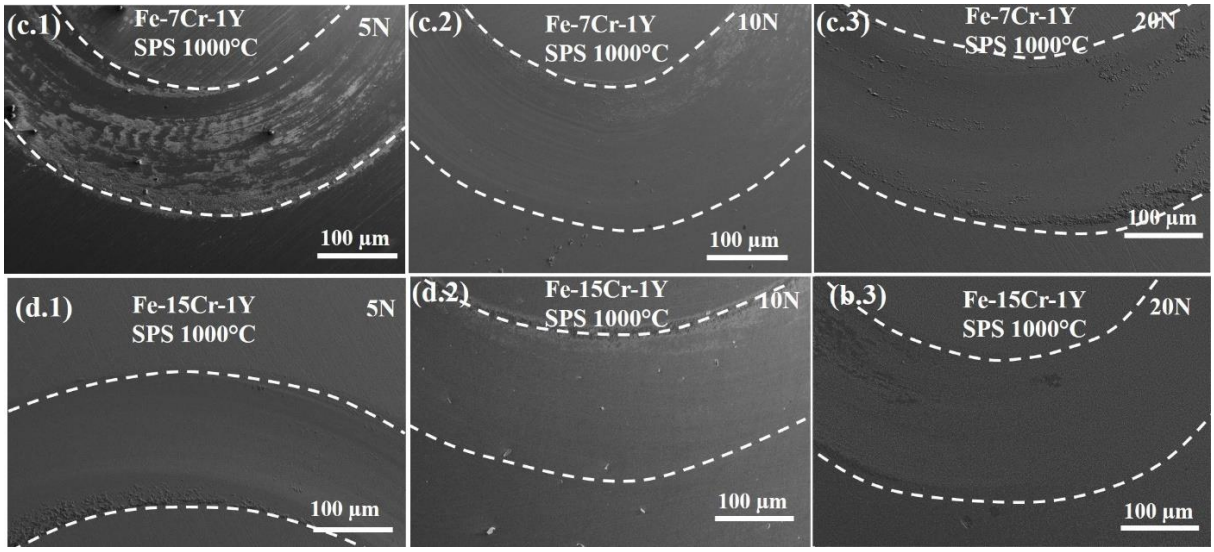

Fig. 4.28: SEM micrographs after wear of the (a) Fe-7Cr-1Y and (b) Fe-15Cr-1Y SPSed samples sintered at different temperatures. (c & d) Effect load on the wear track is shown in figure (c) Fe-7Cr-1Y (d) Fe-15Cr-1Y.

To correlate the coefficient of friction and surface profile after the wear test, the wear track surface of the corresponding sintered sample was analyzed from their FE-SEM images. Figs. 4.28a_1-a_3 & b_1-b_3 show the wear track surfaces of the samples sintered at different temperatures with 20N load. It can be noticed from Figs. 4.28a_1 and b_1 that the wear track surfaces were much wider and a large amount of material wore out from the surface of the low temperature (800ºC) sintered samples of the Fe-7Cr-1Y and Fe-15Cr-1Y alloys with 20N load. A large number of particles are found to pull out from both the surfaces because of improper bonding of the powder particles. On the other hand, the wear track width was found to gradually narrow down (indicating better wear resistance) as the sintering temperature increased. The minimum wear track width is achieved for the high Cr content Fe-15Cr-1Y alloy sintered at 1000°C (Fig. 4.28b_3). The wear track width is found to be highly consistent with the worn depth & width of the corresponding samples. Cui et al. (2007) also reported that addition of Cr in Cu-Pb alloy strengthened the matrix and improved the wear resistance. Addition of 2wt.% Y in a cobalt-base alloy (stellite-6) was reported to increase its wear resistance at room temperature as well as elevated temperatures due to the increased strengthening effect of Y (Wang et al., 2003). They also reported that the worn surface of the Y-free sample showed larger wear track as compared to that of the 2wt.% Y alloy (Wang et al., 2003).

4.2.2.3 Corrosion behavior

Wear resistance and corrosion resistance are extremely important for the Fe-based alloys. Like wear behavior, attention has also been given to improve the corrosion properties of different parts of nuclear power plant, hot acid container, heat exchanger, petrochemical industries and automobiles parts, where corrosion resistance is extremely vital (Baddoo 2008; Gupta et al., 2008; Ningshen et al., 2013; Oka et al., 2007; Peckner et al., 1977; Singh et al., 2018; Sorour et al., 2011) Therefore, the stabilized grade Fe-Cr-Y alloy can also be one of the possible advanced materials for the above applications, if the desired level corrosion resistance is fulfilled. Also, the role of Cr and Y could enlighten on the corrosion and wear mechanisms of SPSed Fe-Cr-Y samples, which could be useful for academic interest and other wear resistance and chemical-related applications. Therefore, the corrosion behavior has been discussed in the following section.

Figs. 4.29a and b, respectively, show the potentiodynamic polarization curves as a function of current density for the Fe-7Cr-1Y and Fe-15Cr-1Y samples sintered at 800, 900 and 1000°C. The potentiodynamic polarization tests were conducted at room temperature with an aerated 3.5wt.% aqueous sodium chloride solution. The corrosion rate (CR) was determined using the following formula (Fontana 2005):

CR (in mil per year) = 0.13 x i_{corr} (μAcm^{-2}) × [eqv. wt. of sample/density of sample]

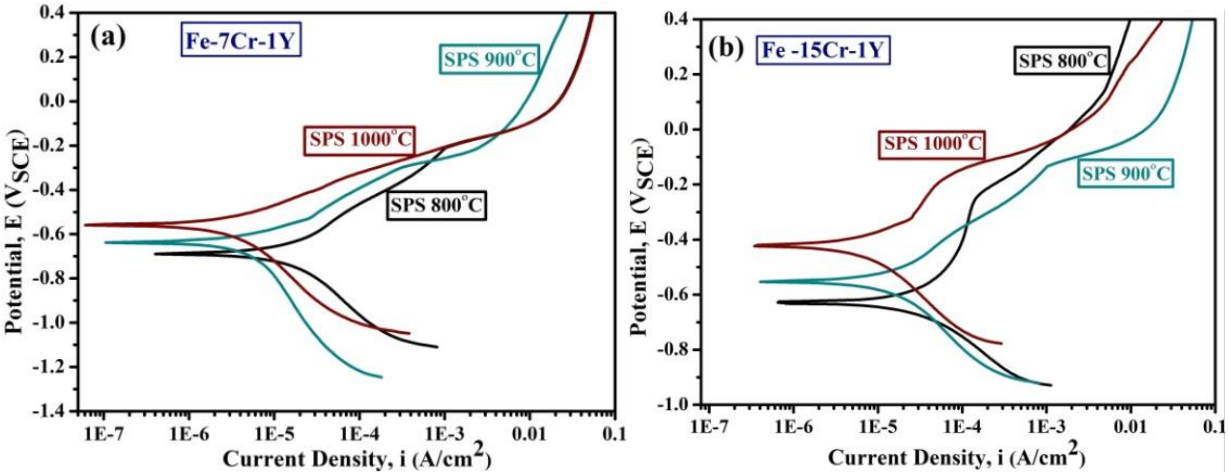

Fig. 4.29: Variation of potentiodynamic polarization curves as a function of current density in 3.5 wt% NaCl solution of (a) Fe-7Cr-1Y and (b) Fe-15Cr-1Y samples sintered at various temperatures.

Tafel extrapolation method was used to calculate the corrosion current density (i_{corr}) and corrosion potential (E_{corr}) from the polarization curves as shown in (Fig. 4.29). The determined

values of current density (icorr), potential (Ecorr) and corrosion density (CR) of the sintered samples are tabulated. for better convenience in Table 4.3.

Composition	**Sintering Temperature (°C)**	**Corrosion results**		
		E_{corr} (V_{SCE})	**I_{corr} (μA/cm^2)**	**CR (mpy)**
Fe-7Cr-1Y	800	-0.691	40.70	18.58
	900	-0.629	23.90	10.9
	1000	-0.590	7.55	3.46
Fe-15Cr-1Y	800	-0.618	29.10	13.29
	900	-0.586	14.20	8.52
	1000	-0.456	7.52	3.43

It can be noticed from Table 4.3 (as well as from Fig. 4.29) that the corrosion resistance gradually improved with increase in the sintering temperature for both the alloys. The improvement of the corrosion resistance for the SPSed (1000°C) sample of the Fe-15Cr-1Y alloy could be ascertained from the corresponding values of E_{corr}, i_{corr} and CR values (Table 4.3). For the Fe-7Cr-1Y alloy sintered at 800°C, the estimated E_{corr}, i_{corr} and corrosion rate are found to be -0.691 V_{SCE}, 40.70 μA/cm^2 and 18.58 mpy, respectively. Further, when the sample was sintered at 1000°C, the corresponding values were found to be nobler (i.e. -0.590 V_{SCE}, 7.55 μA/cm^2 and 3.46 mpy, respectively, (Fig. 4.29a) as compared to the sample sintered at 800°C. The CR of the SPSed sample (sintered at 1000°C) is quite low (only 3.43 mpy) in comparison to that (13.29 mpy) of the sample sintered at 800°C (Fig. 10b). Moreover, the corrosion resistance is found to be better for the Fe-15Cr-1Y alloy as compared to that of the Fe-7Cr-1Y composition (at both the sintering temperatures). For example, the CR of the Fe-15Cr-1Y alloy sintered at 1000°C is only 3.43 mpy as compared to 3.46 mpy for the Fe-7Cr-1Y alloy sintered at the same temperature. The improvement of the corrosion resistance can be accomplished to the improvement of the densification percentage and presence of a large amount of noble Cr content in the Fe-15Cr-1Y alloy.

Overall, it is observed that the Fe-7Cr-1Y and Fe-15Cr-1Y alloys sintered at 1000°C showed the maximum densification and hardness values. It clearly indicated that Fe-15Cr-1Y sample sintered at 1000°C showed high corrosion resistance due to the presence of less porosity as compared to the other sintered samples. Guo et al. (2014) also observed the similar corrosion behavior for the sintered Ti-Nb24-Zr4-Sn7.9 samples. The sample of lower density always contains a high level of interconnected porosities. When sintering temperature increase, the

density also increases by eliminating the interconnected pores (Guo et al., 2014). Hence, there is less opportunity for the corrosive electrolyte to penetrate into the highly dense sample thereby increasing the corrosion resistance. It is known that when the porosities in the sintered samples are filled up with corrosive medium, it forms stagnation in the pores, leading to crevice corrosion (Guo et al., 2014). Li et al. (2016) investigated that in the Fe-xCr-3.5Mo-5Ni-10P-4C-4B-2.5Si alloy, an increase in the Cr content increased its thermal stability and corrosion resistance significantly. They have also explained that 4at.% of Cr was very effective in improving the corrosion resistance of the alloy in 3.5wt.% NaCl solution at room temperature. Wang et al. (2008) reported that the addition of 2at.% yttrium to the bulk Fe-Cr-Mo-C-B metallic glass played an important role to have very effective corrosion resistance in 1mol/L of HCl solution. It was explained that addition of yttrium enhanced the formation of passive films susceptible, which improved the corrosion resistance of the bulk metallic glass.

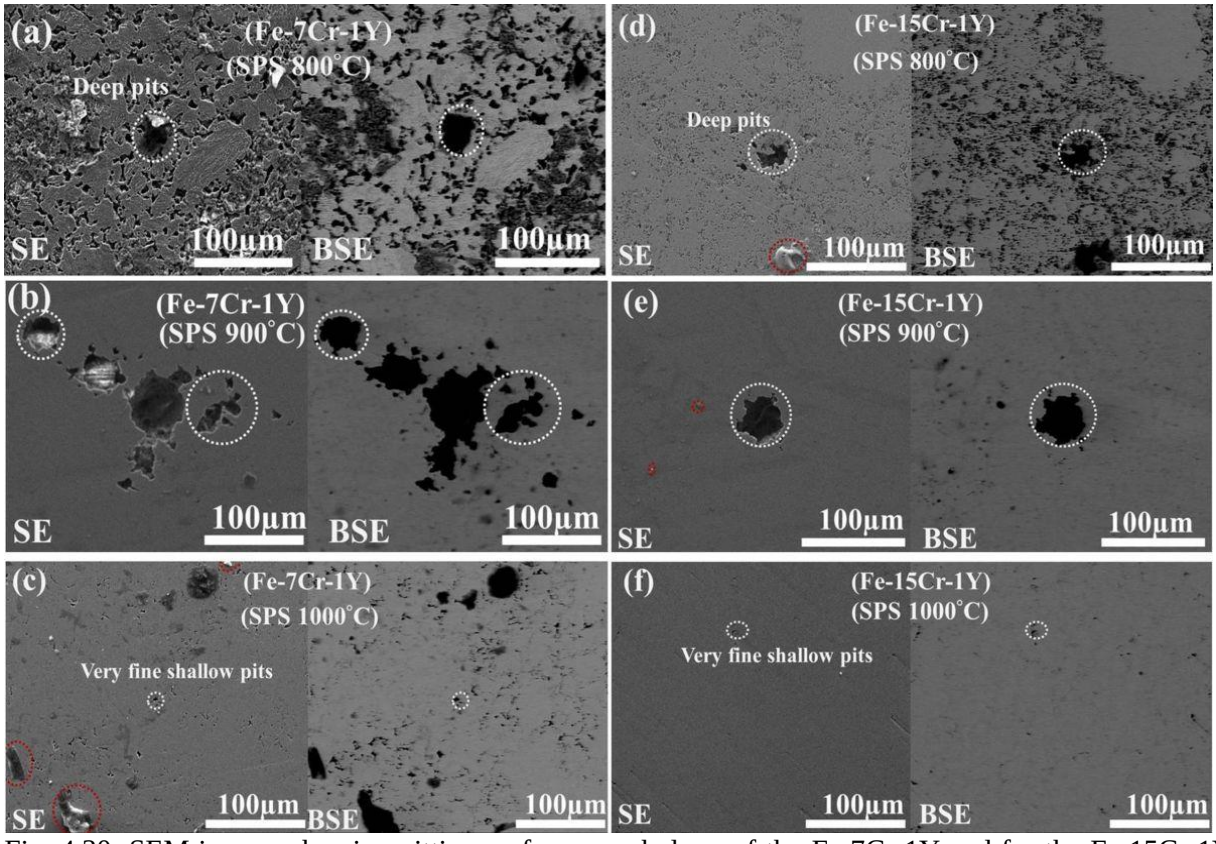

Fig. 4.30: SEM images showing pitting surface morphology of the Fe-7Cr-1Y and for the Fe-15Cr-1Y alloy samples sintered at various temperatures.

Figs. 4.30a-f show SEM images of the SPSed samples sintered at 800, 900 and 1000ºC after the potentiodynamic polarization test. The samples sintered at 800 and 900ºC (Figs. 4.30a and d) revealed deeper pits indicating severe corrosion of the specimens. Further, the samples sintered

at 1000ºC revealed very fine and shallow pits (as can be seen from Figs. 4.30c & f) mainly because of less interconnected porosities present in the sample. Also, the specimens sintered at lower temperatures contained more open and interconnected porosities, which provided more opportunity to form deeper and larger pits. It is also reported that high Cr content alloy leads to excellent corrosion resistance under potentiodynamic polarization test condition (Fontana 2005). It is known that when Cr alloyed with Fe changes the passivating potential of Fe to more active values and drastically lowers the critical current density required for passivation (Fontana 2005). Therefore, at very small i_{corr} values, self-passivation occurs to form an impervious passive film of Cr_2O_3, if the steel contains more than 12% Cr. In the present study also, the high Cr content (14.03 wt.%) alloy (i.e. Fe-15Cr-1Y) showed a better corrosion resistance and less pit formation because of the formation passive impervious film on the highly dense sample (Guo et al., 2014; Li et al., 2016). Addition of yttrium in Fe-Cr-Mo alloy also reported to enhance formation of passive film susceptibly thereby improve the corrosion resistance (Wang et al., 2008).

4.2.2.4 Summary

Bulk size nanocrystalline Fe-7Cr-1Y and Fe-15Cr-1Y alloy samples have been synthesized successfully by mechanical alloying (MA) followed by spark plasma sintering (SPS). The SPS process has been optimized to obtain near full density bulk samples, which show high wear resistance & hardness and improved corrosion resistance. In this regard, the following outcomes could be concluded from the study.

(a) The maximum densification of 97% was achieved for the Fe-15Cr-1Y alloy when sintered at 1000°C. The high level of sintered density is ascribed to the prevalent grain-boundary diffusion at higher sintering temperature and formation of necks due to the deformation at contact points (because of applied pressure).

(b) The TEM and EDSD analysis confirmed that the grain size of the sintered sample depicts a bimodal grain structures: more than 50% grains are within a range of 200 nm and remaining grains are in the range 200 nm-2 µm. The EBSD grain size corroborated well with the TEM grain size.

(c) The Vickers hardness values were found to be quite high (9.27 and 9.58 GPa for the Fe-7Cr-1Y and Fe-15Cr-1Y samples, respectively) even after sintering at 1000ºC. The wear rate of the Fe-15Cr-1Y SPSed sample was estimated to be very low, which was

confirmed from the wear volume ($0.00196 \times 10^{-2} mm^3$) analysis and COF (0.25) of the corresponding sample. The wear resistance was found to consistent well with the SEM images of the worn surface.

(d) The corrosion resistance of the highly dense Fe-15Cr-1Y sample (sintered at 1000ºC) was detected to improve (corrosion rate=3.43 mpy) as compared to that of the other sintered samples (13.29 mpy). The SEM images of the corroded samples also confirmed the same.

4.3 Development of Fe-Cr-Nb alloys

In this section, Nb (up to 1at.%) is added in Fe-7Cr and Fe-15Cr alloys instead of Y to verify the roles of it in the formation of Fe-Cr-Nb solid solutions by MA and on the thermal stability of the Fe-Cr alloy system. On the basis of crystallite size and microhardness data of the as-milled and annealed (600-1200°C) samples of Fe-Cr alloys (Cr=7, 11, 15 & 19 at.%), Fe-7Cr and Fe-15Cr alloys have been selected for further investigation. These two alloys were reproduced in addition with Nb to investigate the effect of Nb on the formation of Fe-Cr-Nb solid solutions and their thermal stability. Fe-7Cr and Fe-15Cr alloys after adding Nb (Nb=0.25, 0.5 and 1 at.%) were reproduced by MA under same conditions of milling. After that, the formation of ternary Fe-Cr-Nb solid solutions has been analyzed for phase evolution, microstructure and their thermal stability. On the basis of the thermal stability of the alloys, some selected alloys were consolidated by SPS. The SPSed samples were further analyzed for the microstructure, mechanical properties and corrosion behavior, which are discussed in the subsequent sections.

4.3.1 Formation of Fe-Cr-Nb alloys by MA and its thermal stability

The Fe-7Cr-Nb and Fe-15Cr-Nb (Nb=0.25, 0.5, 1at.%) alloys were developed by MA for 25 h under the same milling conditions as followed in the Fe-Cr system. Then, phase evolution, their microstructural features and thermal stability have been investigated and discussed in details in the subsequent sections.

4.3.1.1 Effect of Nb on phase analysis of Fe-Cr-Nb alloys and its microstructural analysis

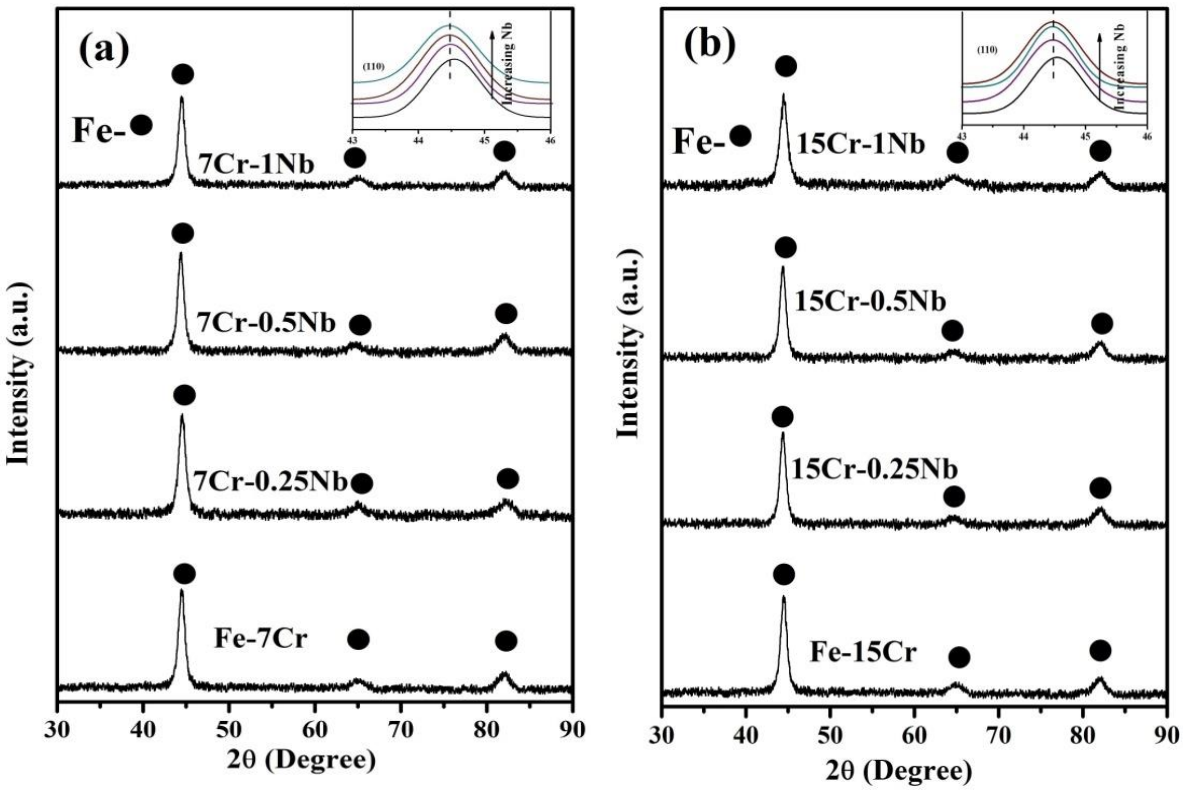

Fig. 4.31: X-ray diffraction patterns showing the alloy formation by mechanical alloying for 25 h; (a) Fe-7Cr-Nb & (b) Fe-15Cr-Nb (Nb=0.25, 0.5 and 1 at.%). Shifting of peak and peak broadening with Nb content are shown in the inset.

Figs. 4.31a and b, respectively, show the XRD patterns of Fe-7Cr-Nb and Fe-15Cr-Nb alloys with varying concentration of Nb (Nb=0.25, 0.5 & 1 at.%). The choice of Cr content in Fe, in the present study, was reported in the earlier section. XRD phase analysis of both the compositions shows that no intermetallic phase(s) or free Cr/Nb is detectable. As per the XRD phase analysis, it is observed that after 25 h of milling the added Nb and Cr atoms completely dissolved in the Fe matrix. It can be clearly observed from 2θ positions (preferably from higher side) that the peak intensity decreased gradually and peak width at full-width half of maximum (FWHM) also increased with increase in the Nb content. This may be due to the crystallite size refinement and accumulation of larger amount of lattice residual strain because of higher amount of Nb present in the solid solution. It can also be observed that with increase in the Nb content, the peak position shifts towards left (lower 2θ position). In the inset of Figs. 4.31a and b illustrated the (Fe-110 reflection) peak broadening, peak shift (towards left) and decrease in the intensity as a variation of Nb concentration. It is known that sensitivity of the XRD analysis has its own limitations to detect the presence of <2wt.% of any secondary phase(s) in the

matrix (Cullity 1978; Suryanarayana et al., 1998). Therefore, it is not possible to confirm only by XRD phase analysis that the added Cr/Nb is completely dissolved in the Fe lattice.

Along with XRD peak analysis, the variation of lattice parameter of solid solutions and TEM diffraction analysis could confirm the solid solubility of Nb and Cr in Fe matrix (TEM analysis is discussed later in this section). It is known that the solution of solute atoms to form a solid solution changes the lattice parameter of the matrix (Cullity 1978; Koch et al., 2008). Therefore, this could be an important tool to correlate solid solubility extension of a solute element in the matrix (Cullity 1978; Koch et al., 2008).

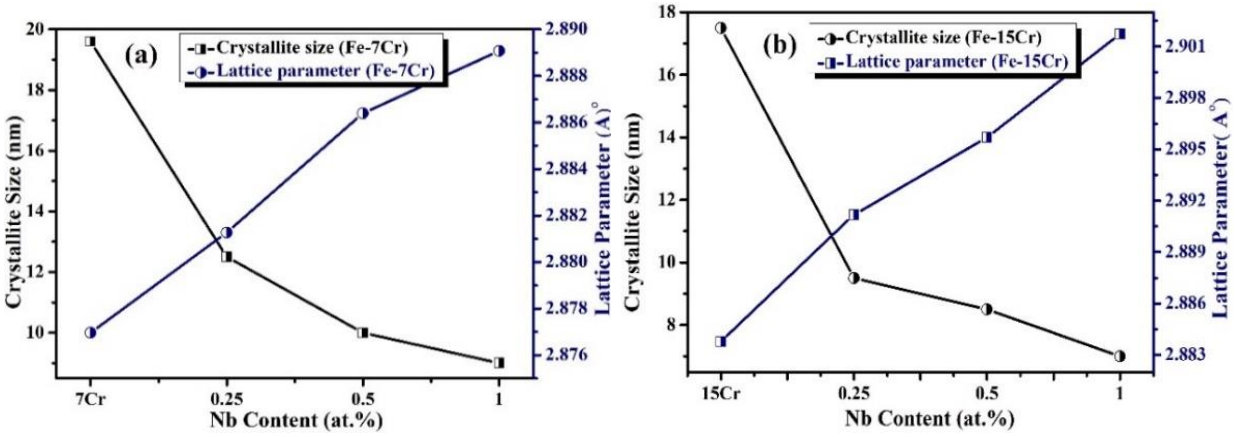

Figs. 4.32a & b: Shows the variation of lattice parameters and crystallite size as a function of Nb content.

Figs. 4.32a and b, respectively, show the variation of the lattice parameter of the Fe-based alloys (a_{Fe}) and crystallite size as a function of Nb concentration of the as-milled Fe-7Cr and Fe-15Cr alloys. Analysis of XRD data was used to estimate the precise lattice parameter (aFe) and crystallite size. Williamson-Hall analysis (Cullity 1978) was used to determine the average crystallite from the XRD peaks of the corresponding sample. The plot between $B_r\cos\theta$ *vs*. $\sin\theta$ is used to exclude the peak broadening due to the lattice residual strain to calculate crystallite size. The average crystallite size decreased with increasing the Nb concentration. The average crystallite size of Fe-7Cr alloy decreased from ~12.5 nm (for 0.25% Nb) to 9 nm which corresponds to 1% Nb addition. The average crystallite size was determined to be ~19.6 nm for Fe-7Cr alloy without any Nb addition.Similar observations were made for the Fe-15Cr alloys where the average crystallite size decreased from ~9.8 nm (for 0.25% Nb) to 7.4 nm for the 1% Nb alloy. The crystallite size of Fe-15Cr alloy without addition of Nb was found to be ~17.5 nm. The lattice parameter (a_{Fe}) was estimated from all the XRD peaks through extrapolation of a_{Fe} *vs*. ($\cos^2\theta/\sin\theta$) plot to $\cos\theta = 0$ (Cullity 1978; Sheibani et al., 2010; Suryanarayana et al.,

1998). The lattice parameter would change when Cr and/or Nb atoms dissolve into the Fe-matrix to form a solid solution (Cullity 1978; Sheibani et al., 2010; Xu et al., 2014). It is to be noted that the lattice parameter (a_{Fe}) of pure Fe is 2.868Å. It can be seen (Fig. 4.32) that the lattice parameter gradually increases with increasing in the Nb concentration. The maximum increase in the lattice parameter (a_{Fe}) was obtained in the Fe-15Cr-1Nb alloy, and the maximum value is found to be 2.901Å as compared to 2.889Å for the Fe-7Cr-1Nb alloy. Therefore, the lattice parameter increased due to the solid solubility of Cr and Nb atoms into the Fe-Matrix.

TEM analysis of the as-milled sample

As the dark field (DF) imaging mode is of high contrast technique as compared to that of the bright field (BF) imaging (Williams et al.,1996), the DF images were recorded to analyze the grain size from the 25 h milled sample.

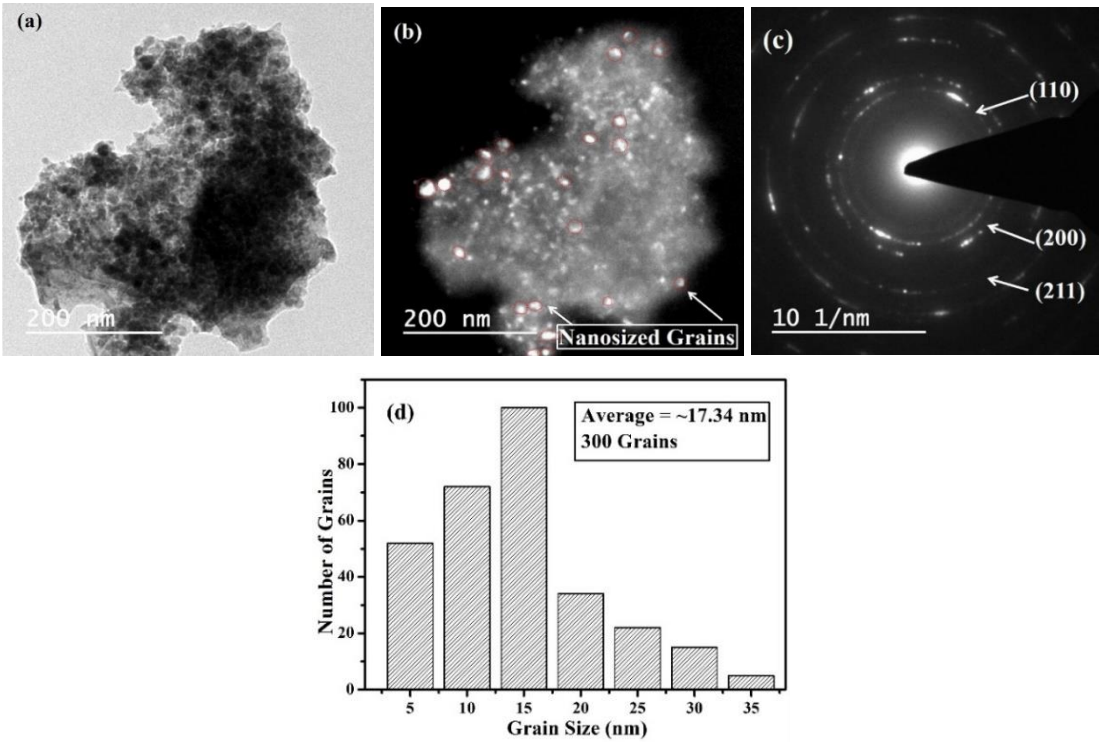

Fig. 4.33: (a) Bright field TEM images, (b) Dark field TEM image (c) selected area diffraction pattern of the 25 h milled sample for the Fe-15Cr-1Nb alloy. (d) Statistical distribution of grains obtained from dark field images.

Fig. 4.33a & b, respectively, shows the BF and DF TEM images for the as-milled Fe-15Cr-1Nb sample. Fig. 4.33a & b clearly shows that the TEM grain size is well within the nanometric range (<100 nm). It can be clearly observed from the SAED pattern (Fig. 4.33c) that all the

major peaks corresponding to the Fe-based alloy, i.e. (110), (220) and (211) are present (Muthaiah et al., 2016; Williams et al., 1996). The presence of continuous rings clearly shows that the grain sizes are within the nanometric level. Moreover, analysis of the SAED patterns does not show any other ring/spot corresponds to elemental Nb/Cr or any intermetallic phase. Therefore, it can be concluded again that a complete solid solution of Fe-15Cr-1Nb has been formed by MA for 25 h. The XRD analysis and variation of a_{Fe} also confirmed that the Cr and Nb atoms are completely dissolved in the Fe matrix after 25 h MA to form a solid solution. The average grain size has been determined from TEM images (as one is shown in Fig. 4.33b) using the statistical distribution of at least 300 grains. The grain size distribution is shown in Fig. 4.33c and the average grain size is determined to be ~17 nm. The average grain size determined from TEM study correlated well with the XRD crystallite size of the corresponding sample (Fig. 4.32b).

4.3.1.2 Thermodynamic analysis

Further, the Gibbs free energy change as per the Toop's model (Miedema et al. 1980a; Niessen et al., 1988) is used to analyse the formation of the ternary Fe-Cr-Nb solid solutions by MA. The analysis of Miedema's semi-empirical model was used to calculate the Gibbs energy change for the binary solid solutions. And these Gibbs free energies were used to calculate the Gibbs energy change for the ternary alloys as per Toop's model. The details of the Toop's model, Miedema's semi-empirical model and the Gibbs free energy change within the materials using analytical equations are discussed in the earlier section 4.2.1.2.

Table 4.4: Thermodynamic analysis parameters for the binary systems as per Miedema's semi-empirical model for Fe-Nb, Cr-Nb and Fe-Cr alloys (Miedema et al. 1980a; Niessen et al., 1988).

Parameters	**Fe**	**Cr**	**Nb**
$n_{ws}^{1/3}$ (cm^{-1})	1.77	1.73	1.64
V_m ($cm^3\ mol^{-1}$)	7.09	7.12	10.83
ϕ (V)	4.5	4.65	4.05
K (* 10^{10} Nm^{-2})	17	16.02	17
G (* 10^{10} Nm^{-2})	8.2	11.53	3.8
T (K)	1811	2130	2477

The change in enthalpy (ΔH), entropy (ΔS) and Gibbs free energy (ΔG) to form stable Fe-Cr and metastable Fe-Nb & Cr-Nb solid solutions at room temperature have been calculated using the formulae as per Toop's and Miedema's models (discussed in the earlier section 4.2.1.2.) and the related graphs are shown in Figs. 4.34a-c.

For the Fe-Cr binary alloy system, the change in the total Gibbs free energy is found to be negative. It is significant that the formation of Fe-Cr solid solution at room temperature is a spontaneous process (i.e. $\Delta G<0$) and there is no need of any non-equilibrium technique to prepare Fe-Cr solid solution. According to the Hume-Rothey's rule, the atomic size difference is very small between Fe (0.126 nm) and Cr (0.128 nm) atoms and thereby, it easily forms a substitutional solid solution under equilibrium conditions (Callister et al., 2007). The change in the total Gibbs free energy for the binary systems of Fe-Nb and Cr-Nb alloys is found to be positive (i.e. $\Delta G>0$ non-spontaneous reactions) in the entire compositional scale, and there is no possibility to form a disordered solid solution under equilibrium condition (Rafiei et al., 2013). Hence, the formation of disordered solid solutions for Fe-Nb and Cr-Nb systems cannot be developed by any equilibrium processing approach. Therefore, non-equilibrium processing methods such as mechanical alloying (Guang et al., 2006; Rafiei et al., 2013; Salemi et al., 2016) can be one possible way to produce disordered solid solutions of Fe-Cr-Nb.

The enthalpy contribution due to chemical reaction, $\Delta H_{chemical}$ is observed to be partially more dominant (positive) for the Fe-Nb and Cr-Nb systems due to the small differences in the work function and electron density of the constituent elements. Therefore, there is almost no chance for Nb atoms to interact chemically with the Fe-Cr alloys to form any intermetallic phase. Meanwhile, the elastic contribution is found to be more positive than the chemical part in the Fe-Nb and Cr-Nb systems as the atomic size difference between Fe (0.126 nm)/Nb (0.147 nm) and Cr (0.128 nm)/Nb (0.147 nm) is large.

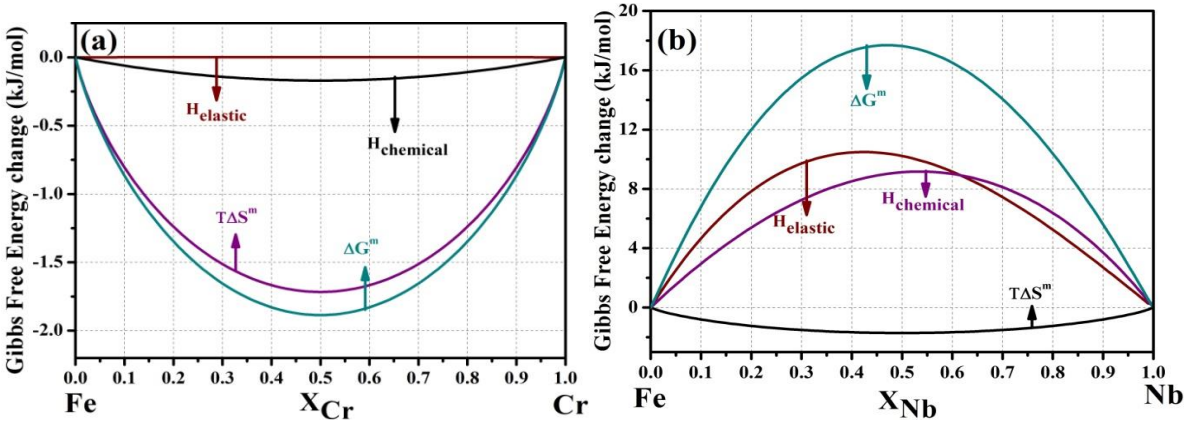

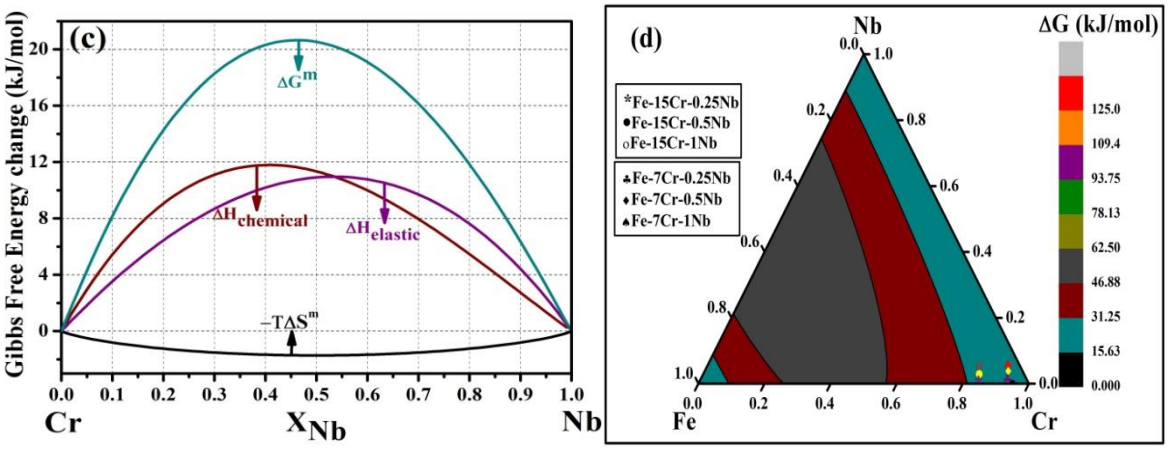

Fig. 4.34: Enthalpy, entropy and Gibbs free energy change for the formation of stable/metastable solid solution in (a) Fe-Cr (b) Fe-Nb (c) Cr-Nb, and (d) Fe-Cr-Nb ternary system.

Fig. 4.34d shows the change in Gibbs free energy required in the formation of solid solutions in Fe-Cr-Nb ternary systems. According to the Toop's model, the change in the Gibbs free energy is determined to be positive for the Fe-7Cr-(0.25, 0.5 and 1) Nb and Fe-15Cr-(0.25, 0.5 and 1) Nb compositions. That means, to form a disordered solid, the excess free energy has to be supplied to the system by a nonequilibrium method and it must be stored within the processed materials. The excess energy could be added to the system mainly in the form of grain boundary energy and dislocation strain energy. The calculated Gibbs free energy values for the Fe-Cr-Nb ternary alloy as per Toop's model and experimental calculations are shown in Table 4.5.

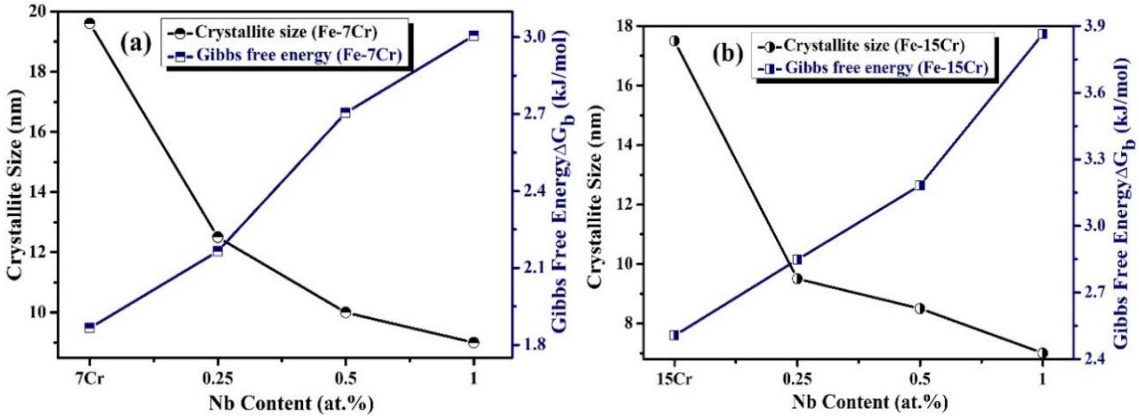

Fig. 4.35: Changes in crystallite size and Gibbs free energy (ΔG_b) as a function of Nb concentration (a) Fe-7Cr and (b) Fe-15Cr.

Figs. 4.35a and b, respectively show the changes in crystallite size and Gibbs free energy (ΔG_b) as a function of Nb concentration for the Fe-7Cr and Fe-15Cr alloys. The average crystallite size decreases with an increase in the Nb concentration as discussed in the earlier section (Figs.

4.32a and b). The surface free energy, ΔG_b, is found to increase because of the crystallite size refinement which is due to an increase in the total surface area. The ΔG_b was estimated by the (Eq.4.10) explained in the earlier section 4.2.1.2. It can be observed from the Figs. 4.35a and b (as-milled condition) that the ΔG_b increased from 1.86 kJ/mol for the Fe-7Cr alloy to 3.00 kJ/mol due to 1at.% Nb addition in the same composition. Similarly, the ΔG_b increased from 2.50 kJ/mol for the Fe-15Cr alloy to 3.86 kJ/mol in the Fe-15Cr-1Nb alloy. The increase in ΔG_b occurs not only due to the addition of Nb but also because of Cr solution. Further, a better grain size refinement influenced by more amount of Cr atoms in the solid solution of Fe is indicated with the increase in the more surface free energy in Fe-15Cr-1Nb alloy.

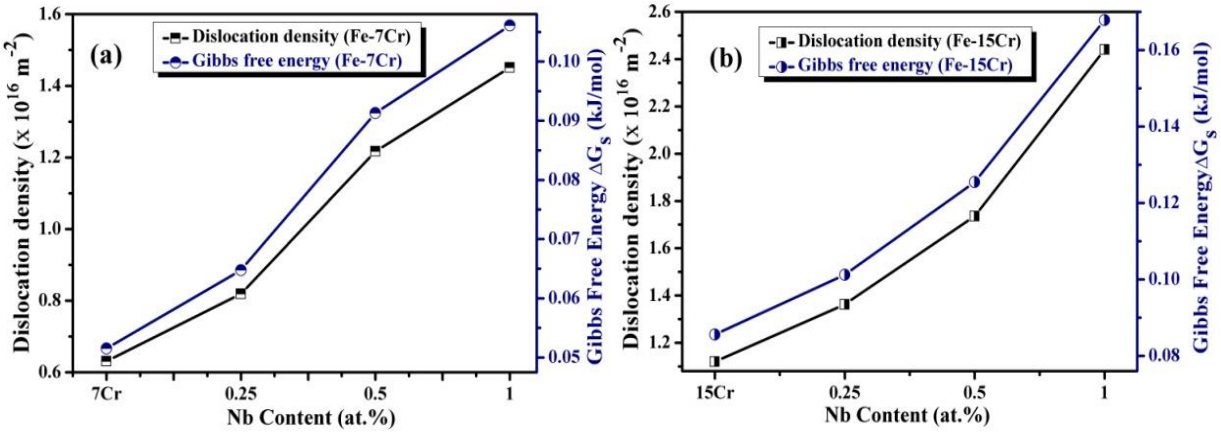

Figs. 4.36a & b: shows change in Gibbs free energy, (ΔG_s) due to increase in dislocation density as a function Nb content for the Fe-7Cr-Nb and Fe-15Cr-Nb alloys.

Figs. 4.36a and b show the variation of change in the Gibbs free energy because of the dislocation density (ΔG_s) for Fe-7Cr and Fe-15Cr alloys. It can be observed that the ΔG_s increased to 0.106 kJ/mol corresponding to a dislocation density of $\rho = 1.450 \times 10^{16}$ m^{-2} for the Fe-7Cr-1Nb sample in the as-milled condition from a value of 0.051 kJ/mol ($\rho = 0.630 \times 10^{16}$ m^{-2}) for Fe-7Cr sample. The maximum value of the ΔG_s is found to be 0.167 kJ/mol ($\rho = 2.441 \times 10^{16}$ m^{-2}) for the Fe-15Cr-1Nb alloy in the as-milled condition. Table 4.5 shows that the total Gibbs free energy stored, i.e. $\Delta G_T = \Delta G_b + \Delta G_s$, is determined to be 4.03 kJ/mol in the disordered solid solution of Fe-15Cr-1Nb. According to the Toop's model, the change in the theoretical value of Gibbs free energy, ΔG_{Toop} (discussed in the earlier section 4.2.1.2.) is 3.58 kJ/mol. It can be observed from Table 4.5 that the value of ΔG_T is higher than that of ΔG_{Toop} for all the Fe-Cr-Nb compositions studied in the current investigation. Therefore, as the resultant ΔG_T, is higher than ΔG_{Toop} in the as-milled condition, it can be concluded that the Fe-7Cr-1Nb

and Fe-15Cr-1Nb disordered solid solutions could be produced by MA according to the Toop's model. Earlier, the XRD and TEM diffraction analysis also confirmed the same. The following assumptions were made in the above calculation: (i) The lattice microstrain, crystallite size and dislocation density estimated from the XRD analysis may have some calculation errors. (ii) The change in enthalpy due to the structural contribution ($\Delta S_{structural}$) from Nb was avoided as it showed a very small positive value.

Table 4.5: The changes in total Gibbs free energy ($\Delta G_T = \Delta G_b + \Delta G_s$) due to the decrease in the crystallite size and increase in the dislocation density which was compared with that obtained from Toop's model.

Alloy (all in at.%)	ΔG_b **(kJ/mol)**	ΔG_s **(kJ/mol)**	$\Delta G_T = \Delta G_b + \Delta G_s$ **(kJ/mol)**	ΔG **Toop (kJ/mol)**
Fe-7Cr-0.25Nb	2.16	0.064	2.22	1.35
Fe-7Cr-0.5Nb	2.70	0.091	2.79	1.88
Fe-7Cr-1Nb	3.00	0.106	3.11	2.80
Fe-15Cr-0.25Nb	2.84	0.101	2.94	1.89
Fe-15Cr-0.5Nb	3.18	0.125	3.30	2.65
Fe-15Cr-1Nb	3.86	0.167	4.03	3.79

4.3.1.3 Thermal stability and mechanical properties

The thermal stability is extremely important for any structural material during its service condition, i.e. service temperature, loading condition etc. The thermal stability of the component completely depends on the stability of its microstructure under the given service conditions, i.e. the component under service should not undergo plastic deformation, grain coarsening or any kind of phase transformation. The mechanical properties totally depend on the thermal stability of the component. If there is any alteration of the microstructure, the mechanical properties will be deteriorated; for example, yield strength would be decreased if the initial grain size of the component increases as per Hall-Petch relationship. Therefore, thermal stabilization of the microstructure is extremely important for any structural application. Thermal stabilization involves the second phase particle pinning (Zener pinning), solute drag and solute segregation on the grain boundary. The annealing of the Fe-7Cr-1Nb and Fe-15Cr-1Nb alloy samples was carried out in batches for 1 h from 600-1200°C under controlled Ar+2% H_2 atm and after that the XRD data were recorded.

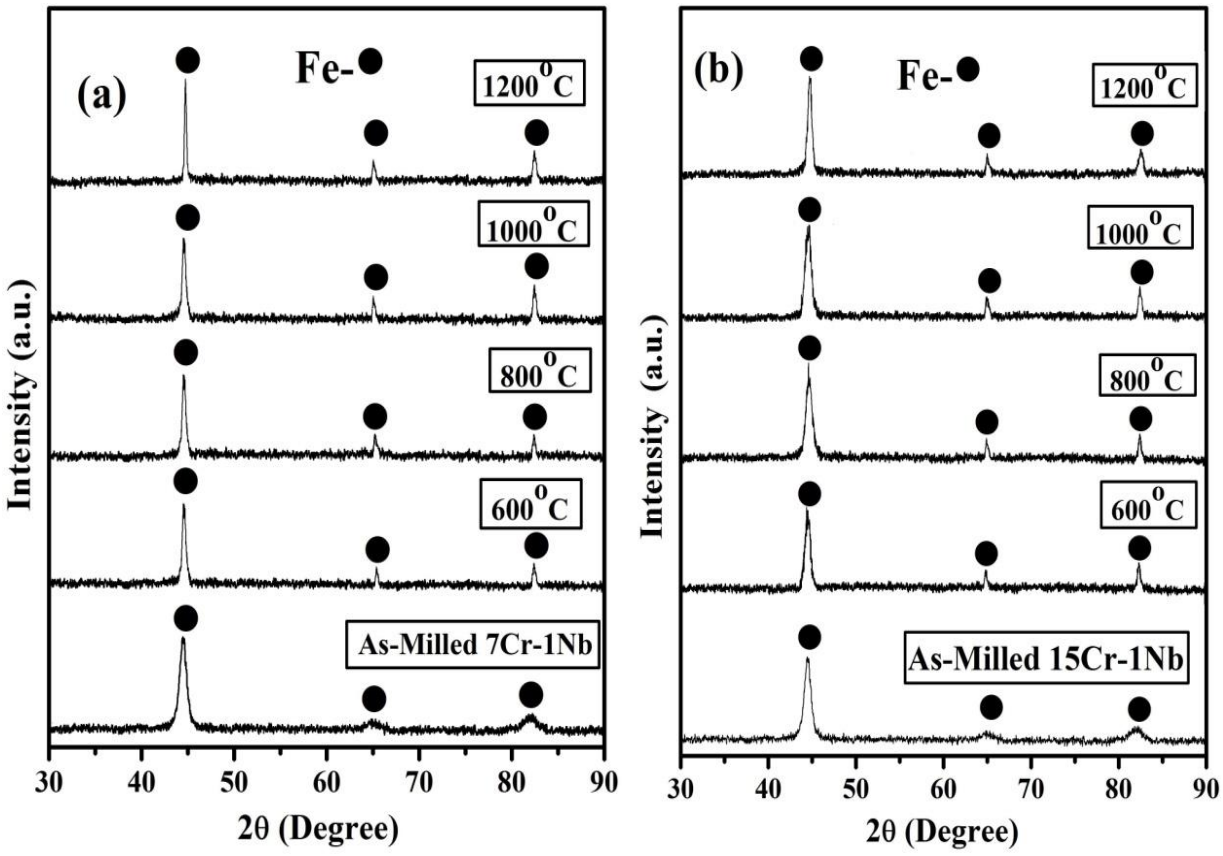

Figs. 4.37 a & b: XRD patterns of annealed samples up to 1200°C for the composition of (a) Fe-7Cr-1Nb and (b) Fe-15Cr-1Nb.

Figs. 4.37a and b, respectively, show the XRD patterns analysis of the annealed samples of Fe-7Cr-1Nb and Fe-15Cr-1Nb compositions. It clearly showed that the peak width decreased and peak intensity increased with increasing the annealing temperature (e.g. Fe-110 reflection). It can be observed that any peak related to Cr or Nb is not observable from the XRD patterns of any samples even after annealing at 1200°C. Moreover, formation of any intermetallic phase(s) is not revealed from the XRD phase analysis. It indicates that the Fe-Cr-Nb solid solutions did not decompose (maintained solid solubility) after the annealing treatment.

Figs. 4.38a & b show the variation in the average crystallite size of the Fe-7Cr-Nb and Fe-15Cr-Nb samples annealed at different temperatures. It can be observed that the crystallite size of both the compositions has almost similar trends of variation at different annealing temperatures. Fe-Cr alloys without Nb content showed a typical grain coarsening tendency (i.e. rapid grain growth) at an annealing temperature of 800°C and above. The crystallite size of Fe-7Cr-1Nb and Fe-15Cr-1Nb alloys in the as-milled condition was found to be 9 and 7.4 nm, respectively, as mentioned earlier (Figs. 4.32a and b).

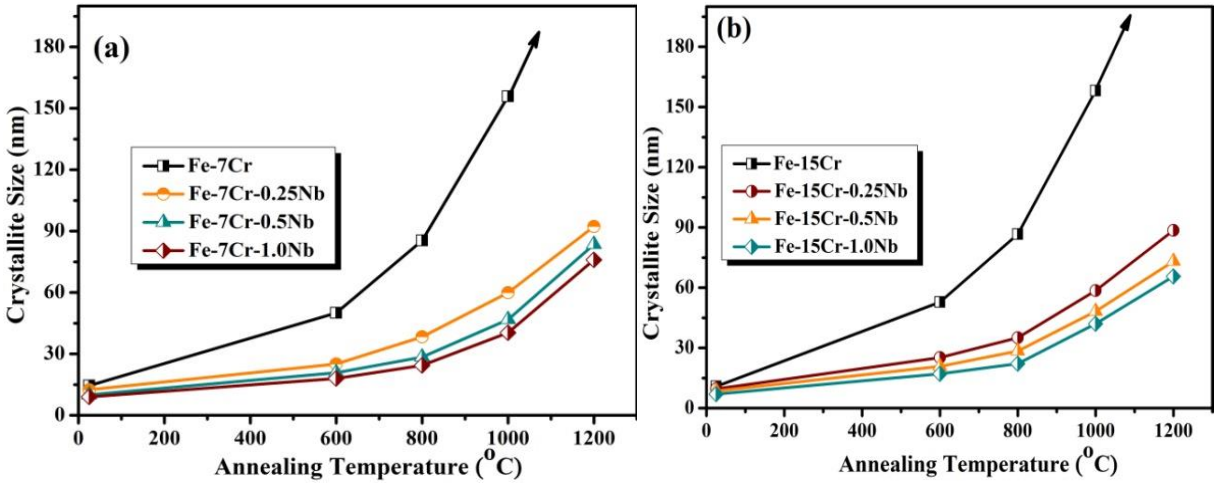

Figs. 4.38a & b: Variation of the crystallite size annealed at different temperatures for the alloys: (a) Fe-7Cr-1Nb (b) Fe-15Cr-1Nb.

When the samples of Fe-7Cr-1Nb and Fe-15Cr-1Nb were annealed at 600°C, the crystallite size increased to 18 and 17 nm, respectively. The crystallite size increased slowly and stabilized at an annealing temperature of 1000°C (i.e. exhibited an excellent thermal stability). After the annealing at 1000°C, the corresponding crystallite size was found to be only 41 and 42 nm, respectively, for the Fe-7Cr and Fe-15Cr alloys with 1% Nb. It shows that Nb provides a better effect on the stabilization of Fe-Cr alloys which retained the grain size below 50 nm even after annealing at 1000°C. Mula et al. (2012) studied the effect of Nb addition (up to 16 at.%) in Cu and concluded that better thermal stability (<100 nm) was achieved when annealed up to 800°C. The segregation of oversize solute atoms, especially Nb along the nanocrystalline grain boundaries (by thermodynamic approach) played a vital role to stabilize the Fe-Cr matrix grains within 50 nm.

TEM analysis of the annealed sample

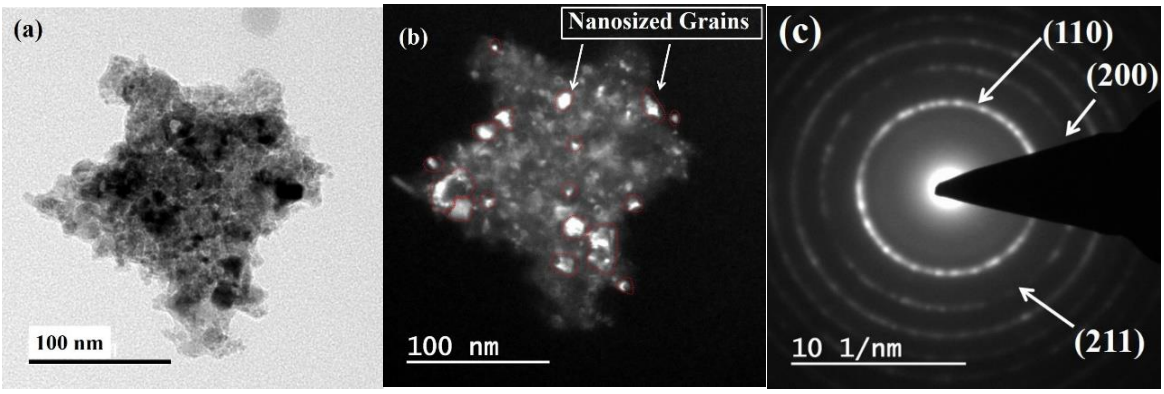

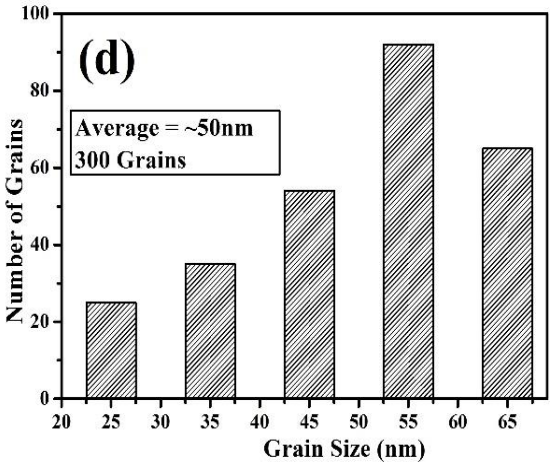

Fig. 4.39: (a) BF TEM image (b) DF TEM image (c) SAED pattern for the Fe-15Cr-1Nb alloy annealed at 1000˚C. (d) Statistical distribution of grains obtained from the dark field images as one shown in Fig. 4.39a & b.

Figs. 4.39a, b & c, respectively, show the BF and DF TEM micrographs and its diffraction pattern of the selected area of the Fe-15Cr-1Nb alloy annealed at 1000°C. It can be observed from Figs. 4.39a & b that the individual grain sizes are well within the nanometric scale (<100 nm). The SAED pattern (Fig. 4.39c) shows the presences of continuous rings, which confirm that the grain sizes are extremely fine and lower range of nanometer level. Moreover, analysis of the SAED pattern does not reveal any other ring/spot corresponds to Nb/Cr or any intermetallic phase. It can be observed that all the major peaks of Fe (110), (220) and (211) are clearly visible from the SAED patterns. The XRD analysis also did not show any phase other than the Fe (Figs. 4.37a and b). The average grain size was assessed from the DF TEM images (as one shown in Fig. 4.39b) using statistical distribution of 300 grains. The statistical grain size distribution is as shown in Fig. 4.39d and the average grain size is calculated to be ~50 nm. The TEM grain size is found to corroborate well with the XRD crystallite size of the same sample (Fig. 4.38b).

Figs. 4.40a & b show the variation in the microhardness values as a function of the annealing temperature for the Fe-7Cr-Nb and Fe-15Cr-Nb alloys, respectively. Fig. 4.40c depicted the images where Vickers microhardness values were measured on individual particles within the compacts. To prevent the influences of the indentation plastic zone on particle boundaries, the indentations were made in the middle regions of larger size particles. The microhardness value of the as-milled Fe-7Cr-1Nb sample is estimated to be 10.2 GPa and the same is measured to be 10.4 GPa for Fe-15Cr-1Nb alloy in the as-milled condition.

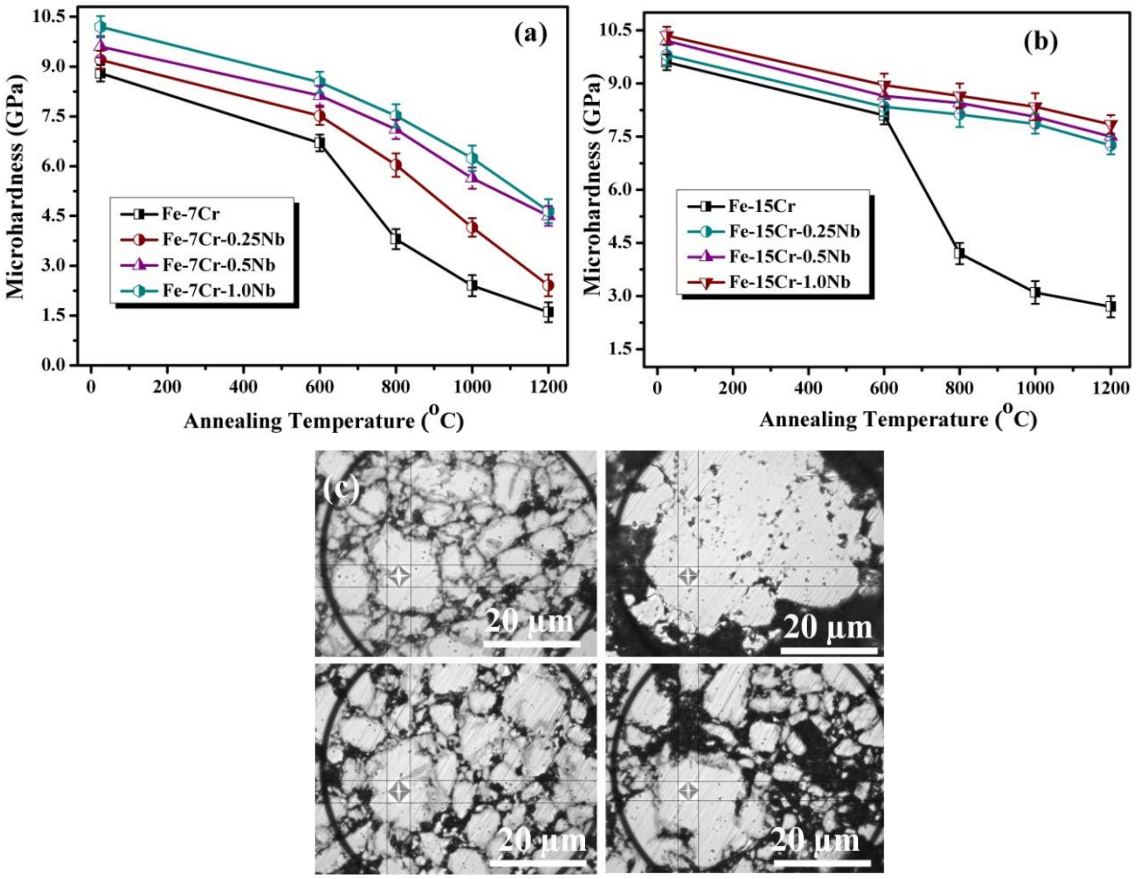

Fig. 4.40: (a, b) variation of microhardness values of Fe-Cr-Nb alloys in as-milled and annealed conditions at various temperatures, (c) Indentation marks made during microhardness measurements within the particles**.**

The microhardness value is found to decrease with increase in the annealing temperature for both the alloys; but the rate of decrease is more for the Fe-7Cr-1Nb alloy (Fig. 4.40a) as compared to that of the Fe-15Cr-1Nb composition (Fig. 4.40b). The slow deterioration of the hardness clearly dictates that the Fe-15Cr-1Nb alloy exhibited enhanced thermal stability compared to that of the Fe-7Cr-1Nb alloy. The better thermal stability could be ascribed to the complete dissolution of more amount of Cr along with 1% Nb in the Fe-matrix. Moreover, although no oxide formation is detected through XRD and the TEM analysis, formation of extremely fine nanoparticles of Cr/Nb oxides might have played an important role to have such high thermal stability and hardness (Xu et al., 2014). Xu et al. (2015) also reported that formation of ~4 nm HfO_2 particles in Fe-14Cr-Hf alloys produced effective kinetic pinning to stabilize the ferritic nanocrystalline structure. Formation of infinitesimal oxide particles could be detected through high-resolution TEM analysis. It can be observed that almost all the Fe-

15Cr-Nb alloys have stabilized at around 600°C; whereas, the hardness of the Fe-7Cr-xNb alloys decreases continuously with increase in the annealing temperature. For illustration, the microhardness value of the Fe-15Cr-1Nb alloy is measured to be ~9.0 and 8.3 GPa, respectively, when annealed at 600°C and 1000°C. On the other hand, the hardness value of the Fe-7Cr-1Nb is only 6.2 GPa after annealing at 1000°C as compared to 8.5 GPa after annealing at 600°C. It can be noted (from Fig. 4.38) that the XRD crystallite sizes for both the alloys were retained almost same at a particular annealing temperature, i.e. ~17 nm at 600°C and 42 nm at 1000°C. Therefore, the extra hardening of the Fe-15Cr-1Nb alloy (e.g. 2 GPa at 1000°C) can be ascribed to the solid solution strengthening of the extra Cr in Fe-based disordered solid solution. It can also be noticed that due to 0.25% Nb addition, Fe-15Cr alloy showed excellent thermal stability (7.8 GPa hardness); whereas with the addition of 1% Nb to Fe-7Cr alloy did not provide enough thermal stability (only 6.2 GPa hardness at 1000°C). From the above explanation, it can be established that in presence of a small amount of Nb, Cr content played the important part in the stabilization of ternary alloys. Effect of Nb addition and better thermal stability of Cu-Nb alloys were also observed by Mula et al. (2012); Ray et al., (2012). Li et al. (2014) reported that Fe-14Cr alloy with up to 4 at.% Hf maintained a nanoscale grain size (<40 nm) even at 1000°C, and the resultant measured microhardness value was 5.2 GPa. As discussed earlier that the thermodynamic approach of solute atom segregation along the grain boundary is mostly accountable to attain such higher hardness values (i.e. thermal stability).

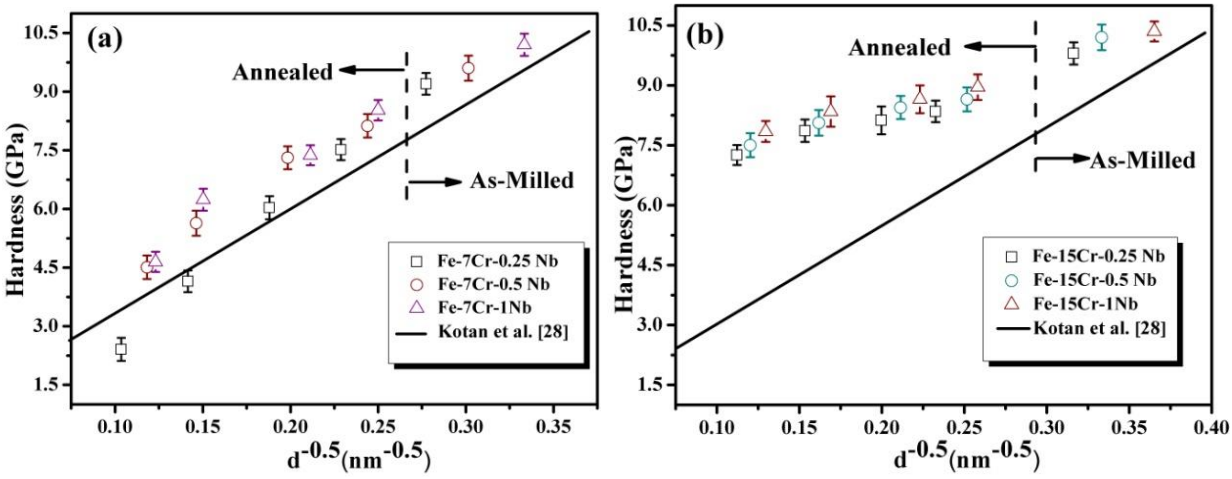

Fig. 4.41: (a,b) Hall-Petch analysis of the microhardness and grain size of the as-milled and annealed samples of the Fe-7Cr-Nb and Fe-15Cr-Nb alloys. The straight line indicates the Hall-Petch effect of pure iron.

Hall-Petch plots (as shown in Figs. 4.41a and b) have been made to study the effect of grain size on the strengthening of the Fe-Cr-Nb alloys. The same has been correlated with the classical Hall-Petch relationship investigated for the pure Fe in Kotan et al., (2012); Shen et al. (2007). For all the compositions, the effect solid solution strengthening of Cr/Nb atoms can be confirmed from the variation of the classical Hall-Petch relation of the pure Fe. It can also be noticed from Figs. 4.41a and b that the as-milled samples of Fe-15Cr-Nb showed bit extra hardening effect (as indicated by the dotted line on the right-hand side) than that of the Fe-7Cr-Nb. The additional hardening of the Fe-15Cr-Nb alloys is mainly due to the extra Cr dissolved in the Fe matrix. The XRD analysis, variation of lattice parameter, TEM diffraction analysis and changes in Gibbs free energy calculated using Toop's model confirmed the formation of Fe-Cr-Nb solid solutions by MA for 25 h. The dotted lines on the left-hand side in Figs. 4.41a and b clearly indicate that strengthening effect in Fe-7Cr-Nb alloys gradually get lost with increasing the annealing temperature; whereas, the Fe-15Cr-Nb alloys exhibit a significant stability of the strength. Though with increasing annealing temperature, there was a minor decrease in the microhardness values, the retained strengthening effect is still much higher as compared to that of the Fe-7Cr-Nb alloys. For example, the Fe-15Cr-0.25Nb alloy showed higher stability (hardness=7.8 GPa) than the Fe-7Cr-1Nb (hardness=6.2 GPa), both annealed at 1000°C. This study again confirmed that, in presence of Nb, the Cr content played a pivotal role to obtain such high thermal stability in the Fe-Cr-Nb ternary alloy system.

4.3.1.4 Estimation of ultimate tensile strength and yield strength

Cahoon et al., (1971) further improved the relation of ultimate tensile strength (UTS) by commutating equation (4.14) as

$$UTS = \left(\frac{H}{2.9}\right)\left(\frac{n}{0.217}\right)^{n} \tag{4.14}$$

where, H is the Vickers hardness and n is the strain-hardening coefficient. Cahoon et al. (1971) proposed a relationship to estimate the yield strength of metals (steels, Cu & Al) from simple hardness measurement by following equation (4.15).

$$YS = \left(\frac{H}{3}\right)\left(\frac{1}{10}\right)^{n} \tag{4.15}$$

It can be noticed that all the proposed methods require the consideration of strain-hardening coefficient, which can be directly determined from the uniaxial tensile or compression test and indirectly through Meyer's hardness measurement and empirical relations as proposed in (Dieter 1961; Moteff et al.,1975).

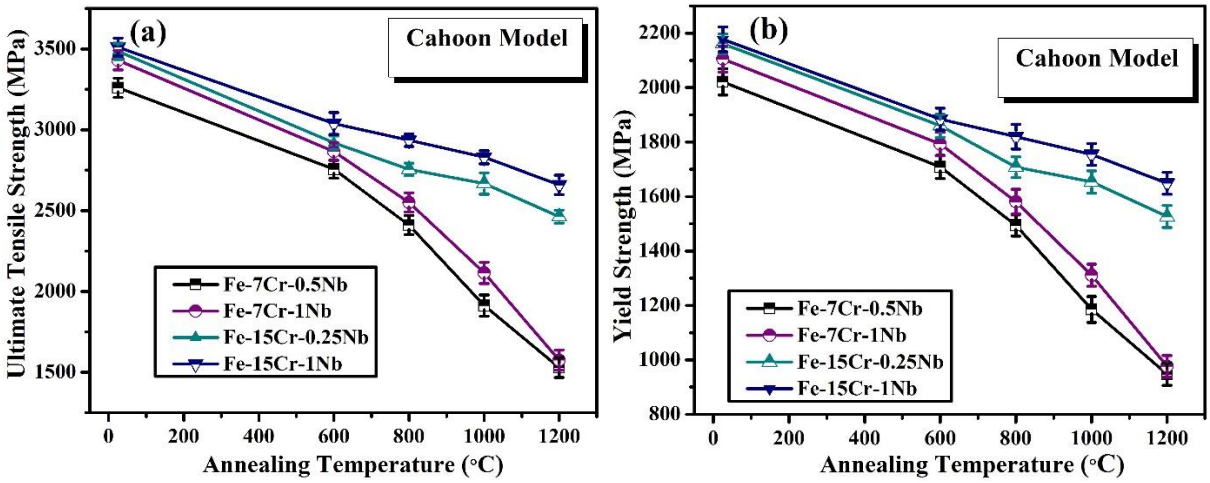

Figure 4.42: The variation of the ultimate tensile strength (a) and yield strength (b) for the Fe- 7Cr-0.5Nb, Fe- 7Cr-1Nb, Fe-15Cr-0.25Nb and Fe15Cr-1Nb alloys.

Figs. 4.42a and b, respectively, show variation of ultimate tensile strength (UTS) and yield strength (YS) of Fe- 7Cr-0.5Nb, Fe- 7Cr-1Nb, Fe-15Cr-0.25Nb and Fe15Cr-1Nb alloys as a function of annealing temperatures. The values of UTS/YS have been estimated as per Cahoon model for those alloy compositions, which showed effective thermal stability. The UTS values estimated are found to be very close to each other for the as-milled samples. It can be noted that the Fe-7Cr-0.5Nb and Fe-7Cr-1Nb alloys showed sharp decrease in the strength as compared to that of the Fe-15Cr-0.25Nb and Fe-15Cr-1Nb alloys as annealing temperature increased. The average UTS value of the Fe-7Cr-0.5Nb and Fe-7Cr-1Nb alloy could be ~3260 and 3430 MPa in the as-milled condition and decreased to ~1912 and 2184 MPa, respectively, after annealing at 1000°C (Fig. 4.42a). Similarly, the average UTS value of the Fe-15Cr-0.25Nb and Fe-15Cr-1Nb alloys in the as-milled state are found to be ~3485 and 3511 MPa and the alloys are almost stabilized in the range of 600-1000°C, and retained a quite high range of tensile strength (2830-3039 MPa) (Fig. 4.42a).

The estimation of yield strength by using Cahoon model shows quite different values of YS for the four alloy compositions. For example, the YS of the as-milled sample of the Fe-7Cr-0.5Nb and Fe-7Cr-1Nb alloys are found to be 2021 and 2105 MPa, respectively (Fig.4.42b). Similarly, the YS of the as-milled Fe-15Cr-0.25Nb and Fe-15Cr-1Nb alloys are found to be 2161 and

2177 MPa, respectively. The variation of the YS with annealing temperature follows the similar trend as that of the UTS values of the four alloy samples, i.e., the YS decreased sharply for the Fe-7Cr-0.5Nb and Fe-7Cr-1Nb alloys, whereas, it showed the stabilization for the Fe-15Cr-0.25Nb and Fe-15Cr-1Nb alloys in the range of 600-1000°C (Fig. 4.42b). The stabilized YS values of the Fe-15Cr-0.25Nb and Fe-15Cr-1Nb alloys are found to be quite attractive (1750-1800 MPa after annealing at 1000°C. Therefore, from analysis of the UTS/YS through Cahoon model, it can be concluded that the UTS and YS showed good agreement with the thermal stability of the low and high-Cr content Fe-Cr-Nb alloys. Also, it confirmed that Fe-Cr-Nb alloys could provide excellent thermal stability if significant amount of Cr is added in presence of small concentration of Nb (0.25-1 at.%). Krishna et al. (2013) reported that the experimental YS/UTS of copper alloys validated well with estimated values of YS/UTS obtained using different models' calculations. Pavlina aet al. (2008) also found a linear relationship of hardness with the YS and UTS of some hypo-eutectoid non-austenitic steels.

4.3.1.5 Summary

Fe-7Cr and Fe-15Cr alloys in addition with the varying concentration of Nb (Nb=0.25, 0.5 and 1 at.%) were developed by MA for 25 h. The following points are concluded as the major outcomes of the present study.

(a) Formation of the nonequilibrium Fe-7Cr-Nb and Fe-15Cr-Nb solid solutions has been validated through XRD analysis, lattice parameter variation and change in Gibbs free energy calculated using Toop's model. TEM-SAED investigation also confirmed the formation of complete solid solutions.

(b) Annealing of the Fe-Cr-Nb alloys up to 1200°C showed no indication of precipitation of any intermetallic phases or elemental Nb/Cr. It was confirmed by the XRD phase analysis as well as by TEM diffraction analysis. Addition of 0.25% Nb in the Fe-15Cr alloy has been found extremely effective to stabilize the alloy at high temperature (1000°C). Further, the average grain sizes of the annealed samples of the Fe-15Cr-xNb alloys were found to retain well within the nanometric range (i.e. <50 nm) even after annealing at 1000°C. The better thermal stability of the alloys has been explained in the light of thermodynamic mechanisms of solute segregation.

(c) The microhardness value was found to decrease sharply for the Fe-7Cr-Nb alloys with increasing the annealing temperature. On the other side, the hardness of the Fe-15Cr-1Nb alloys stabilized and showed a quite high hardness (8.34 GPa) even after annealing at 1000°C. For example, the microhardness value of the annealed (1000°C) Fe-15Cr-0.25Nb sample measured to be quite high (7.8 GPa) in contrast to the 6.2 GPa for the Fe-7Cr-1Nb alloy treated under the same condition. Therefore, the extra hardening effect of the Fe-15Cr-Nb alloys can be attributed to the solid solution strengthening of extra Cr in presence of Nb.

(d) The estimation of UTS /YS as per Cahoon model is found to correlate well with the thermal stability and microstructural features (e.g. nanocrystalline grain sizes) of the Fe-Cr-Nb alloys. The YS of the Fe-15Cr-1Nb alloy as per the (Cahoon model) was found to quite attractive (i.e. 1754 MPa) after annealing at 1000°C.

4.3.2 Consolidation of Fe-7Cr-Nb and Fe-15Cr-Nb by SPS

This section deals with the investigation of microstructural stability, mechanical properties and corrosion behavior of the spark plasma sintered (SPSed) Fe-7Cr-0.25Nb, Fe-7Cr-1Nb, Fe-15Cr-0.25Nb and Fe-15Cr-1Nb alloys. Because of the superior thermal stability of Fe-7Cr-0.25Nb, Fe-7Cr-1Nb, Fe-15Cr-0.25Nb and Fe-15Cr-1Nb (as compared to other Fe-Cr-Nb alloys) spark plasma sintering was carried out for these four alloys at 800, 900 and 1000°C to investigate their bulk mechanical properties.

Figs. 4.43a-d, respectively, show the XRD patterns and its analysis for the four alloys (Fe-7Cr-0.25Nb, Fe-7Cr-1Nb, Fe-15Cr-0.25Nb and Fe-15Cr-1Nb) SPSed at 800, 900 and 1000ºC in comparison to that of the 25 h as-milled samples. Figs. 4.43a-d show that neither the Cr nor the Nb peaks are detectable from the XRD patterns of the sintered and as-milled samples. The XRD patterns of the as-milled samples clearly show that the added Cr and Nb were completely dissolved in Fe-matrix after 25 h of MA. The formation of complete solid solution of the Fe-Cr-Nb alloys and their thermal stability were already discussed in details in earlier section 4.3 (Muthaiah et al., 2018). Moreover, the XRD patterns of the sintered samples also indicate that the dissolved Cr and Nb atoms remained in the solid solutions of Fe matrix even after sintering at 1000°C. The change of the peak width (at half intensity of maximum) and peak intensity with increase in the sintering temperature have been shown for Fe-110 peak for all the 4 alloys in the inset of the corresponding XRD plot.

4.3.2.1 Microstructural analysis of the SPSed specimens

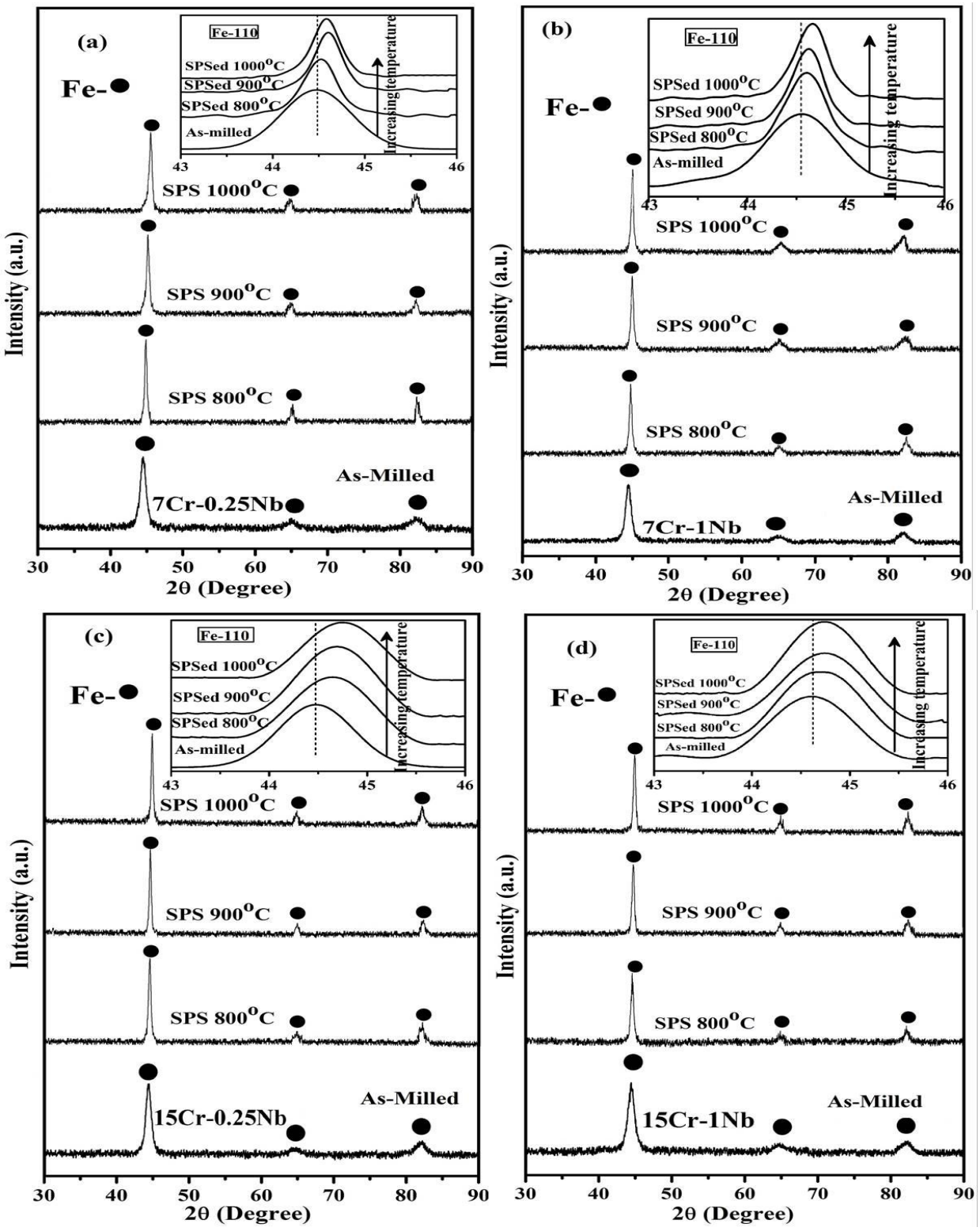

Fig. 4.43: X-ray diffraction patterns of the specimens sintered at various temperatures (800, 900 & 1000ºC); (a) Fe-7Cr-0.25Nb, (b) Fe-7Cr-1Nb, (c) Fe-15Cr-0.25Nb and (d) Fe-15Cr-1Nb.

It can clearly be observed from the analysis of XRD patterns that the peak width (at half intensity of maximum) decreased and peak intensity increased with increase in the sintering temperature (e.g. Fe-110 reflection). This is ascribed to the increase in the crystallite size, decrease in the dislocation density and relief of the acquired (during milling) lattice microstrain.

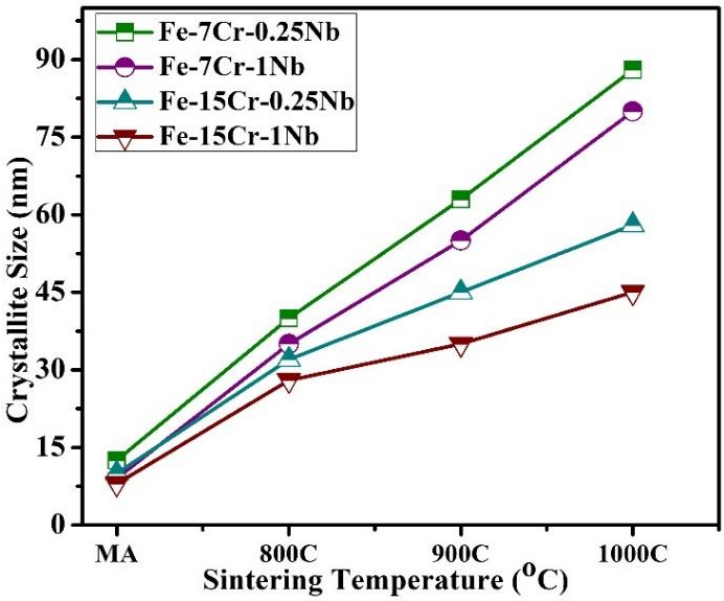

Fig. 4.44: Variation of crystallite size as a function of sintering temperature of Fe-Cr-Nb alloys.

Fig. 4.44 shows the variation of crystallite size as a function of sintering temperature. Williamson-Hall analysis (Suryanarayana et al., 1998) was used to calculate the crystallite size from the major XRD peaks of the corresponding sample. The plot between $B_r\cos\theta$ *vs.* $\sin\theta$ was used to exclude the peak broadening due to the lattice microstrain. XRD peak broadening was determined by measuring width of the peak at intensity equal to half of the maximum intensity (FWHM). The crystallite size of all the four as-milled samples was found to be <100 nm. The crystallite size is found to increase with increasing the sintering temperature. The crystallite size for the four alloy specimens sintered at 800°C was calculated to be 40, 35, 32 and 28 nm, respectively, for Fe-7Cr-0.25Nb, Fe-7Cr-1Nb, Fe-15Cr-0.25Nb and Fe-15Cr-1Nb alloys. Further, when the sintering temperature was gradually increased to 1000°C, the crystallite size enhanced to 88, 80, 58 and 45 nm, respectively. Moreover, the crystallite size is found to be much smaller in size for the Fe-15Cr-1Nb as compared to that of Fe-7Cr-1Nb. This could be ascribed to the larger amount solid solution strengthening effect due to more Cr dissolved in Fe-15Cr-1Nb. Overall, the crystallite size of all the four alloys remained <100 nm even after sintering at 1000°C.

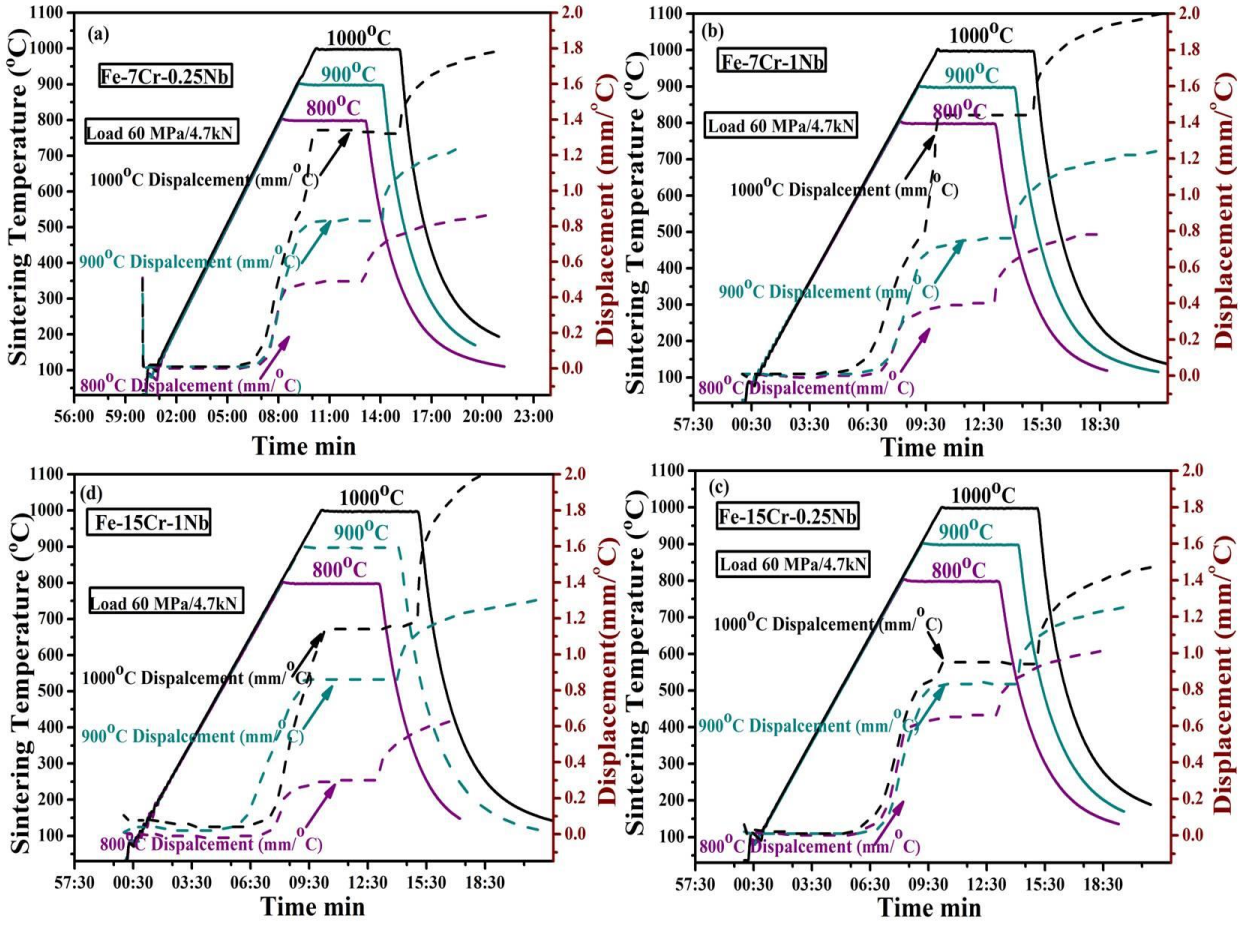

Fig. 4.45: Temperature *vs*. displacement profiles of (a) Fe-7Cr-0.2Nb, (b) Fe-7Cr-1Nb, (c) Fe-15Cr-0.2Nb & (d) Fe-15Cr-1Nb during sintering at various temperatures.

Figs. 4.46a-d show the displacement (mm/°C, dotted lines) and typical sintering temperature profiles over the densification during SPS of the four alloy samples as a function of dwell time. The four alloy samples were sintered at various temperatures (800, 900 and 1000°C) at an applied constant pressure of 60 MPa. The sintering was carried out at a heating rate of 100°C/min with a holding time of 5 min. The densification of the samples during SPS at different sintering temperatures reflected through the changes in the displacement curve (as shown in Fig. 4.45). The (wave logger) software permanently inbuilt with the SPS machine was used to stimulate the displacement and temperature graph during the real-time of sintering (Brendon et al., 2015). Figs. 4.45a-d revealed that the displacement increased with increase in the sintering temperature for all the alloy compositions. The displacement of the sintered samples may be affected by three major factors such as time, pressure and temperature. The relative density during densification of the sintered samples is discussed in the later section.

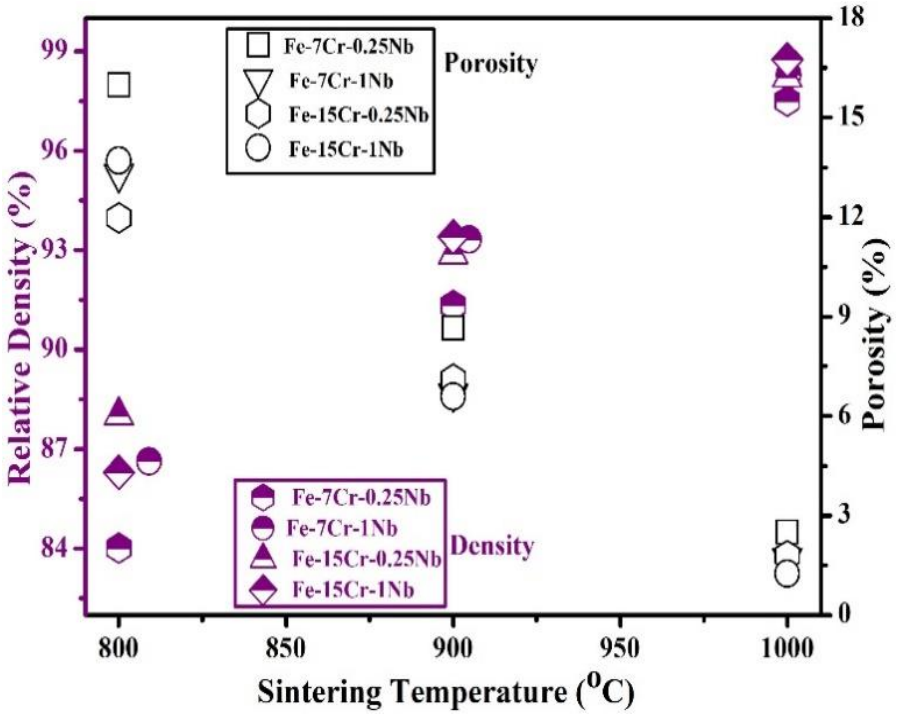

Fig. 4.46: Variation of relative density and porosity of four different compositions as a function of sintering temperature.

Relative sintered density and corresponding porosity of four different sintered samples (Fe-7Cr-0.25Nb, Fe-7Cr-1Nb, Fe-15Cr-0.25Nb and Fe-15Cr-1Nb) as a function of sintering temperature are shown in Fig. 4.46. The relative density was measured by using the Archimedes method and was estimated to be in the range of 84-88% when sintered at 800°C for all the four alloy samples (Fig. 4.46). The sintered density is found to increase with increasing in the sintering temperature. The maximum sintered density was estimated to be in the range of 97-98% when SPSed at 1000°C. Further, the porosity level decreased with gradual increase in the sintering temperature. But, a bit porosity is still present in the SPSed samples after sintering even at 1000°C. For the sample SPSed at 1000°C, the porosity level obtained is found to extremely low (~2%) as compared to the samples SPSed at 800°C (12%). In general, it is observed that when the samples were sintered at a higher temperature, the porosity level decreased. This is due to interfacial bonding between the adjacent particles and elimination of pores through bulk diffusion, grain boundary diffusion and surface diffusion.

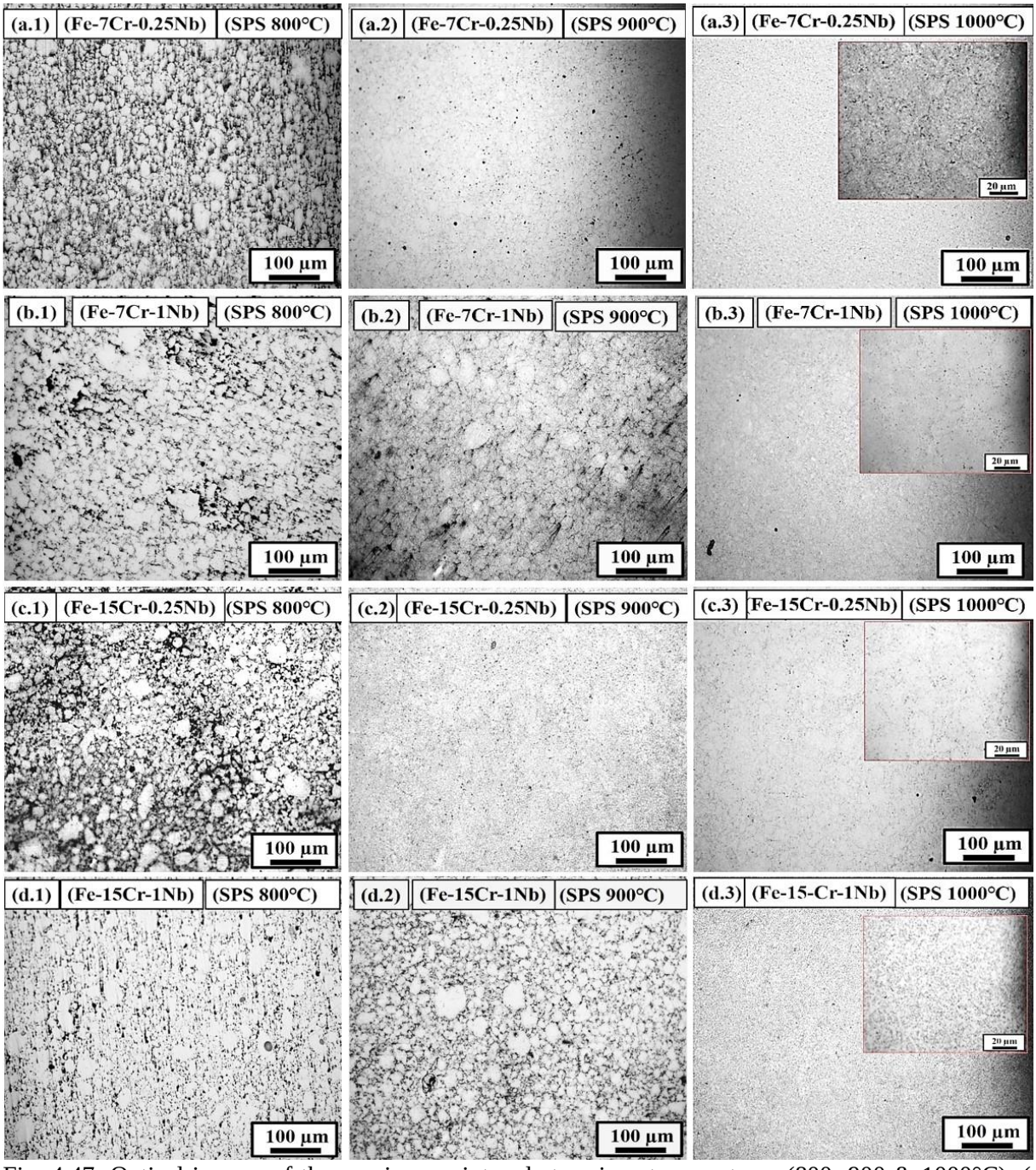

Fig. 4.47: Optical images of the specimens sintered at various temperatures (800, 900 & 1000°C); (a) Fe-7Cr-0.25Nb, (b) Fe-7Cr-1Nb, (c) Fe-15Cr-0.25Nb & (d) Fe-15Cr-1Nb alloys compositions.

Figs. 4.47a-d, respectively, show the optical micrographs of the bulk samples of Fe-7Cr-0.25Nb, Fe-7Cr-1Nb, Fe-15Cr-0.25Nb and Fe-15Cr-1Nb SPSed at 800, 900 and 1000ºC. It can be detected from Figs. 4.47a_1-d_1 that samples sintered at 800ºC have high-level of porosity and corresponding sintered density was measured to be in the range of 84-88%. The sintered density for these samples (sintered at 800ºC) is very low and not suitable for any structural

applications. The micrographs showed large as well as small pores indicating the improper bonding between the particles and hence low densification. It can clearly be seen from Figs. 4.47a_1-a_2, b_1-b_2, c_1-c_2 and d_1-d_2 that the microstructures of the samples sintered at 800 and 900°C do not show any neck-formation with the adjacent particles.

Further, they exhibited numerous free-standing particles. This can occur due to the insufficient grain-boundary diffusion at low sintering temperature and less holding period. The micrographs shown in Figs. 4.47a_3-d_3 revealed that the porosity level decreased due to an increase in the density when sintered at higher temperature (i.e. at 1000°C). The relative sintered density enhanced significantly when the sintering temperature was gradually increased to 1000ºC. The maximum sintered density was measured to be 97-98% for the four alloy samples when SPSed at 1000ºC. The corresponding porosity level also became very less as reflected from Figs. 4.47a_3-d_3. The highly magnified micrographs shown in the inset of Figs. 4.47a_3-d_3 clearly revealed that the porosity level reduced to almost zero and a near full density is attained for the alloy specimens when SPSed at 1000°C.

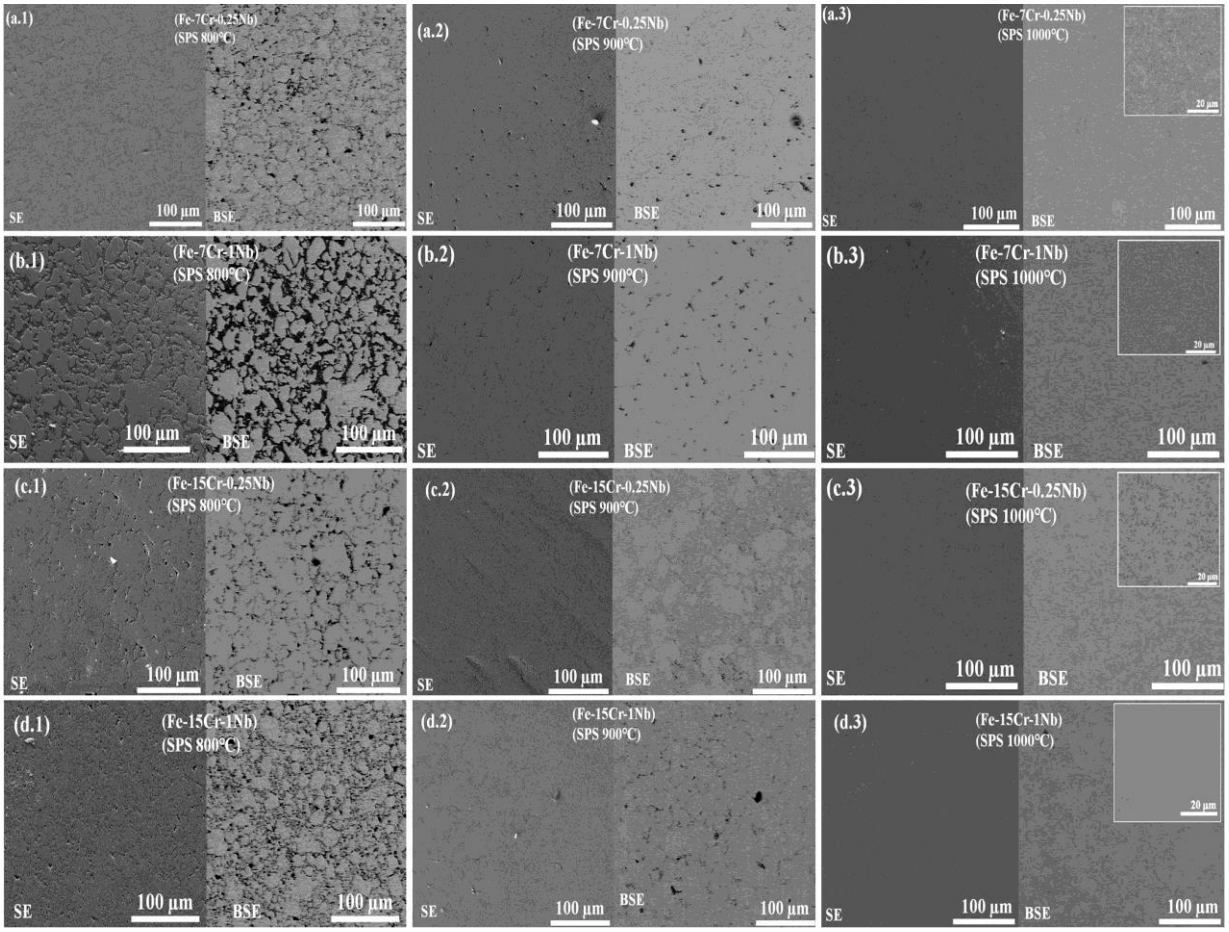

Fig. 4.48: SEM micrographs under secondary (SE) and backscattered electron (BSE) image modes of the specimens SPSed at different temperatures.

SEM micrographs (SE and BSE modes) of different alloy samples sintered at different temperatures are shown in the Figs. 4.48a-d. The Figs. 4.48a-d clearly show that the relative density gradually increased with increase in the sintering temperatures and hence corresponding porosity level decreased. It can be noted that the backscattered electron (BSE) imaging technique is more predominant to reveal the porosity (if any) as compared to the secondary electron imaging mode. The BSE micrographs (Figs. 4.48a_1-a_2, b_1-b_2, c_1-c_2, and d_1-d_2) indicate that the samples sintered at 800 and 900^{o}C exhibit the presence of numerous large and small pores. When the sintering temperature was raised to 1000^{o}C, the porosity level decreased and attained nearly full density for all the four alloy samples. In some micrographs, the presence of alumina (Al_2O_3) particles could be visible which are plausibly embedded during the cloth polishing of the sintered samples. Overall, it can be concluded that the SEM images under SE and BSE modes qualitatively corroborate well with the optical micrograph, relative density and porosity level. Also, the relative sintered density of the corresponding sample estimated by Archimedes method is found to be highly consistent with the SEM and OM micrographs.

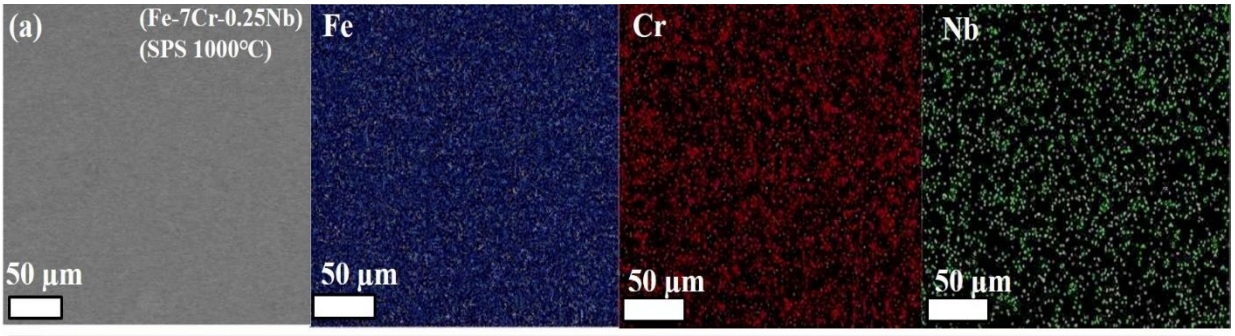

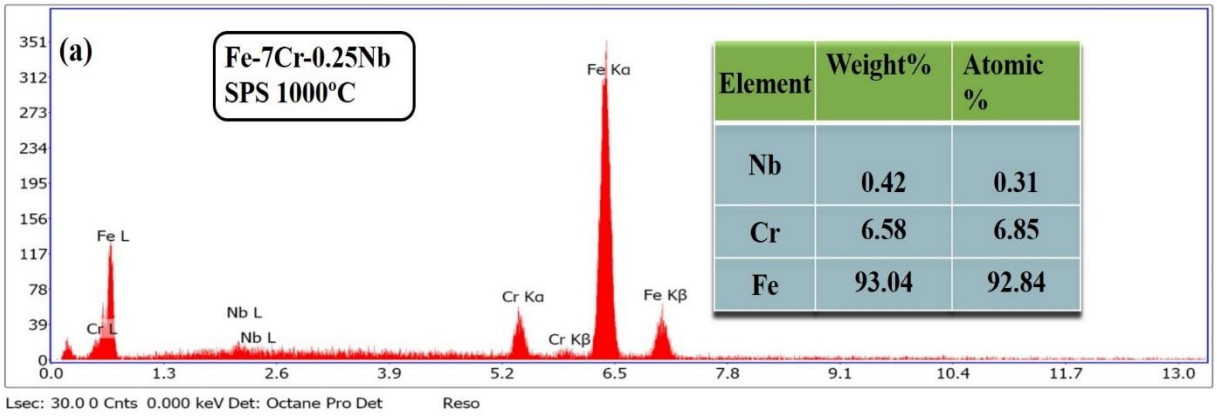

Element	Weight%	Atomic %
Nb	0.42	0.31
Cr	6.58	6.85
Fe	93.04	92.84

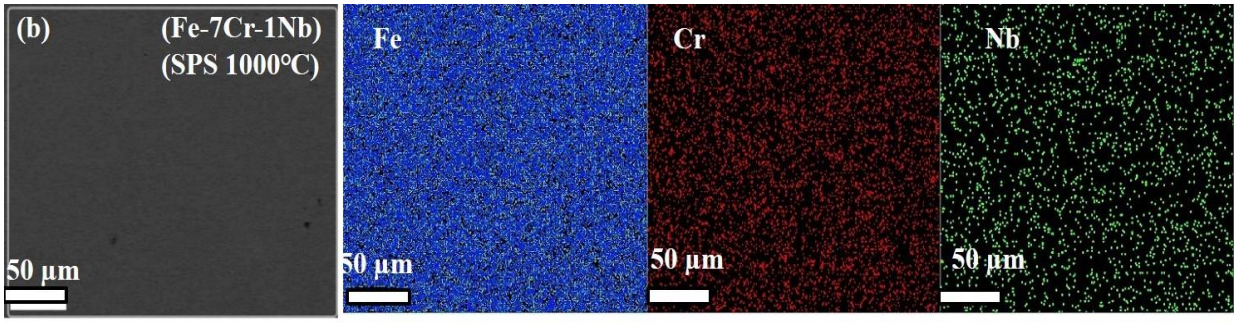

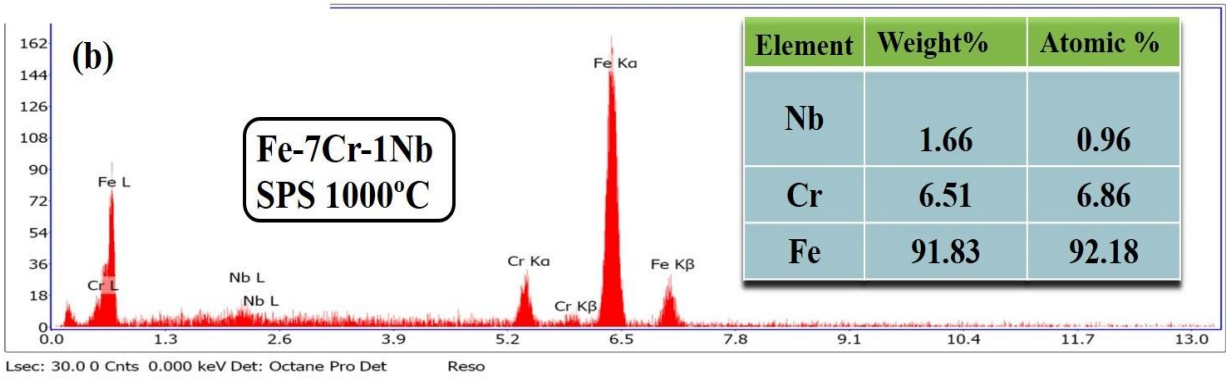

Element	Weight%	Atomic %
Nb	1.66	0.96
Cr	6.51	6.86
Fe	91.83	92.18

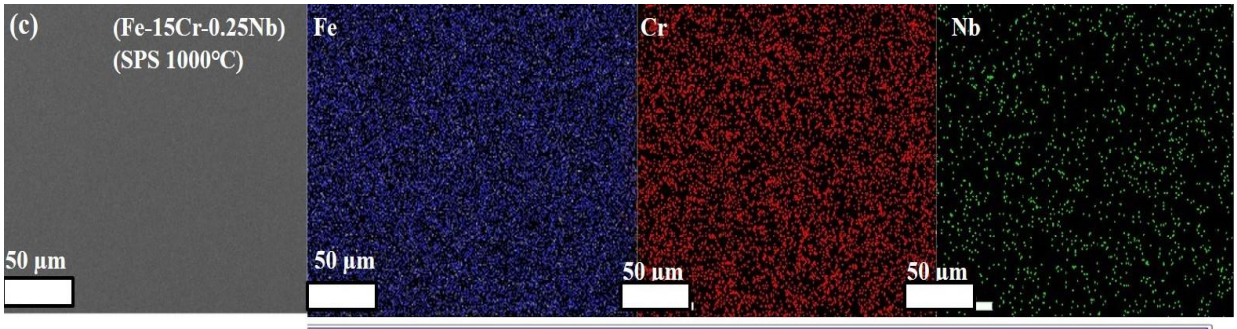

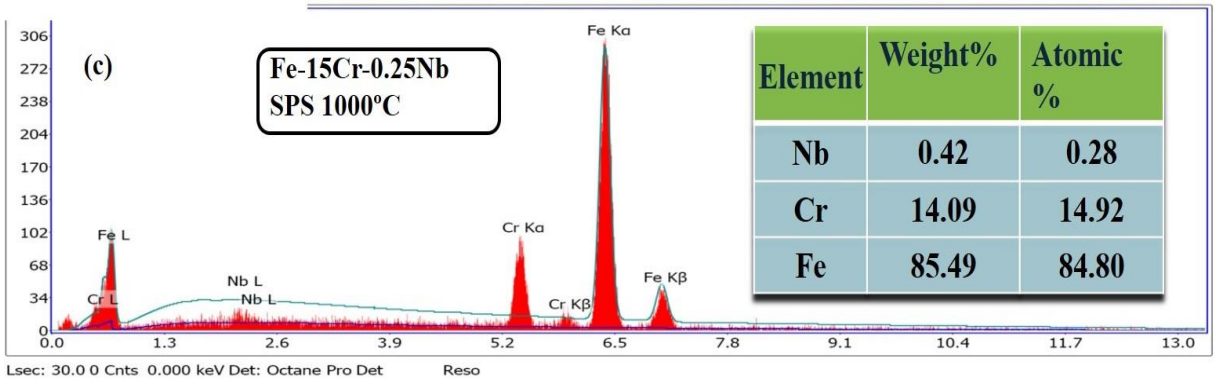

Element	Weight%	Atomic %
Nb	0.42	0.28
Cr	14.09	14.92
Fe	85.49	84.80

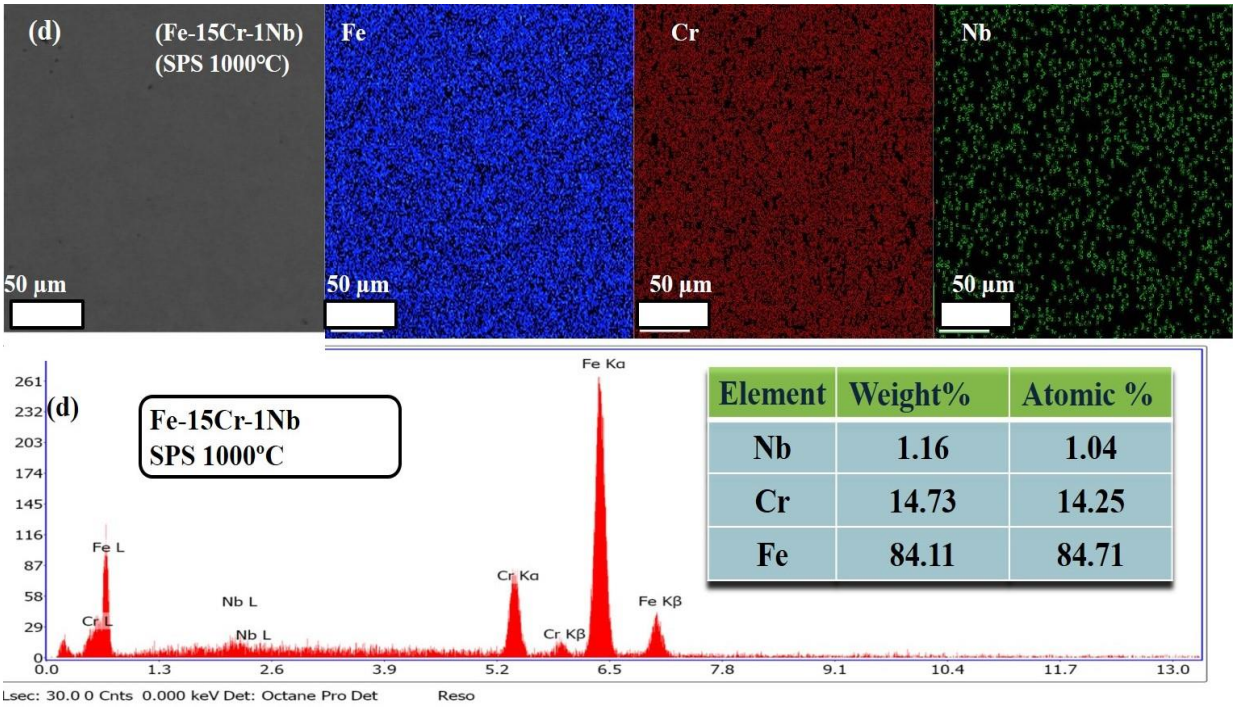

Fig. 4.49: Backscattered electron images, corresponding elemental area maps along with the EDS data: (a) Fe-7Cr-0.25Nb, (b) Fe-7Cr-1Nb, (c) Fe-15Cr-0.25Nb & (d) Fe-15Cr-0.25Nb alloys SPSed at 1000ºC.

Figs. 4.49a-d, respectively, show BSE images along with elemental mapping and EDS results of Fe-7Cr-0.25Nb, Fe-7Cr-1Nb, Fe-15Cr-0.25Nb and Fe-15Cr-0.25Nb samples SPSed at 1000°C. The elemental distribution of the bulk SPSed samples shows that Cr and Nb elements are homogeneously distributed in the Fe matrix. The quantitative EDS analysis confirmed that the elemental distribution in the SPSed samples is highly homogeneous and the estimated composition from the EDS analysis is found almost same as the blend composition of the corresponding alloy.

TEM analysis of the sintered samples

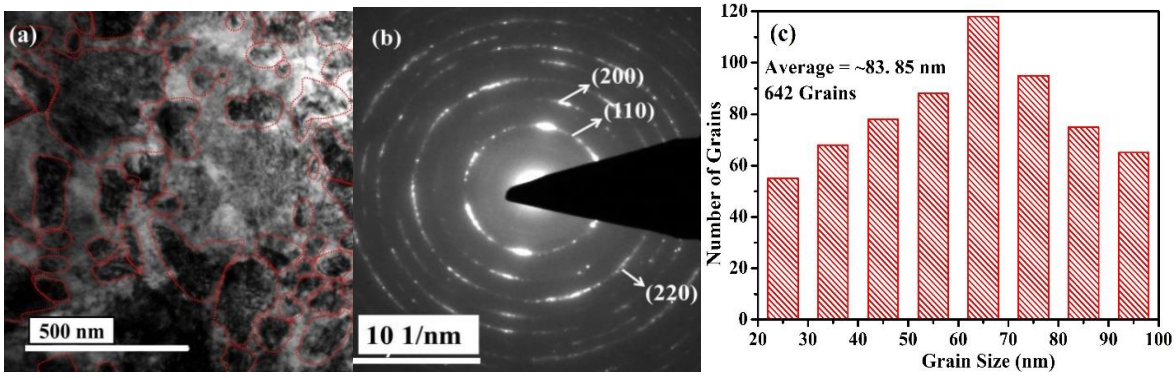

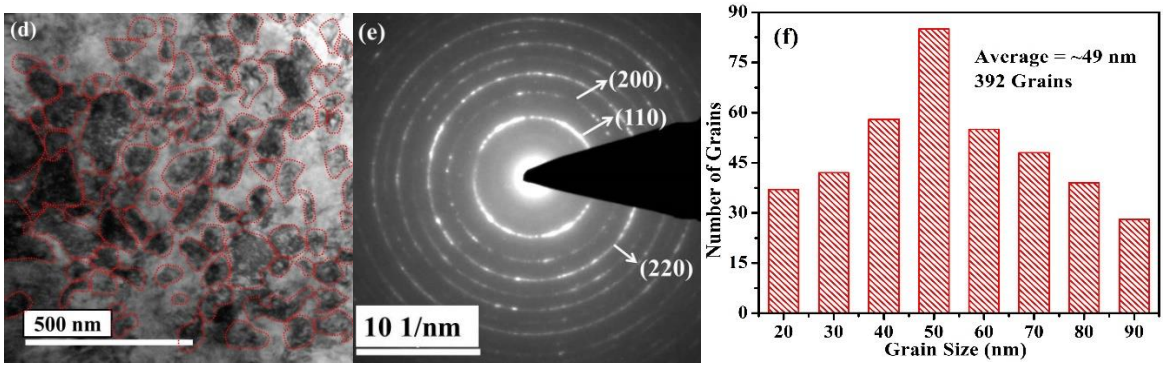

Fig. 4.50: (a & d) bright field (BF) TEM images of Fe-7Cr-1Nb and Fe-15Cr-1Nb samples SPSed at 1000°C; (b & e) selected area electron diffraction pattern (SAED) of the corresponding samples. (c & f) statistical bar diagrams for the grain size distribution of 382 and 340 grains obtained from the TEM microstructures as shown in (a & d).

Fig. 4.50 shows bright field TEM images along with their corresponding selected area electron diffraction (SAED) patterns and grain size distribution of the Fe-7Cr-1Nb and Fe-15Cr-1Nb samples sintered at 1000°C. The SAED patterns were recorded from the encircled region as shown in Figs. 4.50a & d. The bright field TEM images in Figs. 4.50a & d clearly show that the grain size remained within the nanoscale range even after SPS at 1000°C. Statistical grain size distribution shown in Figs. 4.50c & f was obtained from the analysis of TEM images as one is shown in Fig. 4.50a/d. On the basis of the statistical analysis (Figs. 4.50c & f), the average grain size estimated (from at least 642 and 392 grains) are found to be 84 nm and 49 nm, respectively, for the Fe-7Cr-1Nb and Fe-15Cr-1Nb samples sintered at 1000°C. The grain size analysis using TEM microstructures is found to consistent well with the XRD crystallite size (68 and 57nm, respectively) as discussed earlier. As shown in Figs. 4.50b & e, the corresponding SAED pattern shows continuous rings indicating the presence of nanocrystalline features in the microstructure. The ring patterns were established as the major peaks of the matrix which correspond to the Fe (110), (220), (200) planes and there is no indication to form any intermetallic phase or presence of free Cr/Nb. The analysis of SAED patterns clearly established that a complete solid solution was formed during MA and the solid solubility is retained even after sintering at 1000°C. The formation of complete solid solution was also ascertained from the X-ray diffraction phase analysis of the SPSed specimens as discussed earlier section (Figs. 4.43a & b). Moreover, neither the SAED nor the XRD patterns revealed the presence of any free Cr/Nb or any intermetallic phase. It clearly showed that the added Cr and Nb elements were completely dissolved in Fe-matrix to form a solid solution during MA without formation of any intermetallic phases and remained in the solid solution of Fe-matrix

without precipitation of any free Cr/Nb or any intermetallic phase(s) after SPSed at 1000°C. The Cr and Nb elements play a vital role to retain the matrix grain sizes within the nanometric regime at such an elevated temperature and also improved the hardness of the sintered Fe-Cr-Nb samples as discussed later (Fig. 4.51a). Almost similar type of strengthening effect was obtained in Cu-Nb alloys (Mula et al., 2012).

4.3.2.2 Mechanical Properties of the (Fe-Cr-Nb alloys) sintered samples

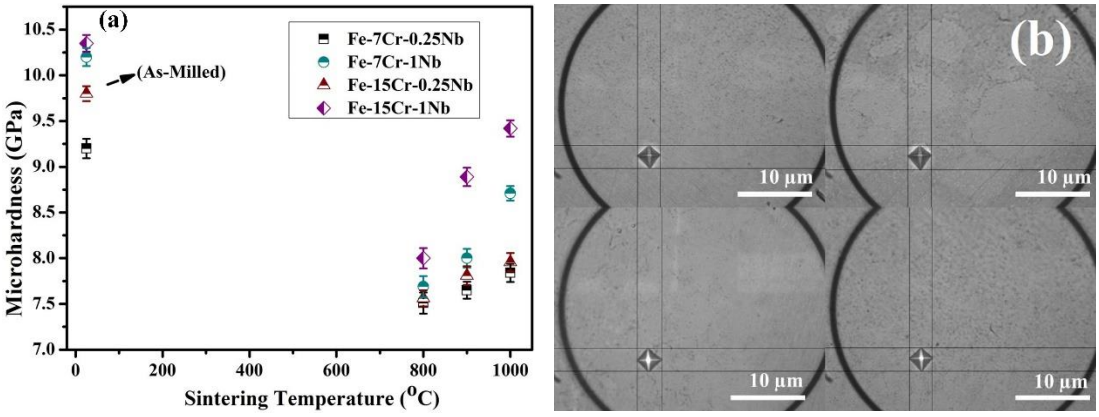

Fig. 4.51: (a) Microhardness values of the bulk samples SPSed at different sintering temperatures. (b) Microhardness indentation marks on the SPSed samples taken after microhardness measurements.

Fig. 4.51a shows the changes in microhardness values as a function of sintering temperature for the samples of Fe-7Cr-0.25Nb, Fe-7Cr-1Nb, Fe-15Cr-0.25Nb and Fe-15Cr-0.25Nb. It can be noticed from the Fig. 4.51a that the hardness value gradually increased with increase in the sintering temperature. Moreover, the highest hardness value is estimated to be 8.7 and 9.4 GPa, respectively, for the samples of Fe-7Cr-1Nb and Fe-15Cr-1Nb SPSed at 1000°C. Further, the maximum hardness of the SPSed specimens of the Fe-7Cr-0.25Nb (7.8 GPa) and Fe-15Cr-0.25Nb (8.0 GPa) is determined to be less as compared to Fe-7Cr-1Nb (8.7 GPa) and Fe-15Cr-1Nb (9.4 GPa). The microhardness values of the as-milled samples of Fe-7Cr-0.25Nb, Fe-7Cr-1Nb, Fe-15Cr-0.25Nb and Fe-15Cr-0.25Nb were found to be 9.2, 10.2, 9.8 and 10.4 GPa, respectively. The crystallite size of the as-milled samples was in the nanometric range (i.e., <100 nm) for all the four alloys. It is also to be noted from Fig. 4.44 that the crystallite size of the samples sintered at 800ºC of Fe-7Cr-1Nb and Fe-15Cr-1Nb was 35 and 28 nm, respectively, as compared to 80 and 45 nm, when the samples of the same composition sintered at 1000ºC. Overall, the average crystallite size and hardness values gradually increased with increase in the sintering temperature.

Hence, increase in the microhardness value at higher sintering temperatures can be ascribed mainly to two reasons: (i) increase in the sintered density at higher sintering temperature (ii) solid solution strengthening to the Fe-matrix. The increase in the hardness values was due to the densification which overcompensated the decrease in the hardness due to the grain growth. It can be observed from the Fig. 4.51a that the maximum hardness in the sintered samples is less than that of the corresponding as-milled sample. This may be ascertained to the small amount of porosity present in the SPSed samples (98% sintered density) and coarsening of the grains after sintering. The hardness test of the SPSed specimens was carried out at alternative places on the mirror finish polished surface which may contain small pores; whereas, the indentations were made on the bigger size particles of the as-milled samples. Fig.4.51 shows the microhardness indentation marks made on the surface of the SPSed samples during microhardness measurement. Zhang et al. (2005) also reported that at higher sintering temperature the average microhardness value increased due to an increase in the sintered density of the Fe-0.8% C steel though the crystallite size increased.

Fig. 4.52 shows typical stress-strain curves accumulated during compression tests for the Fe-7Cr-1Nb and Fe-15Cr-1Nb samples sintered at 1000°C. The compression tests were repeated for three times to confirm the repeatability of the data. The ultimate compressive strength (UCS) of the Fe-7Cr-1Nb and Fe-15Cr-1Nb samples (sintered at 1000°C) is found to be 1860 and 2400 MPa, respectively. The corresponding yield strength (YS) is estimated to be 1265 and 1800 MPa, respectively.

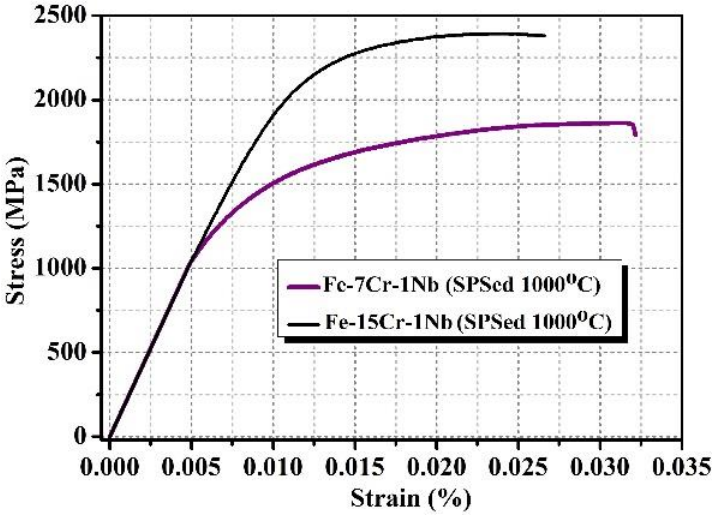

Fig. 4.52: Variation of compressive stress-strain curves of Fe-7Cr-1Nb and Fe-15Cr-1Nb samples SPSed at 1000°C.

The compressive strength value of the Fe-15Cr-1Nb sample is significantly higher than that of the Fe-7Cr-1Nb sample sintered at same conditions due to the fact of more Cr dissolved in the matrix. Moreover, as discussed earlier that the relative density was the maximum for the Fe-15Cr-1Nb sample sintered at same conditions (Fig. 4.45). From the compressive stress-strain curves, it could be observed that the failure has occurred after a significant amount of plastic deformation, i.e. after a certain amount of yielding. The extremely high yield strength of Fe-15Cr-1Nb sample can be attributed to three major strengthening mechanisms, namely, solid solution strengthening (high amount of Cr), grain size refinement (49 nm as compared to 84 nm) (Hall-Petch effect) and dislocation strengthening (discussed later).

Analysis of strengthening mechanisms and validation of yield strength (YS)

This section deals with the various strengthening mechanisms which have been analyzed to estimate yield strength of the Fe-7Cr-1Nb and Fe-15Cr-1Nb samples sintered at 1000^{o}C and further correlated with the experimentally measured compressive strength and Vickers hardness values. The experimentally measured YS has been estimated from the hardness values using the relationship, σ_y =1/3 of HV and from the compression stress-strain curves of the sintered samples of Fe-7Cr-1Nb and Fe-15Cr-1Nb. The various strengthening mechanisms analyzed here are grain size strengthening (σ_{gs}), solid solution strengthening (σ_{ss}) and dislocation strengthening (σ_{dis}), respectively (Muñoz-Morris et al., 2002; Srinivasan et al., 2006). The YS has been calculated using the following equation (4.16):

$$\sigma_{y=}\sigma_{ss}+\sigma_{dis}+\sigma_{gs} \quad (4.16)$$

Solid solution strengthening (σ_{ss})

The solid solution strengthening (σ_{ss}) involves in both interstitial and substitutional elements in the alloy compositions. From the Fe-Cr-Nb alloys, the Cr and Nb are the two alloying elements dissolved in the Fe-matrix. According to the Hume-Rothery's rules, the atomic size difference is very small between Fe (0.126 nm), Cr (0.128 nm) and Nb (0.147) atoms and thereby, it easily forms a substitutional solid solution. The strength due to substitutional solid solution strengthening (σ_{ss}) is expressed as per the equation (4.20) (Lacy et al., 1944; Li 2003) as follow as:

$$\sigma_{ss} \approx 0.00689KX^{n} \quad (4.17)$$

where, X is the equilibrium concentration of substitutional alloying elements (in at.%), n=0.75 is constant for the all the elements and K is the strengthening coefficient. For example, K values of chromium and niobium are 1400 and 4000, respectively (Lacy et al., 1944; Li 2003). The value of 0.00689 is used to convert from psi (pound per square inch) to MPa (Li 2003). The solid solution strengthening due to substitutional elements, Cr and Nb for the Fe-7Cr-1Nb and Fe-15Cr-1Nb are found to be 80 and 110 MPa, respectively (estimated by using Eq.4.17).

Grain size strengthening (σ_{gs})

Reduction in the matrix grain size into the range of nanocrystalline regime increases the mechanical strength, such as hardness, compressive strength significantly. The effect of grain size strengthening is attributed through Hall-Petch equation:

$$\sigma_{gs} = \sigma_0 + kd^{-1/2} \quad (4.18)$$

where, σ_0 is the friction stress (for pure iron σ_0 =30 MPa), k is a constant and k=0.274 $MN^{m-3/2}$ is a reported value for ultrafine grained steel (Lacy et al., 1944), d is grain size (nm). The average grain size calculated from the TEM images was found to be 84 nm for Fe-7Cr-1Nb and 49 nm for Fe-15Cr-1Nb samples sintered at 1000°C. The above-mentioned parameters were used to calculate the yield strength of the Fe-7Cr-1Nb and Fe-15Cr-1Nb samples and the calculated YS (i.e. σ_{gs}) are 975 and 1267 MPa, respectively.

Dislocation strengthening (σ_{dis})

Dislocation strengthening of the SPSed samples can be estimated from the following equation (Taylor 1934):

$$\sigma_{dis} = \alpha MGb\sqrt{\rho} \quad (4.19)$$

where, M is the Taylor's factor (3.06 for the BCC polycrystalline materials) (Stoller et al. 2008), α is a constant (0.25-1), b is the burgers vector (0.251 nm), *G* is the shear modulus (for pure iron *G*=83 GPa) and ρ is the dislocation density. Dislocation density ρ can be calculated from the Eq. 4.20. Hence, the yield strength due to the dislocation density, σ_{dis}, can be estimated easily. The calculated dislocation density was found to be $2.33\times10^{14} m^{-2}$ and $8.26\times10^{14}\ m^{-2}$ for the Fe-7Cr-1Nb and Fe-15Cr-1Nb, respectively.

$$\rho = \frac{2\sqrt{3}}{D\times b}\ (\varepsilon^2)^{1/2} \quad (4.20)$$

where, D is the average crystallite size (80 and 45 nm for the Fe-7Cr-1Nb and Fe-15Cr-1Nb, respectively), b is the Burgers vector (nm) and ε is the lattice microstrain, which was estimated from the X-ray diffraction analysis. The calculated yield strength of the Fe-7Cr-1Nb and Fe-15Cr-1Nb due to dislocation strengthening (i.e. σ_{dis}) is found to be 194 and 366 MPa, respectively.

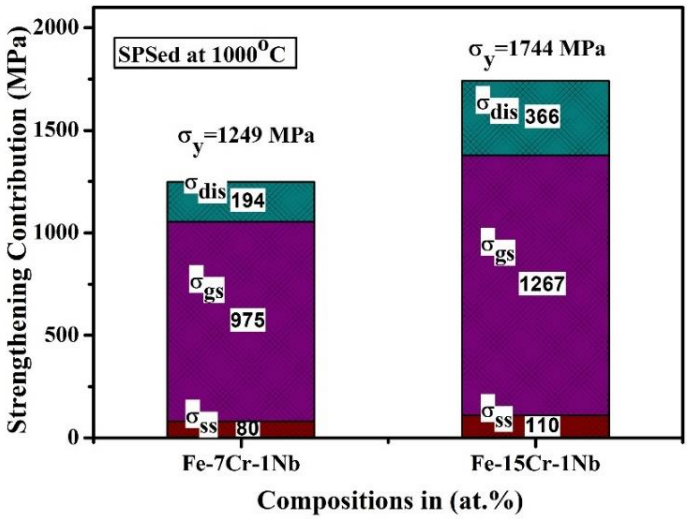

Fig. 4.53 Contribution of different strengthening mechanisms on the total yield strength of the Fe-7Cr-1Nb and Fe-15Cr-1Nb samples sintered at 1000°C.

The contribution of various strengthening mechanisms' on the total predicated yield strength for the Fe-7Cr-1Nb and Fe-15Cr-1Nb samples sintered at 1000°C is shown in Fig. 4.53. It can be noted that the total predicated yield strength obtained from the contribution of different strengthening mechanisms (such as solid solution, grain size and dislocation strengthening) is highly corroborated with the compressive yield strength of the corresponding sample. For example, in case of the Fe-15Cr-1Nb sample sintered at 1000°C, the experimental values of UCS (2400 MPa) and YS (1800 MPa) are highly comparable to the total YS (1744MPa) calculated from the different strengthening mechanisms, and UTS (2830 MPa) and YS (1754 MPa) calculated from the hardness values of the corresponding sample. It can also be observed that the grain size strengthening mechanism plays the vital role to enhance the yield strength. Grain size strengthening due to the dissolution of Nb and Cr atoms in Fe-matrix plays an important role to stabilize the matrix grains in nanometric regime even after SPS at 1000°C. It is discussed in the earlier section about the TEM microstructure of the Fe-7Cr-1Nb and Fe-15Cr-1Nb sintered samples which showed that the grain size was in the nanometric range. Further, the grain size strengthening and dislocation strengthening contributed significantly to the total yield strength as compared to that of the solid solution strengthening.

Wear Properties

Recently, an attention has been made to replace the traditional 167Nb-S and 51Nb-S roller press by stabilized Fe-based alloys such as Fe-Cr-Nb-C alloys to improve the service life of the cement industry machine parts (e.g. cladding roller press) (Scandella et al., 2004). The major part of the cement industry is roller press, where the wear resistance is extremely important. A very high hardness value of Fe-15Cr-1Y alloy is obtained after SPS at 1000°C (Muthaiah et al., 2016). In the present study also, the SPSed sample of the Fe-15Cr-1Nb alloys shows very high level of hardness (9.4 GPa) for the sample sintered at 1000°C. Therefore, this stabilized Fe-Cr-Nb alloy could be a possible candidate to replace the traditional materials such as16Nb-S, 51Nb-S and Fe-Cr-Nb-C steels for high wear resistance applications (e.g. roller press).

The dry sliding wear behavior of the SPSed Fe-7Cr-1Nb and Fe-15Cr-1Nb samples has been examined and the variation of coefficient of friction (COF) of the specimens as a function of time is displayed in Figs. 4.54a & b. As could be seen from the plots that the COF gradually decreases as the sintering temperature increased for both the alloys (Figs. 4.54a & b).

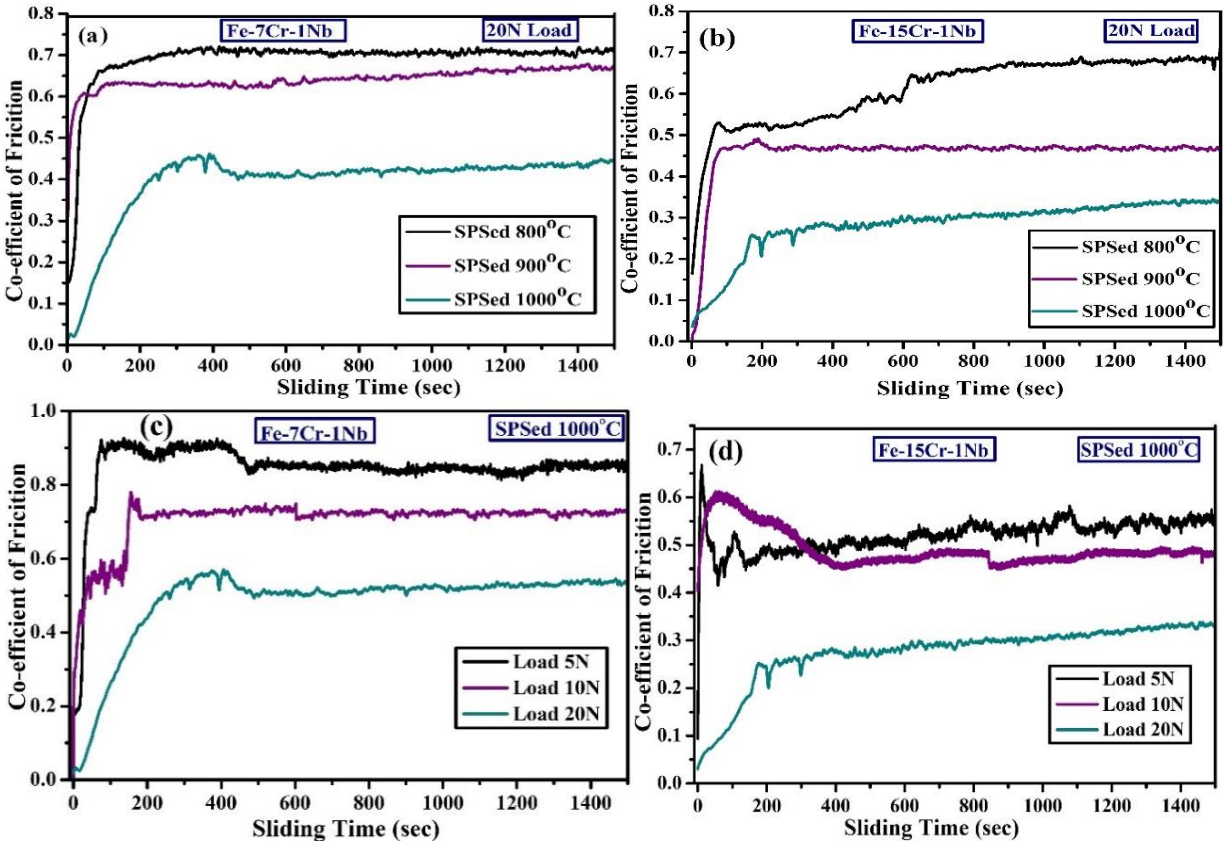

Fig. 4.54: Variation of coefficient of friction as a function of sliding time for the samples SPSed at different temperatures (a) Fe-7Cr-1Nb (b) Fe-15Cr-1Nb. Effect load on the wear behavior is shown in figure (c) Fe-7Cr-1Nb (d) Fe-15Cr-1Nb as a function of sliding time.

As the sintering temperature increased from 800 to 1000°C, the COF of the Fe-7Cr-1Nb samples decreased from 0.72 to 0.5 (Fig. 4.54a). The COF for the Fe-15Cr-1Nb SPSed samples decreased to 0.3 from 0.65 (Fig. 4.54b) as the sintering temperature increased to 1000°C from 800°C. Moreover, the COF of the Fe-15Cr-1Nb samples is found to be less than that of the Fe-7Cr-1Nb samples sintered at any particular temperature. As discussed earlier (in the Fig. 4.45 and Fig. 4.46), the sintered density increased with increasing sintering temperatures. The enhancement of the wear resistance, therefore, could be ascribed to the proper bonding of the powder particles and achieving near full density sintered samples at higher temperature (at1000ºC). The wear resistance increased due to the proper bonding of the powder particles was also reported in Mula et al. (2011). Increase in the sintering temperature resulted better bonding and hence densification (Shashanka et al., 2017). Therefore, higher hardness is resulted at higher sintering temperature. Zhang et al. (2015) reported that formation of oxide debris and it is entrapped between the contact surface of the ball and sample in case of the low-density sample; which, in turn, increases the frictional force further during sliding and induces extra wear. The wear resistance of the sintered sample is found to correlate well with the Vickers hardness values of the corresponding sample (Fig. 4.51a), i.e. the sample, which showed higher hardness, is less susceptible to wear. Many other researchers also reported that the highly dense Fe-based alloys having high Cr and Nb showed excellent tribological performance and wear resistance (Yang et al., 2017). Yang et al. (2017) reported that the wear resistance of the hard-facing Fe-13Cr-C-Nb-Ti alloys significantly increased due to the strengthening and protecting effect of the carbide precipitates of NbC & TiC. Moreover, similar kind wear behavior was observed in the Fe-15Cr-Ni-M0-Si-B-Nb alloys (Zhang et al., 2008). The Cr and Nb elements played a vital role to improve the wear resistance and decreased the coefficient of friction (Yang et al., 2017; Zhang et al., 2008).

Effect of load variation on the COF of the SPSed Fe-7Cr-1Nb and Fe-15Cr-1Nb samples (sintered at1000°C) as a function of sliding time is shown in Figs. 4.46c & d, respectively. It can be noted that the COF values of the sintered samples decrease with increasing the load from 5 to 20 N. The COF values of the SPSed (at 1000°C) Fe-7Cr-1Nb samples are measured to be 0.85, 0.7 & 0.5, respectively, for the 5, 10 & 20N loading conditions (Fig. 4.46c). Similar trend of the COF (0.53, 0.43 & 0.3) could be observed for the SPSed Fe-15Cr-1Nb samples tested under same conditions (i.e. 5, 10 & 20N load) (Fig. 4.46d).

It could be seen that the COF value of any particular sample is higher at lower loading condition (e.g. 5N) as compared to that of the higher load (e.g. 20N). Chowdhury et al. (2013a,b) reported that the COF of SS304 decreased with an increase in the applied load (10-20N). Moreover, at an applied load, the fluctuation and average value of COF decreased with increasing the sliding load (Li et al., 2010). At the lower normal loads, plowing action is resulted due to the less contact of asperities, which increases the COF. At higher load, surface roughness is increased, which reduces the total contact area between the surfaces, thereby reduces the COF. Larger amount of wear debris is also supposed to decrease the COF due to increase in the load (Chowdhury et al., 2013a,b). Similar type of wear behavior has been explained for the SPSed samples of Fe-Cr-Y samples in section 4.2.2.2. The detailed wear mechanism has been discussed under 'Wear' at 4.2.2.2 section.

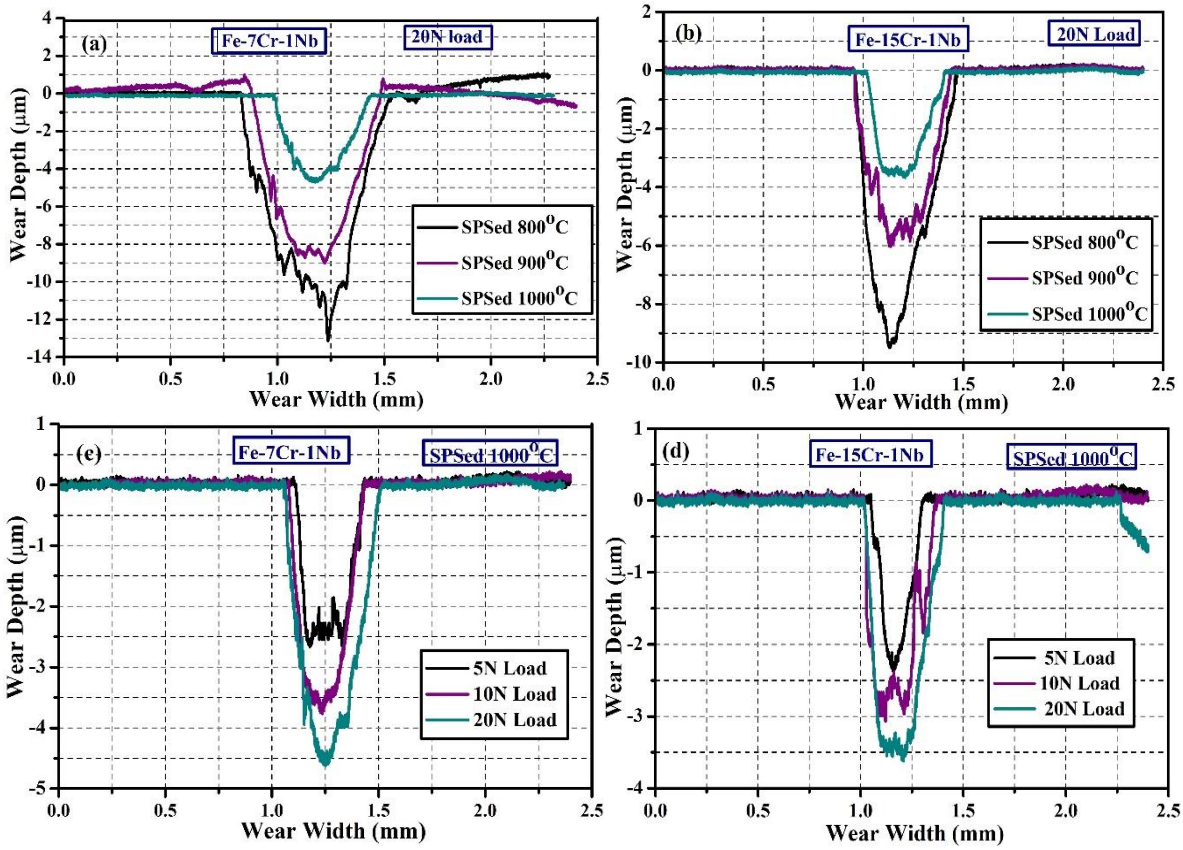

Fig. 4.55: Typical cross-sectional surface profiles of the worn tracks of (a) Fe-7Cr-1Nband (b) Fe-15Cr-1Nb alloy samples sintered at different temperatures. Effect load on the wear track is shown in figure (c) Fe-7Cr-1Nb (d) Fe-15Cr-1Nb.

Figs. 4.55a and b, respectively, show the cross-sectional surface profiles of the worn tracks of the sintered Fe-7Cr-1Nb and Fe-15Cr-1Nb samples tested under 20N load. Both, the depth and width of the sliding wear tracks were measured at different locations by using surface

profilometer. Figs. 4.55a and b indicate that the wear depth and wear width values are larger for the samples, which were sintered at lower temperature (e.g. Fe-7Cr-1Nb:12.95 µm & 0.72 mm and Fe-15Cr-1Nb:9.2 µm & 0.66 mm for the sample sintered at 800°C). The worn depth and width of the same samples tested under the same load (i.e. 20N) decreased to only 4.2 µm & 0.45 mm and 3.4 µm & 0.39 mm, respectively, as the sintering temperature increased to 1000ºC. At the beginning, the wear width and depth increased very rapidly due to the initial loading effect and presence of porosities. This effect is more prevalent for the low-density samples as large amount of loosely bound particles are pulled out from the surface. Therefore, more wear debris would be accumulated on the surface of the low-density samples. Figs. 4.55c and d show the effect of load on the wear profiles of the Fe-7Cr-1Nb and Fe-15Cr-1Nb samples sintered at 1000°C. It can be observed that wear width and depth increased with increase in the load for both the alloys. For example, the wear width and depth of the Fe-15Cr-1Nb samples are found to steadily increase (i.e. 2.7 µm & 0.27 mm, 3.0 µm & 0.35 mm and 3.4 µm & 0.39 mm) as the load increases from 5 to 20N. Moreover, the wear width and depth for the Fe-15Cr-1Nb samples (e.g. 3.4 µm & 0.39 mm) is found to be less than that of the Fe-7Cr-1Nb (4.2µm & 0.45 mm). The possible wear mechanisms of the sintered samples at various loads already been discussed in the previous section. Overall, it could be concluded that the COF is correlated well with wear width and depth of the corresponding sample.

On the basis of the surface profiles, the wear volume was calculated using Archard's formula (Archard 1953) as follows:

Wear volume (mm^3) = 2π×track radius× track width ×wear depth.

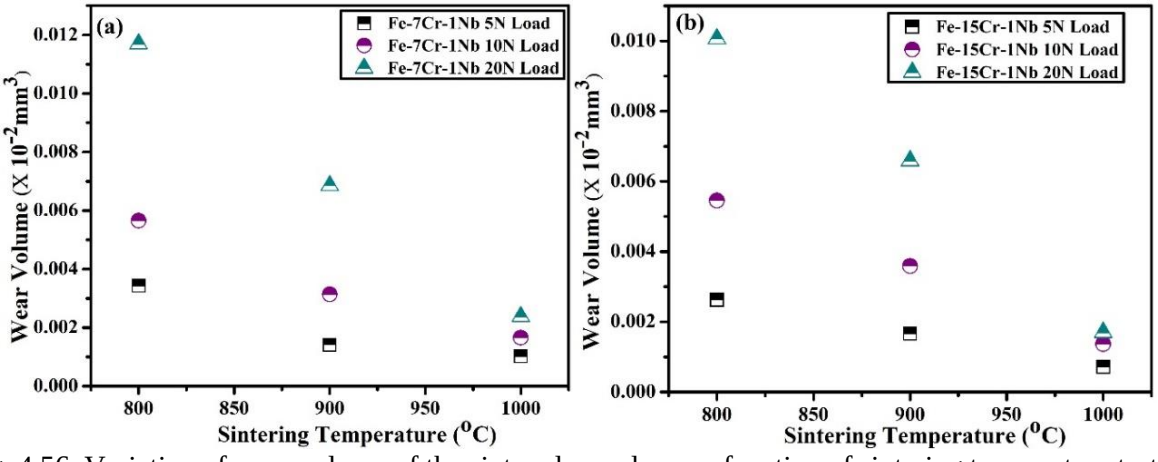

Fig. 4.56: Variation of wear volume of the sintered samples as a function of sintering temperature tested at different loads (a) Fe-7Cr-1Nb and (b) Fe-15Cr-1Nb.

Figs. 4.56a & b, respectively, demonstrate the wear volume of the sintered samples as a function of sintering temperature. It can be noted that the wear volume decreased with increase in the sintering temperatures for both the alloys. For the samples sintered at 800ºC with 20N load, the wear volume is estimated to be 0.0117 and 0.0106×10^{-2} mm^3, respectively, for the low and high Cr content alloys. The wear volume decreased to only 0.0023 and 0.0017×10^{-2} mm^3, respectively, when the sintering was carried out at 1000ºC. As mentioned earlier that the wear resistance increased due to the increase in the relative sintered density and formation proper bonding between the alloy particles. Also, the Cr and Nb played a vital role to improve the wear resistance due to their solid solution strengthening effect (Cui et al., 2007; Wang et al., 2003).

Moreover, effect of variation of applied load on the wear volume has been examined and correlated with the wear profile of the corresponding sample. It can be noted that at any particular sintering temperature (say at 1000°C), the wear volume of both the alloys gradually increases with increasing the applied load. For example, the wear volume of the Fe-7Cr-1Nb alloy sintered at 1000°C is estimated to be 0.00103×10^{-2}, 0.00165×10^{-2} and 0.0023×10^{-2} mm^3, respectively, for the 5, 10 and 20N applied load (Fig. 4.56a). The wear volume is found to decrease to very low level when the sintering temperature was raised to 1000ºC. For example, the wear volume of the Fe-15Cr-1Nb samples tested at 5-20N is estimated to be 0.00071×10^{-2}, 0.00137×10^{-2} and 0.0017×10^{-2} mm^3, respectively. Moreover, it can be observed from the Figs. 4.56a & b that at any particular sintering temperature, the wear volume of the Fe-15Cr-1Nb sample (sample sintered at 1000°C: 0.0017×10^{-2} mm^3) is relatively less than that of the Fe-7Cr-1Nb sample (sample sintered at 1000°C: 0.0023×10^{-2} mm^3) sintered at same condition.

To correlate the coefficient of friction and surface profile after the wear test, the wear track surface of the corresponding sintered sample was analyzed from their FE-SEM images. Figs. 4.57a_1-a_3 & b_1-b_3 show the wear track surfaces of the samples tested with 20N load. It can be noticed from Figs. 4.57a_1 and b_1 that the wear track surfaces are much wider and a large amount of material is worn out from the surface of the low temperature (800ºC) sintered samples. A large number of particles are found to pull out from both the surfaces because of improper bonding of the powder particles. On the other hand, the wear track width was found to gradually narrow down (indicating better wear resistance) as the sintering temperature increased. The minimum wear track width is achieved for the high Cr content Fe-15Cr-1Nb alloy sintered at 1000°C (Fig. 4.57b_3).

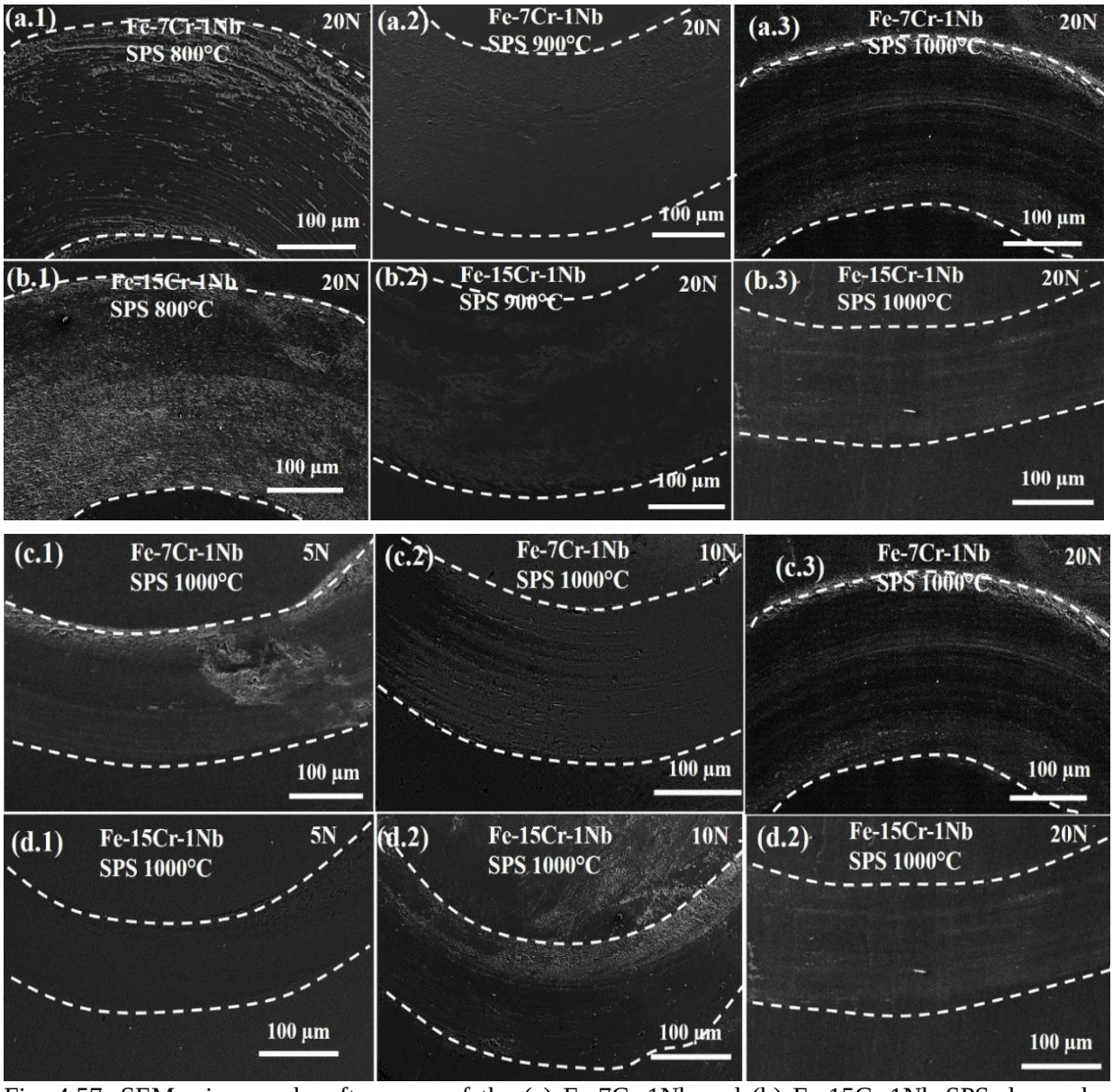

Fig. 4.57: SEM micrographs after wear of the (a) Fe-7Cr-1Nb and (b) Fe-15Cr-1Nb SPSed samples sintered at different temperatues. (c & d) Effect load on the wear track is shown in figure (c) Fe-7Cr-1Nb (d) Fe-15Cr-1Nb.

The wear track width is found to be highly consistent with the worn depth & width of the corresponding samples. Cui et al. (2007) also reported that addition of Cr in Cu-Pb alloy strengthened the matrix and improved the wear resistance. The nature of worn out surface is found to correlate well with the COF and wear behavior of the corresponding sample.

4.3.2.3 Corrosion behavior

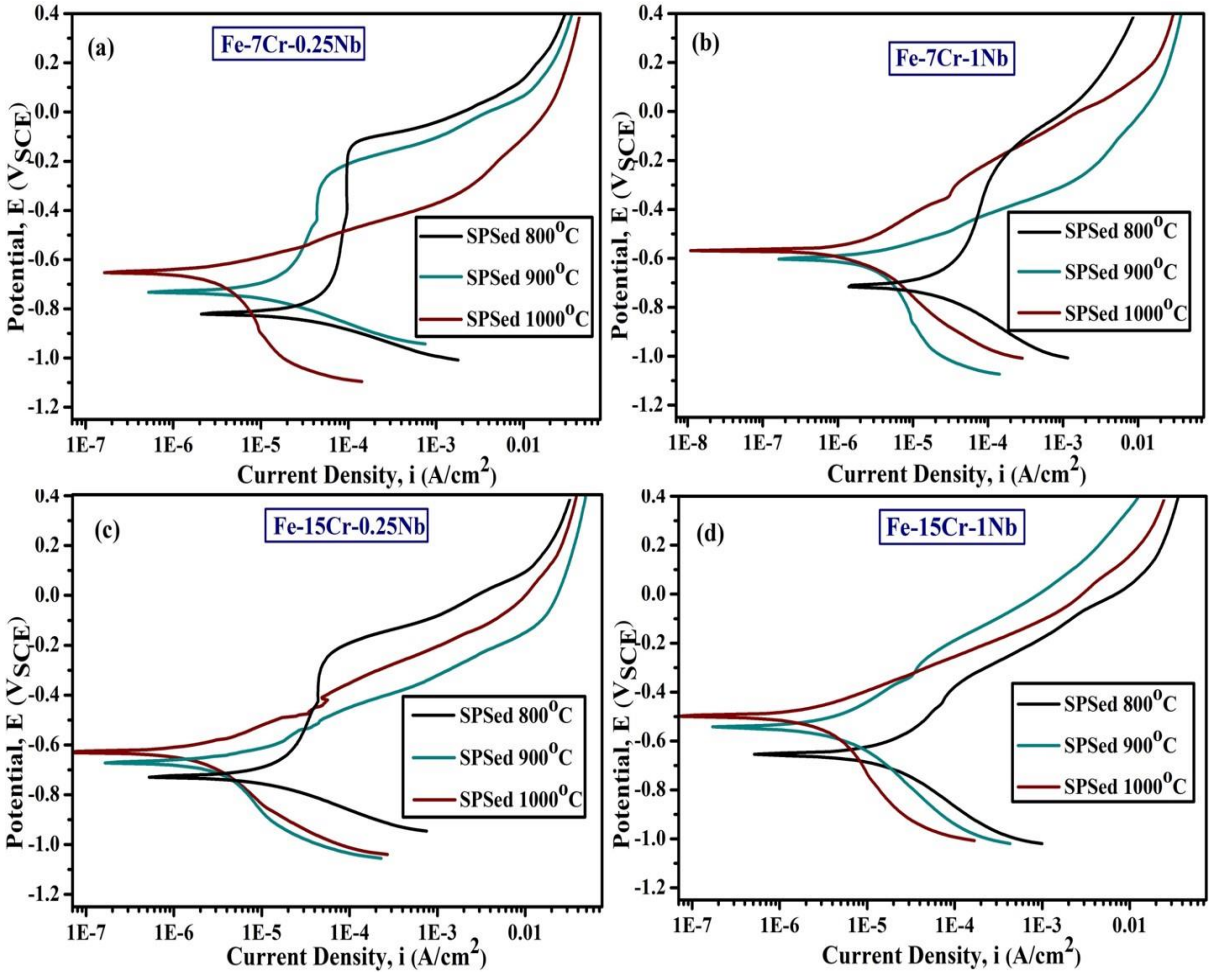

Fig. 4.58: Potentiodynamic polarization behavior as a function of current density with 3.5 wt.% NaCl solutions for the samples of (a) Fe-7Cr-0.25Nb (b) Fe-7Cr-1Nb, (c) Fe-15Cr-0.25Nb and (d) Fe-15Cr-1Nb alloys sintered at different temperatures.

Figs. 4.58a-d, respectively, show the potentiodynamic polarization data as a function of current density for four alloys, i.e. Fe-7Cr-0.25Nb, Fe-7Cr-1Nb, Fe-15Cr-0.25Nb and Fe-15Cr-1Nb sintered at 800, 900 and 1000°C. The potentiodynamic polarization tests were performed in an aerated 3.5wt.% aqueous NaCl solution at room temperature. The corrosion rate (CR) was determined using the following formula (Fontana 2005):

CR (in mil per year) = $0.13 \times i_{corr}$ (μAcm^{-2}) × [eqv. wt. of sample/density of sample]

The corresponding E_{corr} and i_{corr} values were acquired from the corresponding polarization curve (Figs. 4.58a-d) using Tafel extrapolation method. The estimated values of E_{corr}, i_{corr} and corrosion rate (CR) of the corresponding sintered samples are shown in Table 4.6.

Composition	Sintering Temperatures (°C)	Corrosion results		
		E_{corr} (V_{SCE})	I_{corr} (μA/cm^2)	CR (mpy)
Fe-7Cr-0.25Nb	800°C	-0.834	35.40	19.73
	900°C	-0.733	24.08	11.88
	1000°C	-0.649	16.10	8.21
Fe-7Cr-1Nb	800°C	-0.730	28.20	15.90
	900°C	-0.628	20.58	9.52
	1000°C	-0.578	13.20	6.03
Fe-15Cr-0.25Nb	800°C	-0.745	19.30	8.81
	900°C	-0.678	15.50	7.07
	1000°C	-0.605	7.73	4.66
Fe-15Cr-1Nb	800°C	-0.652	15.90	7.59
	900°C	-0.554	10.60	6.81
	1000°C	-0.508	6.78	4.12

It can be noticed from Table 4.6 (as well as from Figs. 4.58a-d) that the corrosion resistance gradually improved with increase in the sintering temperature. It can be clearly observed from the values of E_{corr}, I_{corr} and CR of the corresponding samples. The CR of the samples SPSed at 1000°C is quite low (only 4.12 & 4.66 mpy) in comparison to that (18.81 & 7.59 mpy) of the samples sintered at 800°C (Fig. 4.58c & d). Moreover, the corrosion resistance of the SPSed Fe-15Cr-1Nb sample is much better than that of the SPSed Fe-7Cr-1Nb sample. For example, the CR of the Fe-15Cr-1Nb alloy sintered at 1000°C is only 4.12 mpy as compared to 6.03 mpy for the Fe-7Cr-1Nb alloy sintered at the same temperature. The improvement of the corrosion resistance can be accomplished to the improvement of the densification percentage and presence of larger amount nobler Cr present in the Fe-based solid solution.

It is found that the four alloy samples sintered at 1000°C showed high corrosion resistance due to presence of less porosity as compared to the other sintered samples. Guo et al. (2014) also observed the similar corrosion behavior for the sintered Ti-Nb24-Zr4-Sn7.9 samples. The sample of lower density always contains high level of interconnected porosity. When sintering temperature increase, the density also increases by eliminating the interconnected pores (Guo et al., 2014). Hence, there is less opportunity for the corrosive electrolyte to penetrate into the highly dense sample thereby increasing the corrosion resistance. It is known that when the porosities in the sintered samples are filled up with corrosion medium, it forms stagnation in pores, which further lead to crevice corrosion (Guo et al., 2014). Li et al. (2016) reported that the increase in Cr content in Fe-xCr-3.5Mo-5Ni-10P-4C-4B-2.5Si alloy increased its thermal

stability and corrosion resistance. They have also explained that 4at.% of Cr was very effective in improving the corrosion resistance of the alloy in 3.5wt.% NaCl solution at room temperature. Wu et al. (2018) investigated the effect of Nb (0.25-1.25 wt.%) on the corrosion resistance of 316 stainless steel plate and reported that addition of Nb increased corrosion resistance (lower corrosion rate) in 3.5wt.% NaCl solution.

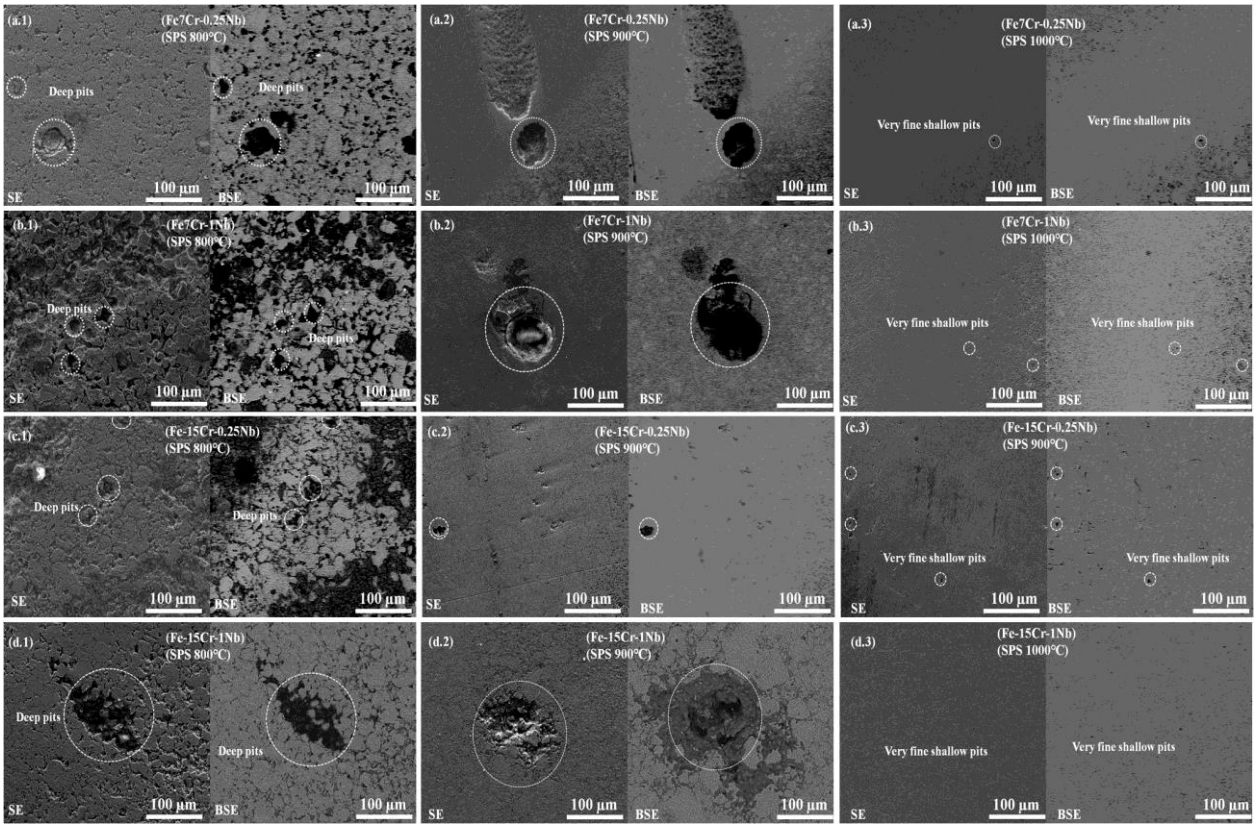

Fig. 4.59: SEM images showing pitting surface morphology of the (a) Fe-7Cr-0.25Nb (b) Fe-7Cr-1Nb, (c) Fe-15Cr-0.25Nb and (d) Fe-15Cr-1Nb alloy samples sintered at various temperatures.

Figs. 4.59a-d show SEM images of the SPSed samples sintered at 800, 900 and 1000ºC after the potentiodynamic polarization test. The samples sintered at 800 and 900ºC (Figs. 4.59a_1, a_2, b_1, b_2, c_1, c_2 and d_1, d_2) revealed deeper pits indicating severe corrosion of the specimens. Further, the samples sintered at 1000ºC revealed very fine and shallow pits (as can be seen from Figs. 4.59a_3, b_3, c_3 & d_3) mainly because of less interconnected porosities present in the sample. Also, the specimens sintered at lower temperatures contained more open and interconnected porosities, which provided more opportunity to form deeper and larger pits. It is also reported that high Cr content alloy leads to excellent corrosion resistance under potentiodynamic polarization test condition. It is known that when Cr alloyed with Fe changes the passivating potential of Fe to more active values and drastically lowers the critical current

density required for passivation (Fontana 2005). Therefore, at very small i_{corr} values, self-passivation occurs to form an impervious passive film of Cr_2O_3, if the steel contains more than 12% Cr. In the present study also, the high Cr content (14.03 wt.%) alloy (i.e.Fe-15Cr-0.25Nb & Fe-15Cr-1Nb) showed a better corrosion resistance and less pit formation because of the formation passive impervious film on the highly dense sample (Guo et al., 2014; Li et al., 2016) Addition of Nb in novel 316 stainless steel also reported to enhance formation of passive film susceptibly thereby improve the corrosion resistance (Wu et al., 2018).

4.3.2.4 Summary

In the present study, bulk size Fe-7Cr-0.25Nb, Fe-7Cr-1Nb, Fe-15Cr-0.25Nb and Fe-15Cr-1Nb samples were developed successfully by MA followed by SPS. The SPS process parameters such as dwell time, temperature and pressure have been optimized to obtain the near full density bulk nanostructured samples with high hardness and high compressive yield strength. The following outcomes from the present investigation have been concluded.

(a) The maximum sintered density was determined to be 97-98% for the four alloy samples sintered at 1000°C. The maximum level of sintered density could be ascribed to the prevalent grain-boundary, surface and bulk diffusion at higher sintering temperature and formation of necks due to deformation at contact points (because of applied pressure).

(b) TEM investigation confirmed that the individual grain size was retained within the nanometer range (i.e. <100 nm) for the Fe-7Cr-1Nb and Fe-15Cr-1Nb alloy samples after SPS at 1000ºC. Moreover, retention of the complete solid solubility of Cr and Nb after SPS at 1000ºC is ascertained from the TEM-SAED and XRD pattern analysis. This might have improved the mechanical properties.

(c) The Vickers hardness values were estimated to be quite high 8.7 and 9.4 GPa for the Fe-7Cr-1Nb and Fe-15Cr-1Nb samples sintered at 1000ºC. Ultimate compressive strength of the near full density Fe-15Cr-1Nb SPSed (at 1000ºC) sample was found to be quite attractive (2400 MPa). The predicted yield strength (Fe-15Cr-1Nb:1744 MPa) calculated from the solid solution strengthening, grain size strengthening and dislocation strengthening mechanisms is highly correlated with the experimentally determined compressive yield strength (1800MPa). Retaining of complete solid solubility of Cr and Nb, achieving near full density nanocrystalline structure and

dislocation hardening could be ascribed for obtaining such high mechanical strength of the SPSed samples.

(d) The wear resistance of the SPSed Fe-15Cr-1Nb alloy is found to be superior than that of any other samples sintered at the same conditions. Moreover, the samples which were sintered at higher temperature, showed better corrosion resistance. For example, the wear rate of the Fe-15Cr-1Nb SPSed sample was estimated to be very low, which was confirmed from the wear volume (0.00169×10^{-2} mm^3) analysis as compared to wear volume of 0.00240×10^{-2} mm^3 for the SPSed Fe-7Cr-1Nb sample. The better wear resistance is ascribed to the maximum densification of the corresponding sample.

(e) The superior corrosion resistance of the highly dense Fe-15Cr-1Nb sample (sintered at 1000ºC) is accomplished to the maximum densification and retaining of complete solid solubility of more amount of Cr after sintering. Formation of Cr_2O_3 impervious oxide layer plays an important role for the better corrosion resistance of the Fe-15Cr-1Nb alloy. The SEM images of the corroded samples corroborate well with corrosion rate of the corresponding sample.

4.4 Development of Fe-7Cr-Zr and Fe-15Cr-Zr alloys by MA

On the basis of crystallite size and microhardness data of the as-milled and annealed (600-1200°C) samples of Fe-Cr alloys (Cr=7, 11, 15 & 19 at.%), Fe-7Cr and Fe-15Cr alloys were selected for further investigation. Hence, Fe-7Cr-Zr and Fe-15Cr-Zr (Zr=0.25, 0.5 and 1at.%) alloys were produced under same milling conditions to investigate the effect of Zr on the formation of Fe-Cr-Zr solid solutions and their thermal stability. Validity of formation of ternary Fe-Cr-Zr solid solutions has been analyzed in the light of phase analysis, change in the Gibbs free energy etc. On the basis of the thermal stability, some selected alloys were consolidated by SPS and the SPSed samples were further analyzed for the microstructure and mechanical properties. First analysis of formation of Fe-Cr-Zr solid solutions and its thermal stability, and then consolidation by SPS and mechanical properties would be discussed in the subsequent sections.

4.4.1 Formation of Fe-Cr-Zr alloys by MA and its thermal stability

First, effect of Zr content was studied on the thermal stability of Fe-Zr alloys and it was found that the Zr could be a good stabilizer of nanocrystalline Fe (Sooraj et al., 2016). Since, Zr showed good

thermal stability, it is expected to stabilize the Fe-Cr-Zr alloys also. The selected Fe-7Cr-Zr and Fe-15Cr-Zr (Zr=0.25, 0.5, 1at.%) alloys were developed by MA for 25 h under the same milling conditions as done in the Fe-Cr, Fe-Cr-Y and Fe-Cr-Nb systems. Then, phase evolution, their microstructural features and thermal stability have been investigated and discussed in details in the subsequent sections.

4.4.1.1 Effect of Zr on phase analysis of Fe-Cr-Zr alloys and its microstructural analysis

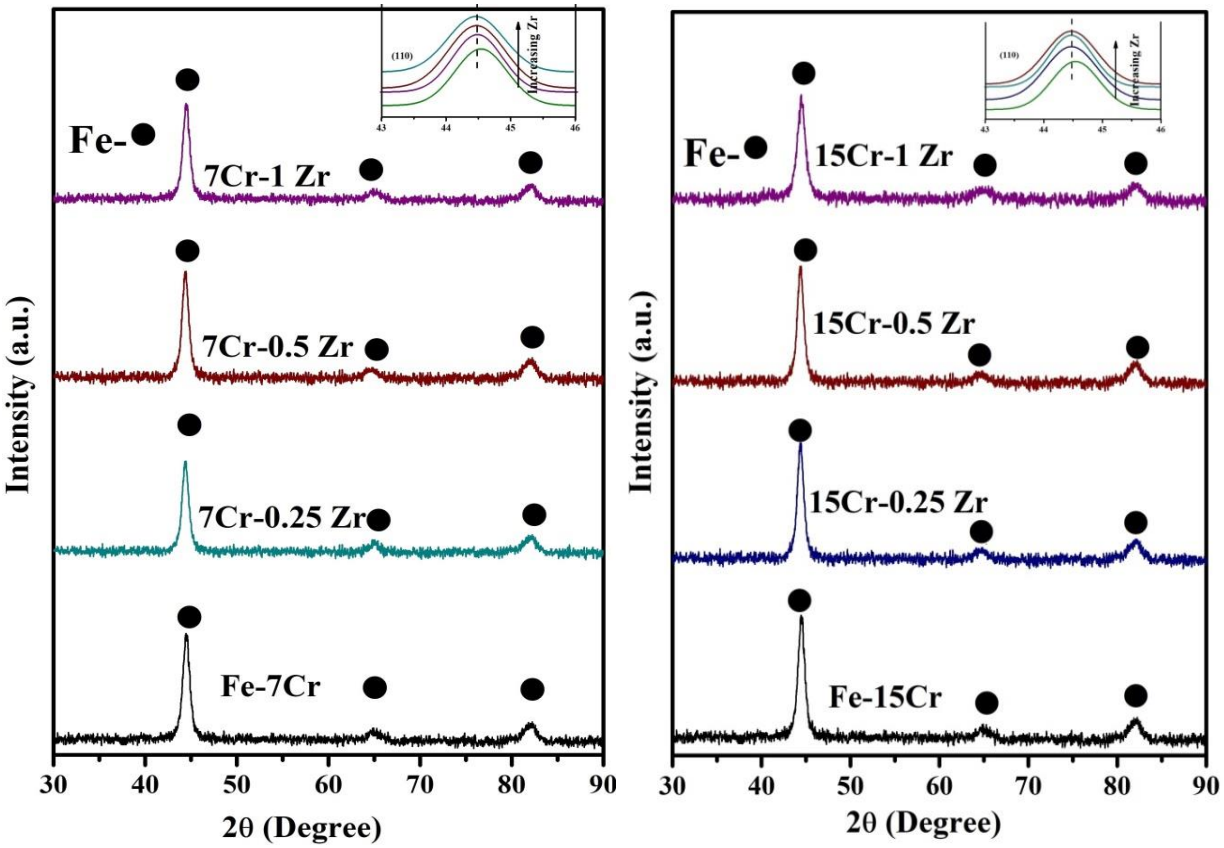

Fig.4.60: X-ray diffraction patterns showing the alloy formation by MA for 25 h; (a) Fe-7Cr-Zr & (b) Fe-15Cr-Zr (Zr=0.25, 0.5 and 1 at.%). Shifting of peak and peak broadening with Zr content are shown in the inset**.**

Figs. 4.60a and b, respectively, show the XRD patterns of Fe-7at.%Cr and Fe-15at.%Cr alloys with varying concentration of Zr (Zr=0.25, 0.5 & 1 at.%). The choice of Cr content in Fe, in the present work, was determined and discussed in the earlier section 4.1.1. It can be noticed that the formation of any intermetallic phase(s) or presence of free element Cr or Zr is not detectable from the XRD patterns of any composition. As per the XRD phase analysis, it is observed that the added Cr and Zr are completely dissolved in the Fe matrix after 25 h of MA. It can be noticed particularly from the high angle peaks, that the peak intensity gradually

decreased and peak width at full-width half of maximum (FWHM) increased with increase in the Zr content. Also, the peak position is found to shift towards left (lower 2θ position) with increase in the Zr content. The peak shift, peak broadening and decrease in the intensity as a function of Zr content are illustrated for the (110) peak in the inset of Figs. 4.60a and b. The sensitivity of the XRD analysis is limited to detect the presence of any secondary phase(s) (<2wt.%) in the matrix (Cullity 1978; Suryanarayana et al., 1998). Therefore, it will not be wise to comment about the complete solid solubility of Cr and Zr in the Fe lattice from the XRD phase analysis only. It is known that if solute atoms dissolve in the matrix the lattice parameter of the matrix would be changed (Koch 2007; Suryanarayana et al., 1998). Therefore, this could be an important tool to correlate solid solubility extension of a solute element in the solvent (Koch 2007).

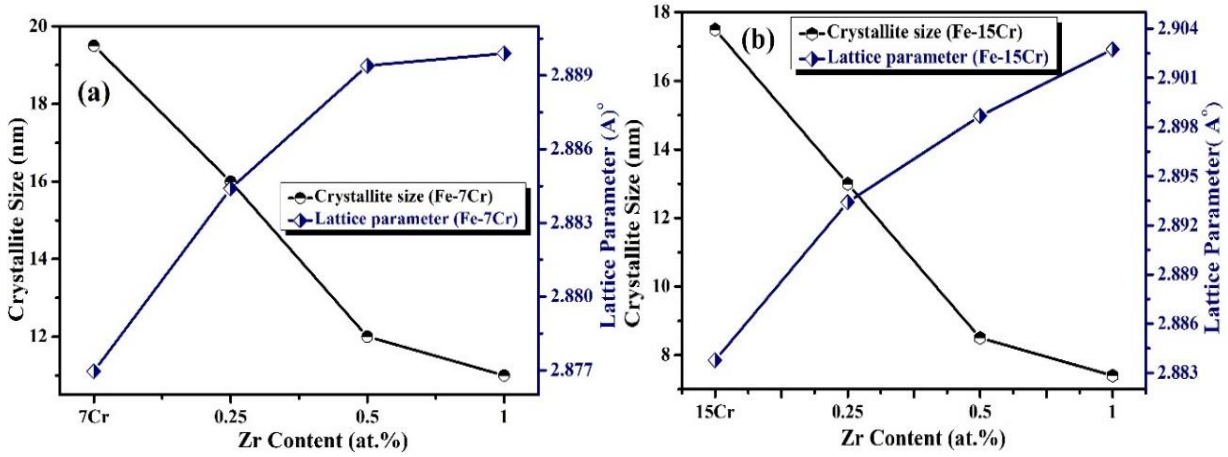

Figs. 4.61a & b: Show the variation of lattice parameters and crystallite size as a function of Zr concentration.

Figs. 4.61a and b, show the variation of the lattice parameter of the Fe-based solid solutions (a_{Fe}) and changes in the crystallite size as a function of Zr content of the as-milled Fe-7Cr-Zr and Fe-15Cr-Zr alloys, respectively. The average crystallite size was calculated using Williamson and Hall analysis (Cullity 1978; Suryanarayana et al., 1998) from XRD peaks of the corresponding sample. The crystallite size is found to decrease with increase in the Zr content. The average crystallite size for Fe-7Cr-Zr alloys decreased from ~16 nm (for 0.25% Nb) to 11 nm corresponding to 1% Zr. The crystallite size was determined to be ~19.5 nm for Fe-7Cr alloy without any Zr addition. Similar trend is found in the Fe-15Cr alloys where the average crystallite size decreased from ~13 nm (for 0.25% Zr) to 7.8 nm for the 1% Zr alloy. It is to be noted that the estimated crystallite size was ~17.5 nm for pure Fe-15Cr alloy without any Zr. Saber et al. (2012) reported that the average crystallite size was retained <50 nm after

20h MA of Fe-Cr alloy with 1-4 at.% Zr. The lattice parameter of the Fe-Cr-Zr alloys (a_{Fe}) was calculated using all XRD peaks through extrapolation of a_{Fe} vs. ($\cos^2\theta/\sin\theta$) plot to $\cos\theta = 0$ (Cullity 1978; Suryanarayana et al., 1998). The change in the lattice parameter is only possible when the Cr and/or Zr atoms are dissolved into the Fe-lattices to form a solid solution (Koch et al., 2008; Michels et al., 1999; Millett et al., 2007). It is to be noted that the lattice parameter of pure Fe is 2.868Å. It can be found (Figs. 4.61a & b) that the lattice parameter gradually increases with increase in the Zr content. The maximum increase in the lattice parameter (a_{Fe}) was obtained in the Fe-15Cr-1Zr alloy, and the maximum value is found to be 2.902Å as compared to 2.889Å for the Fe-7Cr-1Zr alloy. Therefore, the increase in the lattice parameter, a_{Fe} obtained is not only due to the dissolution of Zr only, but also due to the Cr solution (Saber et al., 2012). Krill et al. (2005) reported that after 24 h MA of Pd-Zr alloys, the grain-size decreased with increasing in the lattice parameter of Pd as Zr content (10-20at.%) increased.

TEM analysis of the as-milled sample

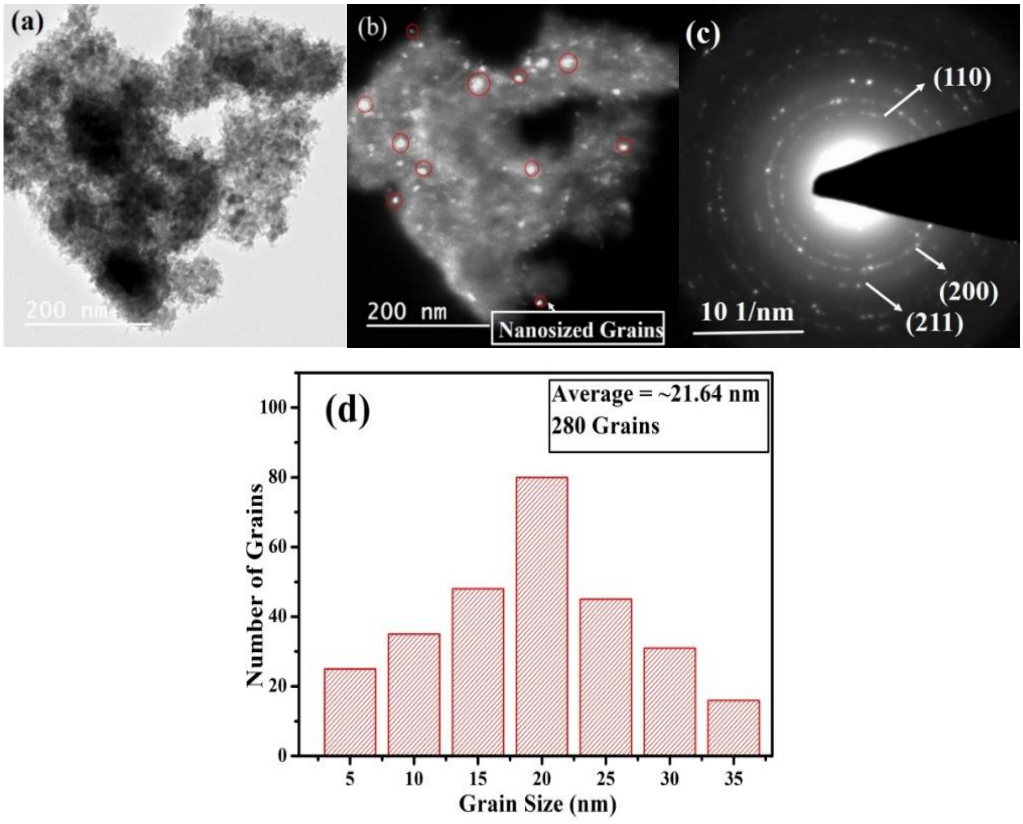

Fig. 4.62: (a) Bright field TEM images, (b) Dark field TEM image (c) selected area diffraction pattern of the 25 h milled sample for the Fe-15Cr-1Zr alloy. (d) Statistical distribution of grains obtained from dark field images.

Figs. 4.62a & b show the bright field and dark field TEM micrographs for the as-milled sample of Fe-15Cr-1Zr. The bright field and dark field TEM images were recorded to analyze the grain size of the as-milled sample. It can be observed from the TEM images (Figs. 4.62a & b) that the grain size is well within the nanometric range (<100 nm). It can be clearly observed from the SAED pattern (Fig. 4.62c) that all the peaks correspond to the Fe-based alloy only, i.e. (110), (220) and (211) (Saber et al., 2012; Williams et al., 1996). The presence of continuous rings clearly show that the grain size is within the nanometric level. Moreover, analysis of the SAED patterns does not show any other ring/spot corresponds to elemental Zr/Cr or any intermetallic phase. Therefore, it can be concluded again that a complete solid solution of Fe-15Cr-1Zr is formed by MA for 25 h. The XRD analysis and variation of a_{Fe} also confirmed that the same. The average grain size has been determined from TEM images (as one is shown in Fig. 4.62b) using the statistical distribution of at least 280 grains. The distribution of grain sizes is shown in Fig. 4.62d and the average grain size is estimated to be ~22 nm. The average grain size obtained through TEM analysis is found to correlate well with the XRD crystallite size of the corresponding sample (Fig. 4.61b).

4.4.1.2 Thermodynamic analysis

Formation of ternary Fe-Cr-Zr solid solutions by MA has been analyzed from the change in Gibbs free energy as per the Toop's model (Miedema et al., 1980b; Niessen et al., 1988). The calculation of Gibbs energy variation as per Toop's model requires the analysis of Miedema's semi-empirical model for the binary solid solutions first and then the same extended for ternary system. The details of the Miedema's semi-empirical model, Toop's model and analytical equations of the Gibbs free energy change were already discussed in the earlier section 4.2.1.2.

Table 4.7: Parameters required for the thermodynamic analysis as per Miedema's model for Fe-Cr, Fe-Zr and Cr-Zr binary systems (Miedema et al., 1980b; Niessen et al., 1988).

Parameters	**Fe**	**Cr**	**Zr**
$n_{ws}^{1/3}$ **(cm^{-1})**	1.77	1.73	1.39
V_m **(cm^3 mol^{-1})**	7.09	7.12	14.02
Φ **(V)**	4.5	4.65	4.12
K **(* 10^{10} Nm^{-2})**	17	16.02	9.11
G **(* 10^{10} Nm^{-2})**	8.2	11.53	3.3
T **(K)**	1811	2130	2128

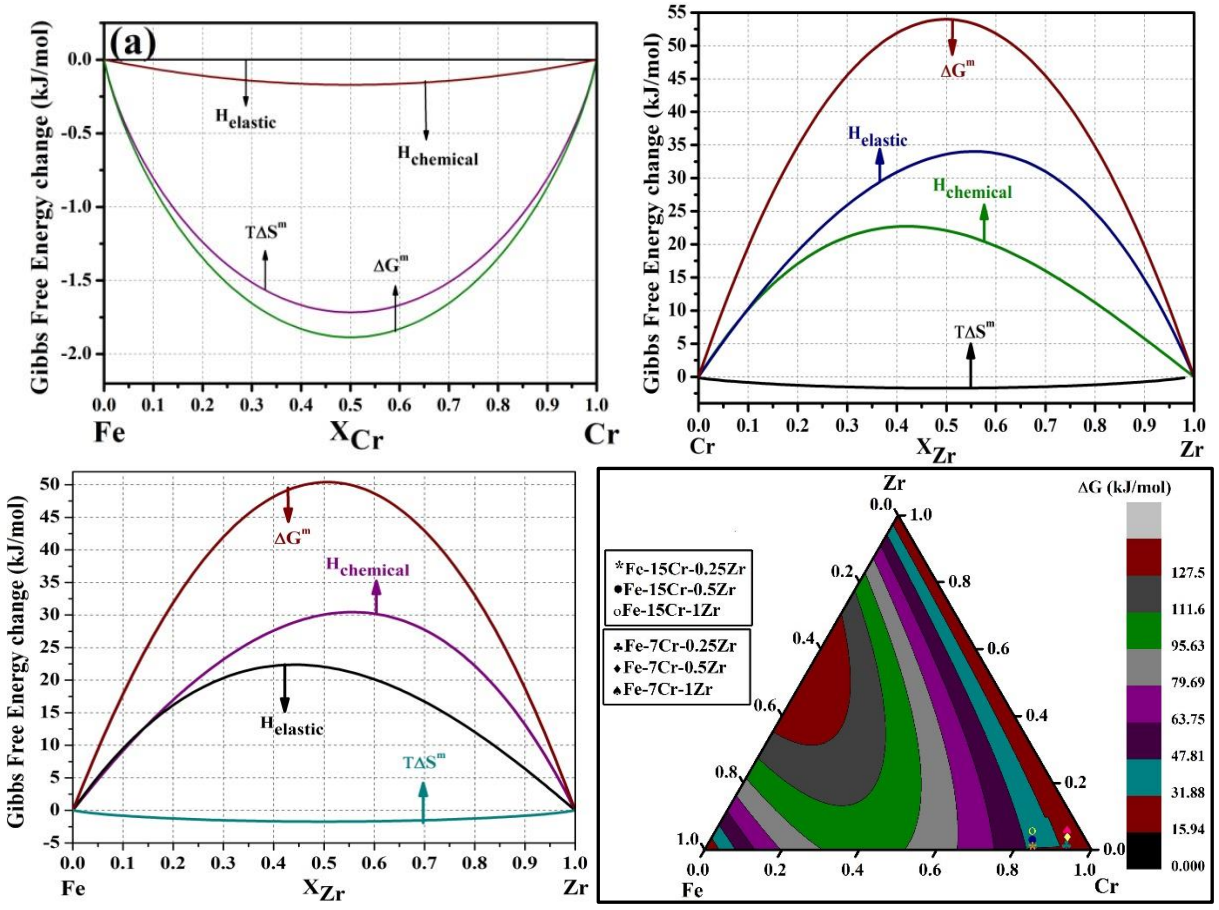

Fig. 4.63: Enthalpy, entropy and Gibbs free energy change for the formation of metastable solid solution in (a) Fe-Cr (b) Fe-Zr (c) Cr-Zr and(d) Fe-Cr-Zr ternary system.

The enthalpy, entropy and Gibbs free energy change to form stable Fe-Cr and metastable Fe-Zr and Cr-Zr solid solutions at room temperature have been calculated using formulae as per Miedema's and Toop's models **(**discussed in the earlier section 4.2.1.2.) and the relevant plots are shown in Figs. 4.63a-c. The total Gibbs free energy change is found to be negative for Fe-Cr binary system according to Hume-Rothey's rule (Callister et al., 2007). The total Gibbs free energy change for both the binary systems of Fe-Zr and Cr-Zr alloys is found to be positive (i.e. $\Delta G>0$ non-spontaneous reactions) in the entire compositional range, and there is no driving force to form a solid solution under equilibrium condition between them. Therefore, formation of solid solutions cannot be achieved for Fe-Zr and Cr-Zr systems by any equilibrium processing method. One possible way of producing Fe-Cr-Zr disordered solid solutions is by non-equilibrium methods such as MA (Bhadeshia 2000; Suryanarayana 2001). The enthalpy contribution due to chemical reaction, $\Delta H_{chemical}$ is observed to be completely positive but the value is smaller than that of the elastic contribution ($\Delta H_{elastic}$) for the Fe-Zr and Cr-Zr systems. This is because of small differences in the electron density and work function of the constituent

elements. Therefore, there is very less chance for Zr atoms to react chemically with Fe/Cr, which may result in the formation of intermetallic phases. Meanwhile, the elastic contribution is more dominant (positive) due to the large atomic size difference between Fe (0.126 nm)/Zr (0.158nm) and Cr (0.128 nm)/Zr (0.158 nm).

The enthalpy of mixing, ΔH^m for the Fe-Cr-Zr ternary alloys was calculated using asymmetrical model predicted by Toop et al. (Toop 1965) (also called Toop's model). This is basically based on the extension of Miedema's model to consider the effect of third element. The Toop's model avoids the large deviation of calculated values from the experiment when constituent elements have different physical properties (Toop 1965). In this model, initially $\Delta H_{elastic}$ and $\Delta H_{chemical}$ of 3 binary systems, i.e. Fe-Cr, Fe-Zr and Cr-Zr were calculated individually, and then finally ΔH^m for ternary Fe-Cr-Zr alloys was computed through interpolation methods, applying the Toop's model (Toop 1965) given in Eq.4.9. Fig. 4.63d shows the Gibbs free energy change needed to form a disordered solid solution of any composition in Fe-Cr-Zr ternary systems. The alloy compositions are found to have positive Gibbs free energy change as per the Toop's model. That means, to form disordered solid solutions of any of the alloy compositions, the excess free energy has to be supplied to the system by a nonequilibrium method. The Gibbs free energy values as per Toop's model and experimental calculations are shown in Table 4.7.

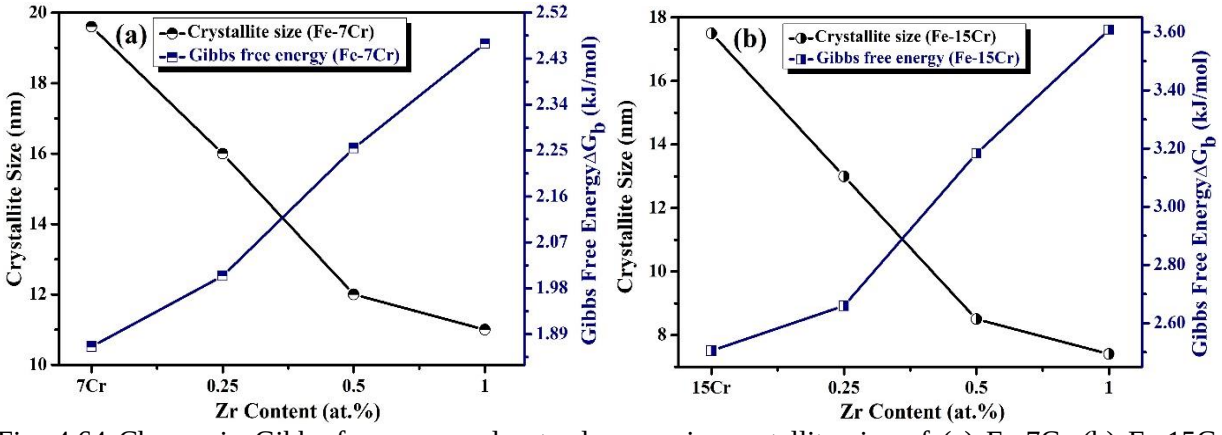

Fig. 4.64 Change in Gibbs free energy due to decrease in crystallite size of (a) Fe-7Cr (b) Fe-15Cr alloys as a function of Zr.

Figs. 4.64a and b, respectively, show change in the crystallite size and Gibbs free energy change (ΔG_b) of Fe-7Cr-Zr and Fe-15Cr-Zr alloys as a function of Zr content. The crystallite size decreased with an increase in the Zr content (Figs. 4.61a and b). The ΔG_b was calculated using the Eq.4.10 (discussed in the earlier section 4.2.1.2). It can be observed from the Figs. 4.64a and b (as-milled condition) that the ΔG_b increased after addition of 1at.% Zr for both the

alloys. For example, the ΔG_b increased from 2.50 kJ/mol for the Fe-15Cr alloy to 3.60 kJ/mol in the Fe-15Cr-1Zr alloy. Moreover, it can be noticed that increase in the ΔG_b is more for the Fe-15Cr-1Zr alloy than that of the Fe-7Cr-1Zr. Hence, it can be concluded that the increase in the ΔG_b occurs not only due to the addition of Zr but also because of Cr solution.

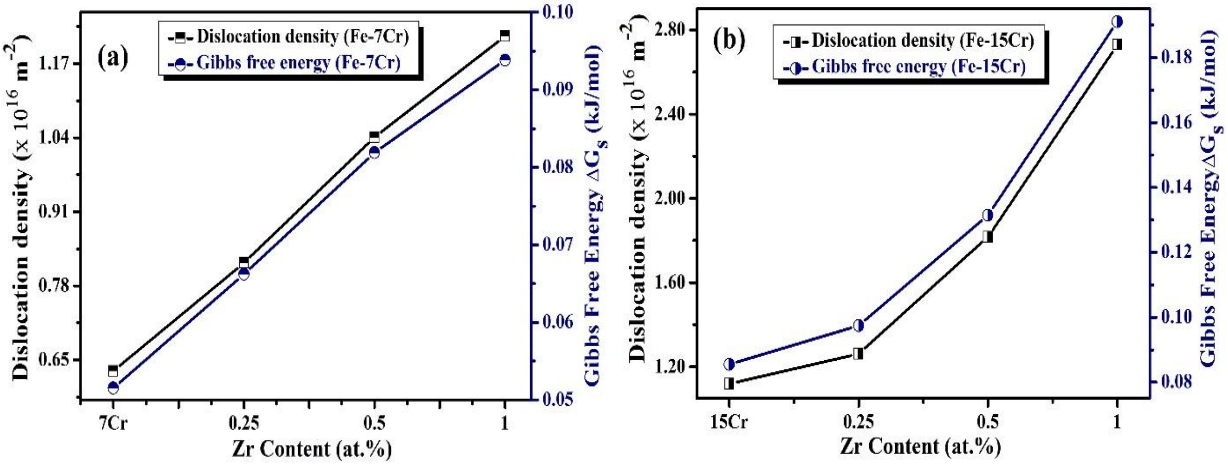

Fig. 4.65: Variation of Gibbs free energy change due to increase in dislocation density (a) Fe-7Cr (b) Fe-15Cr alloy system as a function of Zr.

Figs. 4.65a and b, respectively, show the increase in the Gibbs free energy change due to the increase in the dislocation density for Fe-7Cr and Fe-15Cr alloys as a function of Zr. It was found that ΔG_s gradually increased with Zr content and attained a value of ~0.093 and ~0.192 kJ/mol, respectively, for Fe-7Cr-1Zr and Fe-15Cr-1Zr alloys. It is observed that increase in the ΔG_s is much less as compared to that due to the ΔG_b. Therefore, $\Delta G_T = \Delta G_b + \Delta G_s$, is estimated to be 3.851 kJ/mol for the as-milled Fe-15Cr-1Zr alloy. This value (3.851 kJ/mol) is higher than ΔG_{Toop} (3.68 kJ/mol) as per the as per the Toop's model. It can be observed from Table 4.8 that for all the Fe-Cr-Zr compositions, ΔG_T is higher than ΔG_{Toop}. Therefore, it can be concluded that the total stored energy, ΔG_T is sufficient to form disordered solid solution as per the Toop's model. XRD and TEM diffraction analysis also established the same. Similar observation is made for the Fe-Cr-Y and Fe-Cr-Nb alloys also. Like the other 2 systems studied, here also the enthalpy changed due to structural contribution ($\Delta S_{structural}$) from Zr is neglected for practical simplicity as it is a very small positive value.

Table 4.8: Total Gibbs free energy change ($\Delta G_b+\Delta G_s$) due to the reduction in crystallite size and due to the increase in the dislocation density is compared with that estimated from the Toop's model.

Alloy (all in at.%)	ΔG_b **(kJ/mol)**	ΔG_s **(kJ/mol)**	$\Delta G_T=\Delta G_b+\Delta G_s$ **(kJ/mol)**	ΔG_{Toop} **(kJ/mol)**
Fe-7Cr-0.25Zr	2.00	0.066	2.066	1.56
Fe-7Cr-0.5Zr	2.254	0.081	2.336	1.89
Fe-7Cr-1Zr	2.459	0.093	2.553	2.32
Fe-15Cr-0.25Zr	2.659	0.097	2.756	1.96
Fe-15Cr-0.5Zr	3.182	0.131	3.314	2.92
Fe-15Cr-1Zr	3.659	0.192	3.851	3.68

4.4.1.3 Thermal stability and mechanical properties

Batch annealing was carried out for samples of the Fe-7Cr-1Zr and Fe-15Cr-1Zr alloys at 600, 800, 1000 and 1200°C under controlled Ar+2% H_2 atmosphere for 1 h. After that the XRD analysis was done for the annealed samples. Crystallite size of the annealed sample was calculated from the XRD data and accorded with the same of the as-milled sample. The annealed samples were also examined to validate the microhardness values as compared to that of the as-milled sample. Thus, the changes in the crystallite and corresponding microhardness value after annealing can clarify the thermal stability of the material.

Fig. 4.66a and b, respectively, show the XRD phase analysis of the annealed samples. The phase analysis revealed formation of Fe_2Zr intermetallic phase during annealing of the sample. It can be noticed from Figs. 4.66a and b that number of minor peaks related to intermetallic phase are evolved after annealing the samples. The XRD analysis clearly depicts that the width (FWHM) of (e.g. Fe-110 reflection) the peaks decreased with increase in the intensity as the annealing temperature increases (Fig. 4.66a and b). It is important to note that formation of the complete solid solutions of Fe-7Cr-1Zr and Fe-15Cr-1Zr alloys was confirmed (discussed in the earlier section 4.4.1.1; Figs.4.60a & b). The formation of intermetallic phase is expected to play an important role to stabilize the matrix by Zener pinning. The thermal stability of nanocrystalline Fe-Zr alloys was ascribed to the presence of Fe_2Zr intermetallic compound in Sooraj et al. (2016).

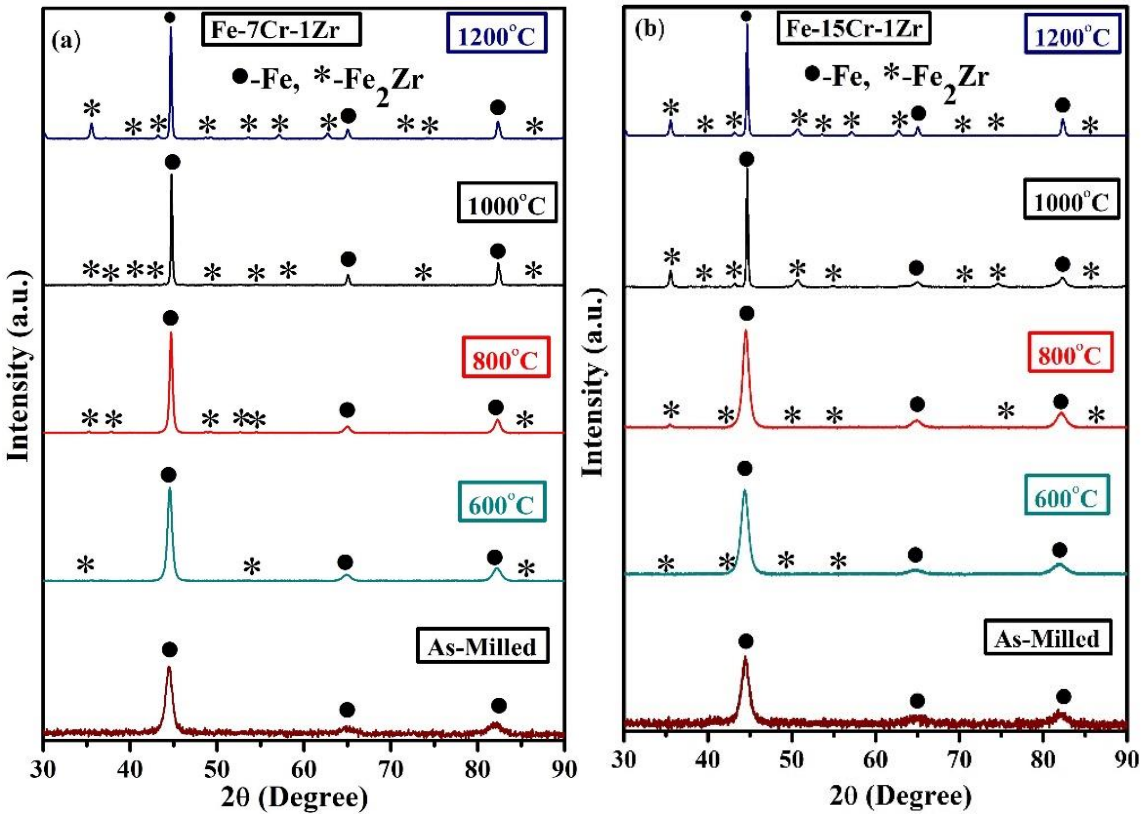

Fig. 4.66: XRD patterns of the as-milled and annealed at different temperatures samples of (a) Fe-7Cr-1Zr and (b) Fe-15Cr-1Zr alloys.

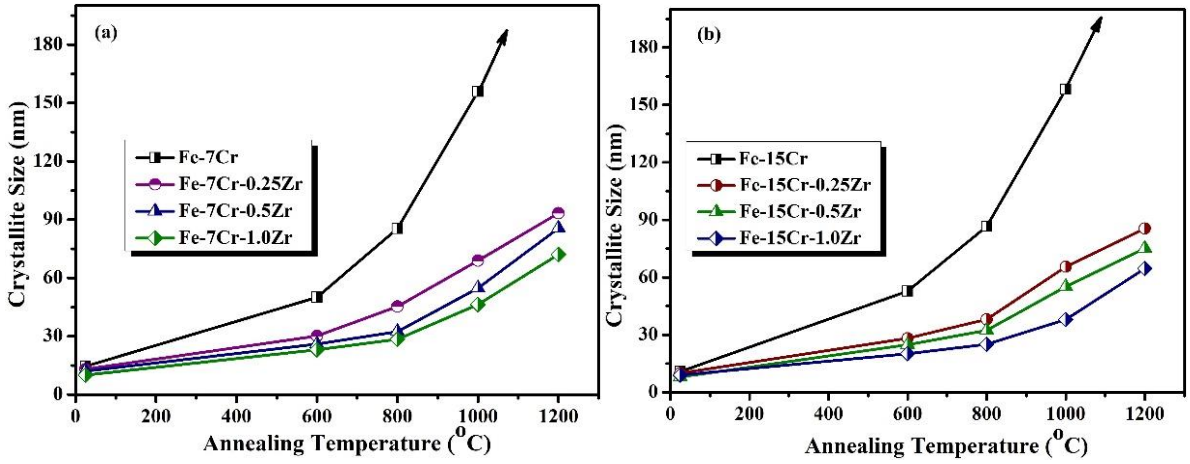

Fig. 4.67: Variation of crystallite size vs. annealing temperatures for (a) Fe-7Cr (b) Fe-15Cr alloy system as a function of Zr.

Figs. 4.67a and b, respectively, show variation of the crystallite size of the Fe-7Cr-Zr and Fe-15Cr-Zr samples annealed at different temperatures. It can be observed that the variation of crystallite size has almost similar trend for both the alloy systems as a function of annealing temperatures. Both the Fe-Cr alloys without Zr showed typical grain coarsening tendency (i.e. rapid grain growth) at 800°C or above. The crystallite size of the as-milled samples of Fe-7Cr-

1Zr and Fe-15Cr-1Zr was measured to be 11 and 8 nm, respectively (Figs. 4.61a and b). The crystallite size is found to increase slowly and stabilize at 1000°C. After annealing the samples at 1000°C, the crystallite size is estimated to be only 47 and 38 nm, respectively, for the Fe-7Cr-1Zr and Fe-15Cr-1Zr alloys. The retaining the grain size at <50 nm after annealing at 1000°C indicates that Zr has a significant stabilizing effect on Fe-7Cr and Fe-15Cr alloys at high temperatures. Excellent thermal stability by Zr atoms in nanocrystalline Fe has been reported by Sooraj et al. (2016). Darling et al. (2010) also reported a good thermal stability of Fe-4at.% Zr alloy at 1373ºC (grain size of 52 nm); whereas pure Fe reached a grain size of 6µm at approximately 700ºC. Saber et al. (2012) also reported that the Fe-Cr alloys with addition of 2at.% Zr could maintain nanaoscale grains up to 900°C. Hence, thermodynamic mechanism of solute segregation, especially by Zr atoms along grain boundaries played the pivotal role to stabilize the Fe-Cr-Zr alloys. Moreover, formation of Fe_2Zr intermetallic phase also played an important role (kinetic pinning) in the stabilization of Fe-Cr-Zr alloys.

TEM analysis of the annealed sample

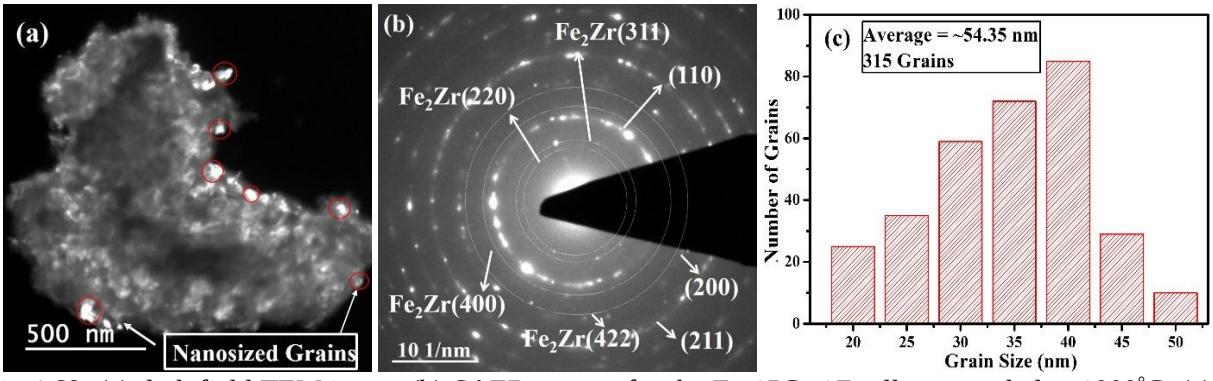

Fig.4.68: (a) dark field TEM image (b) SAED pattern for the Fe-15Cr-1Zr alloy annealed at 1000°C. (c) Statistical distribution of grains obtained from the dark field images as one shown in Fig. 4.67b.

Figs. 4.68a & b, respectively, show the dark field TEM micrograph and SAED pattern of the Fe-15Cr-1Zr alloy annealed at 1000°C. It can be noticed from Figs. 4.68a that the average grain size is well within <100 nm. The SAED pattern shows the presence of continuous spotty rings, which confirm that the grain size is fine and in the nanometer level (Fig. 4.68b). Moreover, analysis of the SAED pattern revealed that the faint rings correspond to Fe_2Zr (220, 311, 400 & 422) intermetallic phase. It can be noticed that all the major peaks of Fe (110), (220) and (211) are clearly visible from the SAED pattern. The average grain size is estimated to be 55 nm as shown in Fig. 4.68c. The TEM grain size is found to corroborate well with the XRD crystallite size (Fig. 4.66b).

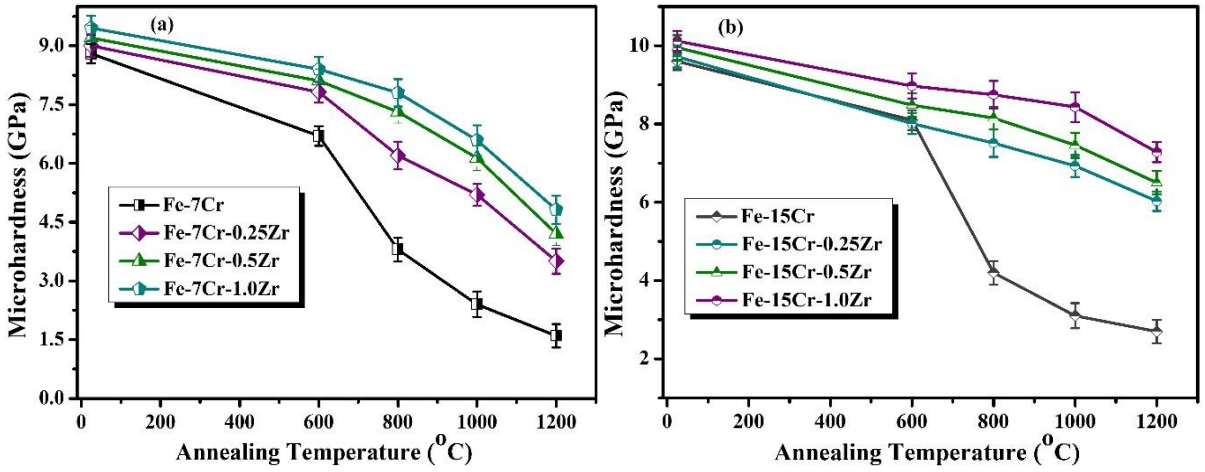

Fig. 4.69: Vickers microhardness vs. annealing temperatures for (a) Fe-7Cr (b) Fe-15Cr alloys as a function of Zr.

Figs. 4.69a and b, respectively, show the variation of microhardness values of Fe-7Cr-Zr and Fe-15Cr-Zr samples annealed at different temperatures in comparison with the hardness of the same alloy without Zr. The microhardness values of Fe-7Cr-Zr alloys are found to decrease sharply as a function of annealing temperature (Fig. 4.69a); while, Fe-15Cr-Zr alloys showed a better stability of the hardness (Fig. 4.69b). Moreover, the reduction in the hardness values of the Fe-7Cr-Zr alloys with temperature is more for the less Zr content alloys. On the other hand, only a minor decrease in the hardness value is observed for the Fe-15Cr-Zr alloys as a function of annealing temperature (Fig. 4.69b). For example, in case of samples annealed at 800°C: the hardness values of Fe-7Cr-1Zr is ~7.81 GPa (grain size 30 nm); whereas, a hardness of ~8.7GPa was measured for the annealed specimen (at 800°C) of Fe-15Cr-1Zr alloy having similar level of grain size (25 nm). Therefore, the extra hardness (0.89 GPa) for the Fe-15Cr-1Zr alloy is obtained due to the solid solution strengthening of extra Cr. Moreover, all the Fe-15Cr-Zr alloys showed much better thermal stability at any temperature as compared to that of the Fe-15Cr alloy without Zr. For example of the samples both annealed at 1000°C; the hardness of Fe-15Cr-0.25Zr alloy is estimated to be as high as 6.9 GPa (grain size 66nm) as compared to only 3.9GPa (grain size >100 nm) of Fe-15Cr alloy. Therefore, addition of 0.25% Zr in Fe-15Cr alloy is highly important to achieve superior thermal stability. On the other hand, even 1% Zr addition in Fe-7Cr alloy revealed inferior thermal stability (6.5GPa). Zr addition up to 4 at.% was reported to stabilize Fe-10Cr and Fe-18Cr alloys effectively and maintained a high hardness of 7 GPa after annealing at 900°C (Saber et al. 2012). The Zener pinning at grain boundaries by Fe_2Zr intermetallic precipitate and/or segregation of Zr atoms to the grain boundary region were identified as the stabilization mechanisms (Saber et al., 2012; Sooraj et

al., 2016). In the present study, the addition of only 0.25-1at.% Zr in Fe-15Cr alloy showed an excellent thermal stability up to 1000°C and maintained nanocrystalline grain size within 50 nm. The corresponding hardness value was measured to be 8.4 GPa, which is quite attractive. Here also, the thermodynamic mechanism of solute segregation along the grain boundaries as well as kinetic mechanism of Zener pinning by second phase particles (such as Fe_2Zr) are found to be responsible to achieve such high thermal stability.

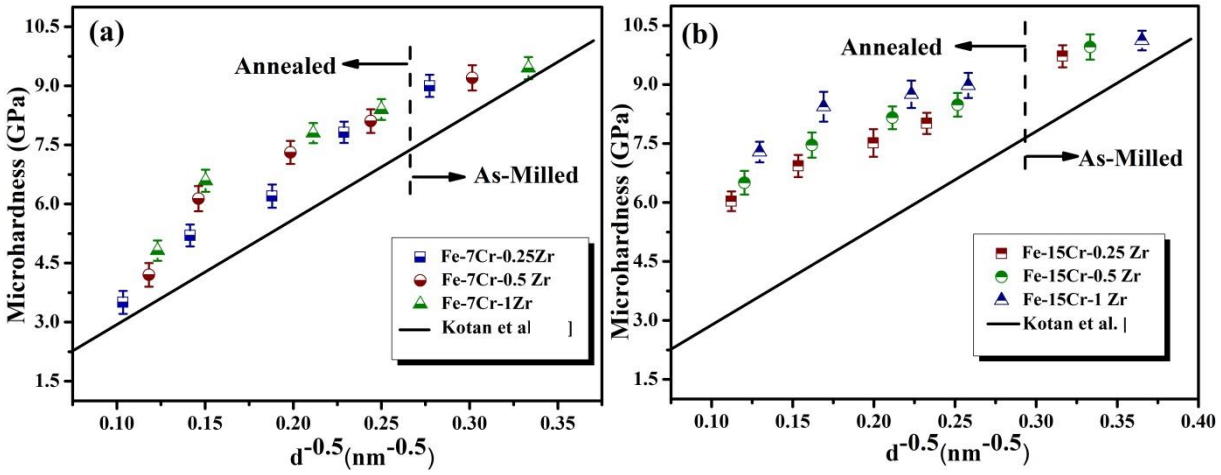

Fig. 4.70**:** Hall-Petch plot for the hardness values of as-milled and annealed samples of (a) Fe-7Cr-Zr (b) Fe-15Cr-Zr alloys.

The solid solution strengthening effect due to Cr and Zr as well effect of Zener pinning could be established from Hall-Petch plots as shown in Figs. 4.70a & b. The deviation of microhardness value from the classical H-P relation of the pure Fe can enlighten about the thermal stability of the Fe-Cr-Zr alloys. It can be observed that the hardness is more for the high solute content alloys. Fe-15Cr-Zr alloys show extra hardening effect as compared to that of the Fe-7Cr-Zr alloys. The extra hardening effect is ascribed to: (i) extra grain size refinement in Fe-15Cr-Zr alloys (ii) extra solid solution strengthening due to more Cr and (iii) the precipitation strengthening by Fe_2Zr. The strengthening effect is retained a bit only for the Fe-7Cr-1Zr composition up to 1000°C (Fig. 4.70a). The sharp decrease in the hardness values of the Fe-7Cr-Zr alloys is due to the coarsening of grains just above 600°C. Though there is minute decrease in the hardness values of the Fe-15Cr-Zr alloys, the retained hardness is superior to that of the Fe-7Cr-Zr alloys. This observation again proved that Cr and Zr together could play an important role to achieve good thermal stability of Fe-based alloys. The minute decrease in the hardness up to 600°C is ascribed to the annihilation of stored dislocations and

grain boundary relaxation. The overall decrease in the strength at higher temperatures (>1000°C) is attributed to the coarsening of matrix grains as well as precipitate particles.

4.4.1.4 Summary

The following points are the major outcomes of the present study.

(a) Similar to the Fe-Cr-Y and Fe-Cr-Nb alloys, Fe-Cr-Zr alloys showed the formation of complete solid solutions after 25 h of MA. After annealing up to 1200°C, Fe_2Zr intermetallic phase was detected to form in Fe-Cr-Zr alloys, which is in agreement with the Fe-Cr-Y alloys, but in contrast to the Fe-Cr-Nb alloys, which showed retaining of complete solid solution after annealing under same condition.

(b) The nanocrystalline alloy powders of Fe-15Cr-Zr showed an excellent thermal stability as compared to that of the Fe-7Cr-Zr. After annealing even at 1000°C, the grain size (by TEM analysis) was found to be reasonably less and stabilized at ~38 nm and depicting a quite high hardness of 8.4 GPa. The high thermal stability of Fe-15Cr-1Zr alloy is ascribed to the stabilization of matrix grains <50 nm due to solute segregation (Zr), extra solid solution strengthening (by Cr) and precipitation hardening by Fe_2Zr.

(c) It is also to be noted that the effective thermal stability of the alloy is realized provided a sufficient amount of Cr (15 at.%) is present along with a small quantity of Zr (0.25-1 at.%). This signifies that Cr together with Zr could play a pivotal role in achieving such high thermal stability.

4.4.2 Consolidation of Fe-7Cr-1Zr and Fe-15Cr-1Zr alloys by SPS

This section deals with the investigation of microstructural stability, mechanical properties and corrosion behavior of the spark plasma sintered (SPSed) Fe-7Cr-1Zr and Fe-15Cr-1Zr alloys. Because of the superior thermal stability, the spark plasma sintering was performed for the Fe-7Cr-1Zr and Fe-15Cr-1Zr alloys at 800, 900 and 1000°C to study its bulk mechanical properties and correlated with corresponding microstructure.

4.4.2.1 Microstructural analysis of SPSed samples

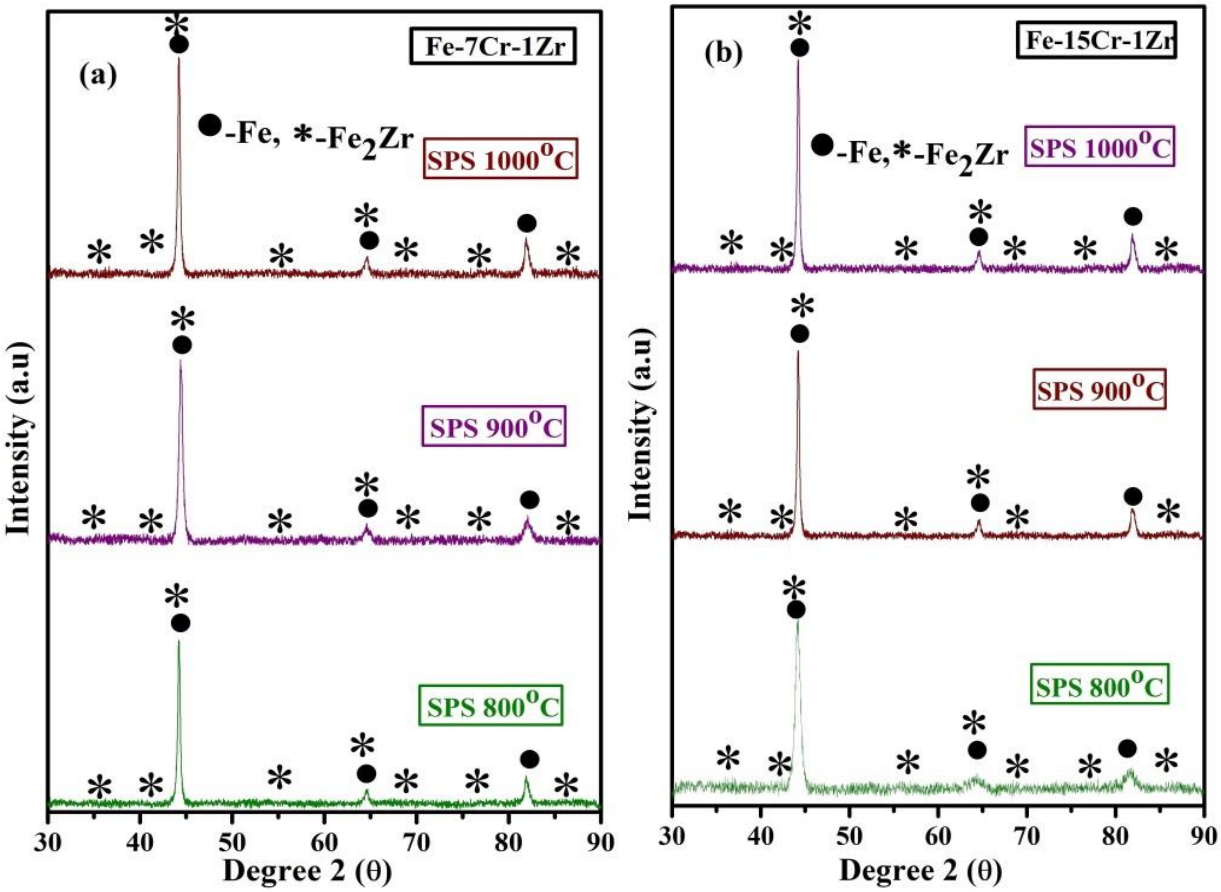

Fig. 4.71: XRD patterns of the as-milled and SPSed samples of (a) Fe-7Cr-1Zr and (b) Fe-15Cr-1Zr alloys sintered at various temperatures.

Figs. 4.71a and b, respectively, show the XRD phase analysis of the SPSed Fe-7Cr-1Zr and Fe-15Cr-1Zr samples in comparison with the as-milled samples. As it is mentioned earlier that the Cr and Zr peak are not detectable in the XRD patterns of the as-milled Fe-Cr-1Zr and Fe-15Cr-1Zr alloys. Therefore, as per the XRD analysis, it can be observed that the complete solid solutions were formed after MA for 25 h (discussed in details in the 4.4.1.1 section). The XRD patterns of the SPSed samples of both the compositions clearly show the formation of Fe_2Zr intermetallic phase, which is consistent with phase evolution of the annealed samples of the same composition as discussed in the 4.4.1.3 section. It can also be observed (especially from the lower angle peaks) that the peak intensity gradually increased and peak width (Fe 110 reflection) at FWHM decreased as the sintering temperature increased. The decrease in the peak width and increase in the peak intensity could be ascribed to the increase in crystallite size and release of accumulated lattice strain due to relaxation and annihilation of dislocations.

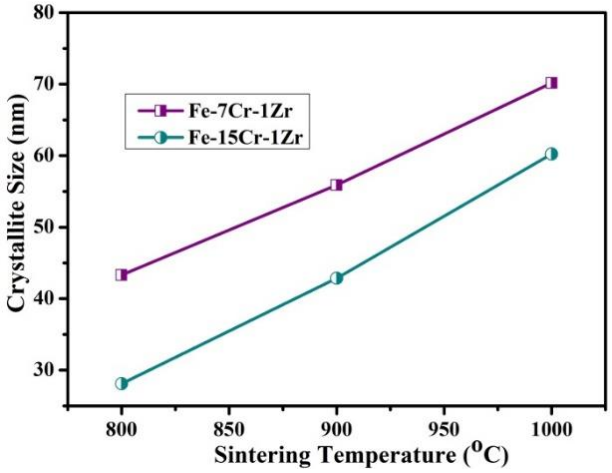

Fig. 4.72: Variation of crystallite size as a function of sintering temperatures for the Fe-7Cr-1Zr and Fe-15Cr-1Zr alloys.

Crystallite size *vs*. sintering temperature plot for the Fe-7Cr-1Zr and Fe-15Cr-1Zr alloys is shown in Fig. 4.72. The three major XRD peaks were used to determine the average crystallite size by using of Williamson-Hall analysis (Suryanarayana et al., 1998). The average crystallite size is found to increase with increase in the sintering temperature. But the increase is more pronounce for the Fe-7Cr-1Zr alloy as compared to that of the Fe-15Cr-1Zr alloy. The crystallite size is found to be ~44 nm and 28 nm, respectively, when sintered at 800°C. Further, the crystallite size increased to 70 nm and 62 nm, respectively, when the sintering temperature was raised to 1000°C. Moreover, the sluggish growth of the crystallite size in Fe-15Cr-1Zr is due to the large amount of Cr dissolved in it. However, the average crystallite size of both the compositions was retained within 100 nm after SPSed at 1000°C.

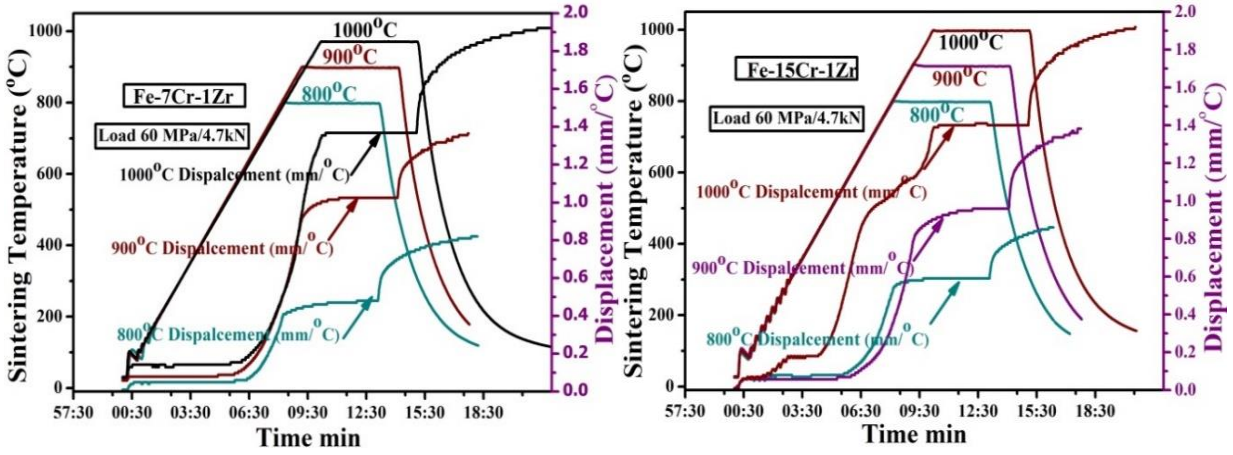

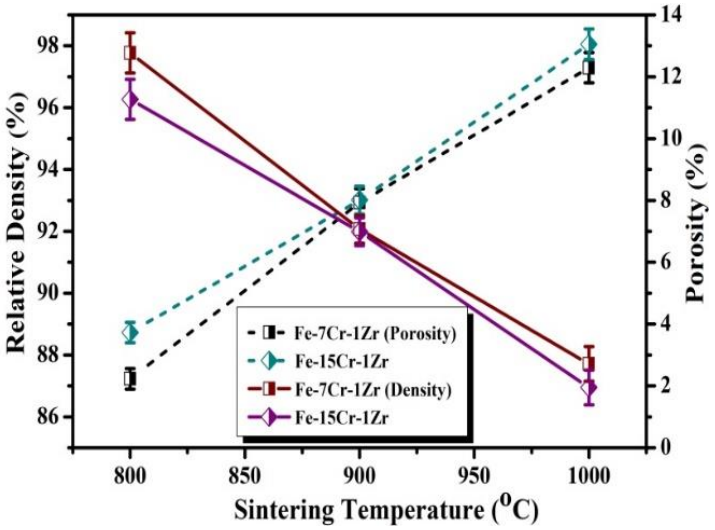

Fig. 4.73: Temperature profiles during SPS of (a) Fe-7Cr-1Zr and (b) Fe-15Cr-1Zr alloys at different temperatures. (c) Relative density and porosity as a function of sintering temperatures.

Typical temperature and displacement (mm/°C, dotted lines) curves over densification during SPS as a function of dwell time are shown in Fig. 4.73. The SPS was carried out using same parameter under same conditions as it was done for the Fe-Cr-Y and Fe-Cr-Nb samples (i.e. at 800, 900 and 1000°C, heating rate of 100°C/min and a holding time of 5 min at a constant pressure of 60 MPa). The relative density during the SPS could easily be measured indirectly from the displacement profiles (mm/°C) shown in Fig. 4.73. The densification during SPS was monitored through displacement curves stimulated from the software (wave logger) installed with the machine (Brendon et al., 2015). The displacement could be monitored by adjusting pressure, time and/or the temperature. The relative density (by Archimedes principle) is found to increase with increase in the sintering temperature. The maximum sintered density is found to be 97 and 98%, respectively, for the Fe-7Cr-1Zr and Fe-15Cr-1Zr SPSed at 1000°C. The level of porosity present in the respective sintered samples could be ascertained from Figs. 4.73c. The larger sintered density is ascribed to the dominant grain-boundary and bulk diffusion at higher sintering temperature.

The optical micrographs of the sintered bulk specimens of Fe-7Cr-1Zr and Fe-15Cr-1Zr alloys are shown in Figs. 4.74. From the micrographs of the sintered samples, it can be observed that the amount of porosity decreased with increasing the sintering temperature. It can be observed from Figs. 4.74a and d, that samples sintered at 800ºC have lot of porosities and corresponding sintered density was found to be low for both the compositions, i.e., 87% (Fe-7Cr-1Zr) and 88% (Fe-15Cr-1Zr) only. The microstructures exhibited a few large and many small porosities a result of improper bonding and densification. Numerous free-standing particles, which do not

exhibit any neck-formation with the adjacent particles, could be observed from the micrographs of samples sintered at 800 and 900°C. This may be ascribed to the insufficient grain-boundary diffusion at low sintering temperature.

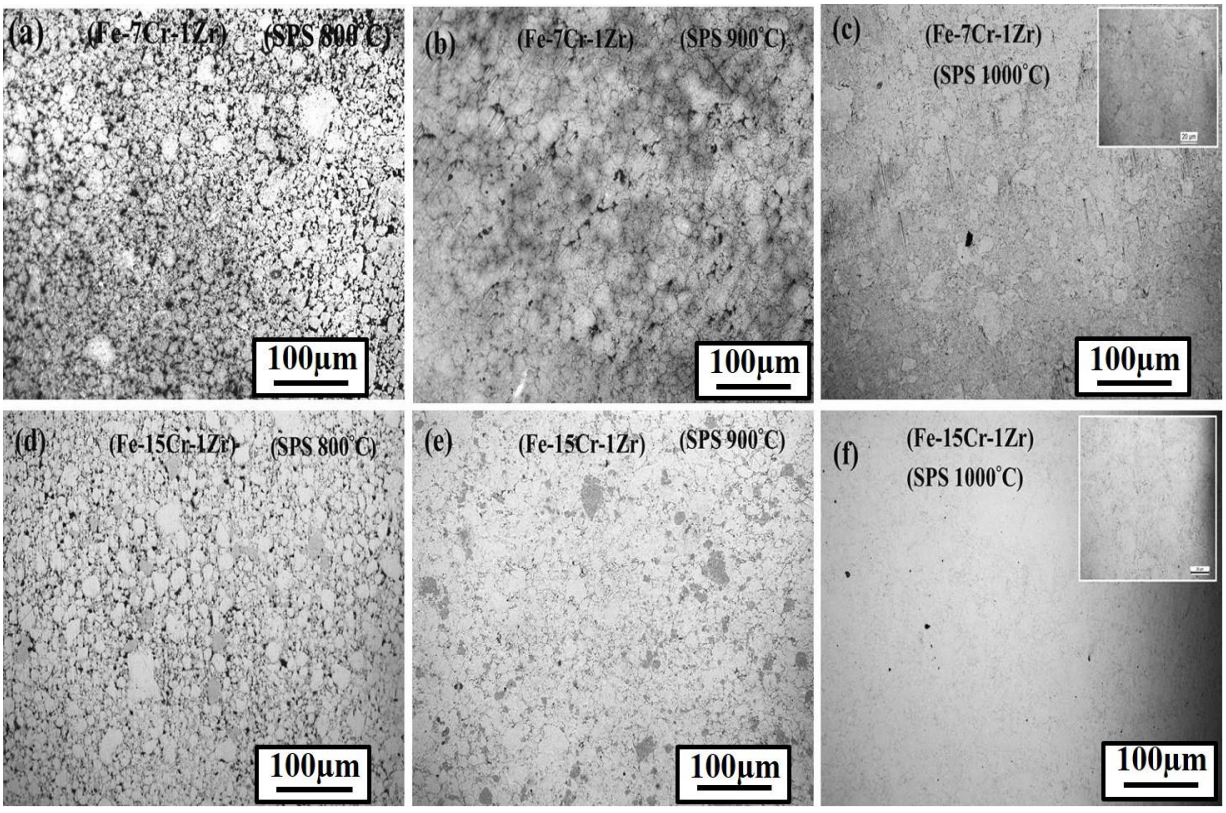

Fig. 4.74: Optical micrographs of bulk samples sintered at (a) 800°C (b) 900°C (c) 1000°C for the Fe-7Cr-1Zr composition; and (d) 800°C (e) 900°C (f) 1000°C for the Fe-15Cr-1Zr composition.

A significant enhancement in the relative sintered density was achieved when sintered at 1000ºC. The maximum sintered density achieved when SPSed at 1000ºC and it was in the range of 97-98%. Hence, the corresponding porosity level also became very less as could be seen from Figs. 4.74c and f. The highly magnified images shown in the inset of Figs. 4.74c and f, distinctly revealed no porosity after SPS at 1000°C.

Secondary (SE) and backscattered electron (BSE) images shown in Figs.4.75a-f also corroborate well with the optical micrograph of the corresponding sample. It is known that the backscattered electron imaging mode is more prominent as compared to the secondary electron imaging to reflect the porosity level. The BSE images clearly revealed the presence of number of small pores in the low temperature SPSed samples (800 & 900°C), whereas, almost no porosity could be detected from the SPSed sample sintered at 1000°C. This observation is in agreement with the calculated relative sintered density of the corresponding sample.

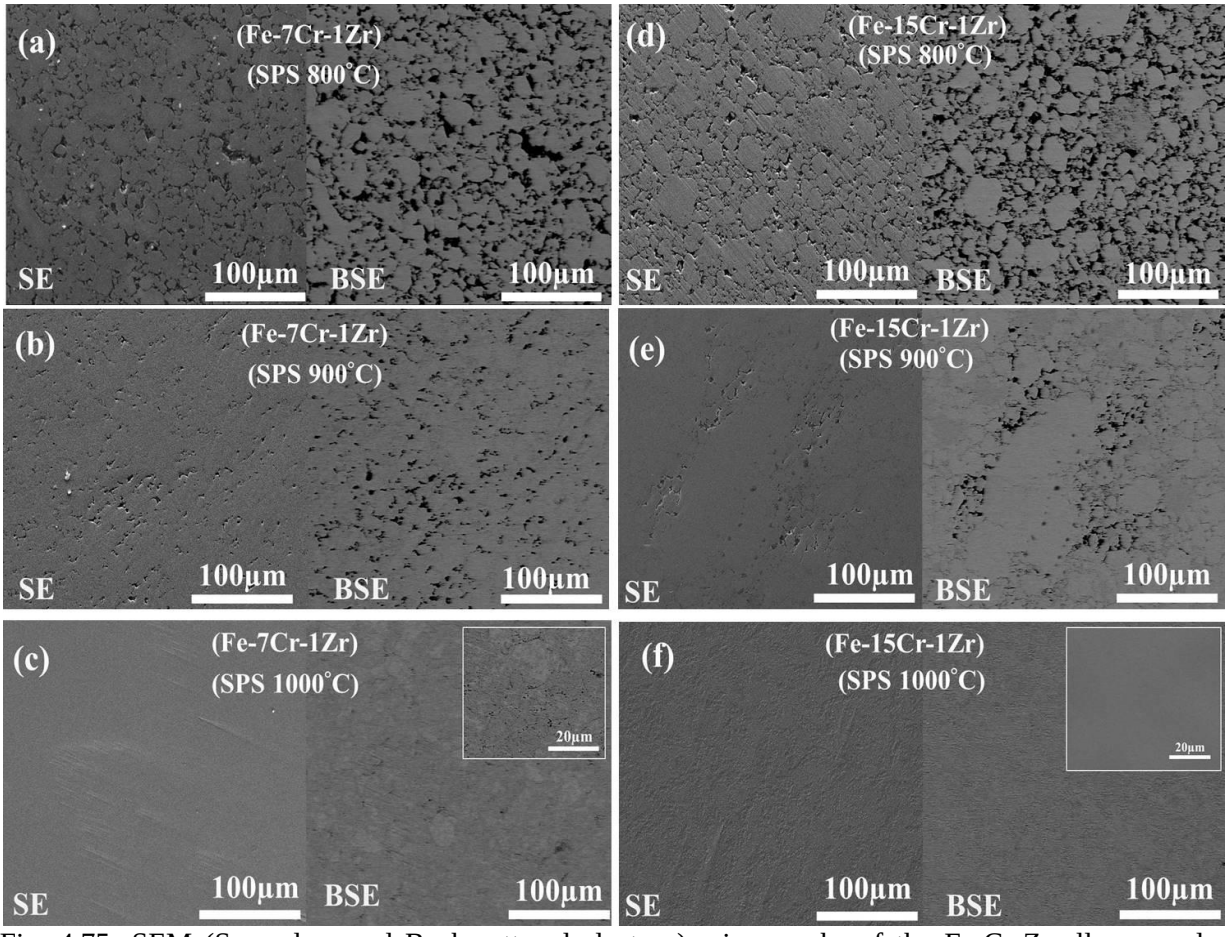

Fig. 4.75: SEM (Secondary and Backscattered electron) micrographs of the Fe-Cr-Zr alloy samples sintered at various temperatures.

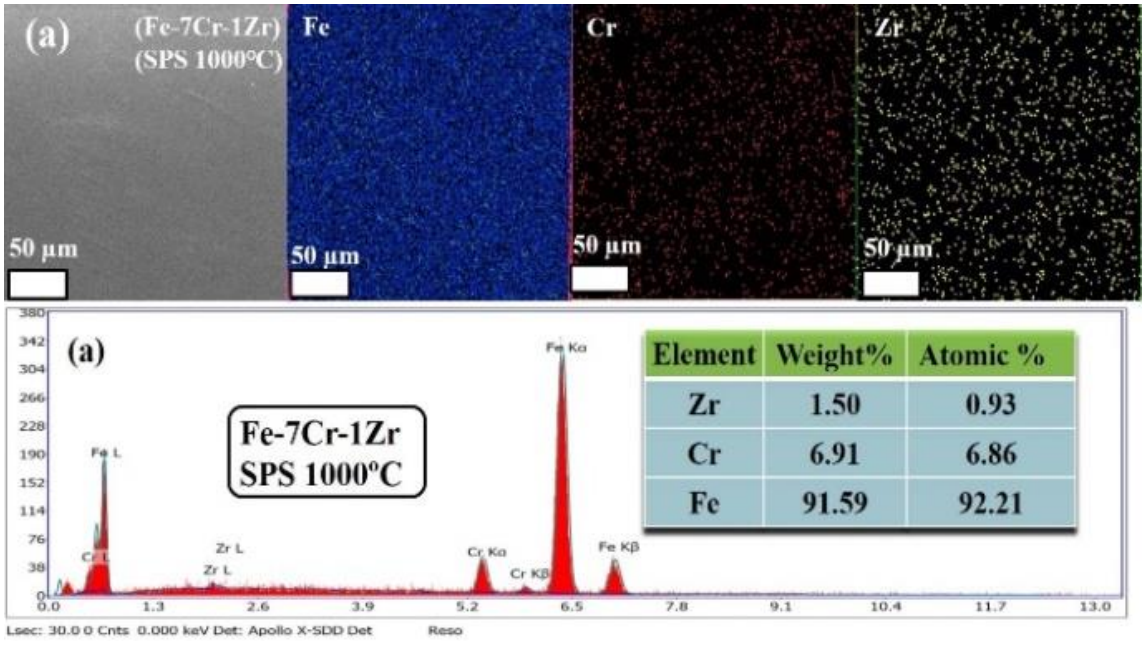

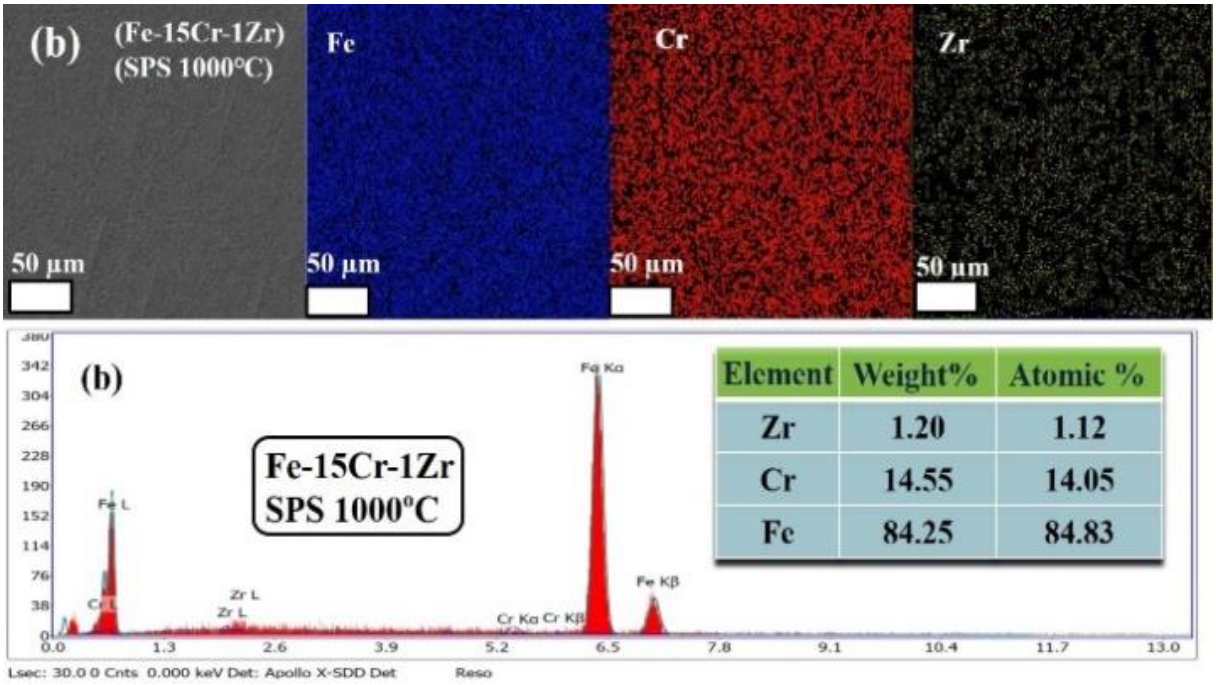

Fig.4.76: Backscattered electron images of (a) Fe-7Cr-1Zr and (c) Fe-15Cr-1Zr alloys SPS sintered at 1000ºC corresponding to elemental area maps. (b) EDS data for the Fe-7Cr-1Zr (d) EDS data for the Fe-15Cr-1Zr.

Figs. 4.76a and b, respectively, show BSE images along with its elemental mapping and EDS results of Fe-7Cr-1Zr and Fe-15Cr-1Zr samples SPSed at 1000°C. It can be noted that homogeneous distribution of Cr and Zr occurs in the Fe matrix. The quantitative EDS analysis also established the same (i.e. homogeneity of the alloys) and revealed almost same composition similar to blend alloys.

TEM analysis of the sintered sample

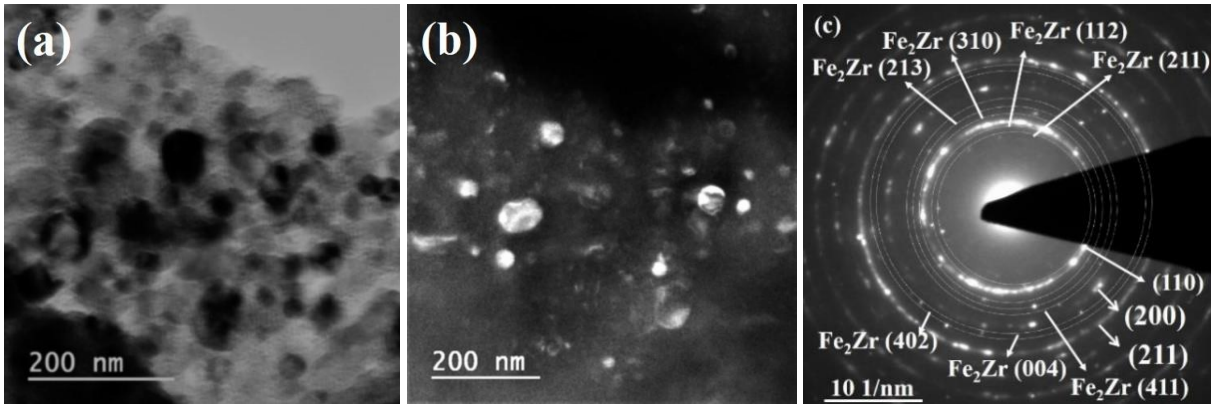

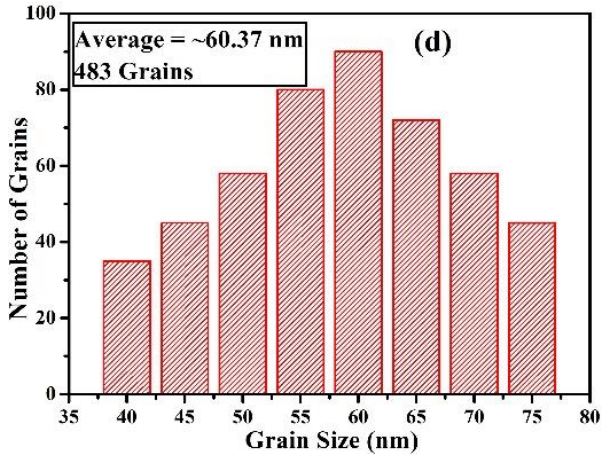

Fig. 4.77: Bright field TEM images of (a) Bright field image, (b) Dark field image of Fe-15Cr-1Zr sample SPS sintered at 1000°C sample. (c) Selected area diffraction pattern (SAED) (d) Statistical grain size distribution of 483 grains obtained from the TEM images as shown in Figs. 4.77a.

Bright field and dark field TEM images of the SPSed Fe-15-Cr-1Zr sample (at 1000°C) is shown in Figs. 4.77a & b. The bright field and dark field TEM images (Fig. 4.77a and b) clearly show that the grain size remained within the nanocrystalline range even after SPS at 1000°C. The SAED pattern was recorded from the encircled region as shown in Fig. 4.77a. Statistical grain size distribution (Fig. 4.80d) was made from the bright field TEM images as one is shown in Fig. 4.77a. Based on the statistical study, the typical TEM grain size was calculated from at least 483 grains and the average TEM grain size was determined to be ~60nm. The TEM grain size is found to corroborate well with the XRD average crystallite size (62 nm) as discussed earlier in the Fig 4.72. The SAED pattern (Fig. 4.77c) shows continuous rings indicating the presence of nanocrystalline feature in the microstructure. As indicated in Fig. 4.77c, the rings were identified as the major reflections from the Fe (110, 220, 200) along with the reflections of Fe_2Zr intermetallic phase (211, 112, 310, 213, 004, 402). The presence of Fe_2Zr intermetallic phase was also detected in the XRD analysis of the corresponding sample (Fig. 4.71b). As, presence of any free Cr and Zr elements are not detected it can be assumed that the dissolved Cr/Zr remained in the solid solution of Fe and Zr partially transformed to form Fe_2Zr intermetallic phase during the SPS.

4.4.2.2 Mechanical properties of SPSed alloys

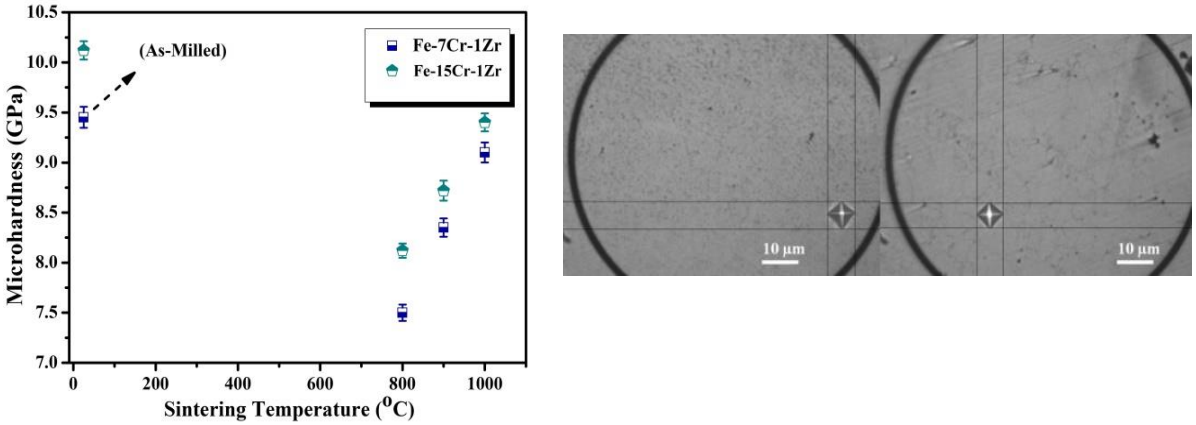

Fig. 4.78: (a) Variation of microhardness values as a function of sintering temperatures. (b) Showing indentation marks made within the surface during microhardness measurements.

Fig. 4.78a shows variation of microhardness values of SPSed Fe-7Cr-1Zr and Fe-15Cr-1Zr samples as a function of sintering temperatures. An important observation is that the microhardness value is found to increase with increase in the sintering temperature. For both the alloys, the maximum microhardness value (9.1 GPa and 9.4 GPa, respectively, for the Fe-7Cr-1Zr and Fe-15Cr-1Zr) is attained when the SPS was carried out at 1000°C. It should be noted that the maximum level of hardness of the SPSed sample is less than that of the as-milled sample. For example, the microhardness values for the as-milled Fe-7Cr-1Zr and Fe-15Cr-1Zr alloys were 9.45 and 10.1 GPa, respectively.The average crystallite size of the corresponding samples (as-milled) was 11 and 8 nm, respectively (discussed in the earlier section 4.4.1.1). On the other hand, the average crystallite size of the SPSed Fe-7Cr-1Zr and Fe-15Cr-1Zr samples sintered at 1000ºC (Fig. 4.72) was 72 nm and 62 nm, respectively. The less microhardness of the sintered specimen than that of the as-milled sample can be ascribed to the coarsening of grains and presence of bit porosity (98% dense sample).

On the other hand, the increase in the microhardness values with sintering temperature can be ascribed to two major factors, viz. (i) an increase in the sintered density and (ii) formation of hard Fe_2Zr intermetallic phase within the matrix (Figs. 4.71a, b). The increase in the microhardness value due to densification overcompensated the decrease in the microhardness due to grain coarsening. Fig. 4.78b shows the indentation marks made on the polished surface of sintered samples during microhardness measurements. Many researchers (Zhang et al., 2005; Hussein et al., 2015) also reported that the average microhardness value increased due to increase in the sintered density (Fe-0.8% C, Nb-Zr alloys).

Compression test

Fig. 4.79 shows typical stress-strain curves accumulated during compression tests for the Fe-7Cr-1Zr and Fe-15Cr-1Zr samples sintered at 1000°C. The compression tests were repeated for three times to confirm the repeatability of the data. The ultimate compressive strength (UCS) of the Fe-7Cr-1Zr and Fe-15Cr-1Zr samples is found to be 1650 and 2200MPa, respectively. The corresponding yield strength could be estimated ~1100 and 1800MPa, respectively.

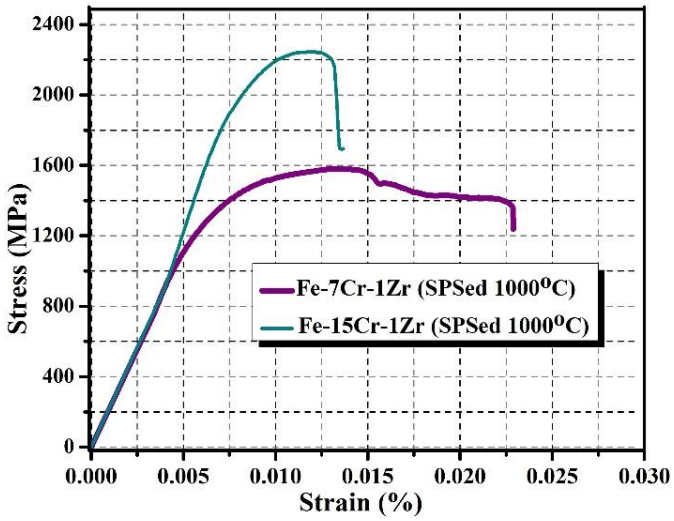

Fig. 4.79: Variation of compressive stress-strain curves of Fe-7Cr-1Zr and Fe-15Cr-1Zr samples SPSed at 1000°C.

The compressive strength of the Fe-15Cr-1Zr sample is significantly higher than that of the Fe-7Cr-1Zr sample sintered at same conditions. This is due to the fact of solid solution strengthening by more amount Cr dissolved in Fe matrix. Moreover, the relative sintered density is also bit higher for the Fe-15Cr-1Zr sample as compared to Fe-7Cr-1Zr alloy sintered at same conditions. From the nature of the stress-strain curves, it could be concluded that a significant amount of plastic deformation occurred before fracture. The superior yield strength of Fe-15Cr-1Zr sample is attributed to the major strengthening mechanisms, namely, solid solution strengthening by high amount of Cr, grain size refinement, precipitation hardening by Fe_2Zr and dislocation strengthening.

Wear Properties

Like the other alloy systems (Fe-Cr-Y and Fe-Cr-Nb), the SPSed samples of Fe-Cr-Zr alloys were studied for dry sliding wear behavior and the variation of COF as a function of time is displayed in Figs. 4.80a and b. As could be seen from the plots, the COF gradually decreases as the sintering temperature increased for both the alloys (Figs. 4.80a & b). As the sintering

temperature increased from 800 to 1000°C, the COF of the Fe-7Cr-1Zr samples decreased from 0.95 to 0.67 (Fig. 4.80a). The same for the Fe-15Cr-1Zr SPSed samples decreased to 0.56 from 0.81 (Fig. 4.80b) as the sintering temperature increased to 1000°C from 800°C. Moreover, the COF of the Fe-15Cr-1Zr samples is found to be less than that of the Fe-7Cr-1Zr samples sintered at any particular temperature. This observation is mainly due to the increase in the relative density.

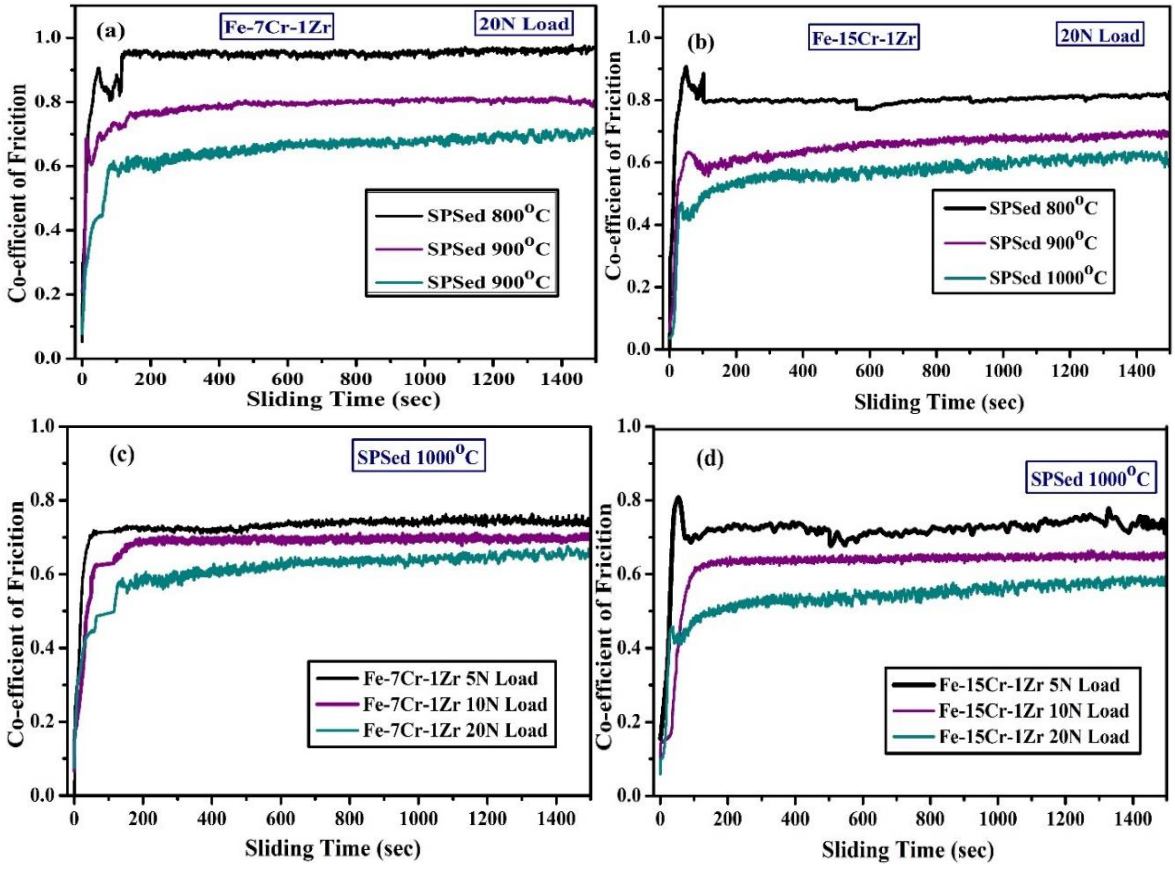

Fig. 4.80: Variation of coefficient of friction as a function of sliding time for the samples sintered at different temperatures (a) Fe-7Cr-1Zr (b) Fe-15Cr-1Zr. Effect load on the wear behavior is shown in figure (c) Fe-7Cr-1Zr (d) Fe-15Cr-1Zr as a function of sliding time.

It is already mentioned earlier that the density of the SPSed samples increased with increasing the temperature. Also the density of SPSed (at 1000°C) Fe-15Cr-1Zr sample (98%) is higher than that of the Fe-7Cr-1Zr (97%). Many other researchers also reported that the highly dense Fe-Cr-Zr alloys showed excellent tribological performance and wear resistance (Kant et al., 2016; Mahmudi et al., 2006). Kant et al. (2016) reported that the addition of Zr and Ti to Fe-Al-C alloys increased strength and improved its wear resistance. It was ascribed due to the precipitation of ZrC and/or TiC carbides and formation of Laves phase $Zr(FeAl)_2$. The COF and wear rate of FeAlC alloys decreased due to higher hardness of TiC and ZrC. Mahmudi et

al. (2006) reported that the wear resistance improved after the addition of Zr in A319 cast alloy. The precipitation of Al_3Zr phase not only induced an increase in the hardness of the alloy but also significantly increased its wear resistance.

Effect of load variation on the COF of the SPSed Fe-7Cr-1Zr and Fe-15Cr-1Zr samples (sintered at1000°C) as a function of sliding time is shown, respectively, in Figs. 4.80c & d. It can be noted that the COF values of the SPSed samples decrease with increasing the load from 5 to 20 N. The COF of the Fe-7Cr-1Zr sintered samples (at 1000°C) decreases from 0.78 to 0.6, as the load increased from 5N to 20N (Fig. 4.83c). Similar trend of the COF (0.7, 0.64 & 0.5) is observed for the SPSed (at 1000°C) samples of Fe-15Cr-1Zr alloy tested under same conditions (i.e. 5, 10 & 20N load) (Fig. 4.80d). Similar trend of wear behavior has been observed for the SPSed samples of Fe-Cr-Y (sections 4.2.2.2). The SPSed samples of Fe-Cr-Zr follow the similar wear mechanisms as discussed in details under 'Wear' section of 4.2.2.2 for the SPSed samples of Fe-Cr-Y.

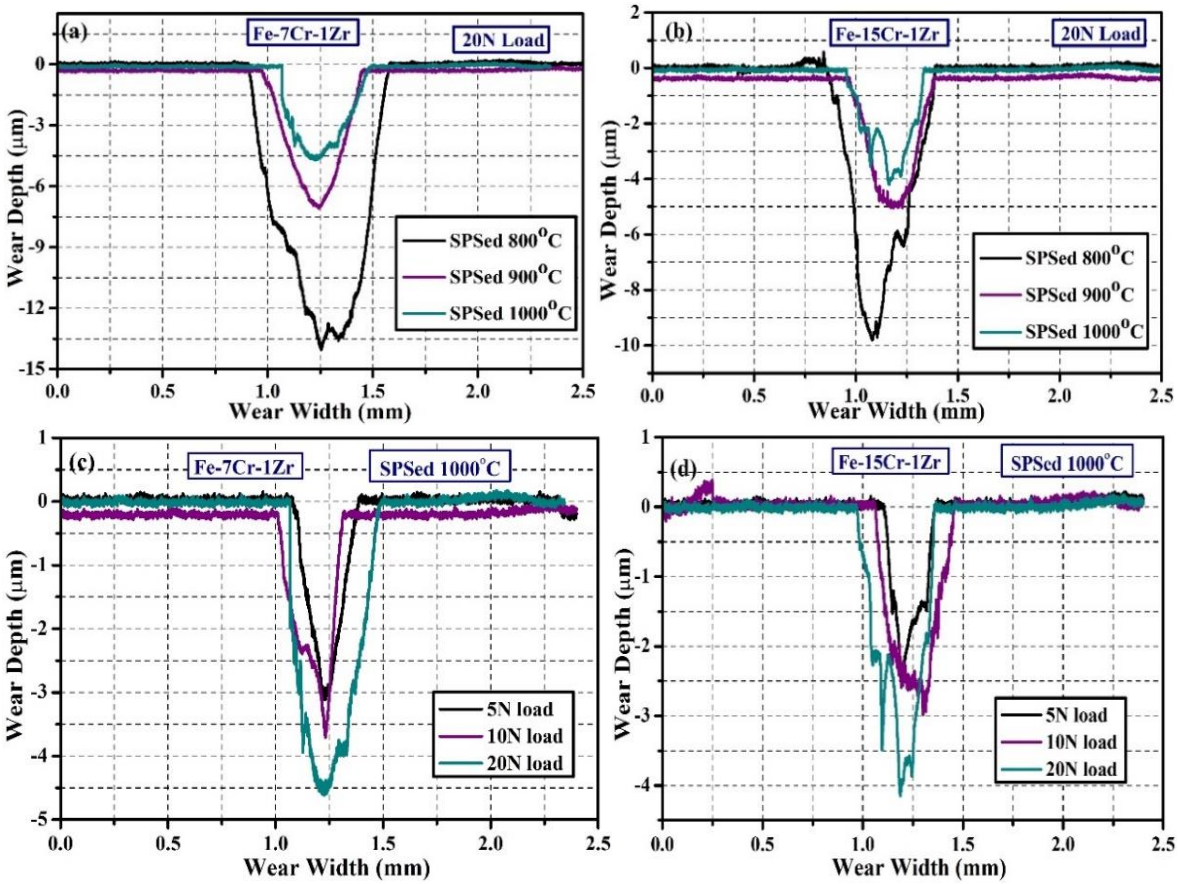

Fig. 4.81: Typical cross-sectional surface profiles of the worn tracks of (a) Fe-7Cr-1Zrand (b) Fe-15Cr-1Zr alloy samples sintered at different temperatures. Effect load on the wear track is shown in figure (c) Fe-7Cr-1Zr (d) Fe-15Cr-1Zr.

The depth and width of the sliding wear tracks of the SPSed Fe-7Cr-1Zr and Fe-15Cr-1Zr samples were measured at different locations by using surface profilometer. Figs. 4.81a and b, respectively, show the cross-sectional surface profiles of the worn tracks developed during testing at 20N load. It can be noticed that the wear depth and wear width values are larger for the samples sintered at lower temperature (e.g. Fe-7Cr-1Zr:13.90 µm & 0.67 mm and Fe-15Cr-1Zr: 9.65 µm & 0.54 mm for the sample sintered at 800°C). The worn depth and width of the same samples tested under the same load (i.e. 20N) decreased (4.5 µm & 0.43 mm and 3.93 µm & 0.37 mm, respectively) as the sintering temperature increased to 1000ºC. Similarly Figs. 4.81c and d show the effect of load on the wear profiles of the Fe-7Cr-1Zr and Fe-15Cr-1Zr samples sintered at 1000°C. It can be observed that wear width and depth increase with increase in the load for both the alloys. For example, the wear width and depth of the Fe-15Cr-1Zr samples are found to gradually increase (i.e. 2.5 µm & 0.25 mm, 3.0 µm & 0.36 mm and 3.93 µm & 0.37 mm) as the load increases from 5 to 20N. Moreover, the wear width and depth of Fe-15Cr-1Zr sample (e.g. 3.93 µm & 0.37 mm) is less than that of the Fe-7Cr-1Zr (4.5µm & 0.43 mm). The mechanisms of wear at various loads are found to be similar as that observed for the Fe-Cr-Y and have been discussed in 4.2.2.2 section.

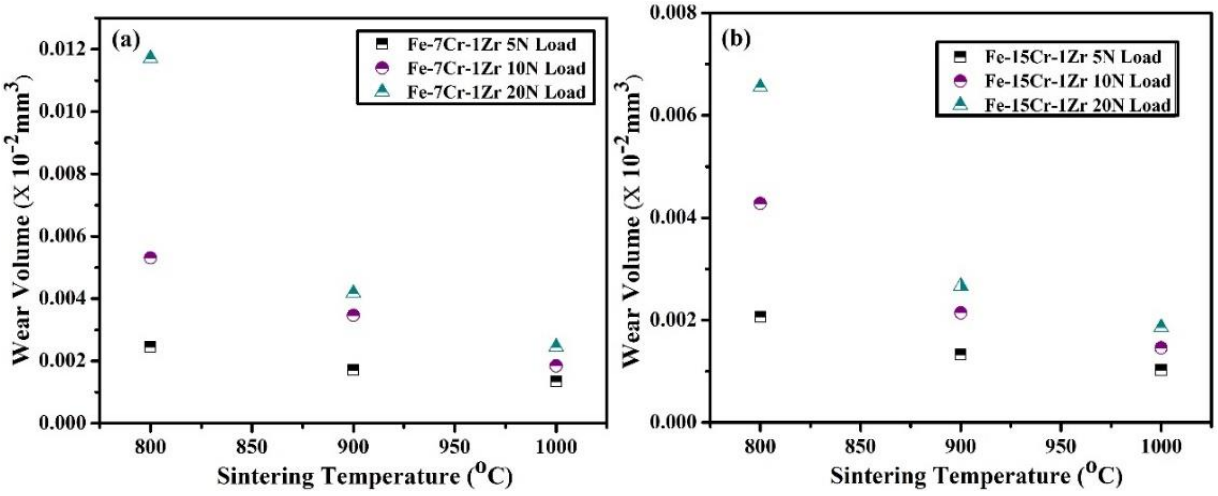

Fig. 4.82: Variation of wear volume of the sintered samples as a function of sintering temperature tested at different loads (a) Fe-7Cr-1Zr and (b) Fe-15Cr-1Zr.

Loss due to wear was calculated using Archard's formula (Archard 1953) and Figs. 4.82a & b, respectively, depict the wear volume of the sintered samples as a function of sintering temperature. The wear volume is found to decrease with increase in the sintering temperatures for both the alloys. Wear volume of the SPSed (at 1000ºC) samples of Fe-7Cr-1Zr and Fe-15Cr-1Zr is only 0.0025×10^{-2} and 0.00186×10^{-2} mm^3, respectively, in contrast to 0.012×10^{-2} and

0.0065×10^{-2} mm^3, respectively, when the sintering was carried out at 800ºC. It can be noted that at any particular sintering temperature (say at 1000°C), the wear volume of both the alloys gradually increases with increasing the applied load. For example, the wear volume of the Fe-15Cr-1Zr samples tested at 5-20N is estimated to be 0.00102×10^{-2}, 0.00146×10^{-2} and 0.00186×10^{-2} mm^3, respectively. Moreover, it can be observed from the Figs. 4.82a & b that at any particular sintering temperature, the wear volume of the SPSed Fe-15Cr-1Zr sample (at 1000°C: 0.00186×10^{-2} mm^3) is relatively less than that of the SPSed Fe-7Cr-1Zr sample (at 1000°C: 0.0025×10^{-2} mm^3) sintered at same condition.

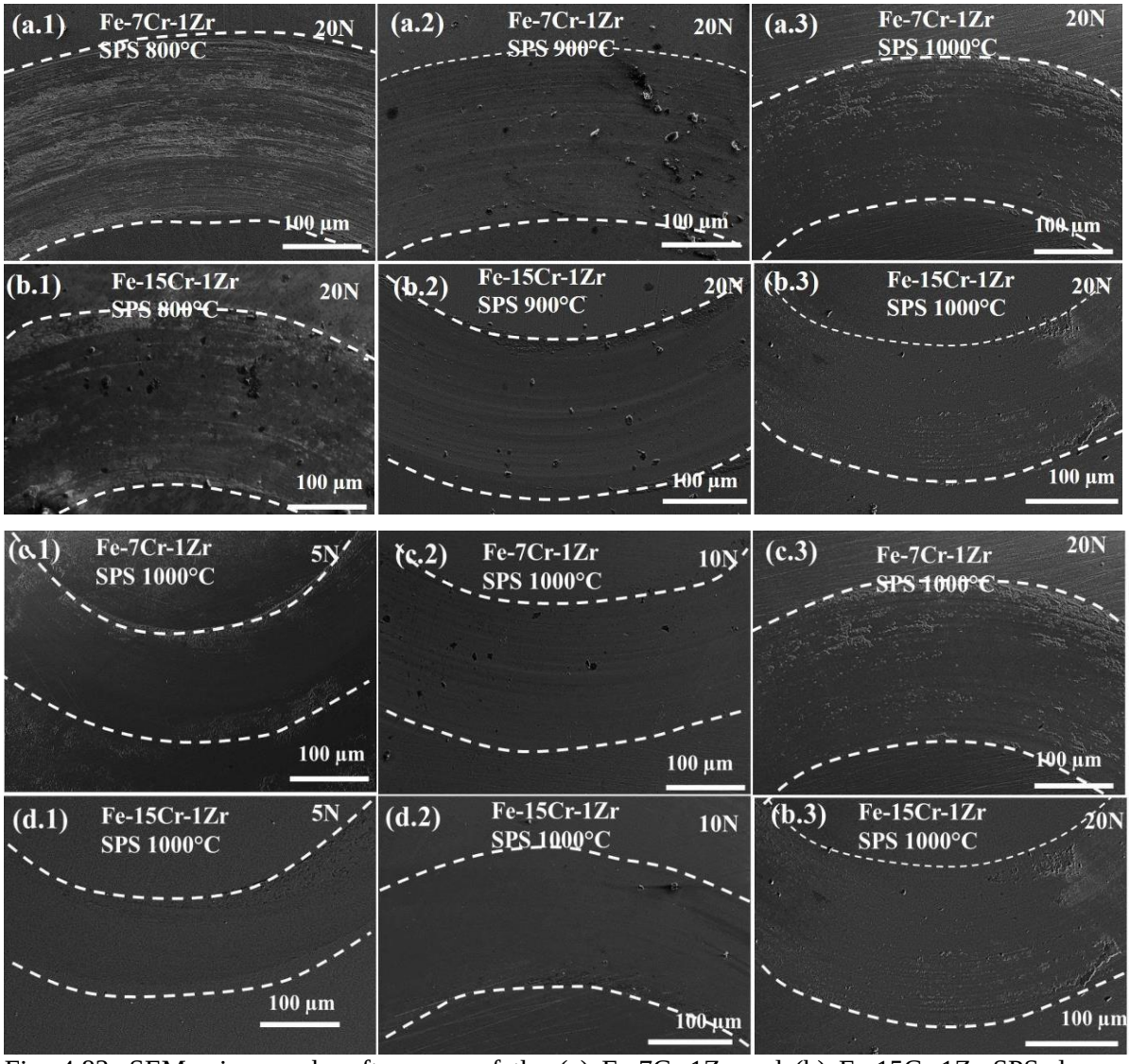

Fig. 4.83: SEM micrographs after wear of the (a) Fe-7Cr-1Zr and (b) Fe-15Cr-1Zr SPSed samples sintered at different temperatues. (c & d) Effect load on the wear track is shown in figure (c) Fe-7Cr-1Zr (d) Fe-15Cr-1Zr.

To correlate the COF and surface profile after the wear test, the wear track surface of the corresponding sintered sample was analyzed using SEM. Figs. 4.83a_1-a_3 & b_1-b_3 show the wear track surfaces of the samples tested at 20N load after sintering at different temperatures. It can be noticed (Figs. 4.83a_1 and b_1) that widths of the wear track surfaces are larger and possibly more material is worn out from the surface due to incomplete sintering (at 800ºC) of the Fe-7Cr-1Zr and Fe-15Cr-1Zr alloys. More particles are possibly pulled out from both the surfaces due to improper bonding between the particles. The wear track width is gradually decreased (indicating better wear resistance) due to proper bonding between particles as the sintering temperature increased. The minimum wear track width is achieved for the Fe-15Cr-1Zr alloy sintered at 1000°C (Fig. 4.83b_3). Similar type of wear behavior has been observed for the Fe-Cr-Y alloys discussed in section 4.2.2.2. Other researchers (Kant et al., 2016; Mahmudi et al., 2006) also reported that wear resistance increases with increase in the sintering temperature and decreases with higher load. Kant et al. (2016) reported that the addition of Zr and Ti to FeAl alloy containing carbon increased strength and wear resistance. Proper bonding between the powder particles as well as formation of ZrC, TiC carbides and $Zr(FeAl)_2$ Laves phase in FeAl alloy (Kant et al., 2016) and formation of Al_3Zr phase in A319 cast alloy (Mahmudi et al., 2006) increased hardness as well as wear resistance of the materials.

4.4.2.3 Corrosion behavior

Corrosion resistance is extremely important for the Fe-based alloys for the applications in petrochemical industry (Baddoo 2008; Gupta et al., 2008; Oka et al., 2007; Peckner et al.,1977; Sorour et al., 2011). Therefore, the stabilized grade Fe-Cr-Zr alloy could be one of the possible candidate for such applications, if the desired level corrosion resistance is fulfilled. Therefore, the corrosion behavior has been studied for the SPSed Fe-7Cr-1Zr and Fe-15Cr-1Zr samples and discussed in the following section.

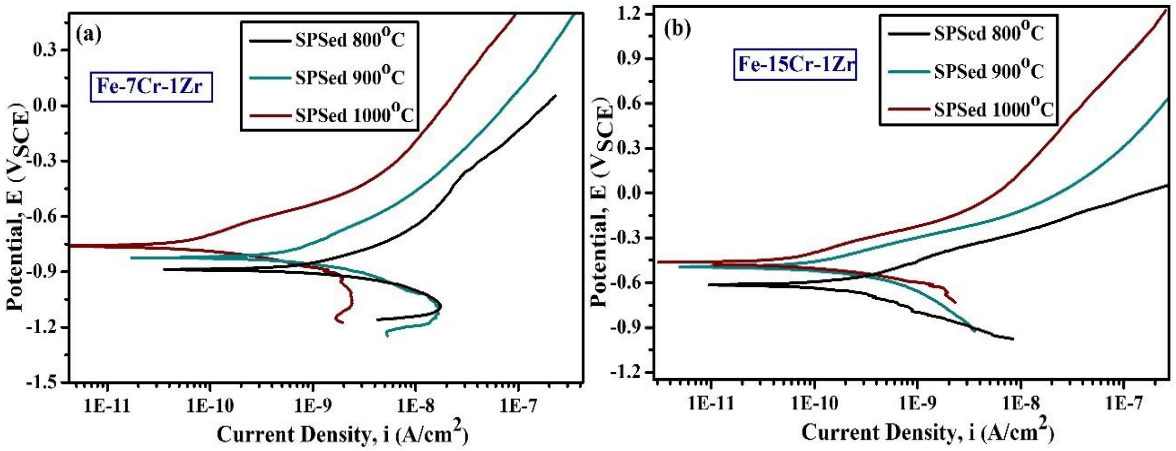

Fig. 4.84: Variation of potentiodynamic polarization curves as a function of current density in 3.5 wt.% NaCl solution of (a) Fe-7Cr-1Zr and (b) Fe-15Cr-1Zr samples sintered at various temperatures.

The potentiodynamic polarization curves as a function of current density is shown in Figs. 4.84a and b, respectively, for the Fe-7Cr-1Zr and Fe-15Cr-1Zr samples sintered at various temperatures. The potentiodynamic polarization tests were conducted using same condition and parameters as done for the Fe-Cr-Y and Fe-Cr-Nb samples (i.e. at room temperature with an aerated 3.5wt.% aqueous NaCl solution). The corrosion rate (CR) was determined using the following formula (Fontana 2005):

CR (in mil per year) = 0.13 × i_{corr} (μAcm^{-2}) × [eqv. wt. of sample/density of sample]

Tafel extrapolation method was used to calculate the corrosion current density (i_{corr}) and corrosion potential (E_{corr}) from the polarization curves shown in Fig. 4.84. The predicated values i_{corr}, E_{corr} and CR of the SPSed samples are tabulated for better convenience in Table 4.9.

Composition	**Sintering Temperature (°C)**	**Corrosion results**		
		E_{corr} (V_{SCE})	**I_{corr} ($\mu A/cm^2$)**	**CR (mpy)**
Fe-7Cr-1Zr	800	-0.902	28.50	20.52
	900	-0.793	19.90	12.9
	1000	-0.755	8.88	4.89
Fe-15Cr-1Zr	800	-0.604	25.89	12.05
	900	-0.492	11.59	8.52
	1000	-0.460	5.96	4.02

The corrosion resistance is found to gradually improve with increase in the sintering temperature for both the alloys. The improvement of the corrosion resistance for the sample sintered at higher temperature (say for Fe-15Cr-1Zr sample SPSed at 1000°C) could be

ascertained from the corresponding values of E_{corr}, i_{corr} and CR values (Table 4.9). Moreover, the corrosion resistance is found to be better for the Fe-15Cr-1Zr alloy sample (sintered at 1000°C) as compared to that of the Fe-7Cr-1Zr composition SPSed at same condition. The improvement of the density due to proper bonding between the powder particles is ascribed to the better corrosion resistance of the high temperature SPSed samples. Addition of Zr in carbon steel was reported to improve corrosion resistance due to the formation of passive films susceptibly (Kovalenko et al., 1964).

Figs. 4.85a-b show SEM images of the SPSed samples after potentiodynamic polarization test. The samples sintered at lower temperatures (Figs. 4.85a_1, a_2, b_1 and b_2) revealed deeper pits indicating severe corrosion of the specimens. Further, the samples sintered at 1000ºC revealed very fine and shallow pits (as can be seen from Figs. 4.88a_3 & b_3) as there was less interconnected porosities were available in the sample. Also, the specimens sintered at lower temperatures contained more open and interconnected porosities. These porosities provided more opportunity to corrode easily to form deeper and larger pits.

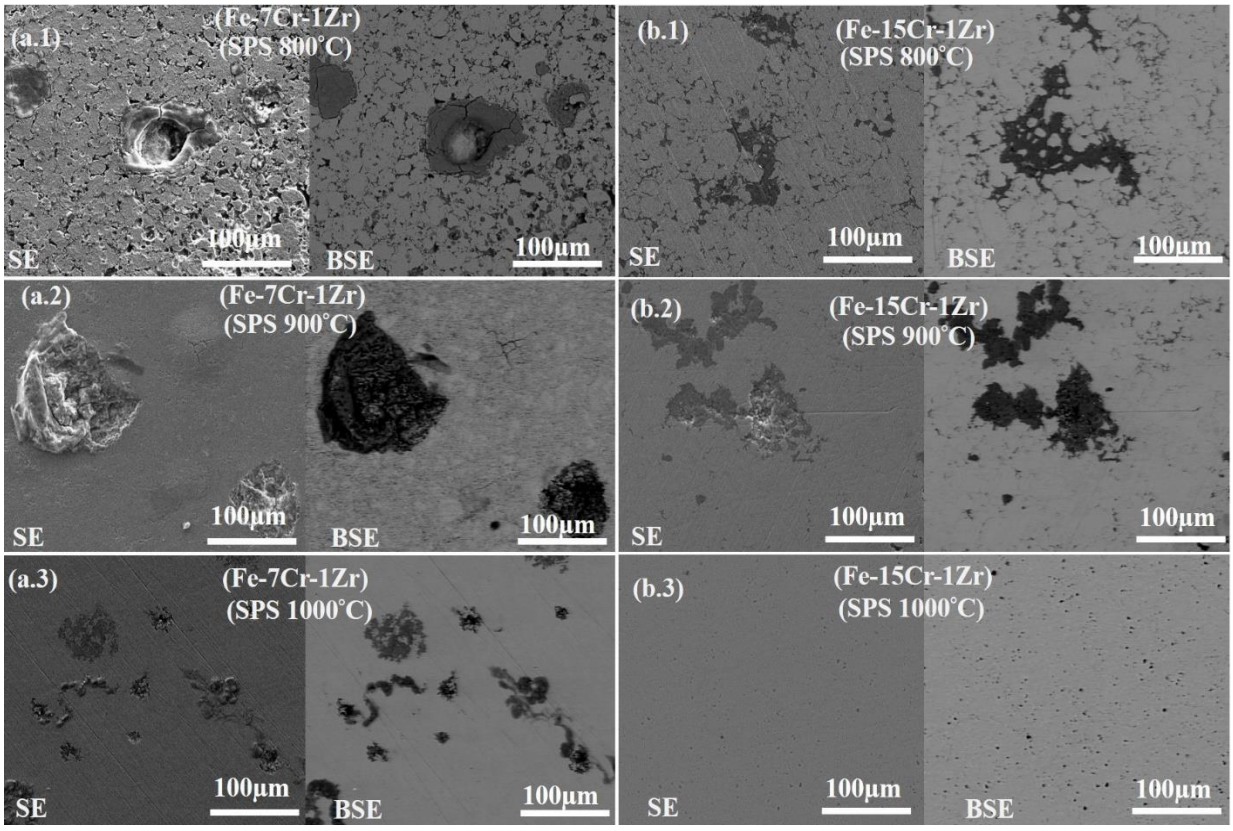

Fig. 4.85: SEM images showing pitting surface morphology of the SPSed Fe-7Cr-1Zr and Fe-15Cr-1Zr alloy samples after corrosion test.

It is known that Cr in Fe-based alloys plays an important role to have excellent corrosion resistance (Fontana 2005). It is known that suitable amount of (>12wt.%) Cr alloyed with Fe changes the passivating potential of Fe to more active values and drastically lowers the critical current density required for passivation (Fontana 2005). Moreover, addition of Zr in carbon steel was reported to improve corrosion resistance due to the formation of passive films by Zr susceptibly (Kovalenko et al.,1964). Akimoto et al. (2018) reported that metal dissolution rate was reduced with increase in Zr content in the Ti-Zr alloys and this was ascribed to the formation of Zr rich passive layer and ZrO_2 oxide layer.

4.4.2.4 Summary

Bulk size nanocrystalline Fe-7Cr-1Zr and Fe-15Cr-1Zr alloy samples have been synthesized successfully by MA followed by SPS. The SPSed samples showed high wear resistance & hardness and improved the corrosion resistance when near full density achieved. The following outcomes are summarized from the present study.

(a) The maximum densification (98%) was achieved for the Fe-15Cr-1Zr alloy when it was sintered at 1000°C. The high level of sintered density is ascribed to the formation of necks due to the deformation at contact points (because of applied pressure) and prevalent grain-boundary and bulk diffusion at higher sintering temperature.

(b) The TEM analysis confirmed that the grain size of the sintered sample depicts a grains size of 60 nm. The TEM-SAED ring pattern analysis revealed the formation of Fe_2Zr intermetallic phase during sintering of the Fe-Cr-Zr solid solutions.

(c) The corresponding Vickers hardness value of the Fe-15Cr-1Zr sample was found to be quite high (9.4 GPa) even after sintering at 1000ºC. Moreover, the wear rate of the SPSed Fe-15Cr-1Zr sample was estimated to be very low (wear volume=0.00186×10^{-2} mm^3) as compared to other sintered samples (e.g. 0.0025×10^{-2}) The wear resistance was corroborated with the SEM images of the worn surface and worn track profile.

(d) The corrosion resistance of the highly dense Fe-15Cr-1Zr sample (sintered at 1000ºC) was detected to improve (corrosion rate=4.02 mpy) as compared to that of the other sintered samples (Fe-7Cr-1Zr 8.88 mpy). The SEM images of the corroded samples also confirmed the same.

4.5 Comparison of the outcomes from the study of Fe-Cr-X (X=Y/Nb/Zr) alloys

4.5.1 Similarity

(a) All the three ternary alloy systems, i.e. Fe-Cr-Y, Fe-Cr-Nb and Fe-Cr-Zr (investigated in the present study) showed the formation of complete solid solutions after mechanical alloying for 25 h when a small amount (up to 1 at.%) of oversize solute atoms of Y/Nb/Zr is added. The formation of disordered solid solutions has been confirmed by XRD phase analysis & lattice parameter variation, thermodynamic feasibility study (i.e. change in Gibbs free energy by Toop's model) and TEM-SAED analysis.

(b) The as-milled samples of Fe-15Cr-1Y/1Nb/1Zr showed highly attractive hardness values (9-10 GPa) corresponding to the matrix grain size of ~10 nm.

(c) After annealing (up to 1200°C), the average crystallite of the Fe-15Cr-1Y/1Nb/1Zr alloys was found to be <100 nm. Moreover, the grain size analysis from TEM images of the Fe-15Cr-1Y/1Nb/1Zr alloys also confirmed the same (i.e. grain size retained in nanometric level even after annealed at 1000°C). The retaining of nanocrystalline grains within 100 nm was also confirmed (by TEM analysis) for the SPSed (at 1000°C) samples of Fe-15Cr-1Y, Fe-15Cr-1Nb and Fe-15Cr-1Zr.

(d) The relative sintered density of the SPSed (at 1000°C) Fe-15Cr-1Y, Fe-15Cr-1Nb & Fe-15Cr-1Zr alloys were estimated to in the range of 97-98%; whereas, the hardness level of the same samples was quite attractive (>9 GPa).

(e) The wear resistance and corrosion resistance are found to be almost similar for the Fe-15Cr-1Y, Fe-15Cr-1Nb and Fe-15Cr-1Zr samples. But, the above properties are found to be much superior for Fe-15Cr-1Y/Nb/Zr alloys (wear volume and CR: $0.00196\times10^{-2}mm^3$ & 3.43 mpy for Fe-15Cr-1Y, $0.00169\times10^{-2}mm^3$ & 4.12 mpy for Fe-15Cr-1Nb and $0.00186\times10^{-2}mm^3$ & 4.02 mpy for Fe-15Cr-1Zr) as compared to that of the other compositions studied (0.0024×10^{-2} mm^3 & 3.46 mpy for Fe-7Cr-1Y, 0.0023×10^{-2} mm^3 & 6.03 mpy for Fe-7Cr1Nb, 0.0025×10^{-2} mm^3 & 4.89 mpy for Fe-7Cr-1Zr). Fig. 4.86a shows variation of wear volume of the Fe-15Cr-1Y/Nb/Zr alloy samples as a function of sintering temperature. It could be noticed that the wear resistance (i.e. indicated by same wear volume) is almost same for all the 3 alloy samples SPSed at 1000°C. Similarly, the corrosion resistance of the SPSed samples is shown in Fig. 4.86b, which indicates that the corrosion resistance of the Fe-15Cr-1Y sample (SPSed at 1000°C) is

found to be superior as compared to the other samples (i.e. Fe-15Cr-1Nb/Zr) sintered at same condition.

The SEM images of the worn and corroded samples also confirmed the same. The superior tribological behavior and corrosion resistance have been described in the light of better densification due to proper bonding between powder particles and retaining of nanocrystalline grains and high hardness values. Therefore, these Fe-based alloys could be suitable for high wear resistance and corrosion resistance applications such as coal mining machinery parts (e.g. mining sliding shoes) and cement industry (e.g. cement roller press).

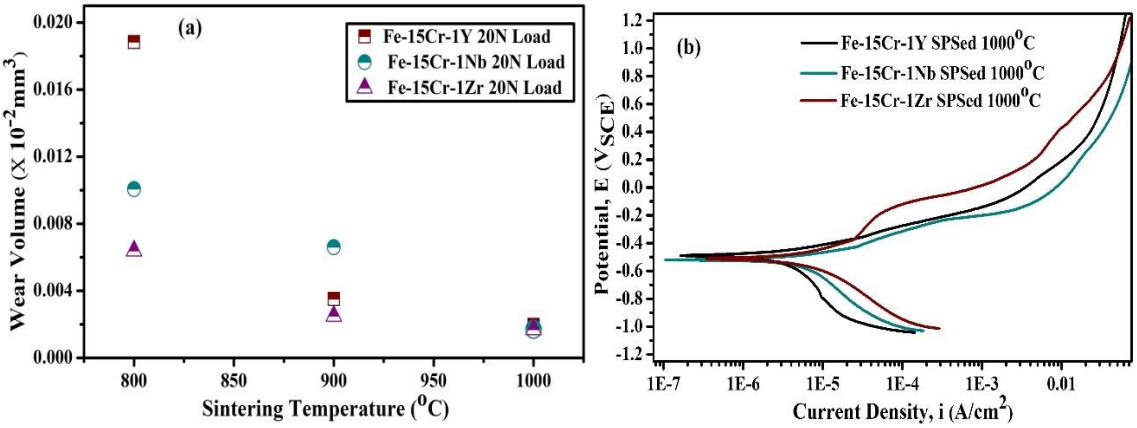

Fig. 4.86: (a) Variation of wear volume of the sintered samples of Fe-15Cr-1Y/1Nb/1Zr alloys as a function of sintering temperature (comparison shown for the samples tested at 20N load), (b) Variation of potentiodynamic polarization curves as a function of current density (tested in a 3.5 wt.% NaCl solution) for the Fe-15Cr-1Y/1Nb/1Zr alloy samples sintered at 1000°C.

4.5.2 Dissimilarity

(a) The annealed (up to 1200°C) as well as SPSed (up to 1000°C) samples of Fe-Cr-Y & Fe-Cr-Zr alloys were found to decompose partially to form a dilute quantity of $Fe_{17}Y_2$ & Fe_2Zr intermetallic phases, respectively, in the matrix of nanocrystalline solid solutions; whereas, the Fe-Cr-Nb alloys retained the complete solid solubility annealing as well as SPS. XRD phase analysis and TEM-SAED pattern analysis of the annealed and SPSed samples confirmed the formation of such intermetallic phases ($Fe_{17}Y_2$ & Fe_2Zr). On the other hand, the Fe-Cr-Nb alloys showed retaining of the complete solid solutions under same conditions of treatment.

(b) Though the thermal stability of Fe-15Cr-1Y/1Nb/1Zr alloys was quite attractive, after annealing (up to 1200°C), the grain size and hardness values were found to bit different in the three alloy systems.

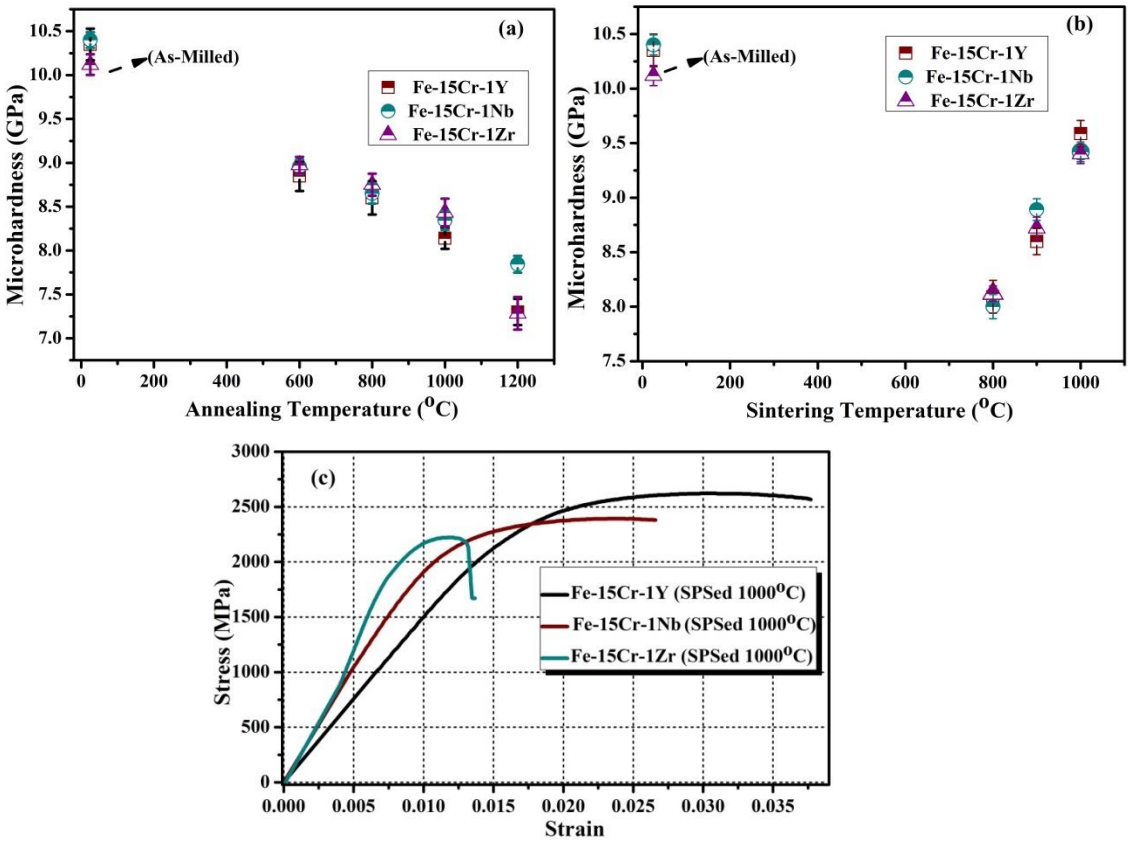

Fig. 4.87: (a) Vickers microhardness of Fe-15Cr-1Y/1Nb/1Zr samples as a function of annealing temperature, (b) Variation of microhardness values of Fe-15Cr-1Y/1Nb/1Zr alloys as a function of sintering temperatures, (c) Variation of compressive stress-strain curves of Fe-15Cr-1Y/1Nb/1Zr alloys SPSed at 1000°C.

For example, TEM grain size after annealing at 1000°C was estimated to be 50 nm, 53 nm and 55 nm, respectively, for the Fe-15Cr-1Nb, Fe-15Cr-1Y and Fe-15Cr-1Zr alloys with corresponding hardness values of 8.3, 8.1 and 8.4 GPa. Variation of the microhardness values of the annealed samples of Fe-15Cr-1Nb, Fe-15Cr-1Y and Fe-15Cr-1Zr alloys is shown in Fig. 4.87a.

(c) The thermal stability of the SPSed samples is found to be quite superior and could be realized from the analysis of grain size, Vickers hardness and compressive strength. TEM grain size of the SPSed sample (at 1000°C) was found to be 49, 72 and 61 nm, respectively, for the Fe-15Cr-1Nb, Fe-15Cr-1Y and Fe-15Cr-1Zr alloys. The corresponding Vickers hardness values (i.e. For the SPSed samples) were estimated to be 9.5, 9.6 and 9.45 GPa, respectively. The experimental compressive strength of the corresponding SPSed (at 1000°C) samples (UCS-2400 MPa, YS-1800 MPa for Fe-15Cr-1Nb; UCS-2600 MPa, YS-2000 MPa for Fe-15Cr-1Y and UCS-2200 MPa, YS-1600 MPa for Fe-15Cr-1Zr) is highly corroborating with the corresponding hardness

values. The comparisons of hardness and compressive strength of the SPSed samples are shown in Fig. 4.87b & c, respectively. The high thermal stability is ascribed to the thermodynamic stabilization of matrix grains by oversize solute segregation along the grain boundaries and/or kinetic mechanism of grain boundary pinning by intermetallic particles.

CHAPTER 5 Conclusions and future scope of the study

5.1 Conclusions

This section concludes the major outcomes and findings as summarizes below.

(a) First, four Fe-Cr alloys (Cr=7, 11, 15 & 19 at. %) were developed by MA and their thermal stability has been investigated. XRD phase analysis and lattice parameter change of the Fe-based alloys (a_{Fe}) confirmed the formation of complete solid solutions for all the Fe-Cr alloys. The crystallite size decreased with increase in the Cr content and attained a value as low as ~16 nm for 19% Cr alloy. The corresponding microhardness value is found to be quite high (~10 GPa) for the corresponding as-milled sample. However, the thermal stability of the Fe-Cr alloys was found very poor at high temperatures (>600°C) due to coarsening of the nanocrystalline grains.

(b) Hence, one low Cr content, i.e. Fe-7Cr and one high Cr content, i.e. Fe-15Cr alloys were selected for further investigation to improve their thermal stability by adding of oversize solute atoms (Y/Nb/Zr) in dilute quantity (0.25, 0.5, 1at.%). The selected Fe-7Cr-X and Fe-15Cr-X (X=Y/Nb/Zr) alloys were developed by MA for 25 h under the same milling conditions as followed in the Fe-Cr system. Then, phase evolution, their microstructural features and thermal stability were investigated. On the basis of the thermal stability (grain size and microhardness values of the annealed samples), Fe-7Cr-1Y & Fe-15Cr-1Y, Fe-7Cr-Nb and Fe-15Cr-Nb (Nb=0.25, 1at.%) and Fe-7Cr-1Zr and Fe-15Cr-1Zr alloys were SPSed at 800, 900 and 1000°C to study their microstructures and mechanical properties.

(c) All the three systems Fe-Cr-Y, Fe-Cr-Nb and Fe-Cr-Zr investigated (in the present study) show the formation of complete solid solutions after mechanical alloying for 25 h when a small amount (up to 1 at.%) of oversize solute atoms of Y/Nb/Zr is added. The formation of disordered solid solutions was confirmed by XRD phase analysis & lattice parameter variation, thermodynamic feasibility analysis (change in Gibbs free energy by Toop's model) and TEM-SAED analysis. Due to the dissolution of Cr and oversize solute atoms in the Fe-lattices, lattice parameter was found to increase in all the three alloy systems. The increase in the lattice parameter indicates the formation of ordered/disordered solid solution because of solute dissolution in the matrix. In addition, for all the three alloy systems, the calculated Gibbs free energy change (due to

the increase in the grain boundary free energy and lattice strain energy due to the increase in the dislocations) was found to be higher than that of the theoretical Gibbs free energy required for the formation of disordered solid solutions as per Toop's model. TEM-SAED pattern analysis also did not reveal any peak related to free Cr and Y/Nb/Zr or any intermetallic phase(s) from the as-milled samples.

(d) After annealing up to 1200°C, the ternary alloys of Fe-Cr-Y & Fe-Cr-Zr were found to decompose partially to form a dilute quantity of $Fe_{17}Y_2$ & Fe_2Zr intermetallic phases, respectively, in the matrix of Fe-based solid solutions; whereas, the Fe-Cr-Nb alloys revealed the retention of the complete solid solubility of the Cr, Y/Nb up to the annealing temperature of 1200°C. Formation of such intermetallic phase was detected by the XRD phase analysis and subsequently was confirmed by the TEM-SAED pattern analysis.

(e) The thermal stability of the Fe-Cr-Y/Nb/Zr as-milled samples is found to be highly attractive as the matrix grain size were found to stabilize within nanometer range (<100 nm) and the hardness values were found to be quite high. For example, TEM grain size was 50 nm for Fe-15Cr-1Nb, 53 nm for Fe-15Cr-1Y and 55 nm for Fe-15Cr-1Zr alloys, respectively, with a corresponding hardness value of 8.3 GPa, 8.1 GPa and 8.4 GPa after annealing at 1000°C.

(f) The relative sintered density of the SPSed (at 1000°C) Fe-15Cr-1Y, Fe-15Cr-1Nb & Fe-15Cr-1Zr alloys were estimated to be in the range of 97-98%. The retaining of nanocrystalline grains (obtained by TEM/EBSD analysis) and formation of intermetallic phase(s) were also confirmed (by XRD and TEM-SAED analysis) for the SPSed samples of the Fe-Cr-Y and Fe-Cr-Zr alloys; whereas, the complete solid solubility is found to retain in the Fe-Cr-Nb alloys after the SPS at 1000°C.

(g) The thermal stability of the SPSed samples is found to be quite superior and could be realized from the analysis of grain size, Vickers hardness and compressive strength. TEM grain size was found to be 49 nm for Fe-15Cr-1Nb, 72 nm for Fe-15Cr-1Y and 61 nm for Fe-15Cr-1Zr alloys after SPS at 1000°C. The corresponding Vickers hardness value was estimated to be 9.5 GPa, 9.6 GPa and 9.45 GPa, respectively. The estimated compressive strength of the SPSed (at 1000°C) samples (UCS-2400MPa, YS-1800MPa for Fe-15Cr-1Nb; UCS-2600MPa, YS-2000MPa for Fe-15Cr-1Y and UCS-2200MPa, YS-1600MPa for Fe-15Cr-1Zr) is highly corroborating with the corresponding density,

hardness value and wear resistance. The high thermal stability is ascribed to the thermodynamic stabilization of matrix grains by oversize solute (Y/Nb/Zr) segregation along the grain boundaries and/or kinetic mechanism of grain boundary pinning by intermetallic particles ($Fe_{17}Y_2$ & Fe_2Zr).

(h) The wear resistance and corrosion resistance are found to be almost similar for the Fe-15Cr-1Y, Fe-15Cr-1Nb and Fe-15Cr-1Zr samples, but these are much superior for these alloys (for example: wear volume and CR: $0.00196\times10^{-2}mm^3$ & 3.43 mpy for Fe-15Cr-1Y, $0.00169\times10^{-2}mm^3$ & 4.12 mpy for Fe-15Cr-1Nb and $0.00186\times10^{-2}mm^3$ & 4.02 mpy for Fe-15Cr-1Zr) as compared to that of the other compositions studied (0.0024×10^{-2} mm^3 & 3.46 mpy for Fe-7Cr-1Y, 0.0023×10^{-2} mm^3 & 6.03 mpy for Fe-7Cr1Nb, 0.0025×10^{-2} mm^3 & 4.89 mpy for Fe-7Cr-1Zr). The SEM images of the worn and corroded samples also confirmed the same. The superior tribological behavior and corrosion resistance have been described in the light of better densification due to proper bonding between powder particles and retaining of nanocrystalline grains and high hardness values.

(i) Overall, the Fe-15Cr-1Y/1Nb/1Zr alloys showed superior thermal stability and the SPSed samples of these alloys revealed highly attractive mechanical properties, such as hardness of 9-10 GPa, excellent wear resistance and outstanding compressive strength. Moreover, the corrosion resistance of these alloys was found highly attractive. Therefore, these Fe-based alloys could be suitable for high wear resistance and corrosion resistance applications such as coal mining machinery parts (e.g. mining sliding shoes), cement industry (e.g. cement roller press), nuclear first wall reactor (750-950°C), automotive (exhaust system operating at 800-850°C), chemical processing unit (such as acid carrying pipes 320-450°C, petrochemical industries U-tube) etc.

5.2 Future scope of the study

(a) The stabilized grade Fe-based alloy powders could be forged to obtain bulk-size samples. Then, bulk mechanical properties at room and high temperatures, such as, tensile, creep and fatigue, could be investigated. These studies could reveal the fundamental mechanisms of high temperature stability, which will be helpful to assess the practical suitability of the high temperature/nuclear applications.

(b) EBSD analysis was made only for SPSed of Fe-Cr-Y alloy. The EBSD study could be made for the powder forged as well as SPSed samples of the Fe-Cr-Nb and Fe-Cr-Zr alloys. Detailed EBSD study can enlighten detailed microstructural features developed after powder forging.

(c) Atom probe tomography could be performed to investigate the segregation of oversize solute elements along the grain boundaries as well as to analyze the chemical composition in atomic scale.

(d) Detailed analysis of the corrosion resistance could be carried out by electrochemical impendence spectroscopy (EIS) analysis.

(e) In-depth wear study could be carried out with different counter-body and loads for the forged bulk size samples.

References

[1] Akimoto T., T. Ueno T., Tsutsumi Y., Doi H., Hanawa T., and Wakabayashi N., (2018), Evaluation of corrosion resistance of implant-use Ti-Zr binary alloys with a range of compositions, Journal of Biomedical Materials Research - Part B: Applied Biomaterials, 106, 73-79.

[2] Alleg S., Souilah S., Sunol J.J., (2013), Thermal stability of the nanostructured powder mixtures prepared by mechanical alloying, (Chapter-ii), 21-48.

[3] Archana M.S., Ramakrishna M., Gundakaram R.C., Srikanth V.V.S.S., Joshi S. V., Joardar J., (2014), Nanocrystalline phases during mechanically activated processing of an iron (Fe) aluminum (40 at.% Al) Alloy, Materials and Manufacturing Processes, 29, 864-869.

[4] Archana M.S., Hebalkar N., Radha K., Joardar J., (2010), Phase formation during mechanically activated annealing of nanocrystalline Cr-60at.% Al, Journal of Alloys and Compounds, 501, 18-24.

[5] Archard J.F., (1953), Contact and rubbing of flat surfaces, Journal of Applied Physics, 24, 981-988.

[6] Arzt E., (1998), Size effects in materials due to microstructural and dimensional constraints: A comparative review, Acta Materialia, 6454, 00231-6.

[7] Atkinson H. V., (1988), Theories of normal grain growth in pure single phase systems, Acta Metallurgica, 36, 469-491.

[8] Atwater M.A., Roy D., Darling K.A., Butler B.G., Scattergood R.O., Koch C.C., (2012), The thermal stability of nanocrystalline copper cryogenically milled with tungsten, Materials Science and Engineering A, 558, 226-233.

[9] Atwater M.A., Scattergood R.O., Koch C.C., (2013), The stabilization of nanocrystalline copper by zirconium, Materials Science and Engineering A, 559, 250-256.

[10] Averback R.S., Zhu H., Tao R., Hofler H., (1996), Sintering of nanocrystalline materials: Experiments and computer simulations, in Synthesis and Processing of Nanocrystalline Powder, (TMS, Warrendale), 203-216.

[11] Azimi M., Akbari G.H., (2011), Development of nano-structure Cu-Zr alloys by the mechanical alloying process, Journal of Alloys and Compounds, 509, 27-32.

[12] Baddoo N.R., (2008), Stainless steel in construction: A review of research, applications, challenges and opportunities, Journal of Constructional Steel Research, 64, 1199-1206.

[13] Bhadeshia H.K.D.H., (2000), Mechanically alloyed metals, Materials Science and Technology, 16, 1404-1411.

[14] Bisht A., Albe K., Jayaganthan R., (2012), Effect of porosity on mechanical behaviour of nanocrystalline metals, International Conference on Emerging Electronics (ICEE), 10-13.

[15] Brammer T., Ray P.K., Misra S., Ye Y.Y., Akinc M., Kramer M.J., (2010), Computational and experimental design of novel high temperature alloys, Advances in Science and Technology, 72, 31-39.

[16] Brendon M., Diouf S., Olayinka M., Apata P., (2015), Effect of sintering temperature on the microstructure and mechanical properties of Fe-30%Ni alloys produced by spark plasma sintering, Journal of Alloys and Compounds, 649, 824-832.
[17] Cahn J.W., (1962), The impurity-drag effect in grain boundary motion, Acta Metallurgica, 10, 789-798.
[18] Cahn R.W., Haasen P., (1996), Phqsical Me tallurgq.
[19] Cahoon J.R., Broughton W.H., Kutzak A.R., (1971), The determination of yield strength from hardness measurements, Metallurgical Transactions, 2, 1979-1983.
[20] Callister W., Rethwisch D., (2007), Materials science and engineering: an introduction, Wiley, New York.
[21] Chen Z., Liu F., Wang H.F., Yang W., Yang G.C., Zhou Y.H., (2009), A thermokinetic description for grain growth in nanocrystalline materials, Acta Materialia, 57, 1466-1475.
[22] Chokshi A.H., Rosen A., Karch J., Gleiter H., (1989), On the validity of the hall-petch relationship in nanocrystalline materials, Scripta Metallurgica, 23, 1679-1684.
[23] Chowdhury M.A., Nuruzzaman D.M., (2013), Experimental investigation of friction coefficient and wear rate of different sliding pairs, Gazi University Journal of Science (GU J Sci) 26, 597-609.
[24] Chowdhury M.A., (2013), Experimental investigation on friction and wear of stainless steel 304 sliding against different pin materials, World Applied Sciences Journal, 22, 1702-1710.
[25] Clementi E., Raimondi D.L., (1967), Atomic screening constants from SCF functions, The Journal of Chemical Physics, 38, 2686-2689.
[26] Cui H., (2007), Effect of Cr addition on microstructure and wear resistance of hypomonotectic Cu-Pb alloy, Materials Science and Engineering: A, 448, 49-55.
[27] Cullity B.D., (1978), Elements of Diffraction.
[28] Dake J.M., Krill C.E., (2012), Sudden loss of thermal stability in Fe-based nanocrystalline alloys, Scripta Materialia, 66, 390-393
[29] Darling K.A., (2011), Stabilized nanocrystalline iron-based alloys: Guiding efforts in alloy selection, Materials Science and Engineering A, 528, 4365-4371.
[30] Darling K.A., Roberts J.J., Mishin Y., Mathaudhu S.N.N., Kecskes L.J.J., (2013), Grain size stabilization of nanocrystalline copper at high temperatures by alloying with tantalum, Journal of Alloys and Compounds, 573, 142-150.
[31] Darling K.A., Vanleeuwen B.K., Koch C.C., Scattergood R.O., (2010), Thermal stability of nanocrystalline Fe-Zr alloys, Materials Science & Engineering A, 527, 3572-3580.
[32] Darling K.A., Kecskes L.J.J., Atwater M., Semones J., Scattergood R.O., Koch C.C., (2013), Thermal stability of nanocrystalline nickel with yttrium additions, Journal of Materials Research, 28, 1813-1819.
[33] Darling K.A., Tschopp M.A., Liu Z.K., (2015), Rebuttal comments on “mitigating grain growth in binary nanocrystalline alloys through solute selection based on thermodynamic stability maps,” Computational Materials Science, 107, 238-242.

[34] Defay R., Prigogine I., Bellemans A., (1966), Surface tension and adsorption. Longmans, London.
[35] Detor A.J., Schuh C.A., (2007), Tailoring and patterning the grain size of nanocrystalline alloys, Acta Materialia, 55, 371-379.
[36] Dieter G., (1961), Mechanical metallurgy, (Second ed. New York: McGraw Hill Book Company.370-371.
[37] Driver J.H., (2004), Stability of nanostructured metals and alloys, Scripta Materialia, 51, 819-823.
[38] Dubiel S.M., Costa B.F.O., Cieslak J., Batista A.C., (2015), Debye temperature of nanocrystalline Fe-Cr alloys obtained by mechanical alloying, Journal of Alloys and Compounds, 649, 1246-1252.
[39] Dybiec H., (2007), Plastic consolidation of metallic materials, Archives of Metallurgy and Materials, 52, 161-171.
[40] Eriksson M., Radwan M., Shen Z., (2013), Spark plasma sintering of WC, cemented carbide and functional graded materials, International Journal of Refractory Metals and Hard Materials, 36, 31-37.
[41] Ertorer O., Topping T.D., Li Y., Moss W., Lavernia E.J., (2011), Nanostructured Ti consolidated via spark plasma sintering, Metallurgical and Materials Transactions A, 42, 964-973.
[42] Fabrègue D., Mouawad B., Buttay C., Soueidan M., Lamontagne A., Forte R., Massardier-Jourdan V., (2012), Elaboration of architectured materials by spark plasma sintering, Materials Science Forum, 706-709, 1885-1892.
[43] Fecht H.J., (1995), Nanostructure formation by mechanical attrition, Nanostructured Materials, 6, 33-42.
[44] Fontana M.G., (2005), Corrosion Engineering. Tata McGraw-Hill.
[45] Fougere G.E., Weertman J.R., Siegel R.W., (1995), Processing and mechanical behavior of nanocrystalline Fe, Nanostructured Materials, 5, 127-134.
[46] Friedel J., (2001), Electronic structure of primary solid solutions in metals, Advances in Physics 3, 446-507.
[47] Fuloria D., Goel S., Jayaganthan R., Srivastava D., Dey G.K., Saibaba N., (2015), Mechanical properties and microstructural evolution of ultrafine grained zircaloy-4 processed through multiaxial forging at cryogenic temperature, Transactions of Nonferrous Metals Society of China, 25, 2221-2229.
[48] Gleiter H., (2000), Nanostructured materials: Basic concepts and microstructure, Acta materialia, 48, 1-29.
[49] Goodwin T.J., Yoo S.H., Matteazzi P., Groza J.R., (1997), Cementite-iron nanocomposite, Nanostructured Materials, 8 (5), 559-566.
[50] Groza J.R., Zavaliangos A., (2000), Sintering activation by external electrical field, Materials Science and Engineering A, 287 (2), 171-177.
[51] Groza J.R., (2007), Nanocrystalline powder consolidation methods, Nanostructured Materials: processing, properties and application, William Andrew Publishing, 173-233.

[52] Guang R., Jing-en Z., Shengqi X., Pengliang L., (2006), Formation of nanocrystalline and amorphous phase of Al-Pb-Si-Sn-Cu powder during mechanical alloying, Materials Science and Engineering A, 416, 45-50.

[53] Guo S., Chu A., Wu H., Cai C., Qu X., (2014), Effect of sintering processing on microstructure, mechanical properties and corrosion resistance of Ti-24Nb-4Zr-7.9Sn alloy for biomedical applications, Journal of Alloys and Compounds, 597, 211-216.

[54] Gupta R., Singh Raman R.K., Koch C.C., (2008), Grain growth behaviour and consolidation of ball-milled nanocrystalline Fe-10Cr alloy, Materials Science and Engineering A, 494, 253-256.

[55] Hadef F., Otmani A., Djekoun A., Grenèche J.M., (2011), Structural and microstructural study of nanostructured Fe50-Al40-Ni10 powders produced by mechanical alloying, Materials Characterization, 62, 751-759.

[56] Hall E.O., (1951), The deformation and ageing of mild steel: III Discussion of Results, Proceedings of the Physical Society. Section B, 64, 747.

[57] Han B.Q., Ye J., Tang F., Schoenung J., Lavernia E.J., (2007), Processing and behavior of nanostructured metallic alloys and composites by cryomilling, Journal of Materials Science, 42, 1660-1672.

[58] Hansen N., (2004), Hall-Petch relation and boundary strengthening, Scripta Materialia, 51, 801-806.

[59] Hillert M., (1965), On the theory of normal and abnormal grain growth, Acta Metallurgica, 13, 227-238.

[60] Hishinuma A., Isozaki S., Takaki S., Abiko K., (1997), Attractive characteristics of high-chromium iron-based alloys for nuclear reactor application, Applied Research, 160, 431-440.

[61] Hondros E.D., Seah M.P., Cahn R.W., Haasen P., (1983), Physical Metallurgy, 3rd edition. Elsevier Sci. Pub.

[62] Hongbin Xuan., Gongjun Cui., (2017), Tribological properties of Fe-Cr-B alloy for sliding boot in coal mining machine under dry sliding condition, Industrial Lubrication and Tribology, 69 (2), 142-148.

[63] Hulbert D.M., Anders A., Andersson J., Lavernia E.J., A.K. Mukherjee., (2009), A discussion on the absence of plasma in spark plasma sintering, Scripta Materialia, 60, 835-838.

[64] Hussein M.A., Suryanarayana C., Al-Aqeeli N., (2015), Fabrication of nano-grained Ti-Nb-Zr biomaterials using spark plasma sintering, Materials and Design, 87, 693-700.

[65] Hussein M.A., Suryanarayana C., Arumugam M.K., Al-Aqeeli N., (2015), Effect of sintering parameters on microstructure, mechanical properties and electrochemical behavior of Nb-Zr alloy for biomedical applications, Materials and Design, 83, 344-351.

[66] Jiang H.G., Rühle M., Lavernia E.J., (1999), On the applicability of the X-ray diffraction line profile analysis in extracting grain size and microstrain in nanocrystalline materials, Journal of Materials Research, 14, 549-559.

[67] Jiang J.Z., Gente C., Bormann R., (1998), Mechanical alloying in the Fe-Cu system, Materials Science and Engineering A, 242, 268-277.
[68] Kant R., Prakash U., Agarwala V., Satya Prasad V. V., (2016), Microstructure and wear behaviour of FeAl-based composites containing in-situ carbides, Bulletin of Materials Science, 39, 1827-1834.
[69] Khor K.A., Yu L.G., Andersen O., Stephani G., (2003), Effect of spark plasma sintering (SPS) on the microstructure and mechanical properties of randomly packed hollow sphere (RHS) cell wall, Materials Science and Engineering A, 356, 130-135.
[70] Kirchheim R., (2002), Grain coarsening inhibited by solute segregation, Acta Materialia, 50, 413-419.
[71] Kirchheim R., (2007), Reducing grain boundary, dislocation line and vacancy formation energies by solute segregation. I. Theoretical background, Acta Materialia, 55, 5129-5138.
[72] Koch C.C., (1997), Synthesis of nanostructured materials by mechanical milling: problems and opportunities, Nanostructured Materials, 9, 13-22.
[73] Koch C.C., (2007), Structural nanocrystalline materials: An overview, Journal of Materials Science, 42, 1403-1414.
[74] Koch C.C., Scattergood R.O., Vanleeuwen B.K., Darling K.A., (2012), Thermodynamic stabilization of grain size in nanocrystalline metals, Materials Science Forum, 716, 323-328.
[75] Koch C.C., Scattergood R.O., Darling K.A., Semones J.E., (2008), Stabilization of nanocrystalline grain sizes by solute additions, Journal of Materials Science, 43, 7264-7272.
[76] Koch C.C., Scattergood R.O., Saber M., Kotan H., (2013), High temperature stabilization of nanocrystalline grain size: Thermodynamic versus kinetic strategies, Journal of Materials Research, 28, 1785-1791.
[77] Koch C.C., Langdon T.G., Lavernia E.J., (2017), Bulk nanostructured materials, Metallurgical and Materials Transactions A, 48, 5181-5199.
[78] Kotan H., Darling K.A., Saber M., Koch C.C., Scattergood R.O., (2013), Effect of zirconium on grain growth and mechanical properties of a ball-milled nanocrystalline Fe-Ni alloy, Journal of Alloys and Compounds 551, 621-629.
[79] Kotan H., Saber M., Koch C.C., Scattergood R.O., (2012), Effect of annealing on microstructure, grain growth, and hardness of nanocrystalline Fe-Ni alloys prepared by mechanical alloying, Materials Science and Engineering: A, 552, 310-315.
[80] Krill C.E., Ehrhardt H., Birringer R., (2005), Thermodynamic stabilization of nanocrystallinity, Zeitschrift fuer Metallkunde/Materials Research and Advanced Techniques, 96, 1134-1141.
[81] Krill C.E., Klein R., Janes S., Birringer R., (1995), Thermodynamic Stabilization of Grain Boundaries in Nanocrystalline Alloys, Materials Science Forum, 179-181, 443-448.
[82] Krishna S.C., Gangwar N.K., Jha A.K., Pant B., (2013), On the prediction of strength from hardness for copper alloys, Journal of Materials, 1-6.

[83] Kumar A.P., Muthaiah V.M.S., Mula S., (2017), Effect of Nb, Y and Zr on thermal stability of nanocrystalline Al-4.5wt.% Cu alloy prepared by mechanical alloying, Journal of Alloys and Compounds, 722, 617-627.
[84] Kumar N., Rao P.N., Jayaganthan R., Brokmeier H.G., (2015), Effect of cryorolling and annealing on recovery, recrystallisation, grain growth and their influence on mechanical and corrosion behaviour of 6082 Al alloy, Materials Chemistry and Physics, 165, 177-187.
[85] Lacy C.E., Gensamer M., (1944), The tensile properties of alloyed ferrites, Transition. American Society of Metals, 32 (88).
[86] Leyla H.S.B., Ebrahim Mousavi S., Lavernia E.J., Schoenung J.M., (2015), The influence of grain size determination method on grain growth kinetics analysis, Advanced Engineering Materials, 17, 1598-1607.
[87] Li J., (2016), Improved corrosion resistance of novel Fe-based amorphous alloys, Materials and Design, 95, 225-230.
[88] Li J., Wang J., Yang G., (2009), On the stagnation of grain growth in nanocrystalline materials, Scripta Materialia, 60, 945-948.
[89] Li L., Saber M., Xu W., Zhu Y., Koch C.C., Scattergood R.O., (2014), High-temperature grain size stabilization of nanocrystalline Fe-Cr alloys with Hf additions, Materials Science and Engineering A, 613, 289-295.
[90] Li Q., (2003), Modeling the microstructure mechanical property relationship for a 12Cr - 2W -V-Mo -Ni power plant steel, 361, 385-391.
[91] Li Z., Zhang C., Liu L., (2015), Wear behavior and corrosion properties of Fe-based thin film metallic glasses, Journal of Alloys and Compounds, 650, 127-135.
[92] Libardi S., Leoni M., Facchini L., D'Incau M., Scardi P., Molinari A., (2007), Effect of the dispersion of nanometric silica particles on the thermal stability of a nanostructured iron based powder, Materials Science and Engineering A, 445-446, 244-250.
[93] Libardi S., Zadra M., Casari F., Molinari A., (2008), Mechanical properties of nanostructured and ultrafine-grained iron alloys produced by spark plasma sintering of ball milled powders, Materials Science and Engineering A, 478, 243-250.
[94] Lin Y., (2012), Strain energy during mechanical milling: Part I. Mathematical modeling, Metallurgical and Materials Transactions A, 43, 4247-4257.
[95] Liu D., (2010), Effect of ball milling time on microstructures and mechanical properties of mechanically-alloyed iron-based materials, Transactions of Nonferrous Metals Society of China, 20, 831-838.
[96] Liu F., Kirchheim R., (2004), Grain boundary saturation and grain growth, 51, 521-525.
[97] Mahmudi R., Sepehrband P., Ghasemi H.M., (2006), Improved properties of A319 aluminum casting alloy modified with Zr, Materials Letters, 60, 2606-2610.
[98] Malow T.R., Koch C.C., (1997), Grain growth in nanocrystalline iron prepared by mechanical attrition, Acta Materialia, 45, 2177-2186.
[99] Mamedov V., (2002), Spark plasma sintering as advanced PM sintering method, Powder Metallurgy, 45, 322-328.

[100] Mandal K., Yan A., Kerschl P., Handstein A., Gutfleisch O., Muller K.H., (2004), The study of magnetocaloric effect in R_2Fe_{17} (R = Y, Pr) alloys, Journal of Physics D: Applied Physics, 37,1-6

[101] Manna R., Mukhopadhyay N.K., Sastry G. V. S., (2012) On the mechanism of grain refinement during ECAP of Al, Materials Science Forum, 710, 241-246.

[102] Manna R., Mukhopadhyay N.K., Sastry G.V.S., (2008), Effect of equal channel angular pressing on microstructure and mechanical properties of commercial purity aluminum, Metallurgical and Materials Transactions A, 39, 1525-1534.

[103] Matijasevic M., (2007), Behaviour of Fe-Cr based alloys under neutron irradiation, Ames, 1-6. Metalurgija, 13(4), 245-250.

[104] Mccrea J.L., Palumbo G., Hibbard G.D., Erb U., (2003), Properties and applications for electrodeposited nanocrystalline Fe-Ni alloys, Advance Material Science, 252-258.

[105] McCrea J.L., Palumbo G., G.D. Hibbard, Aust K.T., Erb U., (2002), An initial analysis of mechanisms leading to late stage abnormal grain growth in nanocrystalline Ni, Scripta Materialia, 47, 83-87

[106] McLean D., (1957), Grain boundaries in metals. Clarendon Press, Oxford.

[107] Michael Ashby (2008), Materials: engineering, science, processing and design, 3rd edition, 23 (2).

[108] Michels A., Krill C.E., Ehrhardt H., Birringer R., Wu D.T., (1999), Modelling the influence of grain-size-dependent solute drag on the kinetics of grain growth in nanocrystalline materials, Acta Materialia, 47, 2143-2152.

[109] Miedema A.R., de Châtel P.F., de Boer F.R., (1980), Cohesion in alloys - fundamentals of a semi-empirical model, Physica B+C, 100, 1-28.

[110] Miedema A.R., de Châtel P.F., de Boer F.R., (1975), On the heat of formation of solid alloys, Journal of the Less-Common Metals, 41, 283-298.

[111] Mihalkovič M., Widom M., (2004), Ab initio calculations of cohesive energies of Fe-based glass-forming alloys, Condensed Matter and Materials Physics, 70, 1-12.

[112] Millett P.C., Selvam R.P., Saxena A., (2007), Stabilizing nanocrystalline materials with dopants, Acta Materialia, 55, 2329-2336.

[113] Moteff J., Bhargava R. K., McCullough W. L., (1975), Correlation of the hot-hardness with the tensile strength of 304 stainless steel to temperatures of 1200°C, Metallurgical and Materials Transactions A, 6, 1101-1104.

[114] Mukhopadhyay N.K., Mukherjee D., Bera S., Manna I., Manna R., (2008), Synthesis and characterization of nano-structured Cu-Zn γ-brass alloy, Materials Science and Engineering A, 485, 673-680.

[115] Mula S., Bahmanpour, H., Mal, S., Kang, P. C., Atwater M., Jian, W., Koch C. C., (2012), Thermodynamic feasibility of solid solubility extension of Nb in Cu and their thermal stability, Materials Science and Engineering A, 539, 330-336.

[116] Mula S., Setman D., Youssef K., Scattergood R.O., Koch C.C., (2015), Structural evolution of Cu(1-X)YX alloys prepared by mechanical alloying: Their thermal stability and mechanical properties, Journal of Alloys and Compounds, 627, 108-116.

[117] Mula S., Mondal K., Ghosh S., Pabi S.K., (2010), Structure and mechanical properties of Al-Ni-Ti amorphous powder consolidated by pressure-less, pressure-assisted and spark plasma sintering, Materials Science and Engineering A, 527, 3757-3763.
[118] Mula S., Sahani P., Pratihar S.K., Mal S., Koch C.C., (2011), Mechanical properties and electrical conductivity of Cu-Cr and Cu-Cr-4% SiC nanocomposites for thermo-electric applications, Materials Science and Engineering A, 528, 4348-4356.
[119] Mula S., Ghosh S., Pabi S.K., (2009), On the formation of phases by mechanical alloying and their thermal stability in Al-Mn-Ce system, Powder Technology, 191, 176-181.
[120] Mulukutla M., Sing A., Harimkar S., (2010), Spark plasma sintering for multi-scale surface engineering of materials, Multiscale Phenomena in Surfaces, 62. 65-71.
[121] Munir Z.A., (2006), The effect of electric field and pressure on the synthesis and consolidation of materials: A review of the spark plasma sintering method, Journal of Materials Science, 41, 763-777.
[122] Munir Z.A., Anselmi-Tamburini U., Ohyanagi M., (2006), The effect of electric field and pressure on the synthesis and consolidation of materials: A review of the spark plasma sintering method, Journal of Materials Science, 41, 763-777.
[123] Muñoz-Morris M.A., Garcia Oca C., Morris D.G., (2002), An analysis of strengthening mechanisms in a mechanically alloyed, oxide dispersion strengthened iron aluminide intermetallic, Acta Materialia, 50, 2825-2836.
[124] Murty B., Datta M., Pabi S., (2003), Structure and thermal stability of nanocrystalline materials, Sadhana Academy Proceedings, 28, 23-45.
[125] Muthaiah V.M.S., Koch C.C., Mula S., (2018), Effect of Nb addition on Fe-7Cr-Nb and Fe-15Cr- Nb metastable alloy formation and their thermal stability, Materials Research Express, 5, 1-14.
[126] Muthaiah V.M.S., Mula S., (2016), Influence of Cr and Y addition on microstructure, mechanical properties and corrosion resistance of SPSed Fe-based alloys, Metallurgical and Materials Transactions A, 49, 1-27.
[127] Muthaiah V.M.S., Babu L.H., Koch C.C., Mula S., (2016), Feasibility of formation of nanocrystalline Fe-Cr-Y alloys: Mechanical properties and thermal stability, Materials Characterization, 114, 43-53.
[128] Nes E., Ryum N., Hunderi O., (1985), On the Zener drag, Acta Metallurgica, 33, 11-22.
[129] Niessen K., Miedema A.R., de Boer F.R., Boom R., (1988), Enthalpies of formation of liquid and solid binary alloys based on 3d metals, Physica B, 151, 401-432.
[130] Ning J.L., Jiang D.M., Kim K.H., Shim K.B., (2007), Influence of texture on electrical properties of ZnO ceramics prepared by extrusion and spark plasma sintering, Ceramics International, 33, 107-114.
[131] Ningshen S., Gupta R.K., Kamal S., Chawla V., Chandra R., Mudali U.K., (2013), Corrosion study of ZrN deposited on 304L stainless steel, Surface Engineering, 29, 264-270.

[132] Noda M., Funami K., Suwahara Y., (2005), Effects of constraint and strain path on evolution of ultrafine grained microstructure by multi-axial alternative forging, Materials Science Forum, 475, 3471-3474.
[133] Nygren M., Shen Z., (2004), Spark plasma sintering: possibilities and limitations, Key Engineering Materials, 268, 719-724.
[134] Oka K., Ohnuki S.,Yamashita S., Akasaka N., Ohtsuka S., Tanigawa H., (2007), Structure of nano-size oxides in ods steels and its stability under electron irradiation, Materials Transactions, 48, 2563-2566.
[135] Omori M., (2000), Sintering, consolidation, reaction and crystal growth by the spark plasma system (SPS), Materials Science and Engineering A, 287, 183-188.
[136] Ouyang G., Ray P.K., Kramer M.J., Akinc M., (2017), Pressureless sintering of Mo-Si-B alloys with Fe additive, Journal of Materials Engineering and Performance, 26, 2417-2422.
[137] Pabi S.K., Joardar J., Murty B.S., (1996), Formation of nanocrystalline phases in the Cu-Zn system during mechanical alloying, Journal of Materials Science, 31, 3207-3211.
[138] Pabi S.K., Joardar J., Manna I., Murty B.S., (1997), Nanocrystralline phases in Cu-Ni, Cu-Zn and Ni-Al systems by mechanical alloying, Nanostructured Materials, 9, 149-152.
[139] Pasebani S., Charit I., (2014), Effect of alloying elements on the microstructure and mechanical properties of nanostructured ferritic steels produced by spark plasma sintering, Journal of Alloys and Compounds, 599, 206-211.
[140] Pavlina E.J., Van Tyne C.J., (2008), Correlation of yield strength and tensile strength with hardness for steels, Journal of Materials Engineering and Performance, 17, 888-893.
[141] Peckner D., Bernstein I.M., (1977), Handbook of stainless steel, 2nd Ed. New York: McGraw Hill Book.
[142] Pellicer E., (2011), Grain boundary segregation and interdiffusion effects in nickel-copper alloys: An effective means to improve the thermal stability of nanocrystalline nickel, ACS Applied Materials and Interfaces, 3, 2265-2274.
[143] Petch N.J., (1953), The cleavage strength of polycrystals, Journal of Iron Steel Institution, 174, 25-30.
[144] Porter D., Easterling K., (1992), Phase transformations in metals and alloys, Chapman & Hall, 439.
[145] Rafiei M., Enayati M.H., Karimzadeh F., (2013), Thermodynamic analysis of solid solution formation in the nanocrystalline Fe-Ti-Al ternary system during mechanical alloying, The Journal of Chemical Thermodynamics, 59, 243-249.
[146] Ray P.K., Akinc M., Kramer M.J., (2010), Applications of an extended Miedema's model for ternary alloys, 489, 357-361.
[147] Ray P.K., Ray P.K., Raja V.S., Murty B.S., Chattopadhyay K., (2006), Modelling and development of a horizontal vibratory rod mill for mechanical alloying: A first report, proceeding of national conference on Emerging Trends in nano technology and innovations in design and manufacturing, 2006, 321-332.

[148] Ray P.K., Brammer T., Ye Y.Y., Akinc M., Kramer M.J., (2010), A multi-stage hierarchical approach to alloy design, Journal of Materials, 62, 25-29.
[149] Ray P.K., Ye Y.Y., Akinc M., Kramer M.J., (2012), Effect of Nb and W substitutions on the stability of the $A_{15}Mo_3Si$ phase, Journal of Alloys and Compounds, 537, 65-70.
[150] Ringer S.P., Li W.B., Easterling K.E., (1989), On the interaction and pinning of grain boundaries by cubic shaped precipitate particles, Acta Metallurgica, 37, 831-841.
[151] Robles-Hernandez F.C., Calderon H.A., (2010), Nanostructured metal composites reinforced with fullerenes, Journal of Materials, 62, 63-68.
[152] Rogl G., (2012), High-pressure torsion, a new processing route for thermoelectrics of high ZTs by means of severe plastic deformation, Acta Materialia, 60, 2146-2157.
[153] Roy D., Mahesh B.V., Atwater M.A., Chan T.E., Scattergood R.O., Koch C.C., (2014), Grain size stability and hardness in nanocrystalline Cu-Al-Zr and Cu-Al-Y alloys, Materials Science & Engineering A, 598, 217-223.
[154] Roy D., Atwater M.A., Youssef K., Ledford J.C., Scattergood R.O., Koch C.C., (2013), Studies on thermal stability, mechanical and electrical properties of nano crystalline $Cu_{99.5}Zr_{0.5}$ alloy, Journal of Alloys and Compounds, 558, 44-49.
[155] Roy D., Deb P., Basumallick A., Basu B., (2009), Studies on optical property of Fe2O3 nano-particles synthesized by mechanical milling, Journal of Optics, 39, 102-109.
[156] Rybalka S.B., (2015), Kinetic model for hydrogen-induced direct phase transformations in R_2 Fe_{17} (R - Sm, Y) type alloys, 5, 437-441.
[157] Saber M., Kotan H., Koch C.C., Scattergood R.O., (2012), Thermal stability of nanocrystalline Fe-Cr alloys with Zr additions, Materials Science & Engineering A, 556, 664-670.
[158] Saber M., Scattergood R.O., Koch C.C., (2013), Thermal stability of nanocrystalline alloys by solute additions and a thermodynamic modeling, Materials Research Letters, 3, 65-75.
[159] Saber M., Xu W., Li L., Zhu Y., Koch C.C., Scattergood R.O., (2014), Size effect of primary Y_2O_3 additions on the characteristics of the nanostructured ferritic ODS alloys: Comparing as-milled and as-milled/annealed alloys using S/TEM, Journal of Nuclear Materials, 452, 223-229.
[160] Saenko I., Udovsky O.F.A., (2017), New thermodynamic assessment of the Fe-Y system, Journal of Phase Equilibria and Diffusion, 38, 684-699.
[161] Sahani P., Mula S., Roy P.K., Kang P.C., Koch C.C., (2011), Structural investigation of vacuum sintered Cu-Cr and Cu-Cr-4% SiC nanocomposites prepared by mechanical alloying, Materials Science and Engineering A, 528, 7781-7789.
[162] Salemi F., Abbasi M.H., Karimzadeh F., (2016), Synthesis and thermodynamic analysis of nanostructured CuNiCoZnAl high entropy alloy produced by mechanical alloying, Journal of Alloys and Compounds, 685, 113-116.
[163] Sarathi R., Sindhu T.K., Chakravarthy S.R., Jayaganthan R., (2007), Processing and characterization of nano aluminium powder using electric explosion process (EEP), IEEE Pulsed Power Plasma Science Conference, 327-327.

[164] Sasaki T.T., Ohkubo T., Hono K., (2009), Microstructure and mechanical properties of bulk nanocrystalline Al - Fe alloy processed by mechanical alloying and spark plasma sintering, Acta Materialia, 57, 3529-3538.
[165] Scandella F., Scandella R., (2004), Development of hardfacing material in Fe-Cr-Nb-C system for use under highly abrasive conditions, Materials Science and Technology, 20, 93-105.
[166] Schneibel J.H., Shim S., (2008), Nano-scale oxide dispersoids by internal oxidation of Fe -Ti-Y intermetallics, 488, 134-138.
[167] Sebayang D., (2011), Microstructure and mechanical properties of nanocrystalline Fe-Cr alloy prepared by spark plasma sintering, 54, 2197-2202.
[168] Shanmugasundaram T., Murty B.S., Subramanya Sarma V., (2006), Development of ultrafine grained high strength Al-Cu alloy by cryorolling, Scripta Materialia, 54, 2013-2017.
[169] Shashanka R., Chaira D., (2017), Effect of sintering temperature and atmosphere on nonlubricated sliding wear of nano-yttria-dispersed and yttria-free duplex and ferritic stainless steel fabricated by powder metallurgy, Tribology Transactions, 60, 324-336.
[170] Sheibani S., Heshmati-Manesh S., Ataie A., (2010), Structural investigation on nano-crystalline Cu-Cr supersaturated solid solution prepared by mechanical alloying, Journal of Alloys and Compounds, 495, 59-62.
[171] Shen T.D., (2007), Effect of solute segregation on the strength of nanocrystalline alloys: Inverse Hall-Petch relation, Acta Materialia, 55, 5007-5013.
[172] Shin C.S., Fivel M.C., Verdier M., Oh K.H., (2003), Dislocation-impenetrable precipitate interaction: A three-dimensional discrete dislocation dynamics analysis, Philosophical Magazine, 83, 3691-3704.
[173] Siegel R.W., (1995), Mechanical properties of nanophase metal, Nanostructure Materials, 6, 205-216.
[174] Singh R., Goel S., Verma R., Jayaganthan R., Kumar A., (2018), Mechanical behaviour of 304 austenitic stainless steel processed by room temperature rolling, IOP Conference Series: Materials Science and Engineering, 330, 012017
[175] Singh R., Kumar S., Mukhopadhyay N.K., Sastry G.V.S., Manna R., (2013), Development of bulk ultrafine-grained cold reducible grade low carbon steel produced by equal channel angular pressing, International Journal of Metallurgical Engineering, 2, 62-68.
[176] Song A.J., (2012), Grain growth and sintering characteristics of Ni-Cu alloy nanopowders consolidated by the spark plasma sintering method, Materials Science and Engineering A, 538, 219-223.
[177] Sooraj S., Muthaiah V.M.S., Kang P.C., Koch C.C., Mula S., (2016), Microstructural evolution and thermal stability of Fe-Zr metastable alloys developed by mechanical alloying followed by annealing, Philosophical Magazine, 96, 25.

[178] Sorour A.A., Strauss H.W., Chromik R.R., Brochu M., (2011), Microstructure and tribology of spark plasma sintered Fe-Cr-B metamorphic alloy powder, Tribology Letters, 44, 269-278.
[179] Wu SQ, Zhang C.H., Zhang S., Wang Q., (2018), Effect of Nb addition on microstructure and corrosion resistance of novel stainless steels fabricated by direct laser metal deposition, Materials Research Express 5, 036524.
[180] Srinivasan D., Corderman R., Subramanian P.R., (2006), Strengthening mechanisms (via hardness analysis) in nanocrystalline NiCr with nanoscaled Y_2O_3 and Al_2O_3 dispersoids, Materials Science and Engineering A, 416, 211-218.
[181] Stoller R.E., Zinkle S.J., (2008), On the relationship between uniaxial yield strength and resolved shear stress in polycrystalline materials, 287, 349-352.
[182] Suryanarayana C., Grant Norton M., (1998), X-ray diffraction a practical approach, Springer US.
[183] Suryanarayana C., (2001), Mechanical alloying and milling mechanical engineering, Progress in Materials Science, 46, 1-184.
[184] Suryanarayana C., Koch C.C., (2000), Nanocrystalline materials - Current research and future directions, Hyperfine Interactions, 130, 5-44.
[185] Taylor GI, (1934), The mechanism of plastic deformation of crystals Part I.-Theoretical, Proceeding of Royal Society A., 145-362.
[186] Tehrani F., Abbasi M.H., Golozar M.A., Panjepour M., (2011), The effect of particle size of iron powder on α to γ transformation in the nanostructured high nitrogen Fe-Cr-Mn-Mo stainless steel produced by mechanical alloying, Materials Science and Engineering A, 528, 3961-3966.
[187] Toop G.W., (1965), Extended Miedema's model for solid solution formation of ternary alloys, Transactions of the Metallurgical Society of AIME, 233, 850-855.
[188] Toor I.H., Ahmed J., Hussein M.A., Al-Aqeeli N., (2016), Optimization of process parameters for spark plasma sintering of nano-structured ferritic Fe-18Cr-2Si alloy, Powder Technology, 299, 62-70.
[189] Trelewicz J.R., Schuh C.A., (2009), Grain boundary segregation and thermodynamically stable binary nanocrystalline alloys, Physical Review B - Condensed Matter and Materials Physics, 79, 094112.
[190] Valiev R.Z., Islamgaliev R.K., Alexandrov I. V., (2000), Bulk nanostructured materials from severe plastic deformation, Progress in Materials Science 45, 103-189.
[191] VanLeeuwen B.K., Darling K., Koch C.C., Scattergood R.O., Butler B.G., (2010), Thermal stability of nanocrystalline $Pd_{81}Zr_{19}$, Acta Materialia, 58, 4292-4297.
[192] Wang W., Chen L. D., Kang Y.S., Niino M., Hirai T., (2000), Effect of plasma activated sintering (PAS) parameters on densification of copper powder, Materials Research Bulletin, 35, 619-628.
[193] Wang L., Li D.Y., (2003), Effects of yttrium on microstructure, mechanical properties and high-temperature wear behavior of cast Stellite 6 alloy, 255, 535-544.

[194] Wang Y., Chen M., Zhou F., Ma E., (2002), High tensile ductility in a nanostructured metal, Nature, 419, 912-915.
[195] Wang Z.M., Ma Y.T., Zhang J., Hou W.L., Chang X.C., Wang J.Q., (2008), Electrochimica Acta Influence of yttrium as a minority alloying element on the corrosion behavior in Fe-based bulk metallic glasses, 54, 261-269.
[196] Wang Z.M., Ma Y.T., Zhang J., Hou W.L., Chang X.C., Wang J.Q., (2008), Influence of yttrium as a minority alloying element on the corrosion behavior in Fe-based bulk metallic glasses, Electrochimica Acta, 54, 261-269.
[197] Weissmuller J., (1993), Alloy effects in nanostructures, Nanostructured Materials, 3, 261-272.
[198] Williams D.B., Carter C.B., (1996), The transmission electron microscope BT-transmission electron microscopy: A textbook for materials science, Boston, MA: Springer US, 3-17.
[199] Wynblatt P., Ku R.C., (1977), Surface energy and solute strain energy effects in surface segregation, Surface Science, 65 (2), 511-531.
[200] Xiao Z., Tang C., Zhao H., Zhang D., Li Y., (2012), Effects of sintering temperature on microstructure and property evolution of $Fe_{81}Cu_2Nb_3Si_{14}$ soft magnetic materials fabricated from amorphous melt-spun ribbons by spark plasma sintering technique, Journal of Non-Crystalline Solids, 358, 114-118.
[201] Xu J., Herr U., Klassen T., Averback R.S., (1996), Formation of supersaturated solid solutions in the immiscible Ni-Ag system by mechanical alloying, 79, 3935-3945.
[202] Xu W., Li L., Saber M., Koch C.C., Zhu Y., Scattergood R.O., (2015), Microstructures and stabilization mechanisms of nanocrystalline iron-chromium alloys with hafnium addition, Metallurgical and Materials Transactions A, 46, 4394-4404.
[203] Xu W.Z., Li L.L., Saber M., Koch C.C., Zhu Y.T., Scattergood R.O., (2014), Nano ZrO_2 particles in nanocrystalline Fe-Cr_{14}-$Zr_{1.5}$ alloy powders, Journal of Nuclear Materials 452, 434-439.
[204] Yang C., (2017), Influence of powder properties on densification mechanism during spark plasma sintering, Scripta Materialia, 139, 96-99.
[205] Yang K., Gao Y., Yang K., Bao Y., Jiang Y., (2017), Microstructure and wear resistance of Fe-Cr13-C-Nb hardfacing alloy with Ti addition, Wear, 376, 1091-1096.
[206] Youssef K.M., Scattergood R.O., Murty K.L., Koch C.C., (2004), Ultratough nanocrystalline copper with a narrow grain size distribution, Applied Physics Letters, 85, 929-931.
[207] Zhang H.W., Gopalan R., Mukai T., Hono K., (2005), Fabrication of bulk nanocrystalline Fe-C alloy by spark plasma sintering of mechanically milled powder, Scripta Materialia, 53 (7), 863-868.
[208] Zhang L., Sun D., Yu H., (2008), Effect of niobium on the microstructure and wear resistance of iron-based alloy coating produced by plasma cladding, Materials Science and Engineering A, 490, 57-61.

[209] Zhao Y.H., Horita Z., Langdon T.G., Zhu Y.T., (2008), Evolution of defect structures during cold rolling of ultrafine-grained Cu and Cu-Zn alloys: Influence of stacking fault energy, Materials Science and Engineering A, 474, 342-347.
[210] Zhu H., Averback R.S., (1996), Sintering of nano-particle powders: simulations and experiments, Materials and Manufacturing Processes, 11, 905-923.